COMPOSITION AND MICROSTRUCTURE EFFECTS ON SUPERPLASTICITY IN MAGNESIUM ALLOYS

A thesis submitted to the University of Manchester
for the degree of Doctor of Philosophy
in the Faculty of Engineering and Physical Sciences

2010

Hossain Mohammad Mamun Al Rashed
School of Materials

Contents

Final Word Count: 48448

List of Tables

List of Figures

Abstract

Magnesium is the lightest structural metal and magnesium alloys are therefore obvious candidates in weight critical applications. The environmental imperative to reduce vehicle emissions has recently led to intensified research interest in magnesium, since weight reduction is one of the most effective ways of improving fuel efficiency. The hexagonal close-packed structure of magnesium results in poor room temperature formability. However, on heating, several magnesium alloys show superplastic properties, with the ability to deform to very high strains (up to 3000%). This opens up the possibility of forming complex components directly by superplastic forming (SPF). As a result, SPF of magnesium is a highly active research topic. The most widely used class of magnesium alloys contain aluminium as the major alloying addition, which has a relatively high solubility in magnesium, and manganese, which has a less solubility. The effect of these elements on the deformation behaviour and failure mechanisms operating in the superplastic regime is not yet well understood. The objective of this work was to gain fundamental insights into the role of these elements. To do this, alloys with different aluminium content (AZ31 and AZ61) and manganese levels have been studied in-depth.

After casting, all alloys were subject to a hot rolling procedure that produced a similar fine grain size and texture in each material. Hot uniaxial testing was performed at temperatures between 300 to 450 °C and at two strain rates to investigate the material flow behaviour, elongation to failure and failure mechanism. All of the alloys exhibited flow curves characterised by an initial hardening and extensive flow softening region. Dynamic recrystallization did not occur, and the flow softening was attributed to grain growth and cavity formation. Increasing the level of aluminium in solution was observed to increase the grain growth rate, and also reduce the strain rate sensitivity. The elongation to failure, however, depended strongly on the manganese level but not on the aluminium content. This attributed to the role of manganese in forming coarse particles that act as sites for cavitation.

To study cavity formation and growth, and its effect on failure, a series of tests were conducted to different strain levels followed by investigation of cavitation in 3-dimensions using X-ray tomography. New methods were developed to quantify the correlation between cavities and coarse particles using X-ray tomography data and it was shown that over 90% of cavities are associated with particles. Cavity nucleation occurred continuously during straining, with progressively smaller particles forming cavities as strain increased. The mechanism of cavity formation and growth was identified, and it has been demonstrated that particle agglomerates are effective sites for cavity formation even when the individual particles in the agglomerates are below the critical size predicted by theory for cavity nucleation sites. These results suggest that to improve the ductility of magnesium alloys in the superplasticity regime, it is most critical to minimise the occurrence of particle agglomerates in the microstructure.

Declaration

No portion of the work referred to in the thesis has been submitted in support of an application for another degree or qualification of this or any other university or other institute of learning.

Copyright

i. The author of this thesis (including any appendices and/or schedules to this thesis) owns certain copyright or related rights in it (the "Copyright") and s/he has given The University of Manchester certain rights to use such Copyright, including for administrative purposes.

ii. Copies of this thesis, either in full or in extracts and whether in hard or electronic copy, may be made **only** in accordance with the Copyright, Designs and Patents Act 1988 (as amended) and regulations issued under it or, where appropriate, in accordance with licensing agreements which the University has from time to time. This page must form part of any such copies made.

iii. The ownership of certain Copyright, patents, designs, trade marks and other intellectual property (the "Intellectual Property") and any reproductions of copyright works in the thesis, for example graphs and tables ("Reproductions"), which may be described in this thesis, may not be owned by the author and may be owned by third parties. Such Intellectual Property and Reproductions cannot and must not be made available for use without the prior written permission of the owner(s) of the relevant Intellectual Property and/or Reproductions.

iv. Further information on the conditions under which disclosure, publication and commercialisation of this thesis, the Copyright and any Intellectual Property and/or Reproductions described in it may take place is available in the University IP Policy (see http://www.campus.manchester.ac.uk/medialibrary/policies/intellectual-property.pdf), in any relevant Thesis restriction declaration deposited in the University Library, The University Library's regulations (see http://www.manchester.ac.uk/library/aboutus/regulations) and in The University's policy on presentation of Theses.

Acknowledgements

I would like to thank my supervisor, Dr. Joseph D. Robson, for his wonderful guidance throughout the course of my research work. I am indebted to him for his continual encouragement and support to carry out the current study.

My appreciation extends to my co-supervisor, Prof Pete S. Bate, who provided inspiration and helped to understand the critical aspects of the current work. Lessons learnt from him about looking into problems from different perspectives were invaluable.

I would like to thank EPSRC and Magnesium Elektron for the financial support for the project.

I would like to acknowledge Dr. R. Bradley for his suggestions about tomography. I greatly appreciate the assistance from M. McDerby, J. S. Perrin and G. Leaver of Research Computing Services of the University of Manchester. I would also like to thank Dr. J. Fonseca for his guidance in Matlab and F. Garcia-pastor for his suggestions about data analysis. Thanks are due to the technical staff S. Dover, K. Gyves, M. Faulkner and workshop lads, and administrative staff O. Richert and S. Kershaw for their cooperation.

I would sincerely thank my colleagues in the Light Alloys Processing group for the enjoyable time I have passed with them. Special thanks go to A. Twier, Dr. O. Rofman, A. Antonysamy and L. Campbell for their help. I am grateful to my friends in Manchester, in particular Dr. J. Siddiqui and Dr. M. Tamal, for the wonderful time throughout the last couple of years.

I am grateful for the support and motivation from my parents and younger brother and thanks to them for believing in me.

Finally, I would like to thank Tanjila for her patience and support.

To my Parents

List of Symbols and Abbreviations

$\dot{\varepsilon}$	strain rate
μCT	X-ray micro-tomography
D_{GB}	grain boundary diffusion coefficient
D_L	lattice diffusion coefficient
Q_L	activation energy for lattice diffusion
Q_{GB}	activation energy for grain boundary diffusion
Q	activation energy
T	absolute temperature
V_c	cavity volume fraction
$\mathbf{b}$	Burgers vector
σ	true/flow stress
ε	true strain
d	grain size
e_f	elongation to failure
m	strain rate sensitivity
n	stress exponent
w	strain hardening coefficient
2D	2-dimensional
3D	3-dimensional
ANOVA	analysis of variance
BSE	back-scattered electron
CCD	charge-coupled device
CRSS	critical resolved shear stress
DRX	dynamic recrystallization
EBSD	electron back-scattered diffraction

ECAP	equal channel angular pressing
EDX	energy dispersive x-ray
GBS	grain boundary sliding
HPT	high pressure torsion
MSB	mean square between
MSE	mean square error
OPS	oxide particle suspension
PDF	probability distribution function
RD	rolling direction
SE	standard error
SEM	scanning electron microscopy
TA	tensile axis

Chapter 1

Introduction

Magnesium was discovered in 1808 by Sir Humphrey Davy, but it started to receive attention in mid-nineteenth century in Germany and its major use was in aircraft and military applications. During the post World War I era, magnesium gained some interest in the automobile industry, but remained mostly limited to military uses. For many years, magnesium was primarily used as an alloying element in aluminium alloy production industries and desulphurising of steel, with very limited use in wrought products, such as sheet, for the space industry. However, partly owing to the CAFE (Corporate Average Fuel Economy) legislation enacted by the US government and public interest in fuel-efficient vehicles, the demand of using magnesium in the automobile industry has increased in the twenty-first century. In fact, the demand for die-cast parts of magnesium has increased by 11.5% per year during the period of 1993 to 2003 (King, 2007). Recent increase in magnesium usage is largely due to the development of more corrosion resistant alloys and the decrease of magnesium prices by the cheap Chinese production route. Die-cast magnesium alloys made their way into the automobile arena, at first, in a Volkswagen car for the crankcases and the transmission housing shortly after World War II (Mordike et al., 2006). At present, heavy body components such as dashboard supports—made by steel—are being replaced by magnesium cast alloys. Some examples of other areas where cast alloys are being used include gearbox housings and engine blocks.

In contrast, wrought magnesium alloys have not yet achieved widespread applications in the automobile industry. Alloys made by rolling and extrusion were used from the mid-twentieth century in Samsonite luggage, military aircraft and space industries. But, in automobiles, the application of wrought alloys is still very limited (Aghion et al., 2001). The key reason is the poor room temperature formability due to basal slip and twinning being the only easy deformation modes at room temperature. Also, anisotropy and asymmetry of properties due to strong texture of the wrought materials make magnesium alloys difficult to process and design with, and thus less attractive. However, prototypes are being made from sheet products

Table 1.1: Usage of magnesium in western world in 2003 (King, 2007)

Application	**Usage**, kt	**Fractions of total**, %
Aluminium Alloying	140	36.18
Die Casting	137	35.40
Iron/Steel Desulphurising	70	18.09
Wrought	8	2.07
Gravity Casting	4	1.03
Others	28	7.24

for outer panels, such as doors, bonnets and boots and interior areas, such as inner door panels.

Table 1.1 shows the usage of magnesium in the western world in 2003 (King, 2007). It can be seen that only 2% of magnesium is used as wrought alloys and 25 to 30% of these wrought alloys are used as structural components (Bohlen et al., 2007).

The hexagonal closed-packed structure of magnesium and resultant limitation in easily activated slip systems limit its formability at room temperature. However, this can be improved by forming at higher temperatures, since extra slip systems are activated at elevated temperature. Such formability can be further improved by superplastic forming, allowing direct production of complex shapes. Superplasticity in a material is constrained by a set of limited temperature and strain rate ranges and microstructure. Modification of microstructure is obtained by thermo-mechanical treatments prior to forming. Superplastic forming can be an excellent route to produce finished products with a reduction of cost. Apart from the fact that this is a slow process, another key disadvantage of superplastic forming is the new establishment cost for fabrication and this can be compensated by the reduced labour, reduction in assembly tooling and most importantly, production of complex shapes in a single operation. Forming of complex shapes in a single operation has the benefit of reducing the weight of the whole part, since the number of connecting components—to assemble the part—is reduced.

Superplasticity in aluminium alloys has been investigated extensively in the last twenty years. But, comparatively, magnesium alloys have received less attention in this area. The recent interest in wrought magnesium products demands a thorough understanding of the alloys in the superplastic regime, since the knowledge of superplastic magnesium alloys needs to be developed to the level of aluminium alloys for comparison and replacement of aluminium parts. There are reports of excellent superplastic properties in certain magnesium alloys, but a detailed study on the mechanisms is still lacking. Most of the work on superplastic magnesium alloys tend

to report only on producing ultra-fine grained alloys and demonstrating excellent elongation to failure. This is partly to demonstrate the better performance compared to aluminium. As will be discussed in the next chapter, strain rate sensitivity is one of the prime factors controlling superplastic behaviour. It is, therefore, necessary to understand the effect of aluminium, the common alloying element in wrought magnesium alloys, on strain rate sensitivity. If higher sensitivity is obtained by adding aluminium, larger strains to failure are expected.

Despite having a large strain rate sensitivity, an alloy may fail early by cavitation. Though cavitation in a magnesium alloy during hot deformation was reported approximately 40 years ago, surprisingly, detailed studies of cavitation are very limited. The presence of particles is, in general, considered to provide sites for nucleation of cavities, but their influence on the formation of cavities in magnesium alloys is not yet understood. Temperature and strain induced grain growth also play important roles during cavitation. It is therefore necessary to understand the fundamental behaviour of cavitation during hot deformation of wrought magnesium alloys.

Two wrought alloys, AZ31 (Mg-3%Al-1%Zn) and AZ61 (Mg-6%Al-1%Zn), were studied at two different manganese contents. The alloys were cast in Magnesium Elektron, UK, followed by hot rolling to produce a refined microstructure. Uniaxial tensile tests were carried out at different test conditions from the sheet specimens. Observation of the failed specimens revealed that cavitation was the failure mode of the alloys. Consequently, a detailed study was performed on cavitation behaviour of the alloys by scanning electron microscopy. The inability of scanning electron microscopy for the determination of particle/cavity association was recognised and further examination was carried out by X-ray micro-tomography.

The study is divided into four parts. Chapter 2 contains a survey of literature for superplasticity and cavitation during hot deformation. Different mechanisms of superplasticity are highlighted and examples of superplasticity in magnesium alloys are introduced and compared with the known mechanisms of superplasticity. Subsequently, a substantial survey of cavitation during hot deformation is presented and the shortcomings of the limited cavitation studies in magnesium alloys are discussed. Together with the discussion of magnesium alloys in the superplastic regime and their cavitation behaviour, a justification is made for the current study.

Chapter 3 gives the experimental procedures applied for hot rolling, hot uniaxial tests, optical and scanning electron microscopy and X-ray micro-tomography of the materials. The statistical methods used are also briefly mentioned. Since tomography is a new field in materials science, a short note on the principles of tomography is presented and followed by the methodology used for reading raw data from tomography.

Chapter 4 includes the results of hot deformation behaviour of the alloys investigated. At first, the refinement of grain size by hot rolling is discussed followed by flow characteristics of the alloys under different temperatures and strain rates. Gauge regions of the tensile specimens are shown and the evidence of concurrent grain growth is outlined. By analysis of variance (ANOVA), the contribution of aluminium and manganese contents on strain rate sensitivity is also estimated. Together with the strain rate sensitivity of flow and grain growth observations, a final judgement on the mechanisms of superplasticity is presented. It is however noteworthy that the alloys investigated in this project did not show true superplastic properties, such as very high strains to failure or strain rate sensitivity values typical of superplastic alloys, in the applied test temperature and strain rate ranges. As the results obtained from this work did not show true superplastic properties and cavitation was identified to govern failure of the test materials, the focus of this project was modified to a detailed cavitation study.

Chapter 5 gives a detailed study on cavitation behaviour of the alloys. Examinations of the gauge regions were performed at different pre-set strains and qualitative and quantitative analyses are presented using optical and scanning electron microscopy. The need for three-dimensional investigation in the cavitation study is identified and an examination of cavities and particles is performed by X-ray micro-tomography. Methodologies developed for the determination of particle/cavity association are outlined and applied to determine the existence of any true particle/cavity association. Using the raw data from tomography, true particle and cavity dimensions, their orientations with the stress axis and their shapes are also determined. Combining the data from scanning electron microscopy and tomography, the nucleation sites and growth of cavities are investigated in depth.

In the final chapter, the key points, extracted from this study of hot deformation and cavitation analysis, are presented.

Chapter 2

Literature Review

2.1 Magnesium and Its Alloys

Magnesium is an alkaline earth metal having an atomic number of 12. The crystal structure of magnesium is hexagonal close-packed (hcp). In Fig. 2.1, a unit cell of magnesium is shown with the atomic arrangement of alternative atom stacking layers of ABAB, where the lattice parameters are $a = b \neq c$. In an ideal stacking of atoms in ABAB layers in an hcp structure, the c/a ratio is 1.633. The c/a ratio of magnesium is 1.6236 (von Batchelder and Raeuchle, 1957), very close to that of an ideal hexagonal unit cell. A key advantage of magnesium is the atomic diameter of 0.32 nm which allows favourable solid solutions with several metals, such as aluminium and zinc. The low density of magnesium ($1.738\,\mathrm{g\,cm^{-3}}$) makes it the lightest structural metal (approximately 35% lower density than aluminium).

Inherently, the hcp crystal structure of magnesium restricts the number of independent slip systems and hence deformation at room temperature is limited. This is discussed further in Section 2.1.3. Mechanical properties of pure magnesium are comparatively poor. Tensile yield strength and elongation to failure (e_f) of a rolled sheet of 99.90 wt% magnesium are approximately 115 to 140 MPa and 2 to 10% respectively at room temperature (Erickson, 1990). To enhance such mechanical properties and deformability, it is therefore necessary to add some alloying elements which can modify certain characteristics of the pure material by solid solution strengthening, precipitation hardening or grain size refinement.

2.1.1 Classification of Magnesium Alloys

The ASTM (American Society for Testing Materials) adopted method for designating magnesium alloys is widely used. The first part of the designation contains letter codes for two major alloying elements and the second part consists of the nominal compositions (in wt%) of those major elements, rounded to whole numbers. The

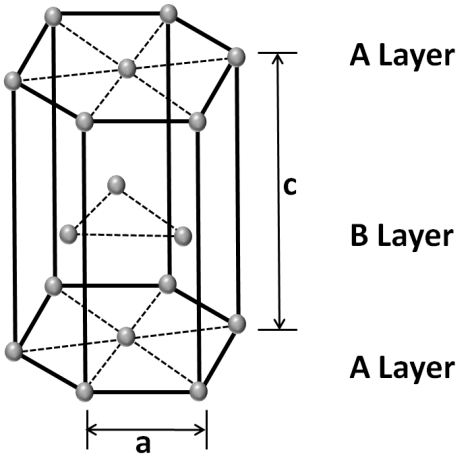

Figure 2.1: A schematic diagram of hcp unit cell of magnesium. c/a ratio is arbitrary in this schematic diagram.

letter codes for major alloying elements are given in Table 2.1. The letter codes are in a descending order, depending on the amount of each element present.

A third part is introduced in the classification system to separate different alloys containing similar amounts of major alloying elements. This part is a single letter code except I and O. A fourth part may be included to show the temper condition. For example, F, O, H23 and T6 represent as fabricated, annealed, strain hardened (and partially annealed) and solution heat treated (and artificially aged) conditions.

An example following this classification system is AZ91E-T6. It indicates the alloy contains approximately 9% aluminium (Al) and 1% zinc (Zn) in wt% and it is ranked as the fifth alloy (E) having a similar composition of 9% Al and 1% Zn. The last part, T6, symbolizes the heat treatment condition.

Magnesium alloys are used in both cast and wrought forms. Depending on the end application of a product, different alloying elements are added to magnesium. Wrought alloys are essentially the low composition variants of cast alloys due to the lack of intensive research in magnesium alloy development. However, since each type of cast and wrought alloys serves a distinctive role, cast and wrought alloys are discussed below in separate sections.

2.1.1.1 Magnesium Cast Alloys

The most common cast alloys belong to aluminium-zinc-manganese (AZ), aluminium-manganese (AM) and aluminium-silicon-manganese (AS) series (Kainer and von Buch, 2003). Among them, AZ91 (Mg-9Al-1Zn-0.25Mn) and AM60 (Mg-6Al-0.4Mn) are the most frequent used in casting.

AZ alloys are the single most widely used family of cast magnesium alloys. AZ91D (Mg-9Al-0.7Zn-0.13Mn), a variant of AZ91, provides satisfactory level of strength

Table 2.1: Letter codes for major alloying elements of magnesium alloys

Letter Code	**Element**	**Example**	**Composition** (wt%)[a]
A	Aluminium	AZ31	3Al-1Zn
C	Copper	ZC63	6Zn-3Cu
E	Rare Earth (RE)	EQ21	2.1Di-1.5Ag
H	Thorium	HK31	3Th-0.6Zr
K	Zirconium	K1A	0.7Zr
L	Lithium	LA141	14Li-1Al
M	Manganese	AM60	6Al-0.13Mn
Q	Silver	QE22	2.5Ag-2RE
S	Silicon	AS41	4.3Al-1Si
W	Yttrium	WE43	4Y-3.4RE
Z	Zinc	ZK61	6Zn-0.7Zr

[a] Remaining is magnesium and some minor inclusions of other alloying elements.

at room temperature, good castability and moderate corrosion resistance in salt-water (Housh et al., 1990). AZ91E (Mg-8.7Al-0.7Zn-0.13Mn), a high-purity variant of AZ91, containing lower amount of iron, nickel and copper, gives better resistance to corrosion in salt-water (Polmear, 2006). In AZ alloys, the $Mg_{17}Al_{12}$ phase is formed in the as-cast condition when the aluminium content is greater than 2%. Heat treatment at 420 °C can dissolve this phase in solution, contributing to solid solution strengthening. Though this phase is beneficial for strengthening, its presence is responsible for lowering of elongation to failure (e_f), especially when the aluminium content is greater than 8% (Polmear, 2006).

If an application requires higher ductility and fracture toughness, then AM alloys (containing 0.2 to 0.4 manganese) become an alternative option. One such alloy, AM60B (Mg-6Al-0.13Mn), has a lower aluminium content than AZ91D, but yield strength and tensile strength are comparable to AZ91D (Housh et al., 1990). The improvement in e_f arises from the reduction of the volume fraction of the $Mg_{17}Al_{12}$ phase at grain boundaries. AM alloys are used in wheels, seat frames and steering wheels in automobiles.

A major drawback of AZ alloys is their poor creep resistance. They provide good resistance up to a maximum of 110 to 120 °C (Polmear, 2006). Alloys of AS series can provide better creep resistance up to 150 °C (Mordike et al., 2006) by reducing the amount of thermally unstable $Mg_{17}Al_{12}$ phase and forming the highly stable Mg_2Si phase. AS41 (Mg-4Al-1Si-0.4Mn) was used in the crankcases of the Volkswagen Beetle, which for a long time was the single largest application for magnesium alloys.

An improvement in creep resistance of alloys containing aluminium as the prime

Table 2.2: Tensile properties of selected cast magnesium alloys at room temperature (Housh et al., 1990; Mordike et al., 2006; Pekguleryuz and Kaya, 2003)

Alloy	**Tensile Strength**, MPa	**Elongation to Failure** (e_f)
AZ91D	250	7
AM60	240	13
AS41	215	6
AE42	230	11
WE43	260	6
QE22	260	3

alloying element is obtained by addition of rare earth (RE) elements—conventionally denoted as the AE series. These alloys form a very thermally stable phase—$Al_{11}RE_3$—which provides resistance to sliding of grains (Pettersen et al., 1996). Higher addition of RE reduces total aluminium available to form $Mg_{17}Al_{12}$ and this gives better creep resistance. However, above 175 °C, creep resistance is poor since $Al_{11}RE_3$ starts to decompose to Al_2RE. As a consequence, more $Mg_{17}Al_{12}$ can precipitate (Polmear, 2006).

To obtain creep resistance at temperatures >200 °C, the most promising alloys are the QE and WE series. But, their low castability and higher price associated with the alloying elements limit the application of these alloys particularly to sophisticated fields such as aircraft and space industries. For example, QE22 (Mg-2.5Ag-2RE-0.7Zr) is used in aircraft landing wheels, gearbox housing, helicopter rotor fittings and WE43 (Mg-4Y-2.25Nd-1RE-0.4Zr) finds its applications in racing car engines and helicopter transmission castings.

Table 2.2 shows tensile strength and e_f of selected cast magnesium alloys at room temperature.

2.1.1.2 Magnesium Wrought Alloys

Contrary to cast alloys, wrought magnesium alloys have received less attention, owing to the lack of interest from industries. The annual consumption of wrought alloys in western world is approximately only 2% of total usage of magnesium, whereas die-cast products occupy 35% (Table 1.1). Sheet alloys (of steel and aluminium alloys) are used in body parts for automobiles and constitute approximately 25% of total vehicile weight (Doege et al., 2003). Magnesium alloys, being lighter than steel and aluminium in sheet form, could become widely used if available with properties comparable to steel and aluminium alloys and of course, at a competitive price.

In cast alloys, the major concern is castability and creep resistance up to a certain

temperature. On the other hand, the key factor for wrought alloys is their formability. The intrinsic restriction to plastic deformation of a magnesium alloy comes from the hcp crystal structure of magnesium, limiting its deformation at room temperature (see Section 2.1.3).

Due to the lack of commercial interest and research in magnesium alloys, only a few wrought specific alloys have been developed, which are essentially the lower alloying element varieties of cast alloys. The major alloying elements in magnesium alloys form intermetallics at different temperatures, which may result in incipient melting and hot cracking during thermo-mechanical treatments. This is one of the reasons for using a lower fraction of aluminium in wrought AZ alloys. To date, the major consumption of sheet products is in the photoengraving industries and extruded products find their main usage in electrochemical applications—as a sacrificial anode (Agnew, 2004).

Commercially used wrought alloys are dominated by the aluminium, zinc and manganese containing alloys. The two alloy series most widely used are the AZ and ZK alloys.

Alloys containing zinc and zirconium (ZK series) usually have the highest strength amongst the commercially used non rare-earth magnesium wrought alloys, but their failure strain compared to AZ alloys is slightly worse at room temperature. Zirconium provides grain refinement and hence, strength is comparatively better in ZK series alloys. One such alloy, ZK60, has received commercial interest.

In the AZ series, AZ31 and AZ61 have received the most interest and research to improve their processing window and understand their formability. Table 2.3 shows the room temperature tensile properties of some wrought alloys. Increasing aluminium content improves tensile strength, but a trade-off is required between strength and forming of the alloy since higher aluminium content needs higher extrusion loads and lower ram speeds (Davies and Barnett, 2004). To produce finished product from the wrought alloys, superplastic forming is an alternative route and the standard AZ magnesium alloys can be commercially processed to give a satisfactory fine grain structure to enable them to show superplastic properties. To date, there is no single magnesium alloy developed solely to meet the requirements of superplastic forming. Hence, commercially used AZ31, AZ61 and ZK60 alloys are being investigated extensively to understand their superplastic behaviour.

2.1.2 Effects of Alloying Elements

It was mentioned earlier that the atomic diameter of magnesium allows suitable alloying with different elements. One such example is aluminium (atomic diameter is 0.282 nm). The atomic mismatch is approximately 13% and aluminium provides a

Table 2.3: Room temperature tensile properties of selected wrought alloys (Polmear, 1994; Stalmann et al., 2001)

Alloy	Tensile Strength, MPa	Elongation to Failure, (e_f)
AZ31	240	11
AZ61	270	9
ZK60	315	8
MA18	210	30

solid solution strengthening effect when added to magnesium. Another such element is zinc (atomic diameter is 0.276 nm) which provides even better solute strengthening. The current study focuses on AZ alloys. The major alloying elements in these alloys are aluminium, zinc and manganese at variable amounts. The effects of these elements in alloying with magnesium are discussed below.

Aluminium

The maximum solubility of aluminium is 12.7 wt% in magnesium (Fig. 2.2a). Castability is improved with increasing aluminium since it improves fluidity of the melt (Luo and Pekguleryuz, 1994). In contrast, increasing aluminium content increases the freezing range and thus increases the chances of shrinkage porosity (Luo and Pekguleryuz, 1994). At room temperature, the maximum tensile strength is obtained at 8 to 10 wt% aluminium content (Polmear, 2006).

The solubility of aluminium is reduced from 12.7 wt% to approximately 2 wt% at room temperature. This causes precipitation of brittle $Mg_{17}Al_{12}$ (44 wt% Al) phase which has an adverse effect on properties. This low melting point (437 °C) eutectic phase can reduce creep resistance. This phase may form as a continuous network around grain boundaries or discontinuous precipitation at boundaries, when the cooling rate is slow.

The $Mg_{17}Al_{12}$ phase is precipitated on basal planes during ageing and is not very effective at blocking basal dislocations (Clark, 1968). Moreover, this phase precipitates as large laths during ageing and the ageing response is thus poor (Celotto, 2000). For this reason, addition of zinc (discussed below) is sometimes favoured to strengthen the alloy.

Zinc

The second important alloying element in AZ alloys is zinc. Maximum solubility of zinc in magnesium is 6.2 wt% (Fig. 2.2b). Like aluminium, it also enhances fluidity of the melt. Zinc improves strength by solid solution strengthening by increasing the critical resolved shear stress (CRSS) for basal slip (Polmear, 2006). Zinc is a more efficient solute solution strengthening element than aluminium, as it forms

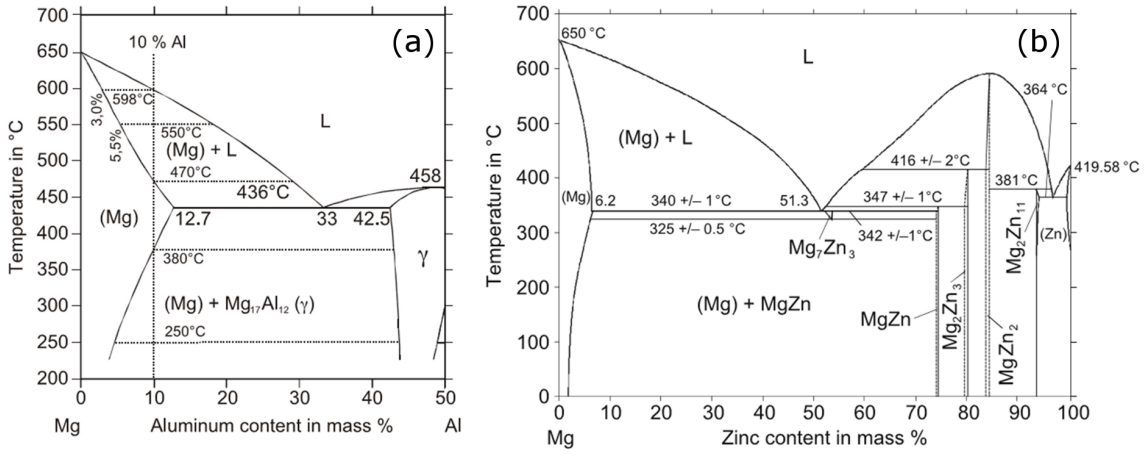

Figure 2.2: Magnesium rich corner of binary phase diagrams of (a) Mg-Al and (b) Mg-Zn (Mordike and Lukac, 2006).

regions of short-range order at the atomic scale (Càceres and Blake, 2002). However, the addition of zinc reduces the CRSS for prismatic slip (Akhtar and Teghtsoonian, 1969), which can improve ductility when prismatic slip operates. The possibility of hot-cracking puts a limit on the higher addition of zinc. To maintain the fluidity of the melt to a satisfactory level, the addition of maximum 1 to 2% zinc is suggested in AZ alloys (Luo and Pekguleryuz, 1994). At this level of addition, zinc remains in solution and does not contribute to age hardening.

Manganese

The maximum solubility of manganese in magnesium is 2.2 wt% (Fig. 2.3a). Manganese is generally added to form denser (compared to molten metal) intermetallics with some harmful impurity elements, such as iron, which partially removes these elements from the melt leading to an increased corrosion resistance in the solid metal. In AZ alloys containing manganese, precipitates of different proportion of aluminium and manganese are formed. Al-Mn particles are often considered as a nucleant for magnesium grains from the melt (Kim et al., 2007). However, the efficiency of one such precipitate—Al_8Mn_5 particles—as a nucleant of magnesium grains is a matter of debate, since atomic mismatch energy between Al_8Mn_5 and magnesium crystal close-packed planes is very high (Fan et al., 2009; Zhang et al., 2005).

Fig. 2.3b shows a magnesium-rich phase diagram for the Mg-3.1Al-1.3Zn-Mn system. There is a narrow temperature range over which the Al_8Mn_5 and $Al_{11}Mn_4$ phase coexist. Otherwise, either the $Al_{11}Mn_4$ or Al_8Mn_5 phase may form.

2.1.3 Deformation Systems of Magnesium Alloys

Deformation of magnesium is constrained by its hcp crystal structure. As a consequence, due to the lack of sufficient slip systems operating ductility is inherently

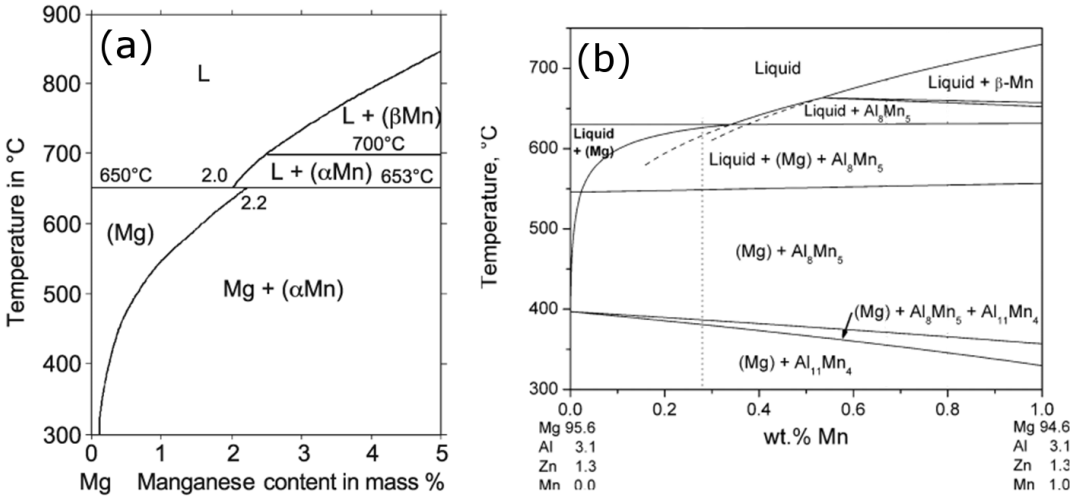

Figure 2.3: (a) Mg-rich binary phase diagram of Mg-Mn system (Mordike and Lukac, 2006). (b) Thermodynamic model predicted Mg-rich part of the phase diagram of Mg-Al-Zn-Mn system (Laser et al., 2006).

limited at low temperature, unlike in cubic metals. However, ductility is greatly enhanced by deformation at elevated temperature, when additional slip systems become active. Understanding the characteristics of deformation of magnesium is of particular interest, since activation of different slip systems and twinning (depending on temperature) controls the mechanical properties.

Deformation of magnesium may occur by slip, twinning or grain boundary sliding (GBS). GBS is discussed in Section 2.3.2. Slip and twinning systems in magnesium crystal are discussed below. Based on the deformation behaviour of magnesium single crystals, the deformation characteristics of polycrystalline magnesium alloys are discussed, including dynamic recrystallization (DRX) phenomenon during thermo-mechanical treatment of magnesium alloys.

2.1.3.1 Slip

Slip is a mechanism by which plastic deformation occurs by sliding or translation of blocks of crystal along the most favourably oriented crystallographic planes (Dieter, 2001). Slip typically involves movement of dislocations along the close-packed crystallographic direction (slip direction) in a plane having the highest atomic density (slip plane). The combination of slip plane and slip direction is termed as a slip system. In magnesium, the basal (0001) plane has the highest atomic density and $\langle 11\bar{2}0 \rangle$ directions are the close-packed directions (Dieter, 2001). Therefore, slip ordinarily occurs in magnesium crystal on basal plane along the $\langle 11\bar{2}0 \rangle$ directions. The extent of slip depends on the shear stress developed by the applied stress, crystal geometry and orientation of slip planes with the direction of shear stress. Slip initiates when the shear stress reaches a minimum value—known as the critical resolved shear stress

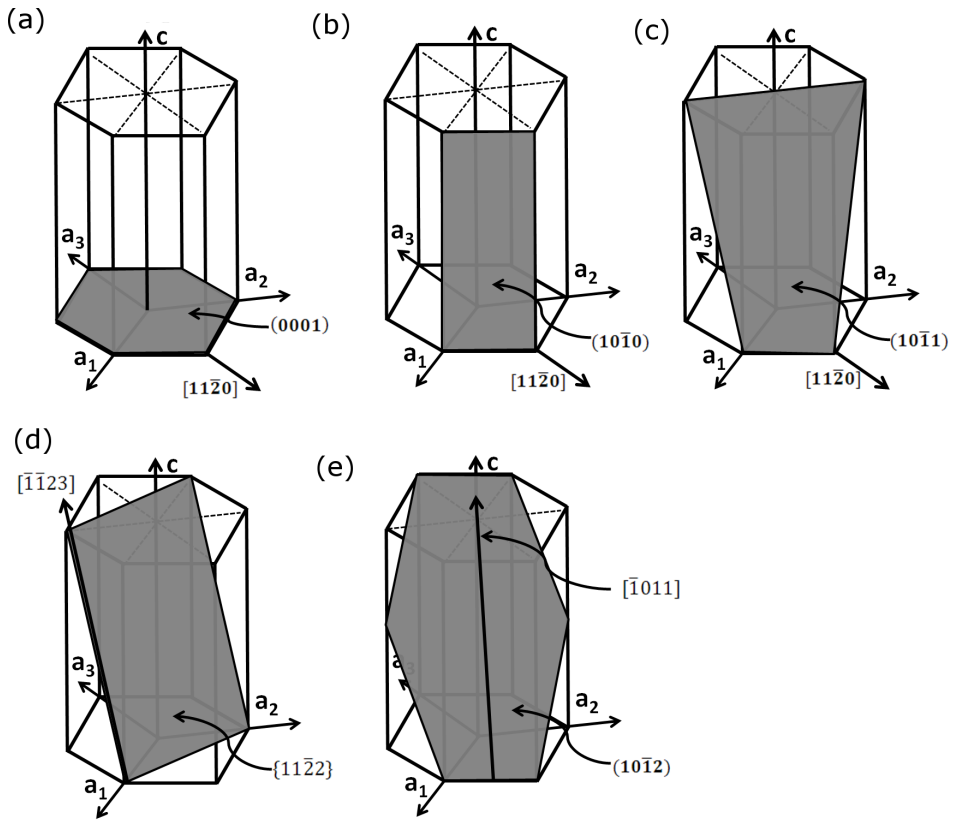

Figure 2.4: Slip and twinning systems in a magnesium crystal are shown for (a) basal $(0001)\langle 11\bar{2}0\rangle$; (b) prismatic $\{10\bar{1}0\}\langle 11\bar{2}0\rangle$; (c) first order pyramidal $\{10\bar{1}1\}\langle 11\bar{2}0\rangle$; (d) second order pyramidal $\{11\bar{2}2\}\langle 11\bar{2}3\rangle$ slip systems and (e) tension twinning $\{10\bar{1}2\}$ $\langle 10\bar{1}1\rangle$

(CRSS). Fig. 2.4 shows the slip systems in a unit cell of magnesium.

According to the von Mises criterion for homogeneous plastic deformation, five independent slip systems, giving five independent deformation modes, are required to produce a general shape change. In brief, there are five independent components of a strain tensor, considering no volume change during deformation. Operation of a single slip system produces a single component of the strain tensor. Therefore, operation of five independent slip systems is necessary to develop an arbitrary strain (Groves and Kelly, 1963). The basal slip system in magnesium provides two independent deformation modes (arranged in three ways). It was mentioned earlier that basal slip is dominant at room temperature. Clearly, this system alone does not fulfil the homogeneous plasticity criterion and is a key reason for poor formability of magnesium at room temperature. If prismatic slip system becomes operational, two more independent deformation modes are available, which still does not meet the requirement of the von Mises criterion. To obtain five independent deformation modes, activation of first order pyramidal slip system is necessary which gives four independent systems, arranged in nine different ways. However, even with activation of all these modes, magnesium alloys can still show poor ductility when tested in

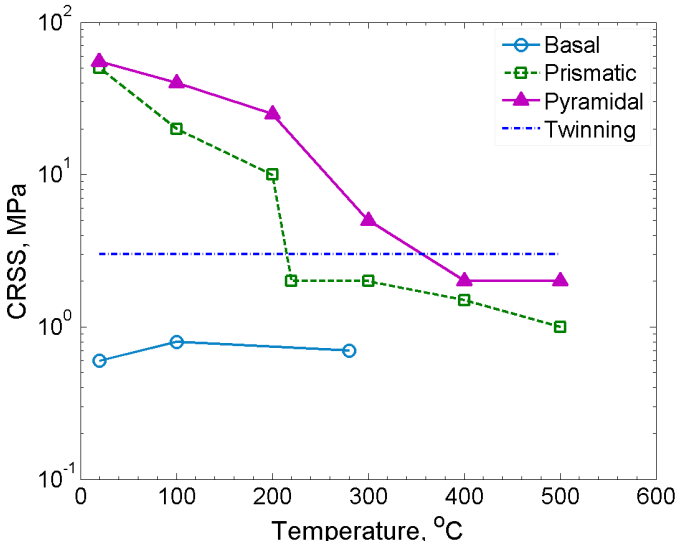

Figure 2.5: A schematic presentation of critical resolved shear stress (CRSS) of different slip systems and twinning in a semi-logarithmic plot. It is drawn based on a summary of CRSS presented elsewhere (Barnett, 2003). It should be noted that for the pyramidal plot, only $\langle c+a \rangle$ slip was considered.

certain directions because none of these systems provides deformation parallel to the c-axis. To accommodate strain in this direction requires second order pyramidal slip or twinning, as discussed later.

The CRSS of different slip systems is shown in Fig. 2.5 for a range of temperature. CRSS of non-basal slip systems is decreased substantially at >200 °C.

Dislocations having Burgers vector of type $1/3\langle 11\bar{2}0 \rangle$ are referred to as $\langle a \rangle$ dislocations. Since $\langle a \rangle$ slip occurs in a direction parallel to the basal plane, it cannot accommodate any deformation out of the basal plane. To accommodate deformation along the c-axis, a slip vector in that direction is necessary. Dislocations having Burgers vector of type $1/3[11\bar{2}3]$ are designated as $\langle c+a \rangle$ dislocations. One such example is the second order pyramidal slip system, $\{11\bar{2}2\}\langle 11\bar{2}3 \rangle$, observed under a constrained condition of c-axis compression (Obara et al., 1973). c-axis compression means stress is applied parallel to the c-axis to cause a contraction in this direction. Slip of $\langle c+a \rangle$ type becomes important in magnesium, since hot rolling produces a bulk texture where c-axis of the grains is preferentially oriented normal to the sheet plane. If stress is applied in the normal direction (perpendicular to c-axis), accommodation of deformation cannot occur by $\langle a \rangle$ slip. In such a condition, $\langle c+a \rangle$ slip or twinning is required. However, the CRSS of this $\langle c+a \rangle$ slip at room temperature is much higher than basal slip (Fig. 2.5). The activation of $\langle c+a \rangle$ slip plays a key role in enhancing ductility (Agnew et al., 2001; Al-Samman, 2009). In AZ31 alloys, $\langle c+a \rangle$ slip is highly active when the temperature reaches 300 °C (Yi et al., 2010).

In summary, owing to its hcp structure, magnesium lacks five independent systems

required for homogeneous deformation. At room temperature, basal slip is the only easily activated slip systems during deformation, owing to its very low CRSS. This provides only two independent systems. When deformation is accomplished at elevated temperatures, non-basal $\langle a \rangle$ and pyramidal $\langle c + a \rangle$ slips are more active as the CRSS values are lowered. Operation of $\langle c + a \rangle$ slip is the only slip mode capable of accommodating strain out of the basal plane.

2.1.3.2 Twinning

Twinning is a deformation mechanism where deformation of a portion of crystal leads to a symmetric orientation related to the orientation of the undeformed portion of the crystal (Dieter, 2001). Atoms experience a coordinated shear displacement in such a way that the twinned region has a mirror-image relationship to the untwinned part of the lattice. Twinning occurs on certain crystallographic planes and only in a direction which produces a mirror image of the neighbour lattice. Twinning can only provide a limited total strain, which depends on the twin shear and orientation. However, twinning may reorient material in a way that promotes some slip activity (Christian and Mahajan, 1995) and gives a secondary effect on plasticity.

Due to the lack of sufficient independent slip systems for plasticity at room temperature, twinning appears as an important deformation mode in magnesium. Twinning at room temperature in magnesium occurs when deformation cannot be accommodated by basal slip, and it is particularly important when stress is applied parallel to the c-axis.

Activation of a twin depends on the direction of the applied stress, in other words, it depends on the extension or contraction of c-axis of a crystal. $\{10\bar{1}2\}\langle 10\bar{1}1\rangle$ tensile twins are usually observed, under the condition of c-axis extension (Wang and Huang, 2007). c-axis extension means the stress is applied in a tensile sense parallel to the c-axis of a crystal. The $\{10\bar{1}2\}$ twin is the most easily activated twinning mode in magnesium. Activation of this mode leads to an 86° reorientation of the lattice in the twin relative to the parent material.

In contrast, $\{10\bar{1}1\}-\{10\bar{1}2\}$ double twins ($\{10\bar{1}2\}$ twins are formed in the interior of $\{10\bar{1}1\}$ twins) are observed under a condition of c-axis compression (Nave and Barnett, 2004). Due to the polar nature of twins, a tension twin cannot accommodate strain by c-axis compression. There are other possible c-axis compression twins in magnesium, e.g., $\{30\bar{3}4\}\langle 20\bar{2}3\rangle$ and $\{10\bar{1}3\}\langle 30\bar{3}2\rangle$ (Reed-Hill and Robertson, 1957), but these are hard to activate and rarely seen. One adverse effect of the compression double twins is that they reorient the material in the double twin favourably for basal slip. For an AZ31 rolled sheet, the occurrence of $\{10\bar{1}1\}-\{10\bar{1}2\}$ double twins has been shown to lead to premature failure at room temperature (Ando et al., 2010).

The extent of twinning also depends on grain size. Ecob and Ralph (1983) showed

Table 2.4: Relative CRSS for pure magnesium, AZ31 and AZ61 (Lou et al., 2007)

Material	τ_{twin}/τ_{basal}	$\tau_{prismatic\langle a\rangle}/\tau_{basal}$
Mg	2.5–4.4	48–87
AZ31	3	5.5
AZ61	-	1.5–2

for a zinc alloy that the contribution of twinning increased linearly with grain size, i.e., a lower fraction of twinning is developed in fine-grained alloys. A transition from twin dominated flow to slip deformation occurs in magnesium by reducing the Hall-Petch slope of the yield stress with decreasing grain size and/or increasing temperature (Barnett et al., 2004).

The relative CRSS for different slip systems and twinning at room temperature are summarised for pure magnesium, AZ31 and AZ61 alloys in Table 2.4.

In summary, twinning provides an extra independent mode of deformation in magnesium, but provides only limited strain and is unidirectional. Twinning can also influence slip by reorienting lattice planes in the twin. The major role played by twinning during deformation is explained in Section 2.1.4.

2.1.3.3 Texture

Each individual grain has its own crystallographic orientation in terms of the unit cell in space. During deformation, such as rolling, a preferred orientation (texture) of grains is developed, where certain planes orient themselves in a preferred way with respect to the axis of principal strain (Dieter, 2001). The development of a preferred orientation by a group of grain is not unexpected since slip and twinning both occur on the most favourable crystallographic planes and directions. During rolling, the deformation texture is described by a set of crystallographic planes parallel to the surface of the rolled sheet and a crystallographic direction contained in that plane having a direction parallel to the rolling direction (RD). Traditionally, texture is represented by a pole figure. A pole figure is a two-dimensional stereographic projection, showing the variation of pole orientation for a certain crystallographic plane.

During rolling of AZ alloys, a strong basal texture is developed (del Valle et al., 2006; Stanford and Barnett, 2008). This means the (0001) basal planes of most grains are oriented parallel to RD and c-axis of those grains are parallel to sheet normal direction (ND). For an AZ31 rolled sheet, orientation of different planes is shown in Fig. 2.6.

The formation of a basal texture is a result of the basal slip and c-axis tension

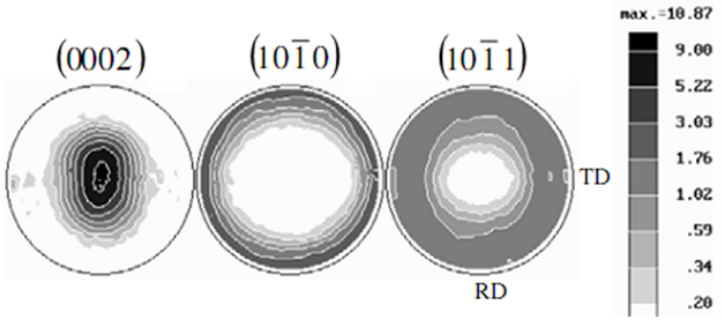

Figure 2.6: A basal texture developed during hot rolling of AZ31 (Lou et al., 2007).

twinning as deformation modes. During rolling of magnesium, both basal slip and dominance of tension twinning reorient the c-axis of grains so that c-axis becomes approximately parallel to the compression axis (ND or sheet thickness direction) (Agnew et al., 2001; Ion et al., 1982). This leads to a favourable alignment of basal planes parallel to the RD.

The orientation of the applied external stress relative to texture has a profound effect on the mechanical properties. For instance, in plane-strain compression, if the basal planes are aligned parallel to the compression stress axis, the operation of non-basal slip is essential to increase the strain to failure (Gehrmann et al., 2005).

2.1.4 Recrystallization and its Significance

A fine grain size is generally considered essential for superplastic forming (see Section 2.2). Fine grains are developed by recrystallization during thermo-mechanical treatments. The characteristics of recrystallization in magnesium alloys are discussed briefly below.

During deformation, dynamic recovery may occur to reduce the stored energy of a material by annihilation and rearrangement of dislocations, leading to subgrain formation (Humphreys and Hatherly, 2004). This metastable state of dynamic recovery may be consumed and new strain-free grains can be developed during a process known as recrystallization, leading to more softening of the material. When recrystallization phenomenon occur during deformation, it is denoted as dynamic recrystallization (DRX).

Ion and co-workers (1982) studied DRX in magnesium and suggested a DRX mechanism by progressive lattice rotation and dynamic recovery. The proposed mechanism is shown in Fig. 2.7. In brief, during deformation, tensile twinning is activated, leading to reorientation of the basal planes perpendicular to the stress axis. As a consequence, basal slip becomes restricted. Lattice rotation at the grain boundaries (Fig. 2.7a) initiates dynamic recovery (Fig. 2.7b) and subgrains are formed. The boundaries of the subgrains migrate locally, leading to coalescence

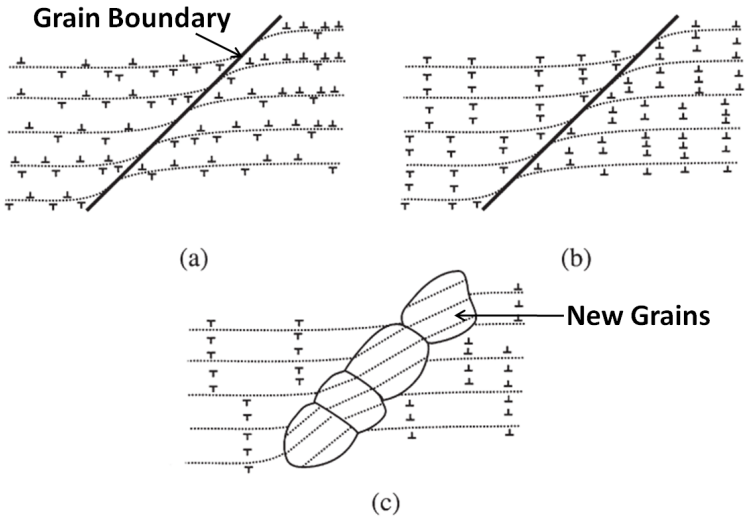

Figure 2.7: A schematic presentation of DRX in magnesium (Humphreys and Hatherly, 2004). During deformation, twinning reorients the basal planes perpendicular to the stress axis. As a consequence, (a) limited rotation of lattice occurs at grain boundaries and (b) dynamic recovery of the dislocations at or near the boundaries leads to (c) formation of new subgrains or grains.

and formation of high-angle boundaries (Fig. 2.7c).

During DRX, ductile shear zones may form in the vicinity of the boundaries by DRX (del Valle et al., 2003; Ion et al., 1982). The nuclei of grains, formed by DRX, may be preferentially oriented for basal slip and/or non-basal slip depending on temperature. The cluster of new grains becomes thicker during straining and provides a path of easy slip. Since the newly formed grains are small in size, there remains a possibility of sliding of grains. But, Ion and co-workers (1982) argued that low misorientation angle and strong texture were not consistent with such a mechanism, rather intense dislocation movements would allow further DRX. More dynamic recovery in these confined regions would develop more subgrains and eventually, high-angle grains would form, leading to progressive refinement during rolling. AZ31 (Jin et al., 2006; Myshlyaev et al., 2002) and AZ61 (del Valle et al., 2003) were reported to recrystallize by this mechanism.

Twinning plays a key role during DRX of magnesium. Sitdikov and co-workers (2003) carried out an investigation under compression on coarse-grained (2000 μm grain size) pure magnesium at 150 to 450 °C at a strain rate of 10^{-3} s^{-1}. They observed that twin-twin intersection of tension twins were important sites for recrystallization. In the surrounded regions of these intersections, nuclei are formed which have a different orientation to the matrix probably due to the lattice rotation during twinning. The formation of nuclei may also occur at the double-twinning feature in magnesium. The nuclei of grains form at the boundary between the tension and compression twin components of the double-twin. Also, if isolated low-angle grain boundaries are formed inside the twins, they may serve as the nuclei of recrystallized

grains. After forming the nuclei by any of the above mentioned process, recrystallized grains are formed by transformation of the low-angle boundaries of nuclei to high-angle boundaries. The driving force for this transformation is the interaction between lattice dislocations and twin boundaries and the accumulation of misfit dislocations formed by the deflection of the basal dislocations upon meeting the twin boundaries. Ultimately, the developed low-angle boundaries migrate to a stable configuration and fully developed equiaxed recrystallized grains are evolved.

The mechanisms discussed above are essentially the mechanisms of DRX by the gradual changes in misorientation of grains (from low-angle subgrain boundaries to high-angle grain boundaries), and are also commonly termed as continuous DRX.

Recently, several investigations have been performed to understand the effect of temperature and slip system activity on the onset of DRX. Galiev and co-workers (2001) studied a ZK60 (Mg-5.8Zn-0.65Zr) alloy having an average grain size of 85 μm under compression. Below 200 °C, the authors observed a dominating operation of basal slip and twinning. This is expected since the CRSS of these modes are comparatively lower than other slip systems. Between 200 to 250 °C, cross-slip assisted dislocation glide was the major deformation mode and in the temperature range of 250 to 450 °C, dislocation climb was identified. It was argued that if deformation was dominated by basal slip, twinning or cross-slip, then rearrangement of dislocations would develop low-angle boundaries, eventually forming high-angle boundaries by continuous DRX. In contrast, if the deformation was controlled by dislocation climb which led to low-angle boundary formation, then a different type of DRX (known as conventional discontinuous DRX) would readily occur.

Discontinuous DRX is a process of recrystallization where separate nucleation and growth phenomena of grains are observed. In brief, during deformation new grains may preferentially form at pre-existing high-angle grain boundaries (Humphreys and Hatherly, 2004). This is initiated by bulging of parts of grain boundaries by strain-induced boundary migration (SIBM) process. Bulging, a precursor to the newly formed grains, occurs between two grains having dissimilar stored energy and the migration of the boundary occurs in the direction towards the grain possessing higher stored energy. In the bulged region, a new grain is nucleated and this grain is essentially a dislocation free structure. However, since the material is experiencing plastic flow, dislocation activity is induced in the new grain and retards growth of the developed grain leading to a stable grain that ceases to grow further. It is notable that the orientation of the newly formed grain remains close to the orientation of the parent grain.

2.1.5 Thermo-mechanical Treatments

Refinement of grains can be accomplished by many deformation processes including hot rolling, extrusion, equal channel angular pressing (ECAP) or high pressure torsion (HPT) of an as-received large grain size material.

Hot rolling can reduce the grain size by a factor of approximately 100. Stanford and Barnett (2008) investigated AZ31 at different rolling temperatures and studied the effect of reducing grain size on tensile behaviour. They observed that the grain size of an as-received AZ31 alloy was refined with increasing rolling strain and rolling between 200 to 400 °C can provide a grain size of 2 to 3 μm after 80% reduction. Multi-pass rolling is beneficial, since a further reduction of grain size is obtained by grain boundary recrystallization (Barnett et al., 2005; del Valle et al., 2003). There is no optimum rolling temperature developed for magnesium. But, typically hot rolling is performed between 300 to 400 °C to obtain a homogeneous refined microstructure.

ECAP produces a refined microstructure by introducing a very high shear stress. In fact, ECAP is used to obtain ultra-fine grains which are usually sub-micron in size. In this process, a material of bar or rod shape is passed through a die. The die is constrained by a channel which is bent around the die. The principles of ECAP have been thoroughly investigated elsewhere (Valiev and Langdon, 2006). A grain size of 0.37 μm was reported for an AZ31 alloy after ECAP processing (Ding et al., 2009). A summary of a large range of materials which were processed by ECAP and provided excellent superplastic properties can be found elsewhere (Kawasaki and Langdon, 2007).

The HPT grain refining method has received significant attention recently. A disc-shaped material is placed between two anvils and is pressed and simultaneously a torsional strain is imposed by rotating the lower anvil. The principles and characteristics of this method can be found elsewhere (Zhilyaev and Langdon, 2008). The grain size produced by this method is usually in nano-meter size. For a Mg-9%Al alloy, HTP led to a refined microstructure of grains less than 0.40 μm in size (Kai et al., 2008).

2.2 Characteristics of Superplasticity

At room temperature, wrought AZ magnesium alloys typically show strains to failure under uniaxial tension that can reach approximately 25% depending on the loading direction with respect to the rolling direction (Koike and Ohyama, 2005; Yi et al., 2010). Under more complex loading conditions, such as biaxial tension, the strain to failure tends to be lower than uniaxial condition, up to a maximum 15 to 18% (Chino et al., 2009). An inability of sheet material to accommodate strain in the sheet

thickness direction is attributed as the cause for this drop in failure strain.

However, at elevated temperatures, elongation to failure (e_f) is increased by substantial activation of non-basal slip. Moreover, under certain microstructural conditions and for a definite set of test parameters, a very high elongation can be obtained. This phenomenon is termed as superplasticity. The major macroscopic feature of a superplastic material is the prolonged resistance to sharp necking. A record ductility of 3050% was reported for a ZK60 magnesium alloy having an initial grain size of 0.80 μm (Figueiredo and Langdon, 2008). The test condition was 200 °C under a strain rate of 10^{-4} s^{-1}. Typically, superplasticity is defined as the ability of a material to show a very large elongation prior to failure. Langdon (2009) proposed that a superplastic material should possess an elongation of at least 400% and a strain rate sensitivity (m) value close to 0.50. For superplastic forming, it is a general requirement that the grain size should be less than 10 μm (Pilling and Ridley, 1989). A detailed study on the historic development of superplasticity in the last century can be found elsewhere (Chokshi et al., 1993a; Langdon, 2009; Sherby and Wadsworth, 1989).

A comparison chart of different superplastic materials is shown in Table 2.5. It is interesting to note that optimum superplastic test conditions vary depending on material and microstructure.

Deformation in the superplastic region is dependent predominantly on grain size, strain rate and temperature. Flow stress is strongly affected by these variables. This is briefly discussed below.

The flow stress in the superplastic regime is low. Superplasticity typically occurs at or above $0.5T_m$ (where T_m is the melting point) (Pilling and Ridley, 1989). The flow stress is reduced as the temperature of deformation is increased. The overall effect of increasing temperature is a higher m-value of deformation. The effect of temperature on flow stress is shown in Fig. 2.8.

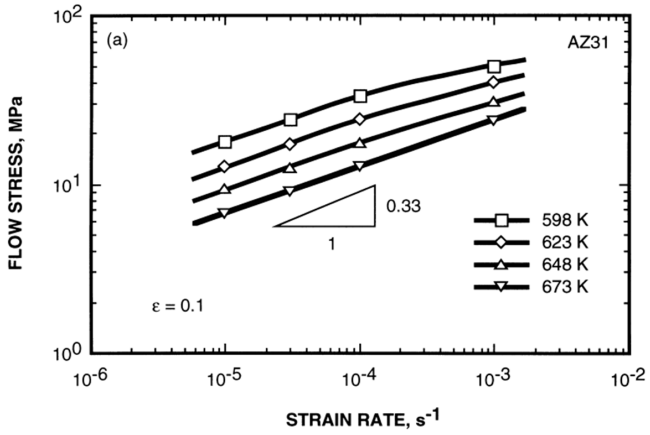

Figure 2.8: Strain rate vs elastic modulus (E) compensated flow stress relationship of AZ61 at different temperatures (Kim et al., 2001).

Table 2.5: Examples of different materials possessing excellent superplastic behaviour

Alloy	**Grain Size, μm**	**Test Temperature, °C**	**Strain Rate, s^{-1}**	**Elongation to Failure, %**	**Reference**
Al 1421	2.6	450	1.4×10^{-2}	3000	Kaibyshev and Osipova, 2005
Al 2024	0.50	400	10^{-2}	500	Lee et al., 2003
Al 5083	0.30	500	10^{-2}	740	Park et al., 2003
Al 7034	0.30	200	3.3×10^{-2}	1110	Xu et al., 2005
Cu-40Zn	1	400	10^{-2}	640	Neishi et al., 2001
AZ31	0.70	150	10^{-4}	460	Lin et al., 2005
AZ61	0.60	200	3.3×10^{-4}	1320	Miyahara et al., 2006
AZ91	0.80	300	3×10^{-3}	570	Chuvil'deev et al., 2004b
ZK60	1	260	6.5×10^{-4}	960	Chuvil'deev et al., 2004a
ZK60	0.80	200	10^{-4}	3050	Figueiredo and Langdon, 2008
Mg-9Al	0.70	273	3.3×10^{-4}	840	Matsubara et al., 2003
Mg-8Li	1–3	200	1.5×10^{-4}	1780	Furui et al., 2007
Zn-22Al	0.60	260	1	2380	Lee and Langdon, 2001
Ti-50Al	0.40	800	8.3×10^{-4}	260	Imayev et al., 2001

Flow stress is also perturbed by strain rate. In the superplastic regime, a sigmoidal relationship between flow stress and strain rate is observed (Fig. 2.9a). m is defined as

$$m = \frac{\delta \ln \sigma}{\delta \ln \dot{\varepsilon}} \tag{2.1}$$

where σ is the stress and $\dot{\varepsilon}$ is the strain rate. The slope of Fig. 2.9a gives the corresponding m-value. The consequences of higher m values are discussed in detail in Section 2.3.4. The effect of strain rate on m is shown in Fig. 2.9b. Based on m, it is possible to define three distinctive regions. As evident from Fig. 2.9b, in the very low and very high strain rate regions, i.e., region I and III, typical m-values are less than 0.30 (Pilling and Ridley, 1989). In the intermediate strain rate region II, the typical m-value is 0.50.

Grain size also has an important influence on flow stress. In Fig. 2.10a, the flow stress is shown for different grain sizes for a range of temperature. The curves

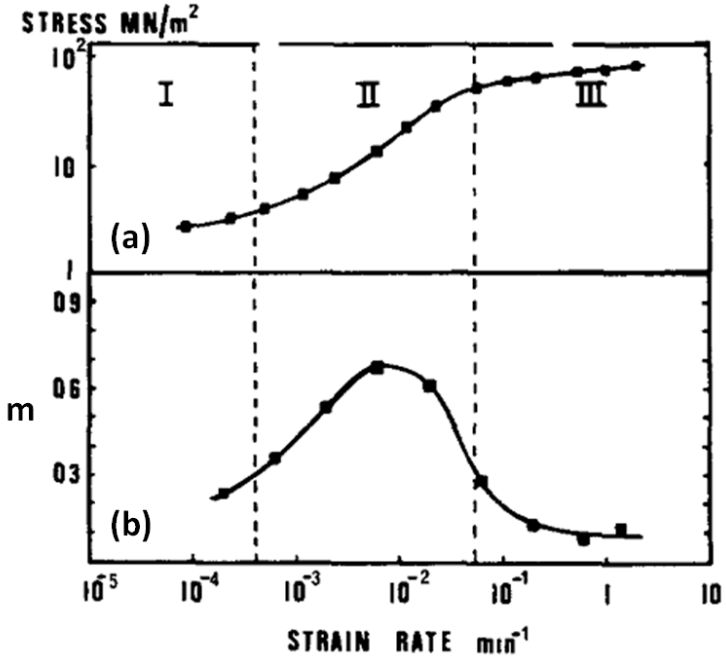

Figure 2.9: The strain rate dependency on (a) flow stress and (b) strain rate sensitivity (m) of an Mg-Al eutectic alloy (Edington et al., 1976; Lee, 1969).

cross approximately at room temperature, where the typical Hall-Petch relationship is observed. But, at higher temperatures, flow stress is increased with increasing grain size. To be precise, at higher temperature flow stress increases linearly with grain size (Alden, 1967; Edington et al., 1976). The increase of flow stress with grain size has some secondary effect on m. If grain size is reduced, the peak in m-value is shifted towards region III (Edington et al., 1976). Therefore, the strain rate range of superplastic deformation is increased.

The benefit of a small grain size for superplasticity is two-fold. It decreases the flow stress at the temperature where superplasticity occurs (Alden, 1967; Hamilton et al., 1982) and increases the strain rate range of superplasticity by increasing the contribution from grain boundary sliding (GBS) (Sherby and Wadsworth, 1989). The dependence of strain rate ($\dot{\varepsilon}$) on grain size (d) is described by the phenomenological constitutive law (Sherby and Wadsworth, 1982):

$$\dot{\varepsilon} = d^{-p} \tag{2.2}$$

where p describes the dependency of grain size on strain rate (i.e., the grain size exponent). p is determined by logarithmically plotting strain rate as a function of reciprocal of grain size. The slope of the line gives the value of p.

The overall effect of grain size and temperature on strain rate and flow stress is illustrated in Fig. 2.10b. If the grain size is decreased from d_1 to d_2 at the temperature T_1, the superplastic region is shifted towards higher strain rates. Similarly, if

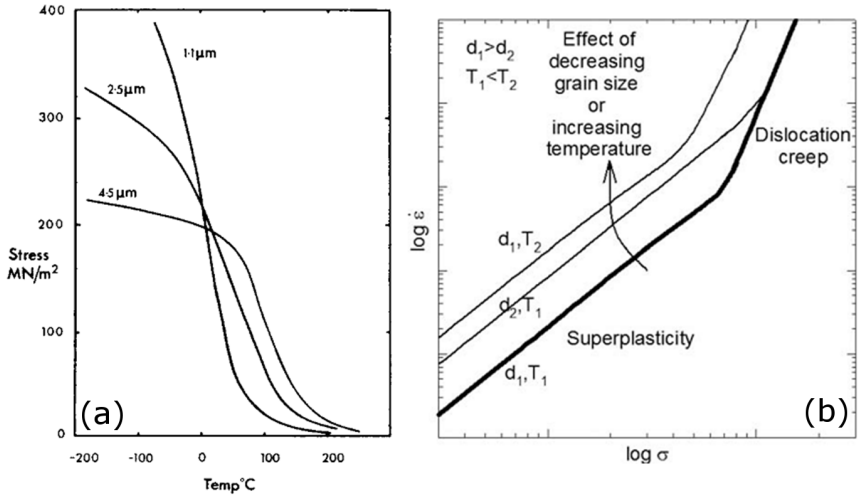

Figure 2.10: (a) The effect of grain size on flow stress for Al-Zn eutectoid alloy (Ball and Hutchison, 1969; Edington et al., 1976); (b) A schematic presentation highlighting the effect of decreasing grain size and temperature on flow stress and strain rate (Figueiredo and Langdon, 2009b).

temperature is increased to T_2 at the fixed grain size d_1, the superplastic region is displaced to higher strain rates.

Fig. 2.11 shows an example of variation of e_f with corresponding strain rate and flow stress. The three distinct regions of behaviour are also highlighted. It is evident that e_f reaches a maximum in region II. In the other two regions, e_f is comparatively low. Comparing the variation of m in Fig. 2.9b with e_f in Fig. 2.11a, it can be anticipated that higher m leads to higher e_f. The physical reason for this comes from the increased resistance to neck growth given by higher m.

The activation energy (Q) of deformation is also an important parameter. Its value suggests the underlying mechanism of accommodation of deformation. Q can be determined from the relationships between flow stress and strain rate at different temperatures (Livesey et al., 1984). In the superplastic region II, activation energies are of two types: (a) activation energy for grain boundary diffusion (Q_{GB}) and (b) activation energy for lattice diffusion (Q_L). Depending on the mechanism of deformation, the accommodation process varies and this gives different Q values.

In summary, increasing temperature and decreasing grain size and strain rate are shown to have a similar effect on flow stress. This behaviour can be rationalised with the m-value, the sensitivity of flow stress to strain rate. The higher m, the more resistance to flow localisation and hence, e_f is increased. Depending on values of m, three regions of strain rate are identified. Differences in flow stress, strain rate, m and e_f indicate control of different deformation mechanisms in each region. This is discussed in the following section.

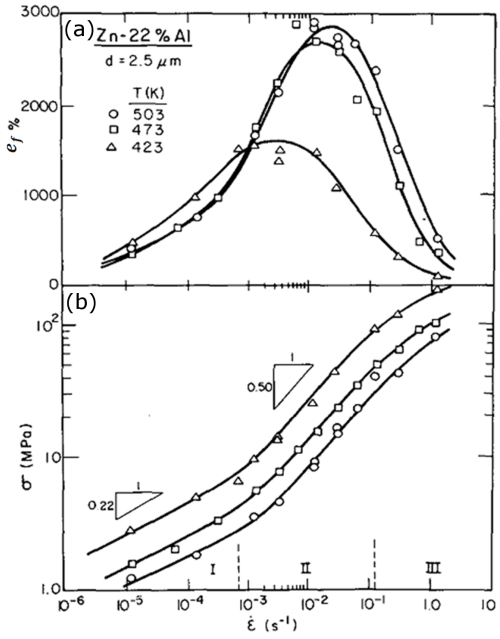

Figure 2.11: Variation of (a) elongation to failure (e_f) and (b) flow stress for a Zn-22%Al alloy at different temperatures (Langdon, 1991).

2.3 Mechanisms of Superplasticity

Though superplasticity was first reported in 1912 by G. D. Bengough (Chokshi et al., 1993b), the mechanism of superplasticity remains a matter of intense debate. However, the observation of different mechanisms is partly due to the differences in microstructure and applied test conditions. In Fig. 2.9, three regions are highlighted. In general, there are distinct characteristics of these regions (Pilling and Ridley, 1989). In region I (low stress and low strain rate), diffusion creep dominates and grain elongation occurs. In region III (higher stress and higher strain rate), the major mechanism is dislocation creep and grain elongation is observed. In contrast to these two regions, in region II (superplastic region), extensive grain boundary sliding (GBS) occurs and the grains remain approximately equiaxed.

It was also shown earlier that increasing temperature or decreasing grain size has a similar effect on flow stress and strain rate has an inverse effect on flow stress. It is useful to understand exactly which mechanisms operate at different level of flow stress. Deformation mechanism maps were first developed by Ashby (1972) showing regions of stress and temperature where a particular mechanism would dominate. Adopting the methodology, a deformation map was developed for superplastic materials (Mohamed and Langdon, 1976), plotting normalised grain size against normalised flow stress at a fixed temperature. An example of deformation mechanism map for magnesium alloys is shown in Fig. 2.12 at 400 °C. It is apparent from the plot that GBS dominates in an intermediate region of flow stress. In this region, the small grain size leads to GBS accommodated by grain boundary diffusion. Otherwise,

accommodation of GBS is dominated by lattice diffusion. At a fixed grain size, increasing temperature depresses the region dominated by grain boundary diffusion and lattice diffusion becomes important (Watanabe et al., 1999a).

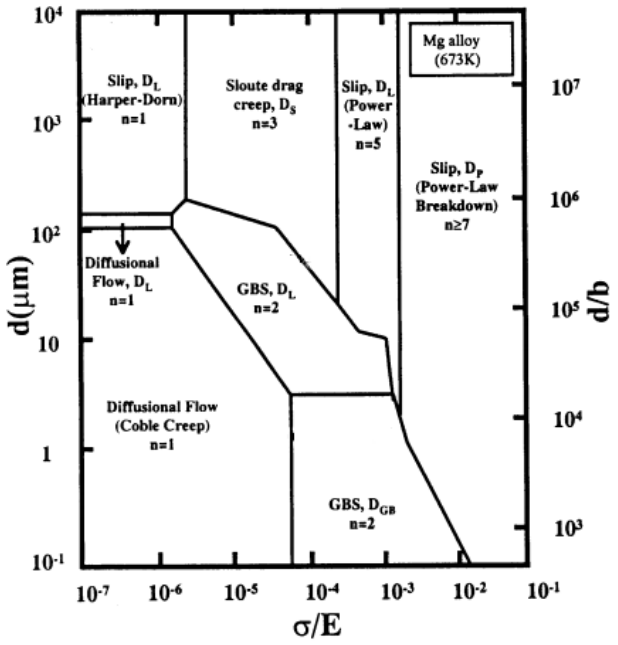

Figure 2.12: Deformation mechanism map of magnesium alloys at 400 °C (Kim et al., 2001). Flow stress (σ) is compensated by temperature normalised elastic modulus (E). In short, at very low stress, diffusional flow dominates for fine grain size and Harper-Dorn creep occurs at very high grain size. In the very high flow stress region, dislocation creep controls deformation irrespective of grain size. In the intermediate flow stress level, GBS dominates for fine grain size. The accommodation of GBS is controlled by grain size. It can be grain boundary diffusion (D_{GB}) or lattice diffusion (D_L) depending on grain size.

Typically, three types of mechanisms are classified during deformation at elevated temperature: sliding of adjacent grains; slip by dislocation movements and atom movements by diffusion. Depending on grain size, temperature and strain rate, each of these mechanisms can act as an accommodation process of another. For example, sliding of grains along grain boundaries may be accommodated by dislocation or diffusional flow. Since superplasticity is a special case of creep, the mechanisms developed for creep materials are, to some extent, applicable to superplastic materials. The major difference between superplastic materials and creep resistant alloys is the small grain size in the superplastic case. This is because creep resistant alloys are designed to resist deformation at elevated temperature whereas superplastic alloys are designed to promote it. Each of these mechanisms will be discussed in turn in the following section, in order of increasing importance as the flow stress increases.

2.3.1 Diffusion Creep

In the low stress regime (region I), diffusion creep dominates (Fig. 2.9a). Diffusion creep occurs when a material is deformed as a consequence of diffusion of atoms through grain boundaries or lattice (interior of a grain) driven by stress. Three types of creep process may occur in this region, namely Nabarro-Herring creep, Coble creep and Harpor-Dorn creep.

The basic mechanism for diffusion creep is that it occurs by flow of vacancies from grain boundaries experiencing compression under stress towards the boundaries experiencing tension (Friedel, 1964). The driving force for this movement is the work done to restore the equilibrium condition under the applied stress. In diffusion creep, boundaries play an important role, since they act as the source and sink for vacancies. Within a grain, vacancies may not be produced, since this would require much higher thermal energy (Friedel, 1964). There are two ways a flux of vacancies (or a counter-flow of atoms) can move from the source to the sink—through the lattice or grain boundary. Grain boundaries are assumed a uniform source and sink for vacancies.

Nabarro suggested that under an applied stress, a material would deform by transferring excess vacancies from one boundary to another. He proposed that diffusion of vacancy flow should be directed from the transverse grain boundaries (normal to applied stress) towards the parallel (to applied stress) boundaries, through the lattice (Fig. 2.13a). Since the concentration of vacancies at a transverse grain boundary is higher than the stress-free condition, vacancies travel to the parallel-to-stress boundaries through the grain and are absorbed. In doing so, a counter-flux of atoms occurs and this leads to a plating of atoms at transverse boundaries. As a consequence, grains are elongated. In summary, the driving force for this mechanism of creep comes from the gradient of vacancies developed by the applied stress and the gradient is largest at transverse boundaries. Herring (1950) studied this theory further and this mechanism is now known as Nabarro-Herring creep.

Some important characteristics of this mechanism are (Edington et al., 1976):

- A linear relationship exists between flow stress and strain rate. This means $m = 1$.
- Grains elongate during deformation.
- Activation energy of deformation is that of lattice diffusion.
- Usually only dominates at very low stress and at $>0.8\mathrm{T}_m$.

The strain rate for this creep process is given by

$$\dot{\varepsilon} = B_1 D_L \frac{\Omega}{kT} \frac{\sigma}{d^2} \tag{2.3}$$

where B_1 is a constant and depends on shape of grains, D_L is the grain boundary diffusion coefficient, d is the grain size, k is Boltzmann's constant, T is the absolute temperature, σ is the flow stress and Ω is the atomic volume. For magnesium, D_L is given by (Frost and Ashby, 1982)

$$D_L = 1.0 \times 10^{-4} \exp\left(-\frac{Q_L}{RT}\right) \text{ m}^2 \text{ s}^{-1} \tag{2.4}$$

where Q_L is the activation energy for lattice diffusion and R is the molar gas constant. Using $\Omega = 0.7\mathbf{b}^3$, where $\mathbf{b}$ is Burgers vector, Equation 2.3 is reduced to (Langdon and Mohamed, 1976)

$$\dot{\varepsilon} = B_2 D_L \frac{G\mathbf{b}}{kT}\left(\frac{\mathbf{b}}{d}\right)^2\left(\frac{\sigma}{G}\right) \tag{2.5}$$

where G is the shear modulus.

Coble (1963) suggested that the diffusion flux might occur along the grain boundary instead of grain interior (Fig. 2.13b). As a consequence, matter would be diffused rapidly along the boundary compared to the bulk of a grain. Coble creep occurs when the deformation temperature is approximately 0.4T_m (Edington et al., 1976). The rate of creep is

$$\dot{\varepsilon} = B_3 \delta D_{GB} \frac{\Omega}{kT}\frac{\sigma}{d^3} \tag{2.6}$$

where D_{GB} is the grain boundary diffusion coefficient, δ is the grain boundary width and is equal to $2\mathbf{b}$. For magnesium, $\delta D_G B$ is determined as (Frost and Ashby, 1982)

$$\delta D_{GB} = 5.0 \times 10^{-12} \exp\left(-\frac{Q_{GB}}{RT}\right) \text{ m}^3 \text{ s}^{-1} \tag{2.7}$$

where Q_{GB} is the activation energy for grain boundary diffusion. Using $\Omega = 0.7\mathbf{b}^3$, the equation is reduced to

$$\dot{\varepsilon} = B_4 D_{GB} \frac{G\mathbf{b}}{kT}\left(\frac{\mathbf{b}}{d}\right)^3\left(\frac{\sigma}{G}\right) \tag{2.8}$$

which shows strain rate varies inversely with the cubic power of the grain size. The characteristics of this creep are (Edington et al., 1976):

- A linear relationship exists between strain rate and stress, i,e., $m = 1$.
- Grain elongation occurs.
- The activation energy for deformation is that for grain boundary diffusion.
- Coble creep dominates at a comparatively low temperature compared to Nabarro-Herring creep.

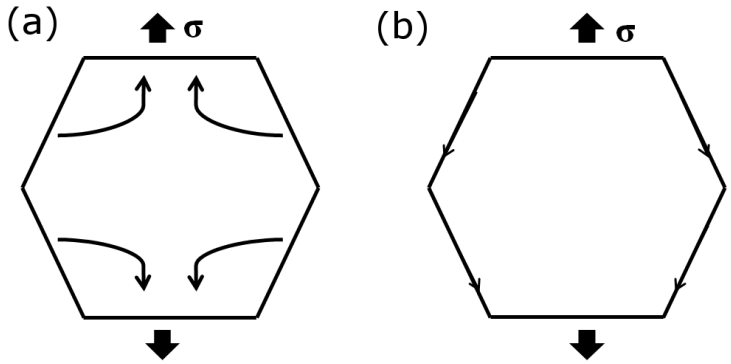

Figure 2.13: Schematic sketches for (a) Nabarro–Herring Creep and (b) Coble Creep. Arrows show the directions of movements of atoms and vacancies are flowing in the opposite to atom flux. Continuous plating of atoms at the transverse (perpendicular to tensile axis) boundaries tends to elongate the grain in the stress direction (σ).

If diffusion occurs along grain boundaries, the total volume available as a diffusion path is small compared to the whole lattice. At high temperature, if there is sufficient energy for activation of lattice diffusion, Nabarro-Herring creep dominates because of the much greater volume for diffusion. At low temperature, on the other hand, the lattice diffusion rate drops sharply because of the higher activation energy and grain boundary diffusion dominates.

Another mechanism, where strain rate varies linearly with applied stress ($m = 1$), is recognised as Harper-Dorn creep (Harper and Dorn, 1957). The theory was developed from the early work of Mott (1953) and Weertman (1955). In brief, a vacancy flux is created between dislocations having a Burgers vector parallel to the tensile axis to those perpendicular to the tensile axis (Nabarro, 2002). This mechanism was observed in Al-Mg alloys having mm size grains, when deformed at $>0.9\mathrm{T}_m$ and the resulting flow stress was $<0.5\,\mathrm{MPa}$ (Yavari et al., 1982). However, in the present work, the maximum deformation temperature was $<0.8\mathrm{T}_m$, and therefore this mechanism is not expected to be important.

Edington and co-workers (1976) argued that diffusion creep alone cannot be a dominating mechanism for superplasticity, since the resultant grain elongation leading to an increase in diffusion path cannot accommodate the large strains experienced in superplastic materials. However, diffusion creep may be important as an accommodation process of GBS (discussed in Section 2.3.2).

2.3.2 Grain Boundary Sliding

Under an applied stress at higher temperature, grains can relatively be displaced at the boundary between them (Bell and Langdon, 1967). This mechanism of sliding of grains is known as grain boundary sliding (GBS). Conventionally, GBS is considered

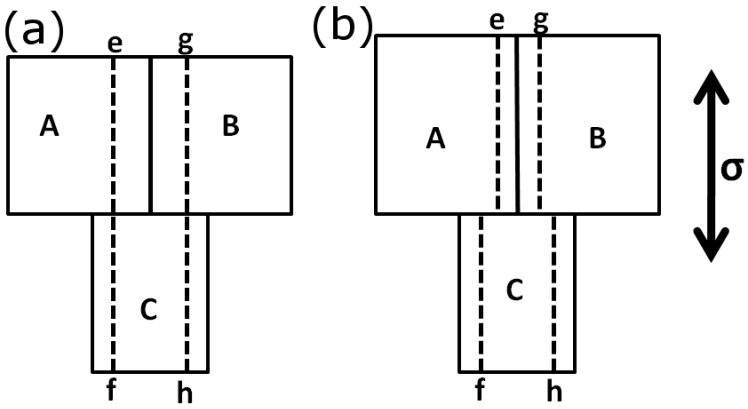

Figure 2.14: A schematic presentation of Lifshitz GBS accommodated diffusion creep (Langdon, 2000). (a) Two marker lines, ef and gh are drawn in grains A, B and C. After atom transfer from the vertical boundary to the transverse boundary, an offset is produced. This resembles sliding of grains.

as a major mechanism in the superplastic regime (region II). The standard configuration that two grains can slide past each other during deformation invokes the presence of an accommodation process, since sliding obviously affects a third grain. Moreover, during sliding, stress is developed at triple points of grains or other perturbations in the microstructure, which must be accommodated to continue deformation (Langdon, 1970). Therefore, GBS is a coupled mechanism. Inadequate accommodation would lead to the formation of cavities.

The diffusion creep mechanisms discussed in the preceding section were developed considering creep of a single grain. To accommodate the elongation to maintain specimen integrity, relative translation of grains is necessary. This was pointed out by Lifshitz and this type of sliding during diffusion creep is known as Lifshitz GBS. Diffusion creep is considered to be accommodated by Lifshitz GBS (Cannon, 1972). Therefore, diffusion creep is recognised by elongation of grains along the tensile direction and relative displacement of grains but there will not be any net increase in number of grains along the tensile axis (Langdon, 2000). In Fig. 2.14a, three grains (A, B and C) are shown, where two marker lines ef and gh are drawn. Now, during diffusion creep, atoms are removed from the parallel-to-stress boundaries and are plated in the transverse boundaries. In such a case, marker lines ef and gh are broken and an offset is produced at the horizontal boundary (Fig. 2.14b), resembling sliding of grains.

It is established that Lifshitz GBS and diffusion creep are paired mechanisms and do not contribute to total strain separately (Gifkins et al., 1975). Langdon (2000), recently, has suggested that to separate pure GBS from diffusion creep by marker offset, grain aspect ratio plays a major role. If grain elongation occurs, the mechanism is diffusion creep accommodated by Lifshitz GBS; otherwise, the sliding is pure GBS.

The term, pure GBS, needs some clarification. This can also be termed as

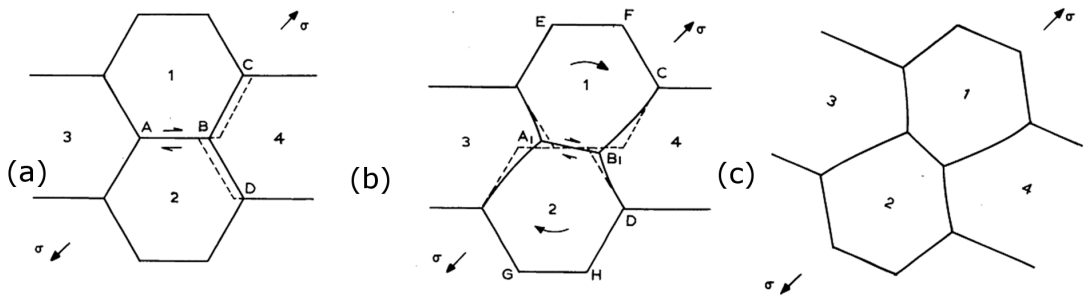

Figure 2.15: A schematic presentation of GBS during deformation (Matsuki et al., 1977). (a) Sliding of grains along AB between grains 1 and 2 moves the boundaries BC and BD in new positions. (b) To accommodate the stress, rotation of grains occur which is actually switching of neighbours. (c) As a consequence of this switching, grains with a new orientation are developed.

Rachinger GBS or only GBS. Rachinger derived a methodology to understand the contribution of GBS during deformation and calculated the relative strain obtained from GBS. In short, GBS is the relative sliding of grains which rearranges grains in such a configuration that there is a net increase in the number of grains along the tensile axis (Cannon, 1972) and no significant elongation of grains. Rachinger GBS can explain the observed large strains in superplastic materials (Langdon, 1994). Consider a simplified sketch in Fig. 2.15, where a group of grains are oriented at 45° with the boundaries. Now, the sliding along AB moves the boundaries BC and BD in opposite directions (dashed lines in Fig. 2.15a). To accommodate the developed stress and continue sliding, rotation of grains and switching of neighbours occurs (Fig. 2.15b), leading to a final configuration as in Fig. 2.15c.

The accommodation process of GBS can be of two types: (a) movements of dislocations by a combination of climb and glide at or adjacent to grain boundaries and (b) diffusional flow. Each of these accommodation processes are discussed below.

2.3.2.1 GBS Accommodated by Dislocation Movements

In this mechanism, GBS is accommodated by the motion of dislocations. The basic principle involves the translation of grains which causes dislocations to move along the grain boundaries and if the sliding is restricted at obstacles such as triple points or particles, the developed stress concentration is relieved by the generation of dislocations which travel through the grains. Based on this principle, several models were proposed.

Ball and Hutchison (1969) proposed a mechanism where a group of grains would slide as a block until blocked by unfavourably oriented grains. Such an obstruction would cause stress concentration, which would be relieved by dislocation movements. This mechanism is based on an idea that the front dislocations from a pile-up against a grain boundary can climb into and along the boundary under stress (Friedel, 1964).

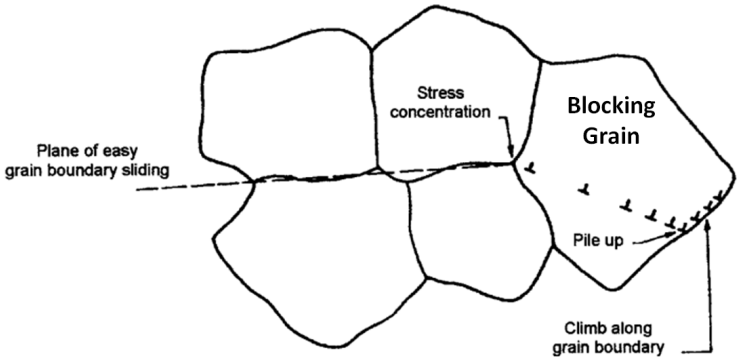

Figure 2.16: A schematic presentation of Ball and Hutchiston model. During sliding, a pile–up of dislocations occur at the opposite boundary of the blocking grain. Dislocations at the ahead of the pile–up can climb to the grain boundary and deformation is, thus, continued (Kassner and Pérez-Prado, 2004).

This mechanism is shown in Fig. 2.16 and is explained below.

In brief, since grains remain equiaxed after deformation and relative sliding of grains occurs, GBS plays an important role in superplastic deformation. Large relative motion of grains is accommodated by either cavity formation or local changes in grain shape. If cavities are not observed at triple points, it must be the grain shape changes which accommodate GBS. When the sliding is obstructed by a grain or protrusion, the applied stress becomes locally concentrated at the obstructed region. In such a case, dislocations are emitted in the blocking grain by local developed stress, which are piled-up at the opposite grain boundary. This pile-up will continue until a back pressure prevents further emission. Now, the dislocations ahead in the pile-up would climb into and along the grain boundary. Thus, the concurrent replacement of dislocations will allow further sliding of the group of grains. The rate of such sliding is controlled by the kinetics of climb to the annihilation sites at boundaries. The climb of dislocations is, in turn, controlled by grain boundary diffusion.

The strain rate by this theory is

$$\dot{\varepsilon} = B_5 D_{GB} \frac{G\mathbf{b}}{kT} \left(\frac{\mathbf{b}}{d}\right)^2 \left(\frac{\sigma}{G}\right)^2 \tag{2.9}$$

where the terms are defined earlier.

However, this model was criticised since dislocation pile-ups are not observed within grains (Pilling and Ridley, 1989). Superplastic deformation is associated with higher temperature and low stress. Therefore, dislocations are expected to climb or cross-slip out of their slip plane within the grain (Edington et al., 1976). Moreover, an exact mechanism of rotation of grains was not included.

Mukherjee (1971) proposed a modified version of Ball and Hutchison mechanism. He suggested ledges at boundaries would obstruct sliding and consequently concentrated stress would develop. According to the author, such a concentrated stress

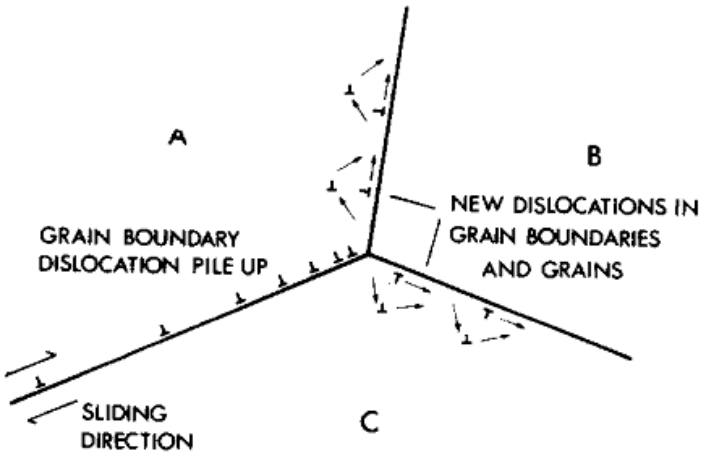

Figure 2.17: A schematic presentation of pile-up of dislocations at grain boundary triple points. This mechanism was proposed by Gifkins (1976). During sliding, pile-up of dislocations occur at the triple point. Dislocations ahead of the pile-up is dissociated into dislocations that travels through boundaries of AB and BC or with the grains of B and C. The dislocations within B and C are annihilated or combined at boundaries.

can generate dislocations, which pile-up at the opposite boundary of the blocking grain. Except for the source of dislocations, the mechanism is identical to the Ball and Hutchison mechanism. Mukherjee explained that rotation of grains to keep coherency of grain shape would occur by rotation of individual grains rather than coordinated rotation of several grains. The sliding rate is controlled by the number of emitted dislocations from ledges. The rate equation is similar to Equation 2.9. However, it is hard to obtain a pile-up of dislocations within a grain due to the reasons mentioned earlier. Moreover, during sliding, the ledges are moving. Therefore, all of the dislocations are not in the same plane. This would further restrict any flow of dislocations.

Gifkins (1976) considered the pile-up of grain boundary dislocations at triple points and proposed another mechanism. This is shown in Fig. 2.17. According to him, the pile-up causes stress concentration and this is relaxed by dissociation of dislocations. These new dislocations can move either into the other two boundaries or within the grains. If the dislocations move into the grains, they can glide/climb in grain boundaries to get annihilated or to combine with old dislocations to form other types of grain boundary dislocation. The whole process would lead to grain rotation. The strain rate expression for this mechanism is similar to Equation 2.9.

GBS accommodated by dislocation movements at boundaries can be considered as core and mantle models (Pilling and Ridley, 1989). The core and mantle are analogous to the structure of earth. The mantle is the periphery of a grain and core is the interior of the grain (Fig. 2.18). When two hexagonal shaped grains are rotating, only the mantle region needs to be plastic (Gifkins, 1994). This mantle region is shown by the

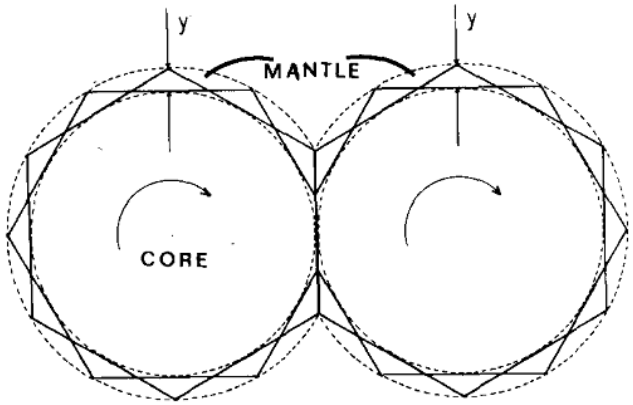

Figure 2.18: A schematic presentation of core and mantle concept (Gifkins, 1994).

dashed circles, and contains part of the grains (triangular areas). The width of the mantle region is predicted as $0.07d$ where d is the grain size. Only the mantle region needs to allow dislocation movements and the core portion can remain undeformed. This idea was applied together with Rachinger GBS by Ashby and Verrall for the first time to explain GBS in superplastic deformation (see Section 2.3.2.2).

Gifkins (1978) analysed the Ashby and Verrall mechanism (see Section 2.3.2.2) and proposed a slightly different model, where dislocations played the role of accommodation. According to this model, sliding of a group of four grains tends to open up a void (Fig. 2.19a). To prevent formation of a void, a grain from another layer moves in to fill the gap. As sliding continues, the gap increases and the whole grain from another layer fills in, forming a new grain E (Fig. 2.19b). The boundary network of the whole group adjust themselves by migration of boundaries. As a consequence, the boundaries of grain E becomes curved and the boundaries of the old grains become slightly curved too (Fig. 2.19c). Accommodation of GBS occurs only in the mantle region by glide and climb of dislocations, contrary to the other mechanisms where dislocations also move through the grain. Accommodation in the mantle region is fast enough to match the rate of GBS, since climb is controlled by diffusion in this region, which is very close to the grain boundaries (Gifkins, 1991). The strain rate expression for this mechanism is similar to Equation 2.9.

In summary, the accommodation of GBS by dislocation movements is widely accepted as the deformation mechanism of superplasticity. The climb of dislocations to relieve the stress concentration produced by microstructural irregularities is governed by diffusion of atoms. The diffusion path is dominated by lattice diffusion at higher temperatures and by grain boundary diffusion at comparatively low temperatures. However, Bate and co-authors (2005) disagree with the domination of GBS during superplastic deformation. The authors reported that slip alone was the dominating superplastic mechanism in an Al-6Cu-0.4Zr alloy. They justified this argument by

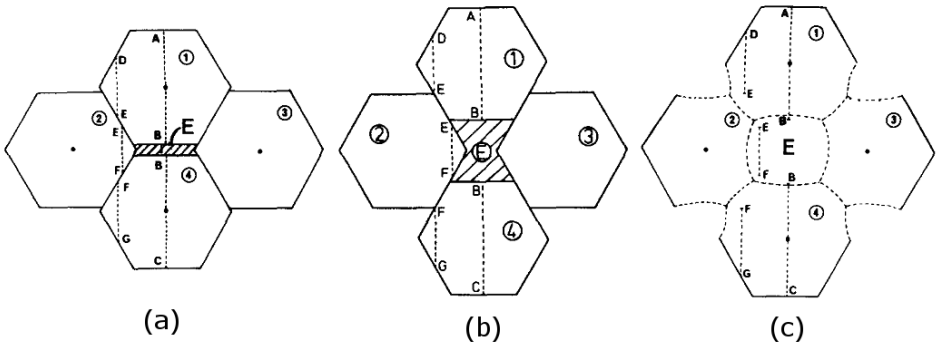

Figure 2.19: A schematic representation of GBS by Gifkins model (Gifkins, 1978). Dislocation movements occur in the mantle region.

the observation of a reduction of texture and persistence of a banded microstructure.

2.3.2.2 GBS Accommodated by Diffusion

Ashby and Verrall (1973) proposed a new physical mechanism of superplasticity based on Rachinger GBS which was, according to their model, accommodated by diffusion. In this grain switching mechanism, accommodation occurs at triple points by diffusion. The driving force for diffusion comes from the stress induced transport of matter from the compressive boundaries to the tensile boundaries (Pilling and Ridley, 1989). Ashby and Verrall argued that grain rotation was inevitable since grains were not of equal size and did not form a perfect hexagonal array.

The mechanism can be explained in terms of a group of four grains (Fig. 2.20a). This group of grains moves by GBS and an intermediate stage is developed (Fig. 2.20b). In this stage, the shape of the grains is changed by diffusion in the mantle region and a quadruple node is formed. Grain boundary migration, together with GBS and diffusion, develops the final shape of the grains (Fig. 2.20c). After the completion of switching, two triple points are again developed. The diffusion in the intermediate stage occurs along the path MQ and matter is transported from the M region to both N and Q regions (Fig. 2.20d). This mechanism considers the existence of a threshold stress where the mechanism becomes operating. This threshold stress arises from the large energy required to change the grain boundary surface area.

The strain rate is described as

$$\dot{\varepsilon} = B_6 D_{eff} \frac{G\mathbf{b}}{kT} \left(\frac{\mathbf{b}}{d}\right)^2 \left(\frac{\sigma - \sigma_o}{G}\right) \tag{2.10}$$

where D_{eff} is the effective diffusivity and σ_o is the threshold stress. Since superplastic materials may exhibit activation energies for plastic flow equal to either grain boundary or lattice diffusion, the use of D_{eff} is suggested to develop a constitutive law (Sherby and Wadsworth, 1982). D_{eff} is expressed as

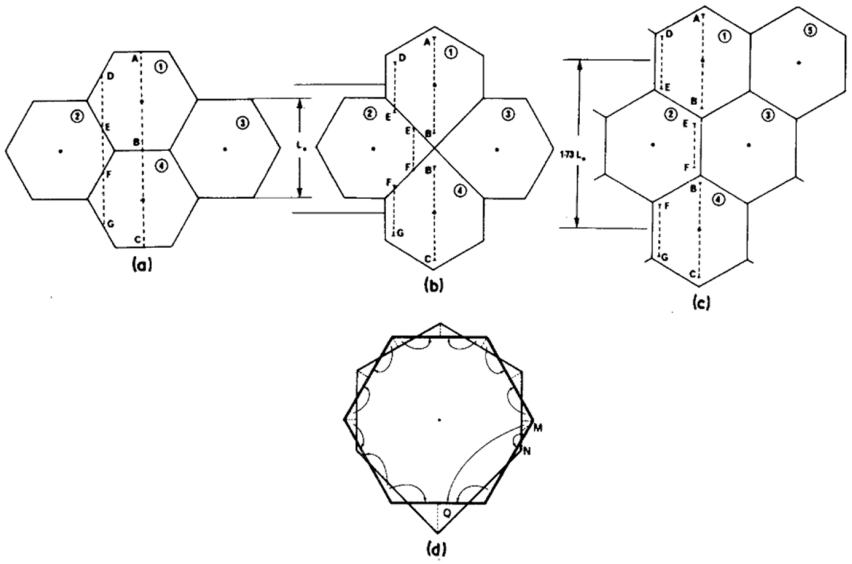

Figure 2.20: A schematic presentation of GBS by Ashby and Verrall model. (a) shows a group of grains is experiencing an applied stress; (b) shows grains change their shape by diffusion and a sharp point is formed; (c) shows the rearrangement of the boundaries to remain equiaxed and (d) shows the diffusion in a grain to form part of the quadruple (Gifkins, 1978).

$$D_{eff} = D_L + x\left(\frac{\pi\delta}{d}\right) D_{GB} \tag{2.11}$$

where x is an arbitrary constant to fit data and has been taken as equal to 1.7×10^{-2} for magnesium (Watanabe et al., 1999a).

However, this model has some limitations. It is obvious that diffusion paths cannot act on a single boundary in two different directions, since diffusion is a stress driven phenomenon acting on normal boundaries (Spingarn and Nix, 1978). Moreover, the described model is not symmetric and elongated grains should be observed (Pilling and Ridley, 1989). A modified mechanism was suggested by Spingarn and Nix (1978), where they corrected the diffusion paths. They considered grain migration should occur along with diffusion to account for the grain switching that occurs in the Ashby and Verrall model, maintaining symmetry. According to the modified mechanism, an array of hexagonal grains becomes elongated by diffusion creep (forming a diamond configuration), followed by migration of the boundaries which leads to the retention of the equiaxed shape of the group of grains. If migration occurs rapidly, then the rate of deformation is controlled by grain boundary or lattice diffusion.

The inconsistency of Ashby and Verrall mechanism regarding symmetry was outlined by Gifkins (1978). He showed that the intermediate condition in Fig. 2.20b was not possible without creating cavities or major adjustment of the outer boundaries. A modified mechanism was developed by him as discussed in Section 2.3.2.1. The development of curved boundaries retains the symmetry and is applicable to an

aggregate of grains.

2.3.3 Dislocation Creep

In region III, the dominating deformation mechanism is dislocation creep. In this mechanism, deformation is controlled by motion of dislocations by glide and climb. Dislocation tangles are formed by condensation of dislocations, forming subgrains. Grain elongation is evident in this region and flow stress is comparatively less sensitive to grain size (Edington et al., 1976). Dislocation creep is controlled by the processes of strain hardening and dynamic recovery. Strain hardening occurs by the hindrance of dislocation movement during deformation and recovery or softening depends annihilation and climb of dislocations. Creep deformation in this regime can be classified as glide and climb controlled mechanisms. Both of them are discussed below.

Dislocation Glide Controlled Mechanism

If deformation is controlled by interaction of gliding dislocations with solute atoms, it is commonly termed as viscous glide creep or solute drag creep. No clustering of dislocation (pile-ups or sub-cells) is observed in this mechanism.

When a crystal contains solute atoms, having dissimilar size to the host/solvent atoms, the lattice of the latter is distorted. This distortion is minimized if the solute locates in a favourable position around the dislocation to enable compensation of the strain fields. This means that solute atoms are drawn towards dislocations as a net result of the interactions of strain fields (Reed-Hill, 1973). The rate of this movement is controlled by diffusion of atoms. At sufficiently higher temperature, diffusion occurs rapidly and the atoms are segregated around a dislocation. As a consequence, an equilibrium state is developed where the concentration of solute atoms is higher around dislocations than in the surrounding areas. This phenomenon is known as a dislocation-solute atmosphere. When such a dislocation glides away from the solute atmosphere, a stress field is developed to keep the solute atoms in equilibrium by jumps of atoms from one position to another. The resulting drag force is, thus, depends on the rate of dislocation movement and diffusion of atoms to maintain the equilibrium state.

Now, it is necessary to check whether glide or climb of dislocations is rate controlling in the situation mentioned above. Weertman (1957) suggested that pile-up of dislocations by the mutual interactions is retarded by a back stress. In this condition, climbing and annihilation of dislocations ahead of the pile-up relieve the stress. Therefore, climb and glide are sequential processes and slower one determines the rate. Usually, climb is considered as a rapid process. In solid-solution alloys, when glide is restricted by the interaction of dislocations and solute atoms (Cottrell

and Jaswon, 1949), the strain rate is (Vagarali and Langdon, 1982)

$$\dot{\varepsilon} = B_7 D_s \left(\frac{G\mathbf{b}}{kT}\right)\left(\frac{\sigma}{G}\right)^3 \tag{2.12}$$

where B_7 is a constant which depends on solute-solvent size difference, concentration of solute atoms and normalised values of k, T, G and $\mathbf{b}$. D_s is the solute diffusivity coefficient. For Mg-Al alloys, D_s is (Vagarali and Langdon, 1982)

$$D_s = 1.2 \times 10^3 \exp\left(-Q_s/RT\right)\ \mathrm{m}^2\ \mathrm{s}^{-1} \tag{2.13}$$

where Q_s is equal to $143\,\mathrm{kJ\,mol^{-1}}$ for diffusivity of aluminium into magnesium.

Solute drag creep becomes dominating (compared to climb controlled creep) when solute concentration is increased and stress is below a critical value (Mohamed and Langdon, 1974). However, increasing solute concentration may not significantly affect flow characteristics of an alloy. For example, in Al-Mg alloys, increasing magnesium concentration from 2.8 to 5.5 wt% gave only a subtle increase in strain rate sensitivity (Taleff et al., 1998). This may be attributed to the saturation effect of magnesium solute in the dislocation atmosphere (McNelley et al., 1989).

The temperature dependence of solute drag creep is related to solute concentration (Sherby and Taleff, 2002). At higher temperature, the concentration of solute atoms in the dislocation atmosphere is decreased. Above a certain temperature, the concentration may become similar to the matrix. When this occurs, creep is controlled by dislocation climb.

Dislocation Climb Controlled Mechanism

Climb describes dislocation motion where a dislocation can move out of the slip plane onto another plane. This process occurs by diffusion of vacancies. When dislocation climb controls deformation, the activation energy of deformation is equal to the activation energy for lattice diffusion at higher temperature and pipe diffusion at low temperature (Sherby and Weertman, 1979). However, in dislocation creep, the activation energy for magnesium deformation can be as high as $230\,\mathrm{kJ\,mol^{-1}}$ (larger than that for lattice diffusion) at $>0.75\mathrm{T}_m$, due to the operation of non-basal slip (Tegart, 1961). In such a case, faster slip by basal or non-basal systems would control the creep rate (Sherby and Burke, 1968).

The basic model of climb-controlled dislocation creep was developed by Weertman (1955). The theory was based on Mott's (1953) suggestion that the stress field of piled-up dislocations (at an obstacle such as grain boundary) induces dislocations from other slip systems to join the group and form an immobile dislocation. Under an applied stress, dislocations glide through the grain until they meet an obstacle, such as grain boundary. At this configuration, they start to pile-up and immobile

dislocations are formed when dislocations from neighbouring slip planes combine. In this condition, dislocations between the immobile dislocations and the obstacle are removed by climb into or along the obstacle and are annihilated. The rate of climb depends on the concentration gradient of vacancies between the equilibrium state and near the climbing dislocation.

If a gliding dislocation is trapped by the jogs formed during the interactions of dislocations, diffusion of vacancies will release the dislocation (Pilling and Ridley, 1989). Moreover, subgrain boundaries (formed by the tangle of dislocations) restrict glide of dislocations and climb may occur to release dislocations from these subgrains. Therefore, the rate of creep is controlled by the rate of availability of dislocations for glide, before climbing. Also, it is suggested that the rate of creep is contributed to by the elastic back pressure created by the accumulation of dislocations in the subgrains (Argon and Takeuchi, 1981; Derby and Ashby, 1987; Gibeling and Nix, 1980).

The strain rate is described as (Kassner and Pérez-Prado, 2004)

$$\dot{\varepsilon} = B_8 D_{eff,p} \frac{G\mathbf{b}}{kT} \left(\frac{\sigma}{G}\right)^5. \tag{2.14}$$

.

where $D_{eff,p}$ is the effective diffusivity controlling the contribution of dislocation pipe diffusion (D_p), following Hart (1957), as (Frost and Ashby, 1982)

$$D_{eff,p} = D_L + \frac{20\delta^2}{\mathbf{b}^2} \left(\frac{\sigma}{G}\right)^2 D_p \tag{2.15}$$

where D_p for magnesium is expressed as (Frost and Ashby, 1982)

$$3 \times 10^{-23} \exp\left(-Q_p/RT\right) \ \mathrm{m}^4 \ \mathrm{s}^{-1}. \tag{2.16}$$

Here, Q_p is the activation energy for pipe diffusion.

2.3.4 Constitutive Laws of Superplasticity

Large elongation, typical of superplastic deformation, is associated with a high strain rate sensitivity (m). Higher m gives a higher degree of resistance toward flow localisation. Localised deformation (necking) starts at maximum load, since strain hardening may increase the load-bearing capacity during deformation. At maximum load, the effect of stress increasing by the reduction of specimen cross-sectional area overcomes the load-bearing capacity by strain hardening (Dieter, 2001). It is noteworthy that in sheet materials, where the thickness reduction is lower than elongation, a diffuse neck is produced. This type of neck may lead to fracture or transform into another instability process known as localised necking. The stability

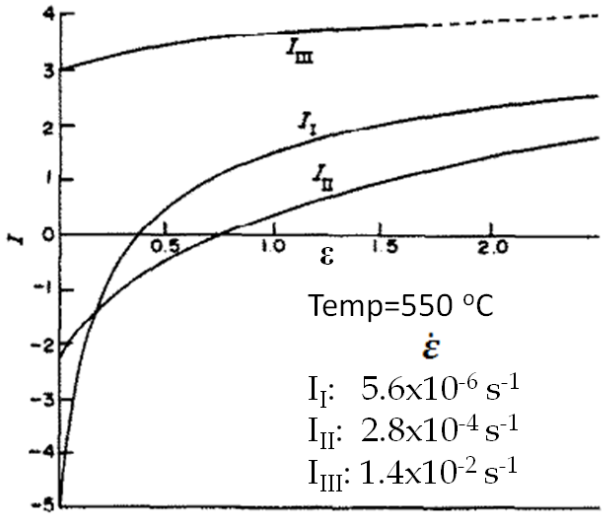

Figure 2.21: The instability parameter, I, showing the plastic instability of different regions (Càceres and Wilkinson, 1984a).

of plastic flow is governed by the condition (Hart, 1967)

$$w + m \geq 1 \tag{2.17}$$

where w is the strain hardening coefficient ($\frac{1}{\sigma}\frac{\partial\sigma}{\partial\varepsilon}$). When the value is < 1, plastic instability occurs. From this equation, it is obvious that both strain hardening and strain rate sensitivity contribute to resist necking.

It is often considered that in region II, $w = 0$ and focus is given to m (Edington et al., 1976). But, strain hardening may occur by strain induced grain growth during deformation at low strain rates. Using the theory of plastic instability, Cáceres and Wilkinson (1984a) developed an instability parameter,

$$I = \frac{1 - w - m}{m} \tag{2.18}$$

which is useful to understand the onset of plastic instability in superplastic materials. Since both region I and II are the regions of low strain rate, higher w is possible. For example, Fig. 2.21 shows that higher w in region I and II leads to a delay in plastic instability (i.e., formation of diffuse necking). In region III, the absence of strain hardening causes a rapid unstable flow. In such a case, necking is rapid. One obvious advantage of strain hardening in region I is the delay of forming diffuse necking. This actually partially compensates for the low m typical of this region. Therefore, necking is not rapid, unlike region III.

The effect of m is more pronounced in retarding neck development. According to Equation 2.17, a higher m provides more resistance to neck growth. A higher m means that as the local strain rate increases in a forming neck, the flow stress

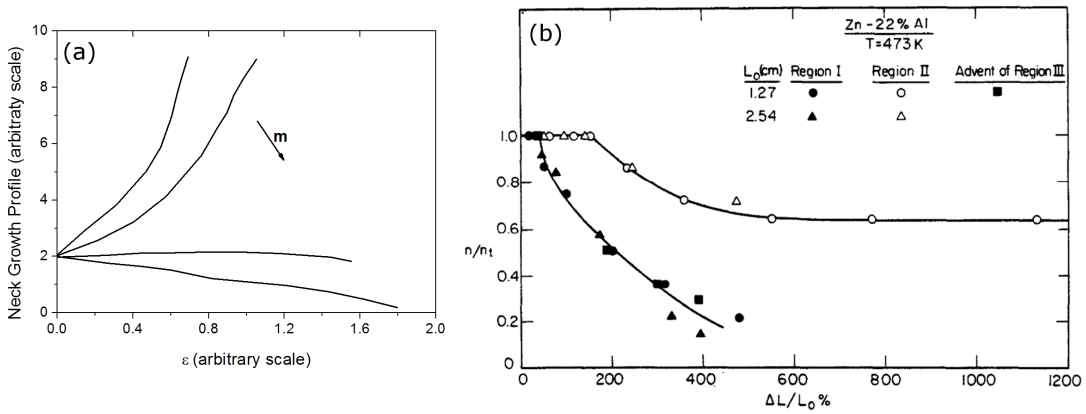

Figure 2.22: (a) A schematic presentation of the effect of strain rate sensitivity (m) on the growth profile of a neck. It is a simplified schematic of an actual profile (Ghosh, 1977). The scale is arbitrary. (b) A plot showing the degree of sharpness of neck during deformation in different regions (Mohamed and Langdon, 1981). L_o represents the initial gauge length which was segmented in 14 sections and n/n_t is the normalised ratio of the number of segments having local elongation ratio equal or greater than total elongation ratio. As n/n_t approaches zero, a sharp neck is developed.

increases rapidly. This increment of local strain rate requires a higher local stress to propagate the neck. Therefore, the growth of the neck is retarded as the applied stress is insufficient to continue its growth. In Fig. 2.22a, the effect of increasing m on the growth profile of a neck is shown. The higher the m-value, the lower the development of neck. The sharpness of neck for superplastic materials was studied by Mohamed and Langdon (1981). They segmented the gauge length into several regions and calculated the local elongation in each segment. The number of segments having similar or higher elongation compared to the total elongation was counted. The normalised ratio of these segments, n/n_t, gives the sharpness of neck. When the ratio is 1, the developed neck is diffuse and a lower value represents flow localisation. In Fig. 2.22b, three regions of superplastic deformation are shown. In region II, flow localisation is resisted for a prolonged time. On the other hand, in region I and III, shortly after the onset of deformation, flow is localised. This behaviour can be explained by m. In region II, m is highest and in other two regions, the value is low.

In the previous section, different strain rates are shown for different deformation mechanisms. The major difference in the expressions for different mechanisms is the variation of the power of stress and grain size. Using the stress exponent ($n = 1/m$) and grain size exponent (p), all those equations can be combined into a single constitutive law as

$$\dot{\varepsilon} = A\frac{G\mathbf{b}}{kT}\left(\frac{\mathbf{b}}{d}\right)^{p}\left(\frac{\sigma}{G}\right)^{n} D\,\exp\left(-\frac{Q}{RT}\right) \tag{2.19}$$

where A is a dimensionless constant, D is the appropriate diffusion constant having

Table 2.6: Values of stress exponent (n) and grain size exponent (p) (Nieh et al., 1997; Sherby and Wadsworth, 1982)

Deformation Mechanism	n	p
Diffusion Creep	1	2 (diffusion is lattice controlled) 3 (diffusion is grain boundary controlled)
Grain Boundary Sliding	2	2 (diffusion is lattice controlled) 3 (diffusion is grain boundary controlled)
Solute Drag Creep	3	0
Dislocation Creep	5	0

an activation energy Q, G is the shear modulus, d is the grain size, p is the grain size exponent reflecting the grain size dependency of flow (Equation 2.2). Temperature dependent G (in MPa) for magnesium was derived by Vagarali and Langdon (1981) from the estimations made by Slutsky and Garland (1957) as

$$G = \left(1.92 \times 10^4 - 8.6T\right) \text{ MPa} \tag{2.20}$$

where T is the absolute temperature.

Now, it is clear that for a particular temperature and microstructure, the unknown parameters are Q, n, p and A. If they are calculated, then the corresponding strain rate of deformation can be calculated.

n can be determined from the inverse slope of a stress-strain rate curve. p can be 2 or 3 depending on the diffusion path. Corresponding A-values for magnesuim can be found elsewhere (Kim et al., 2001). Other parameters are material constants and can be found in Appendix A. The value of D depends on the diffusion process. It may correspond to grain boundary diffusion (D_{GB}), lattice diffusion (D_L), dislocation pipe diffusion (D_P) or diffusivity of solute atoms (D_S).

Therefore, if the value of n and p are known, the mode of deformation can be anticipated. The most important application of the constitutive law (Equation 2.19) is to determine which particular set of experimental conditions and microstructure gives a certain deformation mechanism. The values of n and p are summarised in Table 2.6 for different mechanisms.

2.3.5 Superplasticity in Magnesium Alloys

In this section, superplasticity in different magnesium alloys is discussed together with a summary of the parameters affecting their superplastic properties. In Table

2.7, elongation to failure (e_f) of several AZ magnesium alloys under different test conditions and with different initial microstructures are shown. Although it is often difficult to make a direct comparison of results, since temperature, strain rate and grain size are often all changed between studies, the following broad trends may be identified.

Strain rate plays an important role in superplasticity. For instance, it is generally anticipated that extensive dislocation activity occurs at high strain rates (region III) and low m and grain elongation are common characteristics in this region. However, it is possible that grains do not elongate during dislocation creep (the typical mechanism at a higher strain rate condition) (Panicker et al., 2009). This may occur by the tendency to re-establish dihedral angles of grains by diffusion to get to the equilibrium condition (Raj and Lange, 1985). Therefore, it is very possible that even at higher strain rate condition, grains tend to remain equiaxed. $n \approx 5$ and $Q = Q_L$ in the high strain rate region is consistent with the mechanism of dislocation climb controlled deformation (del Valle et al., 2005; Panicker et al., 2009). Deformation in the high strain rate region, typically gives lower e_f, due to a rapid flow localisation.

In contrast, in the low strain rate test condition, deformation occurs in the superplastic region II. In this region, n is typically 2 and Q can be governed by Q_{GB} or Q_L. In this region, dynamic grain growth (DGG) is quite common and this gives the initial hardening of the flow curve. For example, in an AZ31 alloy, at a strain rate of 10^{-4} s^{-1}, the initial flow stress was increased from 4 to 10 MPa (Panicker et al., 2009), showing the evidence of hardening. The increase of grain size was attributed to the annihilation of low-angle boundaries. However, after a certain strain, DGG was suppressed due to the annihilation of dislocations dynamically in the larger grains. Since GBS is operating dominantly in region II, larger e_f is generally obtained.

Another prominent parameter is temperature. It is noteworthy that a decrease in grain size compensates for a higher strain rate and lower temperature. Therefore, depending on grain size, dislocation creep or GBS dominates. In relatively fine-grained alloys, where GBS dominates, the diffusion path for the accommodation process is found to vary depending on temperature. Following Sherby and Wadsworth's (1982) work, Watanabe and co-authors (1999a) developed a map for the dominant diffusion path as a function of temperature and grain size for magnesium. For example, at 350 °C, lattice diffusion dominates above a grain size of 11 μm. However, it is not clear what the consequences of diffusion path are on e_f. From the latter authors' study, it appears lattice diffusion controlled GBS gave better e_f and m was 0.5 irrespective of diffusion path.

Similarly, if both grain size and temperature are low, GBS is still favoured and accommodation occurs by grain boundary diffusion. For example, in a ZK60 alloy of 6.5 μm grain size, accommodation of GBS was controlled by grain boundary

Table 2.7: A collection of Superplastic Behaviour Observed in AZ31 and AZ61 Alloys

Serial	**Alloy**	**Grain Size, d (μm)**	**Particle**	**Temp (°C)**	**Strain Rate, $\dot{\varepsilon}$ (s^{-1})**	e_f, %[a]	**Deformation Mechanism**	**Failure Mode**	**Reference**
1	AZ31	2.9	NR	400	6×10^{-4}	600	GBS	Cav	(Lee and Huang, 2004)
2	AZ31	4.5	$Mg_{17}Al_{12}$	400	1.4×10^{-3}	360	GBS	Cav	(Yin et al., 2005)
3	AZ31	5–6	$Mg_{17}Al_{12}$	450	3×10^{-4}	220	GBS	Cav	(Zarandi et al., 2008)
4	AZ31	8	NR	400	3×10^{-4}	400	GBS	NR	(Panicker et al., 2009)
5	AZ31	8–25	NR	400	6×10^{-5}	300	GBS	NR	(Watanabe and Fukusumi, 2008)
6	AZ31	11.5	NR	400	2×10^{-4}	140	SDC	NR	(Kim et al., 2001)
7	AZ31	12	NR	450	2×10^{-4}	265	GBS	Nck	(Tan and Tan, 2003b)
8	AZ31	17.5	NR	450	10^{-3}	216	GBS	Cav	(Wang et al., 2006)
9	AZ31	25	NR	450	4.25×10^{-4}	200	GBS	Nck	(Li et al., 2007)
10	AZ31	130	NR	375	3×10^{-5}	196	DCG	NR	(Watanabe et al., 2001)
11	AZ61	6	NR	400	10^{-3}	200	GBS	Nck	(Pérez-Prado et al., 2004)
12	AZ61	5–6	$Mg_{17}Al_{12}$	450	3×10^{-4}	220	GBS	Cav	(Zarandi et al., 2008)
13	AZ61	8.7	$Mg_{17}Al_{12}$	400	2×10^{-4}	500	GBS	NR	(Kim et al., 2001)
14	AZ61	12	NR	300	10^{-4}	800	GBS	NR	(Wang and Huang, 2004)
15	AZ61	17	Al-Mn	375	2×10^{-4}	250	GBS	Cav	(Takigawa et al., 2008)
16	AZ61	20	NR	400	10^{-4}	400	GBS	NR	(Watanabe et al., 1999a)

[a] e_f = Elongation to Failure
[b] Keys: NR= Not reported; GBS=Grain Boundary Sliding; DCG=Dislocation Creep by Glide; SDC= Solute Drag Creep; Cav= Failed by Cavitation; Nck= Failed by Necking

diffusion at $0.5T_m$ (Watanabe et al., 1999b). This is plausible since comparatively low temperature and fine grain size both lead to diffusion dominated by grain boundaries.

It was mentioned earlier that hardening (w) by grain growth provides some stability at least until the increase of m. However, concurrent hardening by DGG may indeed adversely affect e_f since an increase in grain size decreases m. As a consequence, instability may start early and lead to early failure of the material. On the other hand, if a large m (0.5) is maintained to prevent neck growth and less hardening occurs by grain growth, an optimum condition can be obtained, where e_f can be very high. For example, in a ZK60 alloy of 0.8 μm grain size (processed by ECAP), e_f of 3050% was reported (Figueiredo and Langdon, 2008).

It is interesting to note that development of a fine grain size, prior to tensile deformation, may not be necessary in magnesium alloys. This is a consequence of dynamic recrystallization (DRX) during deformation. In the initial stages of deformation, DRX may take place and refine the grains. In the later stages of deformation, such fine grains enhance GBS. This type of behaviour was reported for magnesium alloys during superplastic deformation (Mohri et al., 2000; Tan and Tan, 2003a; Yang and Ghosh, 2008). According to the authors, DRX took place after an initial strain hardening period and refined the grains. After DRX was exhausted, extensive GBS started to occur, leading to an excellent e_f. It was argued that if a microstructure contained a bimodal grain structure, twinning, a nucleant for new grains, occurred at larger grains and a homogeneous fine-grain structure was developed (Yang and Ghosh, 2008). Also, recovery-dominated DRX refines grains (Mohri et al., 2000) by progressive increase of misorientation angle and subsequent conversion of low-angle boundaries to high-angle boundaries (Gudmundsson et al., 1991) up to a certain strain. If grain boundaries are serrated during deformation by the pile-up of dislocations (Tan and Tan, 2003a), dislocations arrange themselves in a low-angle cell structures followed by subgrain formation and thus grain refining occurs. All these behaviours lead to efficient sliding. However, if grain growth occurs continuously, such a behaviour may not be obtained.

2.4 Dynamic Grain Growth

Annealing of a worked material leads to the growth of grains, by consuming smaller grains to achieve a low energy configuration. This is termed static grain growth and usually occurs at elevated temperature. Interestingly, during deformation, another type of grain growth—dynamic grain growth (DGG)—may be observed. In DGG, grains grow by the application of strain. Such strain-induced grain growth is important in superplastic materials, since large strains are typical of superplastic deformation.

DGG can lead to hardening of the flow curve (Ridley et al., 2005). Watts and Stowell (1971) argued that hardening during superplastic deformation is different from typical strain hardening observed in other types of materials. The authors observed that DGG induced hardening was strain rate sensitive, which is not very typical in hardening by dislocation interactions. Also, they ruled out hardening by the local increase of strain rate at the diffuse neck, since this type of hardening is not important in the early stage of deformation. Therefore, they concluded that grain coarsening was the reason for hardening of the flow curves. Such a hardening is important in terms of flow localisation. Since the stress is higher at a diffuse neck than in other areas of the gauge, the local strain rate is higher at the neck, if grain size remains the same (Senkov and Likhachev, 1986). As a consequence, growth of the neck increases (i.e., decrease of cross-sectional area at the neck region) compared to other areas. Now, if strain-induced grain growth occurs at a different rate in the higher strain rate region, such as the neck, neck propagation is retarded by flow strengthening.

Clark and Alden (1973) emphasised the importance of DGG in superplastic deformation during a study of Sn-1Bi alloy. According to the authors, grain rotation during GBS can lead to a configuration where the misorientation between neighbouring boundaries of two grains is eliminated and a single large grain is formed by coalescence. To maintain local equilibrium, some boundary migration of the coalesced grain may occur. Mobility of the boundaries is enhanced by the grain boundary diffusion. Wilkinson and Cáceres (1984) considered DGG as the accommodation process of GBS. According to them, migration of boundaries is required to recover the damage caused by GBS at the triple points and thus DGG occurs during deformation. However, recently Bate (2001) suggested that DGG was a special case of Zener pinned systems, where perturbation of grain structure during straining destroyed the local equilibrium. As a consequence, DGG occurs, given that boundary migration is rapid at the temperature and strain rate of concern.

Equation 2.18 includes the term w, which is a DGG induced hardening coefficient. The contribution of w to stabilise the onset of plastic instability was also discussed earlier. The effect of hardening, at least at the initial stages of deformation, is important. The effect of w and m counter each other (Ash and Hamilton, 1988). Hardening gives the plastic stability to retard growth of neck in the initial stage and m tends to contribute more in the later stages of deformation. However, since superplasticity is largely dependent on GBS, growth of grains will eventually retard sliding of grains (Li et al., 1997) and result in loss of superplastic properties. Therefore, a balance is required, at a particular test condition, between grain growth and GBS.

The simplified grain growth equation is (Wilkinson and Càceres, 1984)

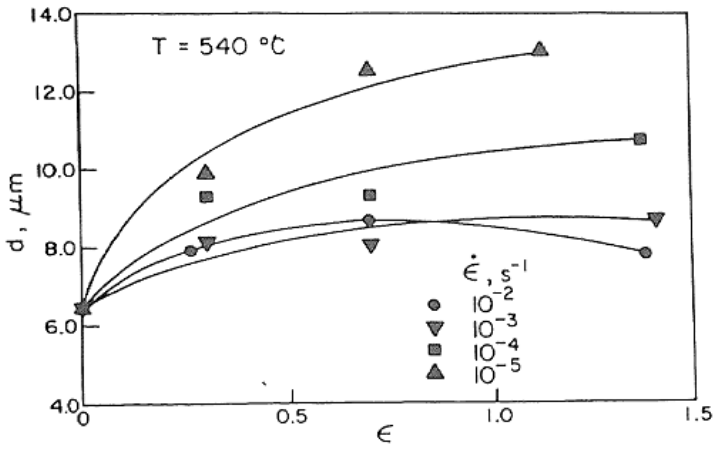

Figure 2.23: Increase of grain size during deformation of an Al-4.7Mg-0.7Mn-0.4Cu alloy at 550 °C (Kashyap and Tangri, 1987).

$$d = d_o \exp(\alpha_g \varepsilon) \tag{2.21}$$

where α_g is the grain growth coefficient and depends on the sliding distance and d_o is the initial grain size.

At a given strain and in the absence of DRX, grain size increases with a decrease in strain rate and an increase of strain (Senkov and Myshlyaev, 1986). Fig. 2.23 shows an example of typical grain growth observed during superplastic deformation. Decreasing strain rate influences the growth of grains. It is interesting to note that though DGG occurs throughout the deformation, in the later stages it does not have any effective contribution to stability and a rapid flow softening may occur by cavitation (Kashyap and Tangri, 1987).

2.5 Cavitation in Magnesium Alloys

A superplastic material fails by two mechanisms: unstable plastic flow followed by necking to a sharp point or nucleation, growth and coalescence of cavities (Pilling and Ridley, 1989). If failure occurs by unstable plastic flow, a fine neck is developed, leading to failure. On the other hand, if cavitation is the failure mode, a rough fracture surface is obtained. Strain rate sensitivity (m) values are typically very high (>0.4) in superplastic materials, which provides an excellent resistance towards necking and ensures large elongation to failure of the material. Another resistance may come from grain growth which gives some local strain hardening, enhancing tensile stability of the gauge. However, the development of cavities suppresses the resistance to failure.

The study of cavity nucleation in magnesium alloys is extremely limited, and the

theories discussed below were developed for creep. These theories were successfully applied to aluminium-, copper- and iron-based alloys. Since the dislocation glide in hcp magnesium is very different to these cubic metals, and this is a key part of some of the theories discussed, it is not yet clear how applicable these equations will be to magnesium. One aim of this study was to assess the validity in using these current theories to understand cavitation in magnesium alloys. In this section, at first, theories related to nucleation and growth of cavities are discussed followed by a discussion of cavitation investigation in aluminium and magnesium alloys. The effects of strain rate, temperature, grain size and deformation mechanisms are also highlighted.

2.5.1 Nucleation of Cavities

Nucleation of a cavity may occur homogeneously or heterogeneously. Homogeneous cavitation may occur within a grain as a direct consequence of the underlying deformation mechanism. In contrast, heterogeneous cavitation takes place preferentially at grain boundaries when deformation is perturbed by the offsets produced at grain boundaries or by obstacles present in the microstructure.

Seitz (1953) showed that a cavity might form by a cluster of vacancies having a very high concentration. Therefore, it is possible that cavities may form at the interior of grains during plastic flow, since dislocations can supply vacancies (Bauer and Wilsdorf, 1973). This leads to a homogeneous distribution of cavities. Vacancies can be accumulated in a grain interior from the dislocation loops surrounding a stacking fault or prismatic loops of dislocations surrounding un-faulted material (Sigler and Kuhlmann-Wilsdorf, 1967).

On the contrary, Balluffi and Seigle (1957) argued that the efficiency of vacancy accumulation in a grain interior depends on climbing of dislocations and if grain boundary sliding (GBS) takes place, grain boundaries become potent sites for nucleation of cavities. The chance of cavity formation at boundaries is high, since vacancy flow between grain boundaries may exist, not in dislocation arrays. In this regard, a strong support comes from the study of Brinkman (1955). He proposed that a very high concentration of stress, instead of concentration of excess vacancies in an order of 100 times greater than the equilibrium values, would cause condensation of vacancies. Such a high local stress is created by a pile-up of dislocations.

The heterogeneous nucleation of cavities at microstructural irregularities may occur by particles, triple points, ledges or jogs. Investigation of copper (99.98% pure), α-brass (70.1% Cu and 29.8% Zn) and magnesium (containing 0.20% Pd and 0.02% Fe) led Greenwood and co-authors (1954) to suggest that, cavities might appear at grain boundaries by diffusion of vacancies. Due to dislocation movement

and thermal vibration, the position of vacancies usually does not remain at a certain location. Condensation of vacancies thus becomes difficult to occur. However, if grain boundaries act as sink for these vacancies, they may accumulate there and form a stable cavity. During deformation, more vacancies are clustered at the newly formed cavity and the cavity grows. Balluffi and Seigle (1957) suggested that vacancies could migrate between the interface of the nucleated cavity and grain boundary rapidly, resulting in stable cavities at boundaries transverse to the applied stress.

However, the work of Greenwood, Miller and Suiter was criticised since an agglomeration of vacancies was not kinetically favourable. Instead, cavity formation at the grain boundary by the impingement of slip is an alternative explanation for cavity formation (Fisher, 1955). Impingement of slip by the screw dislocations leads to local high stresses which may become larger than the applied stress, forming a cavity at the grain boundary.

GBS is a dominating deformation mechanism during superplastic deformation. Sliding is hindered at obstacles, such as particles, ledges and jogs, resulting in a rise of local stress. This stress concentration is developed by the pile-up of dislocations ahead of the obstacle. Such a stress concentration can lead to the formation of a cavity. This is discussed below for grain boundary ledges and jogs followed by the effects of particles.

The assumptions of Fisher were modified by Gifkins (1956) and applied to GBS. Consider sliding occurring between grain 1 and 2 (Fig. 2.24a). Now, a grain boundary jog may be formed by slip occurring in the grains. The size of the jog depends on the number of accommodating dislocations passing to grain 1, resulting in a pile-up of dislocations at grain 2 (Fig. 2.24b). However, boundary migration may annihilate the jog developed in this way. Before this happens, the local stress concentration may cause a de-cohesion of the jogged boundary, followed by an open up of the jog (3) prior to forming a cavity (Fig. 2.24c). If this process is repeated at the adjacent areas simultaneously, a cavity of stable size may appear.

According to Davies and Dennison (1958), the Gifkins model of cavitation at offsets produced by dislocations has some serous limitations. One such limitation is the migration of boundaries, which certainly eliminates the newly formed jog. The authors proposed a slightly different mechanism of ledge formation. In brief, a dislocation containing a screw component transverse to the grain boundary forms a step at the interacting boundary which cannot be removed by grain boundary migration and this step blocks sliding of grains, leading to the formation of a cavity. However, these steps are annihilated if cross slip occurs during deformation. Another modification of Gifkin's model was made by Chen and Machlin (1956) on the basis that any irregularity at the boundaries would be able to produce an excessive stress concentration required to form a cavity.

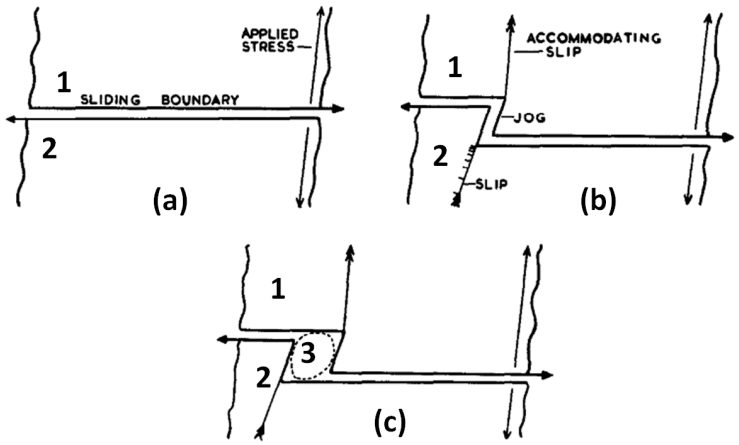

Figure 2.24: A schematic presentation of Gifkins mechanism of nucleation of a cavity during GBS. (a) Two grains (1 and 2) are sliding under an applied stress; (b) slip in Grain 2 may form a jog and the size of the jog depends on the accommodation slip at grain 1; (c) a cavity (3) forms immediately if the jog is not annihilated by boundary migration (Gifkins, 1956).

The models discussed above neglect the effect of particles present in commercial alloys. It was shown that a grain boundary offset can lead to local stress concentrations, forming a cavity. However, a similar effect is established if a microstructure contains particles (Cottrell, 1961). For an Mg-0.8Al-0.005Be Maxnox alloy, Harris (1965) reported that cavities could be associated with particles. Greenwood and Harris (1965) pointed out that the cohesion between particles and matrix should be very low to allow vacancy condensation surrounding a particle. In contrast, McLean (1966) considered dislocation loops might form surrounding the particles and a considerable amount of local stress might lead to a fracture at the interface.

Raj and Ashby (1975) performed a detailed study on the probability of cavity nucleation by particles. They estimated a critical stable cavity size based on applied and interfacial stress. They argued that GBS obstructed at a particle was accommodated by either elastic displacements or diffusional and dislocation flow. The theory is discussed in brief. Diffusion may occur either along the grain boundary or through the lattice. If the developed stress concentration at an interface of a particle and matrix is higher than the applied stress, condensation of vacancies occurs prior to forming a cavity. The incubation time required for vacancy condensation decreases if GBS is operating during deformation, leading to early formation of a cavity. This model is used extensively in describing cavitation in the superplastic regime. The authors estimated the critical stable cavity radius, r_{cav}^{crit}, where the maximum free energy of a cavity is reached. This is expressed as

$$r_{cav}^{crit} = \frac{2\gamma}{\sigma} \tag{2.22}$$

where γ is the surface energy. According to this equation, if the applied stress is increased, the stable critical size of a cavity decreases. Cavities having size less than r_{cav}^{crit} are unstable and sinter out by surface tension (Miller et al., 1979).

It is obvious from the discussion above that grain boundary offsets or obstacles develop local high stress concentrations and if this stress cannot be accommodated rapidly by diffusion or dislocation glide into the surrounding grains, a cavity is developed.

Needleman and Rice (1980) considered the combined effect of diffusion and dislocation glide, based on an early work by Hull and Rimmer (1959) and defined a critical diffusion length, Λ_{GB}, representing the maximum length over which concentrated stress can be relaxed quickly along the grain boundary. This length is considered as the minimum radius of a grain boundary particle in obstructing the relaxation of stress. Now, for an atomic volume of Ω with energy of kT, diffusivity is $\delta D_{GB}/kT$ and the grain size exponent (p) is 3 for grain boundary diffusion. Combining these, the expression becomes

$$\Lambda_{GB} = \left(\frac{\Omega \delta D_{GB}}{kT}\frac{\sigma}{\dot{\varepsilon}}\right)^{1/3} \tag{2.23}$$

where the terms are defined earlier.

However, Chokshi and Mukherjee (1989a) argued for the use of an effective diffusion coefficient, instead of grain boundary diffusion coefficient, and they proposed a slightly modified version of Λ_{GB}, which involved lattice diffusion ($p = 2$). The expression is

$$\Lambda_L = \left(\frac{\Omega D_L}{\pi kT}\frac{\sigma}{\dot{\varepsilon}}\right)^{1/2} \tag{2.24}$$

where Λ_L is the critical diffusion length.

Stowell (1983) proposed another expression for the critical diffusion length (λ_S) including a parameter to incorporate the effect of GBS as

$$\Lambda_S = \left(\frac{2.9\Omega \delta D_{gb}}{\alpha d kT}\frac{\sigma}{\dot{\varepsilon}}\right)^{1/2} \tag{2.25}$$

where α is the fraction of tensile strain accommodated by GBS. Usually, GBS is considered to contribute 50% of the total strain; hence, α is equal to 0.50. But, this model was criticised for higher dependency on GBS (Ridley et al., 2007).

Riedel (1987) summarised the reasons that particles can act as preferential cavity nucleation sites: (a) particles resist GBS followed by stress concentration; (b) they may not be perfectly bonded with the matrix and (c) vacancy condensation is facilitated at the particle/matrix interfaces.

In summary, formation of a cavity may occur by vacancy accumulation, GBS

or dislocation pile-up. Vacancy condensation requires a high local stress. Stress concentration can occur by GBS at heterogeneities such as particles and triple points. Stress concentration can be relieved by diffusion, and so a critical condition is required to form a growing cavity, such that the accumulation of stress concentration exceeds the relief by diffusion.

2.5.2 Growth of Cavities

The growth of an individual cavity may be driven by stress induced diffusion or by dislocation activity during plastic flow. Several mechanisms were proposed in the past to explain the growth of individual cavities. The growth theories are discussed below in separate sections focused on stress driven diffusion growth and plasticity controlled growth. The shape of a cavity is an important factor to identify the operating growth mechanism, which is also discussed in a separate section.

Stress Induced Cavity Growth Mechanisms

A cavity may grow by diffusional flux of atoms from the edge of the cavity along the grain boundary. The driving force for the diffusion flux is the gradient of the chemical potential. Under an applied stress, diffusion flux in the grain boundary is equal to the gradient of the chemical potential times the atomic mobility (Riedel, 1987):

$$J_{gb} = \frac{\delta D_{GB}}{kT} \nabla \mu \tag{2.26}$$

where $\nabla \mu$ is the gradient of chemical potential at the grain boundary. $\nabla \mu$ along a grain boundary is formulated as $\nabla \mu = -\sigma_n \Omega$, where σ_n is the stress acting on transverse to the boundary. $\sigma_n \Omega$ is the contribution of σ_n to the chemical potential and is the work done by σ_n to add an atom to the boundary.

A cavity will grow by diffusion only when the applied stress is larger than the potential of the cavity for losing vacancies (Balluffi and Seigle, 1957). This occurs when the stress term in Equation 2.22 is greater than $2\gamma/r_{cav}$. Hull and Reamer (1959) explained this as the critical cavity size for an applied stress below which cavities would not able to overcome the surface tension. The authors argued that the growth of a cavity occurs by the accumulation of vacancies, obtained from grain boundaries. Major assumptions made in the Hull and Reamer model are: (a) grains are assumed elastic in nature, (b) vacancies are condensed uniformly at boundaries and (c) cavities are formed at the onset of deformation. In reality, grains do not remain elastic during deformation involving dislocation movements. Also, since dislocation glide perturbs the grain structure, a uniform vacancy flux is unlikely to occur along boundaries.

To overcome the limitations of Hull and Rimmer model, Beere and Speight (1978)

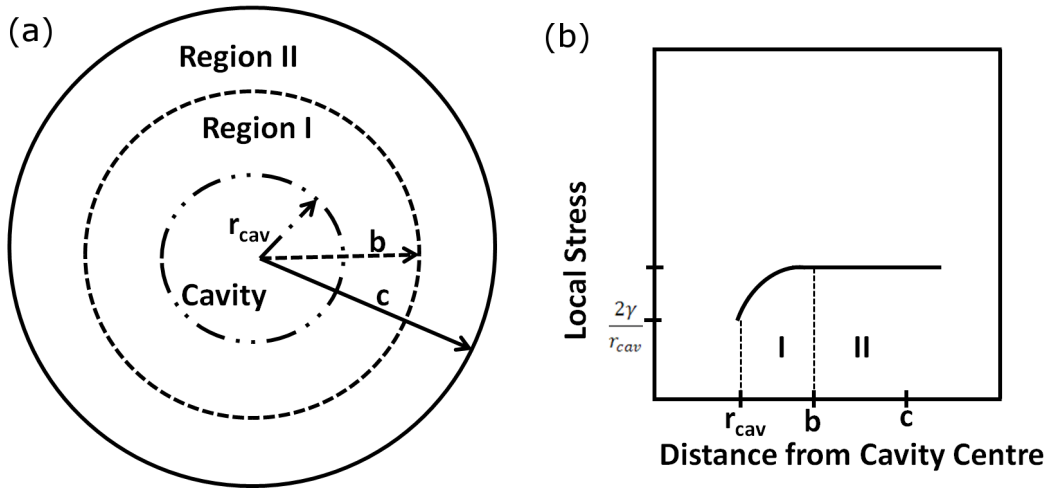

Figure 2.25: (a) An illustration of Beere and Speight (1978) mechanism of cavity growth by stress induced diffusion. (b) Stress gradient across different regions near a growing cavity.

proposed a modified model considering grains do not remain elastic during deformation and the source of vacancies should be close to a growing cavity, unlike the Hull and Rimmer mechanism. This mechanism is widely used to explain growth of cavities in superplastic materials.

This mechanism considers that vacancies are not generated uniformly at the boundary, but more vacancies are created at a close distance to a cavity nucleus. Beyond this distance, locally no vacancies are created and the surrounding area is controlled by plastic flow. However, very close to a cavity, a gradient of stress is developed which accelerates vacancy diffusion between cavity and grain boundary.

The mechanism is illustrated in Fig. 2.25. The whole region is a part of a grain boundary where the cavity is formed. Region I is the diffusion zone surrounding a cavity of radius r_{cav} (Fig. 2.25a). In this region, vacancies are uniformly generated and are diffused to the cavity. Plating of atoms at the boundary moves the boundary apart from the cavity. In region II, no vacancies are created and displacement from region I is countered by dislocation movements. In Fig. 2.25b, the gradient of stress in region I is shown. It is assumed in this model that no gradient exists in region II and therefore no vacancies are generated in this region of grain boundary. The low stress gradient in region I is due to the fact that region I is a low stress elastic volume contained in a plastically deforming region II. In region I, the stress is equal to $2\gamma/r_{cav}$ (see Equation 2.22). A cavity having a radius smaller than r_{cav} will sinter out (Balluffi and Seigle, 1957). The increase of stress away from the cavity allows vacancy diffusion until the stress becomes independent of distance.

The simplified equation for cavity growth by stress induced diffusion is

$$\frac{dr_{cav}}{d\varepsilon} = \frac{\Omega\delta D_{gb}}{5kTr_{cav}^2}\frac{\sigma}{\dot{\varepsilon}} \tag{2.27}$$

where the terms are defined earlier. This expression demonstrates that $dr_{cav}/d\varepsilon \propto 1/r_{cav}^2$. Integration of this expression shows the volume fraction of cavities is linearly related to the strain. As the cavity gets larger, the growth rate decreases parabollically, and this is due to a decrease in vacancy flux. Edward and Ashby (1979) developed a similar expression, adopting the methodology of Beere and Speight. The only difference between both models is in size of the diffusion zone and former authors agreed that the growth rate predicted by both models were similar.

It is very possible that if a growing cavity intersects several grain boundaries, the growth rate would be different than that of Equation 2.27. This was first observed by Pilling and co-authors (1984) during a study of cavity sintering in a Ti-6Al-4V alloy. They noted that if mass transportation occurred by several boundaries due to the typical fine grain size in superplastic alloys, sintering rate would be increased. Based on this supposition, Chokshi and Langdon (1987) proposed a cavity growth mechanism. This is termed superplastic diffusion growth. This is, in fact, very similar to the early developed expressions for diffusional growth, the only difference is the incorporation of grain size (d) effect. However, the fundamental requirement of a very small grain size ($<5\,\mu$m) for this model limits its applicability. The average grain size investigated in the current study is one and half times greater than the limiting requirement; hence, this mechanism may not be important for the current study. However, this does not rule out the idea that intersection of a cavity by several boundaries influences the growth of cavities by diffusion.

Hull and Rimmer did not consider lattice diffusion in their work, since they showed that for silver, at 500 °C, the contribution of lattice diffusion to the total number of atoms transferred by diffusion was only 6% to that of grain boundary diffusion. Hence, they ignored lattice diffusion effect in their mechanism. However, if transfer of atoms is controlled by lattice diffusion, the expression for cavity growth (Equation 2.27) needs to be modified. The potential gradient for this type of atom flux (from cavity surface to the longitudinal grain boundary of a grain of size d) is $2\gamma\Omega/r_{cav}d$ (Burton, 1974). Based on the suggestion by Burton, Chokshi (1986) proposed an expression for diffusion growth controlled by lattice diffusion. The modified diffusion growth equation is

$$\frac{dr}{d\varepsilon} = \frac{\Omega\lambda\delta D_L}{5\pi kT}\frac{1}{r^2}\frac{\sigma}{\dot{\varepsilon}} \tag{2.28}$$

where λ is the cavity spacing. The domination of a particular diffusion path depends on the ratio of $D_{gb}\delta/D_L\lambda$. It was claimed that if this ratio is greater than one, growth is controlled by grain boundary diffusion (Shibutani et al., 1998).

Plasticity Induced Cavity Growth Mechanisms

Sagat and Taplin (1976) investigated a 60/40 brass deformed in the superplastic regime and reported for the first time that a cavity can grow solely by plasticity, not by vacancy condensation. Hancock (1976) also investigated growth of cavities and pointed out that plastic flow, not vacancy concentration, was responsible for growth of a cavity. The deformation of the matrix in close proximity to a cavity in this case drives the growth of a cavity. It is very possible that plastic flow tends to elongate a cavity in the applied stress direction, developing an elliptical cavity shape. For a micron size cavity, Hancock showed that diffusion growth did not remain important and very large cavities were usually elongated along the tensile stress direction. This directionality of cavity axis cannot be produced by the vacancy flux and hence it is attributed to the plasticity controlled growth. The model for the plasticity controlled growth can be expressed as

$$\frac{dr_{cav}}{d\varepsilon} = r_{cav} - \frac{3\gamma}{2\sigma} \tag{2.29}$$

where the terms are defined earlier. Simplifying this gives $dr_{cav}/d\varepsilon \propto r_{cav}$, i.e., growth rate is proportional to the cavity size and volume fraction of cavities increases exponentially with strain.

Hancock emphasised that for small cavities diffusion growth might remain important, but for large cavities, growth should be governed by plastic flow. He also suggested that small cavities lying perpendicular to the applied stress were developed by joining of small cavities. Apart from the consideration of size of a cavity, the plasticity controlled mechanism becomes important when local stress concentration occurs. Hancock identified the importance of the ratio of $\sigma/\dot{\varepsilon}$. If this is low, then the plasticity controlled mechanism is expected to occur in small sized cavities.

Stowell (1980) investigated the cavity growth phenomenon specifically for superplastic alloys. He argued that sub-micron size cavities would grow by diffusion and when the size approaches to one micron (for the iron based alloys), the growth would be controlled by plasticity. According to him, plasticity controlled growth is faster for larger cavities and is expressed as

$$\ln\left(\frac{V_c}{V_o}\right) = \eta\varepsilon \tag{2.30}$$

where V_o is the pre-existing cavity fraction, i.e., volume fraction of cavities at zero strain, V_c is the cavity volume fraction at the strain ε. η is cavity growth rate parameter and is dependent on the applied stress and geometry of deformation (Pilling and Ridley, 1988b). η can be determined from the following expression

$$\eta = \frac{3}{2}\left(\frac{m+1}{m}\right)\sinh\left(2\left(\frac{2-m}{2+m}\right)\right)\frac{\alpha_s}{3} \tag{2.31}$$

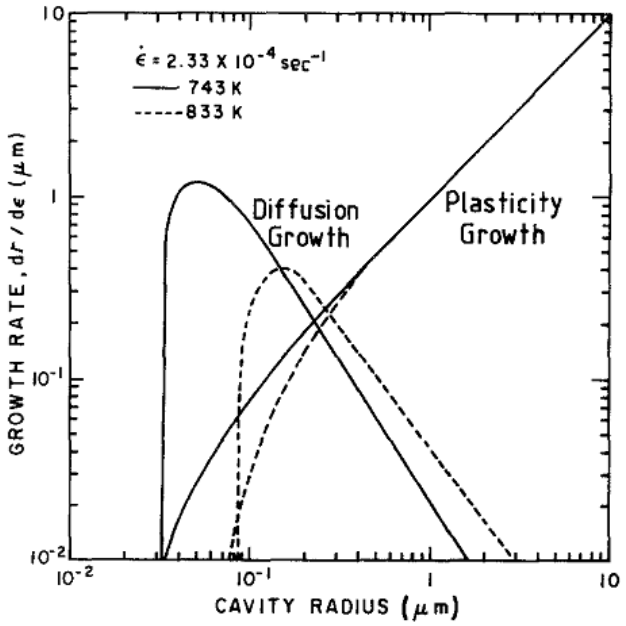

Figure 2.26: Predicted growth rates of cavities by diffusion- or plasticity-controlled mechanisms (Ridley et al., 1984).

where α_s is a constant and depend on the extent of GBS. The value of α_s lies between 1 and 2 (Pilling and Ridley, 1988b). However, Stowell's model is similar to the model proposed by Hancock in a sense that the volume fraction of cavities is $4/3\pi r_{cav}^3 N$, where N is number of cavities and it can be rearranged to get Equation 2.29.

In Fig. 2.26, predicted cavity growth rates by the diffusion and plasticity mechanisms are shown. As mentioned earlier, diffusional growth dominates only in the submicron size cavities; otherwise plasticity controlled growth governs the development of cavities.

In summary, diffusional growth of a cavity occurs, in the presence of a stress, along a grain boundary which is the source of vacancies. A positive chemical potential gradient is developed between the atoms at the boundary and the atoms of the cavity surface by the applied stress by reducing the chemical potential of the atoms at the boundary by a value of $\sigma_n\Omega$ (Miller and Langdon, 1980). As a consequence, atoms are diffused from the vicinity of a cavity under an applied stress. Thus, a cavity grows by diffusion. In contrast, for the large micron sized cavities, diffusion controlled growth does not remain rate controlling and plasticity driven growth becomes important. Diffusion- or plasticity-based cavity growth mechanisms are independent to each other and cavity growth is dominated by the mechanism providing fastest growth rate.

2.5.3 Coalescence of Cavities

The effect of coalescence of cavities is catastrophic. Failure by cavitation occurs by interlinking of cavities. When two cavities grow to become close to each other, they

may join to form a large cavity, given spheroidisation by surface diffusion is rapid. Moreover, joining of cavities results in a deficiency of load bearing capacity in the surrounding area, leading to a higher local cavity growth rate (Càceres and Wilkinson, 1984b). The mechanisms of growth of a cavity discussed in the preceding section do not incorporate coalescence effect and thus may misinterpret the actual growth rate.

Goods and Nix (1978) artificially implanted bubbles in silver to understand cavitation and confirmed the failure of the material occurred by coalescences of cavities (bubbles). In superplastic materials, coalescence is an important feature, since large strains, characteristic of these materials, may allow extensive plasticity controlled growth of cavities. Therefore, initially widely spaced cavities may become close to each other and interlink.

Stowell (1984) analysed the coalescence feature of cavities based on his earlier work (Stowell, 1980) on estimation of the plasticity driven cavity growth rate parameter, η. According to him, surface diffusion has to be rapid to allow the coalesced cavity to become spherical and the growth rate increases significantly if the growth is governed by plasticity. Moreover, Pilling (1985) argued that coalescence of cavities depends on strain level and the volume fraction of cavities. If the volume fraction of cavities is large, then the total number of cavities and their average size should be high. This, in turn, decreases the inter-cavity spacing and the probability of coalescence increases. Coalescences thus become important in the later stages of deformation, where the volume fraction of cavities is, obviously, higher for a material in which cavitation is occurring.

Pilling also performed numerical analysis to develop an expression for coalescence but it was limited by the cavity spacing and size. Based on the investigations by Stowell and Pilling, Nicolaou and Semiatin (1999) proposed a model and considered that cavity coalescence was possible only at a very high cavity growth rate. In a following work (Nicolaou and Semiatin, 2000), they concluded that there existed a critical true strain at which cavity coalescence would commence and coalescence should occur if the cavity volume fraction approached 1%. However, the presence of a critical strain for cavitation cannot be justified, since nucleation of cavities is not uniform throughout the microstructure. Therefore, coalescence cannot depend on a single critical strain.

2.5.4 Shapes of Cavities

In the preceding sections, the growth of cavities under different mechanisms are discussed. It may be interesting to identify the shapes of cavities developed by different mechanisms. It is generally accepted that cavity shape becomes spherical when diffusion controlled growth dominates and the cavities tend to elongate along

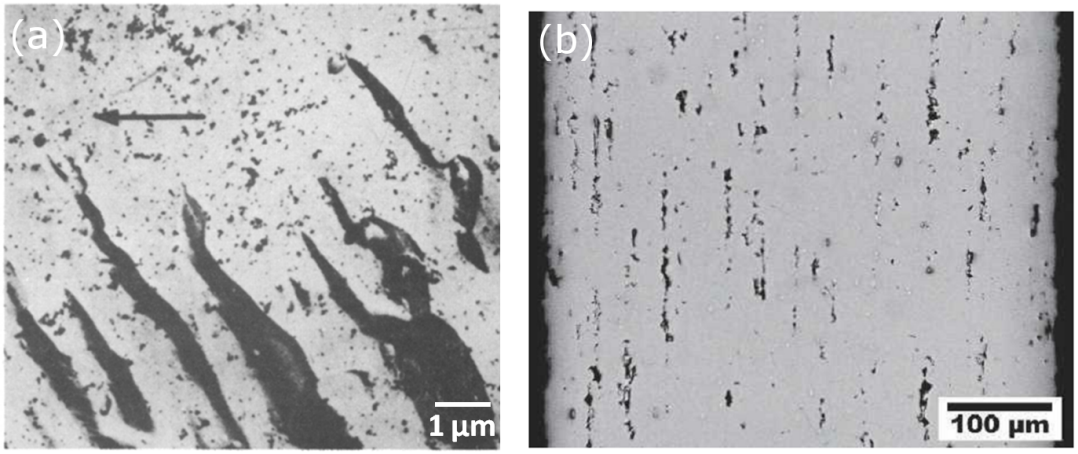

Figure 2.27: (a) An example of cavity shape if deformation occurs by GBS in iron at 650 °C (Davies and Williams, 1969). (b) Stringer-like cavity formation in an Al5083 aluminium alloy at 450 °C (Kulas et al., 2006).

the tensile axis when plasticity driven growth mechanism operates. However, this simple justification is altered depending on several factors, such as deformation mechanism, strain level, presence of particles, etc.

If cavities are formed at jogs, they may further grow by repeated action of plasticity and GBS (Gifkins, 1956). In such a case, long finger shape cavities are developed (Fig. 2.27a). On the other hand, if the solute drag mechanism is dominating, cavities are coalesced along the tensile axis and a stringer-like distribution of the cavities (Fig. 2.27b) is formed (Kulas et al., 2006). Stringers are formed when cavities are aligned in a particular direction in the microstructure.

Stringer-like cavity distribution may develop during deformation of particle containing alloys depending on strain rate and particle position. Stringers of particles may form during thermo-mechanical treatment which may distribute particles along the rolling direction. Cáceres and Wilkinson (1984b) studied a hot rolled copper-based alloy containing particles at 550 °C. The particles were aligned along the rolling direction. Under a high strain rate test condition, cavities were formed at the vicinity of these particles and were elongated along the tensile axis. They were coalesced at higher strain but remained elongated, probably constrained by particles. When the strain rate was reduced, the cavities formed at particles were large, having a shape that was close to spherical. The spherical shape might be misinterpreted as evidence that diffusion controlled growth dominated at the low strain rate condition. However, the authors suggested that the spherical shape of the cavities was instead developed by coalescence.

Similar behaviour was observed in a 5083 aluminium alloy (Kulas et al., 2006), where large coalesced cavities (slightly oriented normal to tensile stress) were observed after GBS controlled deformation. Moreover, the cavities did not elongate in the

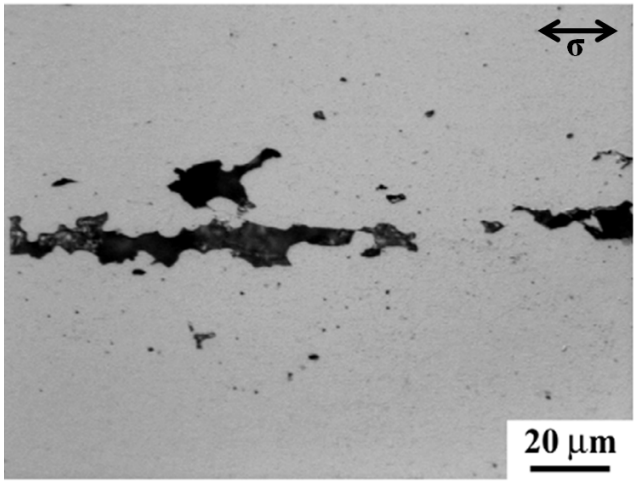

Figure 2.28: Shape of an elongated cavity of 7075 Al alloy deformed at 480 °C under a strain rate of 10^{-2}. The micrograph was taken after deforming to a true strain of 2.5 (Ma and Mishra, 2003).

low strain rate regime as a consequence of a dynamic equilibrium between cavity coalescence along the transverse direction and plasticity driven growth along the tensile axis. It is interesting to note that the direction of stringers of cavities depends solely on rolling direction (in other words, particle alignment direction), irrespective of tensile stress direction (Chokshi and Langdon, 1990).

Kawasaki and co-workers (2005) studied a 7034 (Al-11.5Zn-2.5Mg-0.9Cu-0.2Zr – wt%) aluminium alloy, having an ECAP processed grain size of 0.3 μm. They rationalised orientation and circularity of cavities on the basis of the growth mechansims. For most of the small cavities, the circularity was close to one, as expected for diffusion controlled growth and the orientation of these cavities was between 75 to 90° with respect to the tensile axis. For the largest cavities, the trends were opposite, showing substantial lower values of circularity ($\ll$1) and orientation was approximately within 0 to 15°. This confirms plasticity driven growth for the largest cavities. However, there were some anomalies in their results, such that some largest cavities were aligned approximately normal to the tensile axis. Though the authors did not explain the anomalies, this seems to be the effect of coalescence.

It is interesting to note that large elongated cavities may tend to become spherical, if the deformation temperature is very high (Chokshi and Mukherjee, 1989b). This may occur by transport of matter around the cavity by surface diffusion. The rate of spheroidisation depends on the growth rate of cavities by matrix plasticity, the relative rate of surface diffusion and extent of GBS.

Fig. 2.28 shows a micrograph of a cavity which was grown by plasticity (Ma and Mishra, 2003). The shape is elongated towards the tensile direction and several cavities were also coalesced together.

2.5.5 Cavitation in Aluminium and Magnesium Alloys

Compared to magnesium alloys, cavitation in aluminium alloys has been investigated extensively to understand formation and growth kinetics of cavities. In the following section, cavitation in several aluminium alloys is discussed. Insights into cavitation behaviour fundamentally obtained from aluminium alloys helps to explain cavitation behaviour in magnesium, which to date has only received limited attention.

In aluminium alloys, particles are essentially responsible for nucleation of cavities (Bae and Ghosh, 2002a; Bae and Ghosh, 2002b; Chokshi and Mukherjee, 1989b; Dupuy and Blandin, 2002; Ma and Mishra, 2003; Ridley et al., 2007). If particles are fragmented after thermo-mechanical treatments, there is a possibility that cavities are constrained in the fragmented particles. In such a case, stringer-like cavitation may occur (Dupuy and Blandin, 2002). Such constrained cavities tend to coalesce early and may affect the failure behaviour of an alloy. Nucleation of cavities is found to be continuous, i.e., cavitation occurs throughout the deformation. To nucleate a cavity, a particle must be located at a grain boundary.

If a microstructure contains both grain boundary particles and intragrannular particles, then cavities are observed only at the grain boundary particles, even if the particle size is smaller than the grain interior particles (Jiang et al., 1993).

A major criterion for nucleation of cavities is the size of a particle. Therefore, if a microstructure contains different types of particles, all of them are expected to be equally efficient in forming a cavity if they are larger than the critical particle size. However, for a 5083 aluminium alloy, containing Al_6MnFe and Mg_2Si particles, Mg_2Si particles were claimed to be more efficient in nucleating cavities (Chang et al., 2009). The reason for this behaviour is not clear but may be a consequence of the preferential location of different particle types at grain interiors and boundaries.

The effect of grain size on cavitation has also been established for aluminium alloys. A fine grain size leads to a lower number of nucleated cavities (Humphries and Ridley, 1978) as a direct consequence of the decrease of flow stress in the superplastic regime. For a 7075 (Al-5.6Zn-2.5Mg-1.6Cu-0.23Cr – wt%) aluminium alloy, Ma and Mishra (2003) confirmed this trend for two alloys having grain sizes of 4 and 8 μm.

DGG leads to an increase in cavity formation as a consequence of the lower accommodation rate by grain boundary diffusion, or grain boundary migration, when DGG occurs (Livesey and Ridley, 1982). Moreover, an increase in grain size increases local stress which eventually decreases the critical cavity nucleus size (Equation 2.22). Therefore, DGG assists in formation of more cavities (Pilling and Ridley, 1988a).

The pile-up of dislocations ahead of a particle may lead to stress concentration, ultimately forming a cavity. Cavities formed by direct interaction of dislocations at particles have been observed by several authors in different aluminium alloys (Galano

et al., 2009; Hosokawa et al., 1999; Kawasaki et al., 2005). They estimated critical particle sizes (see Section 2.5.1) required for the formation of cavities and results were in a close agreement with the theories discussed earlier.

When a material is deformed under solute drag creep, cavitation may occur. However, in these materials, usually stringer-like cavities were reported (Chang et al., 2009; Kulas et al., 2006; Taleff et al., 2001). Typically, those materials failed by neck formation. Therefore, the extent of cavitation is less severe than the GBS controlled deformation condition.

It has been shown above that particles play a major role in nucleating cavities in certain test conditions. In magnesium alloys, the efficiency of particles in nucleating cavities has not been investigated in detail, although cavitation in magnesium alloys was reported in 1960s (Harris et al., 1962).

In magnesium alloys, triple points were also reported to nucleate cavities (Aigeltinger and Gifkins, 1977). The shape of the observed cavities was nearly spherical, suggesting diffusion controlled growth dominated during deformation.

Lee and Huang (2004) studied cavitation in a fine-grained AZ31 alloy. They observed that cavities less than $2\,\mu$m in size were grown by diffusion and remained spherical. In contrast, large cavities were grown by a plasticity controlled mechanism and became elongated. The authors concluded that cavity nucleation was not a continuous phenomenon. However, the nucleation of cavities was vaguely presented.

The nucleation rate of cavities in magnesium alloys can be very low, even with a large volume fraction of particles. If the size of particles is less than the critical diameter required to nucleate a cavity, it is very possible that cavitation will be suppressed. For example, in an AZ91 alloy, a low volume fraction of cavities was reported (Mussi et al., 2006), despite having approximately 12% of $Mg_{17}Al_{12}$ particles of an average size of $0.7\,\mu$m.

The effect of grain size on cavity growth rate has been studied in AZ61. A lower growth rate was obtained in a fine-grained microstructure where grain boundary diffusion dominated over lattice diffusion (Somekawa and Mukai, 2007). On the other hand, in a coarse-grained alloy, the authors observed a higher cavity growth rate and accommodation was controlled by lattice diffusion. A similar study was performed on the same alloy (Takigawa et al., 2008) and it was claimed that the nucleation of cavities and their growth would be similar, regardless of the accommodation process. However, the use of a different strain rate and temperature to change the accommodation path, makes it difficult to come to such a conclusion since cavity growth is very sensitive to these variables regardless of the accommodation process.

At elevated temperature, the nucleation of cavities is retarded due to the increased diffusional activity to relax concentrated stress (Bae and Ghosh, 2002b). This can also be related with the decrease of flow stress at higher temperature which increases

the minimum stable cavity nucleus size. In contrast, the growth of cavities may be accelerated at higher temperature (Lee and Huang, 2004) due to the rapid diffusion of atoms. However, depending on microstructural stability, the effect of temperature varies (Pilling and Ridley, 1988a).

In summary, the presence of particles, having a size range larger than a critical particle diameter, results in stress concentration forming a cavity. Stringer-like cavities are formed by aligned particles (formed during thermo-mechanical treatments). On the other hand, spherical cavities are developed if diffusion controlled growth dominates. Since superplastic alloys experience large strains, the retention of such a spherical shape does not usually occur and the growth of cavities is governed by plasticity, resulting in cavity elongation. Test parameters and grain size influence the nucleation and growth of cavities. Nucleation of a cavity is accelerated at higher flow stress and higher strain rate condition and is retarded at higher temperature. In contrast, growth of cavities is increased at higher temperature, owing to higher diffusional activity. DGG increases grain size, which may increase the cavity nucleation rate due to an increase of local stress. Also, the lack of accommodation of GBS due to concurrent grain growth increases cavitation.

2.6 Summary and Potential of the Current Study

Fine-grained magnesium alloys can show superplastic behaviour under a certain set of temperature and strain rate conditions. Incorporating the advantage of fine grains to promote grain boundary sliding, the comparatively faster diffusion rates in magnesium compared to aluminium may make magnesium alloys a suitable candidate for superplastic forming in automobile industries. The effects of aluminium on flow properties, such as flow stress and strain rate sensitivity, are yet to be studied in depth. If aluminium can improve strain rate sensitivity, strains to failure are expected to increase.

Cavitation has a profound effect on maximum attainable strains to failure during superplastic deformation. In magnesium alloys, cavitation has not been studied substantially under different test conditions. Importantly, the effect of particles, e.g., particles formed by manganese addition, on nucleation of cavities remains unclear. Also, dynamic grain growth can provide some resistance to necking. It is necessary to check whether such grain growth affects cavitation in magnesium alloys.

The work performed here investigates the effect of solute aluminium and particles on deformation, grain growth and cavitation in AZ alloys deformed in the superplastic regime. The detailed understanding obtained from this work helps to identify the key features required to improve the superplastic performance of this class of alloys.

Chapter 3

Experimental and Data Analysis Procedures

To understand the effects of aluminium and manganese on the hot deformation behaviour of the magnesium alloys, four different materials have been used in this study. As–cast alloys were homogenised and hot–rolled to develop a uniform and refined microstructure. These rolled sheets were sectioned to prepare specimens for optical and scanning electron microscopy (SEM), and for tensile tests at elevated temperatures. After tensile testing, specimens were taken from gauge and grip regions of the deformed samples and optical and electron microscopy and X-ray micro-tomography (μCT) investigations were carried out. The results from these characterisation techniques, along with the flow curve characteristics obtained from the tensile tests, were analysed and interpreted in different ways to achieve the goal of this project. This chapter focuses on the materials used, preparation of the rolled sheets from the as-cast alloys, sample preparation techniques and the characterisation procedures. To interpret the results obtained from these characterisation techniques, this chapter ends with a section discussing the data analysis methodology.

3.1 Materials Characteristics

Two alloys, AZ31 and AZ61, were received as sand-cast ingots of dimensions $200 \times 200 \times 50$ mm from Magnesium Elektron, UK, with two different manganese levels: 0.30 and 1.20 wt%. The chemical compositions of these alloys (supplied by Magnesium Elektron, UK) are given in Table 3.1. AZ31 and AZ61 denote the differences in aluminium levels (3 and 6 wt% Al) and the designations L and H differentiate the manganese levels in these alloys. This nomenclature is followed throughout this work.

Magnesium Elektron, UK had also supplied another set of these cast alloys of dimensions $230 \times 200 \times 25$ mm which were chill-cast with similar compositions to the

Table 3.1: Chemical compositions of the sand-cast ingots (wt%). L (low) and H (high) represent two different manganese levels, and S denotes sand-cast alloys

Alloy	Zn	Al	Si	Mn	Fe	Ni	Zr	Mg
AZ31LS	0.92	2.8	0.001	0.369	0.0073	0.0012	0	Balance
AZ31HS	0.94	2.91	0	1.204	0.0029	0.0025	0.007	Balance
AZ61LS	0.93	5.88	0	0.26	0.004	0.001	0.007	Balance
AZ61HS	0.94	5.88	0	1.2	0.004	0.001	0.007	Balance

sand-cast ones. The chemical compositions of this new set of alloys (supplied by Magnesium Elektron, UK) are shown in Table 3.2. The major difference observed between these two production routes was the grain size of the ingots; the grain size was finer in the chill-cast alloys.

Table 3.2: Chemical compositions of the chill-cast ingots (wt%). L (low) and H (high) represent two different manganese levels, and C denotes chill-cast alloys

Alloy	Zn	Al	Mn	Fe	Ni	Mg
AZ31LC	0.94	2.8	0.32	0.004	0.0008	Balance
AZ31HC	1.02	2.9	0.90	0.003	0.0007	Balance
AZ61LC	1.02	5.8	0.36	0.003	0.001	Balance
AZ61HC	1.02	5.7	1.03	0.003	0.001	Balance

3.2 Alloy Processing

Prior to further processing of the alloys, it was necessary to reduce micro-segregation, and also to develop a fine grain microstructure. Hence, the cast alloys were homogenised and hot-rolled.

3.2.1 Homogenisation Treatment

Cast alloys are usually homogenised by keeping the material at a certain temperature for a pre-defined time to allow diffusion of the alloying elements from the grain boundaries and other segregated areas. Homogenisation treatment assists in reduction of the micro-segregation, removal of low melting point eutectics which may cause incipient melting during thermo-mechanical processing, and controlling precipitation (Polmear, 2006). Alloys of AZ series typically contain $Mg_{17}Al_{12}$ and Al-Mn phases in the as-cast microstructure (Murai et al., 2003). Using JMatPro thermodynamic software (see Section 3.4.1), stable phase fractions were calculated, under equilibrium condition, for all of the alloys. From the predicted phase fractions, it was clear that only the Al-Mn

phases persist in the temperature range of 400 to 700 °C (see Section 4.1.2.1) (any phase fraction <0.05% was ignored). A homogenisation treatment in the range of 400 to 480 °C would make any other possible intermetallics dissolve. However, significant surface oxidation takes place if magnesium is exposed over 400 °C (Brandes and Brook, 1998). For this, an inert gas atmosphere is a pre-requisite for high temperature heat treatment of magnesium.

The sand-cast alloys were machined down by 5 mm from each surface to remove any surface defect present from the casting and chill-cast alloys were received as machined. They were sectioned to prepare bars of 150 mm dimensions using the vertical band saw and these bars were used for the homogenisation. The sand-cast alloys were homogenised at 420 °C for 24 hours in an electrical resistance heated furnace with an argon gas atmosphere, followed by quenching in water. The chill-cast AZ31L and AZ31H were homogenised at 480 °C, and AZ61L and AZ61H were homogenised at 420 °C at Magnesium Elektron, UK, in an argon gas atmosphere.

3.2.2 Hot Rolling

In order to develop uniform microstructures of similar grain sizes from the homogenised alloys, thermo-mechanical treatment is required. Thermo-mechanical processing routes such as hot rolling, equal channel angular extrusion (ECAE), accumulative roll-bonding or biaxial reverse corrugation can be applied for grain refinement of magnesium alloys (Eddahbi et al., 2005; Janeček et al., 2007; Pérez-Prado et al., 2004; Yang and Ghosh, 2006). In the current study, hot rolling had been chosen as the refining route.

A rolling schedule was developed and followed for all alloys. For the sand-cast alloys, 300 °C was used as the rolling temperature and for the chill-cast alloys, 400 °C was used. Ingots rolled at 300 °C showed some edge cracks at the later stages of rolling and a 400 °C rolling temperature reduced the incidence of edge cracking. Having two different temperatures did not affect the microstructure as the major refinement occurred in the early passes of the processing and both temperatures were in the single phase region of the binary system of Mg-Al.

To calculate the reduction in each rolling pass, the following method was applied.

Initial Thickness, $h_0 = 40\,\text{mm}$

Final Thickness, $h_f = 2\,\text{mm}$ (for tensile testing, a final sheet thickness of 2 mm was required)

Total compressive strain is,

$$\varepsilon = \ln\left(h_o/h_f\right) = 2.996. \tag{3.1}$$

Considering a total of 22 passes (so that the maximum reduction in the first pass

would not go beyond 5 mm to prevent extensive cracking), strain in each pass was $\Delta\varepsilon = 2.996/22 = 0.1198$. Now, the reduction in each pass is

$$\Delta h = h_o \left(\exp^{\Delta\varepsilon} - 1\right) \tag{3.2}$$

where Δh is the reduction in each pass in mm, h_o is the initial reduction in mm.

Using equation 3.2, the rolling schedule was developed. The material was deformed by unidirectional rolling for the first 10 passes and by cross-rolling for the remaining 12 passes. The direction of rolling, as reported, does not have any influence on texture type and rolling in both (unidirectional or cross) directions has the ability to refine the microstructure to similar levels (Al-Samman and Gottstein, 2008). However, the texture was weaker and more symmetric in the cross-rolled materials compared to that of the unidirectional-rolled materials. The sand-cast alloys were rolled from 40 mm initial thickness and the chill-cast alloys were rolled from 25 mm initial thickness to approximately 2 mm final thickness. Reduction in each pass was nearly 12.50% and total reduction was 95% for the sand-cast alloys and 92% for the chill-cast alloys.

Samples were preheated for one hour at the rolling temperature in an air circulating electrical resistance-heated furnace before rolling. However, as the rolls were not preheated, it was necessary to reheat the samples after each pass as the rolls may conduct away significant amounts of heat. Therefore, the samples were kept in the furnace for 2 to 10 minutes depending on the sample thickness (the thinner the sample, the lesser the time required for reheat) to keep the samples as near possible to the rolling temperatures. Rolling was conducted at speed of $0.18\,\mathrm{ms}^{-1}$ with steel rolls of diameter 300 mm. During rolling, the rolls were wiped over several times using paraffin to reduce friction between the roll and the work-piece. The actual measured thickness of the AZ31L sand-cast alloy, after each pass, is shown in Fig. 3.1. Sampling was carried out after different passes to check microstructural development at intermediate rolling stages.

3.3 Experimental Techniques

After homogenisation and hot-rolling, specimens were cut to desired sizes and prepared for optical and electron microscopy, and for hot tensile testing.

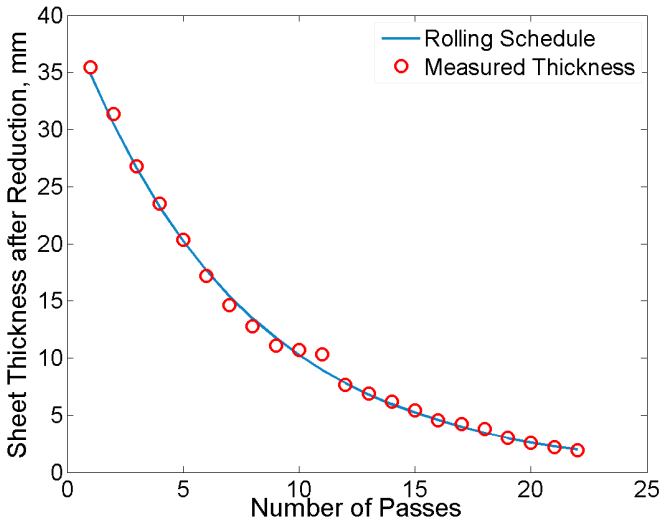

Figure 3.1: A plot of reduction in each pass during rolling of AZ31LS. The solid line represents the rolling schedule and symbols show the measured thickness after each pass. All the alloys were rolled by closely following the rolling schedule.

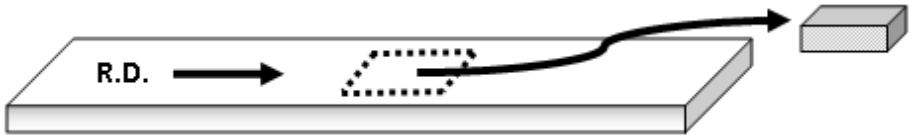

Figure 3.2: A schematic drawing showing a rolled sheet and specimen sectioned for metallography from the middle part of the sheet. R.D. shows the rolling direction.

3.3.1 Microstructural Observation

3.3.1.1 Sample Preparation

Specimens were prepared from the as-cast ingots, homogenised bars and rolled sheets. They were cut down to $10 \times 10 \times 10$ mm size using a vertical band saw and a Stuers Minitom installed with lubricated silicon carbide cutting disk (357CA) rotating at 200 rpm. For the rolled sheet, specimens were cut far from the sheet edges (Fig. 3.2).

Cut samples were cold mounted using acrylic powder and hardener to give better handling during grinding and polishing. Sometimes plastic clips were used to keep the samples located during mounting. Conventional metallographic technique was used. Mounted specimens were first ground using 600 (for 1 to 2 minutes), 1200 (for 1 minute) and 2400 (for 40 s) grit SiC papers with water as the lubricant. Polishing was conducted on cloths using 3 μm and 1 μm diamond pastes for 30 to 60 s on each cloth. Lubricants were used during polishing to prevent surface scratching. During polishing on 1 μm cloth, care was taken to prevent the surface relief effect surrounding the hard particles in the soft magnesium matrix. Final finishing was carried out with oxide particle suspension (OPS) to remove any trace of fine scratches. At every stage

of grinding and polishing, samples were cleaned thoroughly with soap and water followed by rinsing with ethanol. For automatic grinding and polishing, a Stuers TegraPol-31 was used with a force of 30 N.

Polished specimens were etched using Picral solution (4.2 gm picric acid, 10 ml water, 10 ml acetic acid and 70 ml methanol) for 10 to 15 s to reveal grain boundaries.

Some polished specimens were not etched at all, and were observed after OPS finishing. Specimens used for electron back-scattered diffraction (EBSD) were not mounted into resin. They were ground and polished by the technique mentioned above and were then electropolished. Electropolishing smoothes the hills created during grinding and polishing and also brightens the surface by the formation of a thin passivating layer (Weidmann, 1993). It was accomplished by submerging the polished specimens in a magnetically stirred solution consisting of 75 ml nitric acid (69% concentrated) and 175 ml ethanol (3:7 ratio) cooled to −30 °C, using a potential of 12 V for 30 s.

3.3.1.2 Optical and Scanning Electron Microscopy

Etched and unetched samples were examined, using an Olympus BH2 microscope fitted with a Zeiss camera, at different magnifications to reveal the grain sizes, particle distributions and cavities and were saved using the Leica DC View software at a resolution of 1798×1438. Specimens were mounted on glass slides and specimen surfaces were kept flat by modelling clay between slides and specimens.

For imaging and Energy dispersive x-ray (EDX) analysis, a Phillips XL30 Field Emission Gun Scanning Electron Microscope (FEGSEM) was used. Specimens were ground and polished as mentioned in Section 3.3.1.1 and were kept unetched. They were mounted on stubs and conductive paths were drawn using Silver DAG paint. Images were taken at different magnifications using a back-scattered electron (BSE) detector, as BSE can provide a good average atomic number contrast and distinctively show the second phases in the alloys investigated. For EDX analysis, Quantax 1.2 software was used to characterise the elements present in the microstructure using the spot analysis method in FEGSEM with 100 s scanning time. Both atomic and weight percentages of the elements present at a particular spot and the corresponding spectrum were saved. Imaging was conducted at 8 kV and 20 kV accelerating voltages and EDX was conducted at 20 kV, and spot size 3 was used; the spatial resolution obtained at this size was sufficient for imaging.

The EBSD technique was used to obtain the texture of the rolled sheets. A Cam-Scan Maxim 2040 FEGSEM was used to acquire backscattered diffraction patterns using a charge-coupled device (CCD) camera with a sample stage tilt of 70°. A 20 kV accelerating voltage, 20 mm working distance and spot size 6 were used. The acquisition step size was set to 20 μm at a magnification of $\times 250$ to allow a sufficient

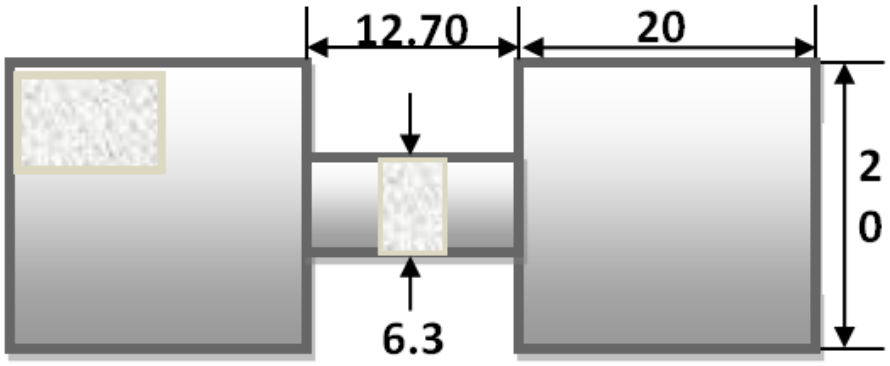

Figure 3.3: A schematic drawing showing the tensile specimen geometry. Two areas are marked in the grip and gauge regions. Specimens were taken from those positions for the metallography. All dimensions are in mm.

number of grains to be analysed, and scanning was applied for 7×7 matrix areas such that, after scanning the first defined area, the stage was moved by 5 μm away from that area and data acquisition started (so that a sufficient number of grains could be sampled). The diffraction patterns were acquired and interpreted using the HKL Channel Five Flamenco and Mambo software, supplied by Oxford Instruments.

3.3.2 Tensile Tests

To investigate the deformation behaviour at different alloy compositions, a series of uniaxial hot tensile tests were performed using a custom-built tensile machine (made by Alcan International Ltd) containing an electrical resistance-heated furnace chamber. Four thermocouples were incorporated in the machine—three at the top, middle and bottom parts of the furnace and one very near to the tensile specimen—to control temperature precisely and to maintain a uniform temperature distribution inside the chamber. Then, using the built-in software, load and displacement data were recorded which were used for further calculations, such as true stress, true strain, elongation to failure and strain rate sensitivity.

Tensile specimens of gauge length 12.70 mm and gauge width 6.30 mm were made from the rolled sheet by machining, keeping the tensile axis of the specimen parallel to the rolling direction. Specimens had simple square tag ends. A schematic drawing of the tensile specimens is shown in Fig. 3.3.

A range of temperatures and two different strain rates were used. All alloys were tested at two mean strain rates, 5×10^{-4} and $5 \times 10^{-3}\,\mathrm{s}^{-1}$, with temperatures of 300, 350, 400 and 450 °C. To determine the strain rate sensitivity values, perturbed-rate tests are very useful and convenient (Ridley et al., 2005). The strain values are varied by a small, but significant, amount so that the resulting difference in stress is measurable. In the current study, a ±10% variation of nominal strain rate for every

0.1 strain step was used.

For cavitation analysis, a temperature of 350 °C and a strain rate of $5 \times 10^{-4}\,s^{-1}$ were chosen as the test conditions after analysing the results from perturbed-rate tests. Constant strain rate was used and tests were conducted up to strain levels of 0.8, 0.9, 1.0 and 1.05, so that cavity formation and growth, and grain growth, could be studied.

The furnace was heated to the required temperature and then the specimen was placed in the grips and 15 to 20 minutes were allowed to stabilise the temperature before tests were initiated. Temperature fluctuation was within ±2 °C and all tests were conducted in air.

3.3.3 X-Ray Micro-Tomography

2-dimensional (2D) observations by the optical microscopy and scanning electron microscopy have some limitations, such that connected components (correlated particles and cavities, different phases, etc.), complex shapes of the regions of interest, the actual number of regions in the whole volume, etc. cannot be measured properly. One cavity region and one particle region may be identified as not connected in 2D but actually that cavity region may be connected with another particle region just beneath the surface of observation. X-ray micro-tomography has enabled investigation through a whole volume of the material so that a true relationship between the particles and cavities can be determined.

The X-ray system consists of a source, sample holder and a detector coupled by a caesium-iodide scintillator (to convert X-rays to visible light), magnifying objective lenses and a cooled CCD (charged-couple device), which collects visible lights from lenses. X-rays are sent from a cone beam source to the rotating sample and the transmitted beams are then recorded in the detector. The number of transmitted photons depends on the attenuation (absorption) coefficient of the material which, in turn, is dependent on the density and atomic number of the material, and energy of the incident photons. Full details of the technique are presented elsewhere (Stock, 2008). Fig. 3.4 shows a schematic view of the X-ray micro-tomography system.

An area of approximately 1.3 mm^2 from the middle of the gauge sections of the specimens deformed to different pre-set strains were scanned using a Xradia MicroXCT tomography machine. The accelerating voltage used was 75 kV, power was 10 W and an optical lens magnification of ×20 successfully resolved the features present in the material. Absorption mode was used by keeping the sample stage very close to the detector. During the rotation of the specimen stage from 0° to 180°, a total of 723 images were acquired, with radiographs (projected profiles) captured at every 0.25° using a 50 s exposure time for each radiograph. The collected projections

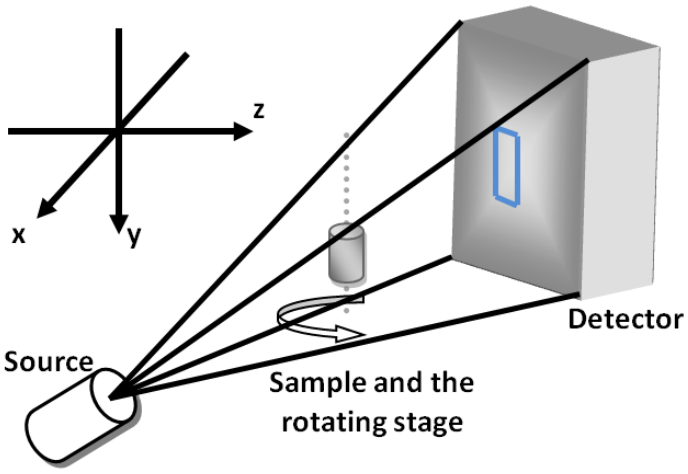

Figure 3.4: A schematic drawing showing the X-ray micro tomography setup. X-ray beams are transmitted through the specimen and corresponding projected radiographs are recorded on the detector (consists of objective lenses for magnification and CCD). The sample stage can rotate from 0° to 180°. The rotation steps are assigned so that radiographs are taken at each angular step followed by reconstruction of all the collected radiographs. Z-direction is the X-ray incident direction, and x and y directions are the rotation axes.

were reconstructed, using Feldkamp-Davis-Kress (FDK) algorithm for cone beam geometry (Feldkamp et al., 1984), by calculating the spatial distribution of attenuation coefficients of each voxel (volume element – 3D representation of pixels) (Maire et al., 2001). During reconstruction, each voxel was assigned to a specific grey-value depending on the average attenuation coefficient of that voxel which was dependent on the attenuation coefficients of matrix, particles and cavities. Particles and cavity regions had distinct levels of grey-values from the matrix material. Matrix material had grey-values within a range of 30k to 36k for the 16 bit data and values smaller and greater than this range corresponded to cavities and particles respectively. Centre shift and beam hardening corrections were also performed during reconstruction using the integrated Xradia reconstruction software. The volume of each voxel in the reconstructed tomography data set was 1.22 μm^3 at the magnification used.

3.4 Data Analysis

3.4.1 Thermodynamic Modelling

JMatPro v4.1 (Saunders et al., 2003) was used for the thermodynamic modelling of the phase formation of the alloys at different temperatures using the equilibrium solidification model (Glicksman and Hills, 2001). A 5 °C step size was used and prediction was made for the temperature range of 700 to 200 °C.

3.4.2 Grain Size Determination

The sizes of the grains were determined from the images taken by the optical microscope using the linear intercept method. Lines were drawn on the image in ImageJ 1.43e (Abramoff et al., 2004) and the total number of grain boundaries cutting through each line was counted. Then, dividing the line length by the number of grain boundaries, the average grain size was calculated. A total of 5 to 8 images were used to obtain the final average grain size. The standard deviation of the calculated grain size is defined as

$$s_r = \left(\frac{\sum (x_i - \bar{x})^2}{n_t - 1} \right)^{1/2} \tag{3.3}$$

where x_i is the mean grain size value from image i, $\overline{x}$ is the mean grain size calculated from all the images and n_t is the number of images considered. standard errors (SEs) were calculated from the values of standard deviation. SE provides an indication of fluctuation of the sample means. It shows the variation of the mean grain size obtained from the different images and provides a better estimation of data scattering from the mean where the number of the sample (containing the data population) is more than one. SE is defined as:

$$S.E. = \frac{s_r}{\sqrt{n_t}} \tag{3.4}$$

where the terms are defined earlier.

3.4.3 Measurement of Second Phase Particles and Cavities

BSE images provided good contrast between the matrix and the second phase particles for the alloys studied. 10 images were acquired for each alloy. Using ImageJ, images were converted to 8-bit greyscale images and particle regions were segmented (i.e., separated and labelled) and examined to get the data of area fractions and sizes (feret diameter). Feret diameter is the longest distance between two parallel lines drawn at the tangents of two points within the particle. Particle size distributions were calculated for each alloy and SEs were also estimated using equations 3.3 and 3.4.

BSE images appeared to provide strong contrast between the particles and cavities and were more suitable for cavitation studies compared to the optical images, where the contrast was less obvious. 20 BSE images were taken for each tensile specimen, tested up to the strains of 0.8 to 1.05, at a constant strain rate of 5×10^{-4} s^{-1}. The images were segmented and analysed in a similar method to that used for the particle analysis.

3.4.4 Tomography Data Analysis

Raw data from tomography was imported as a single binary file for further examination by Matlab and, also, as a series of image files for volume rendering to produce a set of 3-dimensional (3D) images of the particles and cavities. Stacks of image files were loaded in Avizo 5.1 (VSG, 2010) software and 3D images were saved showing connected particles and cavities, and the clustering of particles at different enlargements.

For quantitative investigation, Matlab and Fortran software were used. To make the data readable to these software packages, a few pre-processing steps were carried out. The binary tomography file was first loaded in ImageJ. Then, only particle regions were segmented and saved as a binary file. Another binary file was produced for the cavities in the similar way. Then, a Matlab routine (produced by Dr. T. J. Marrow, University of Manchester) was used to load the binary files in Matlab. Then, routines were developed to label (separation and identification of the individual regions) the voxels using the 26 connected-neighbourhood condition and calculate the volume fractions, shape and list of coordinates of the connected voxels.

3.4.5 Calculations of Stress and Strain

From the tensile tests, load and extension data were recorded. Linear or engineering stress and strain were calculated using the following formula:

$$e = \frac{\Delta L}{L_o} \tag{3.5}$$

$$\sigma_s = \frac{P}{A_o} \tag{3.6}$$

where e and σ_s are the engineering strain and stress, ΔL is the extension of length, L_0 is the original gauge length, P is the load and A_0 is the original cross-sectional area of the gauge (calculated from the width and thickness). From the engineering strain and stress data, true strain and stress values were calculated. The advantage of using true strain is that the sum of all instantaneous true strain values is equal to the total true strain measured. True strain and stress at any instance, n, are described by the following expressions as:

$$\varepsilon = \ln\left(\frac{L_n}{L_o}\right) = \ln\left(e + 1\right) \tag{3.7}$$

$$\sigma = \frac{P_n}{A_n} = \sigma_s(e + 1) \tag{3.8}$$

where ε and σ are the true strain and stress, L_n, A_n and P_n are the extension, cross-sectional area and load at the n^{th} step during test and other terms are defined earlier. Elongation to failure (e_f) was also measured using the formula:

$$e_f = \frac{L_f - L_o}{L_o} \times 100\% \tag{3.9}$$

where L_f is the length after failure and other terms are defined earlier. The e_f values were measured from the direct measurements of L_f from the deformed gauge regions using callipers. This direct measurement, however, did not vary largely from the crosshead displacement measurements. A plot was drawn to check the differences and a fit equation of $y = 0.98x + 1.20$ was obtained ($y = e_f$ by direct measurement and $x = e_f$ by crosshead displacement).

From the perturbed-rate tests, polynomial fitting was applied to the -10% and $+10\%$ strain perturbation segments of stress for each 0.10 strain. Then, strain rate sensitivity (m) values were calculated using the formula:

$$m = \frac{\Delta \ln \sigma}{\Delta \ln \dot{\varepsilon}} \tag{3.10}$$

where $\Delta \ln \sigma$ is the difference between the logarithmic of the upper and lower stress levels and $\Delta \ln \dot{\varepsilon}$ is the difference between the logarithmic of the two applied strain rates ($\pm 10\%$ of the nominal strain rate, i.e., if the nominal strain rate is $5 \times 10^{-4} s^{-1}$, then, $\triangle \ln \dot{\varepsilon} = \ln [5.5 \times 10^{-4} - 4.5 \times 10^{-4}]$).

3.4.6 Statistical Analysis

It is important to distinguish the trends in unperfect data obtained from the experimental techniques for better interpretation and understanding of the results. For size and area fraction data of grains, particles and cavities, SE (Equation 3.4) was calculated to show the scattering of data.

For the size distribution of the particles and cavities, Probability distribution functions (PDFs) were evaluated. A PDF illustrates the structural features of a large data set. A PDF gives the probability density of a random variable in a given interval. If $p(x)$ is the PDF of x, then the probability that $x_1 \leq x \leq x_2$ is given by

$$p\left(x_1, x_2\right) = \int_{x_1}^{x_2} p\left(x\right) \mathrm{d}x \tag{3.11}$$

For a data population (x_1,x_2, $\ldots x_n$ with a continuous and univariate density f), a kernel estimator (weighting function) of the PDF is defined as

$$\widehat{f}(x) = \frac{1}{Nh} \sum_{i=1}^{N} K_e \left(\frac{x - x_i}{h} \right) \tag{3.12}$$

where x is the value for which the estimation is being made, x_i is the independent variable from the data set, N is the data size, h is the bandwidth (smoothing parameter) and K_e is the Kernel estimation function. h is the scaling factor and controls the width of the probability mass surrounding a point. An improper bandwidth (h) selection may cause over- or under-smoothing of data. In the current project, the Epanechnikov kernel (Silverman, 1992) and $h = 0.75$ were used. The Epanechnikov kernel is defined as

$$K(u) = \frac{4}{3}\left(1 - u^2\right) \text{ for } |u| \leq 1 \tag{3.13}$$

where $u = \left(\frac{x - x_i}{h}\right)$ and $K_e(u) = 0$ if $u \nleq 1$

3.4.6.1 Factorial Design and Analysis of Variance (ANOVA)

In the current study, factorial designs had been used for the tensile test results to understand the effects of temperature and composition. Factorial design consists of a set of variables or factors (temperature, composition, etc), levels (represents different states of the variables; for a 2 level design, levels are usually denoted as high and low) and responses (values of a certain property or event for each variable and level; e.g., values of the elongation to failure (e_f) data at two different temperatures). A 2^g factorial design represents the 2 level responses of g number of variables. It can be presented in two steps: Pareto charts of the interactions and analysis of variance (ANOVA).

Consider a 2^2 full factorial design. It has two levels: high (+) and low (−), and 2 variables: A and B. This design is shown in Table 3.3. Now, after multiplying the responses of the variables (e.g., strain rate sensitivity values, m) according to the design matrix shown in Table 3.4, the sums of the responses ($\Delta/2$) are calculated (Table 3.4). Then, the half-effects ($\Delta/2$) are plotted in a Pareto chart to illustrate the variation of the responses for different interactions with variables.

To understand the significance of the responses, a factorial ANOVA was performed. In factorial ANOVA, the F-distribution (named after R. A. Fisher) is calculated which compares the spread in the data (mean square error (MSE)) with the shift in the data (mean square between (MSB)). MSE and MSB are described as:

$$MSE = \frac{\sum_{r} (n_r - 1)\, s_r^2}{\sum_{r} (n_r - 1)} \tag{3.14}$$

Table 3.3: A 2^2 full factorial design. A and B are the variables and '$-$' and '$+$' are the high and low levels. AB is the interaction of A and B.

Run	A	B	AB
1	-	-	+
2	-	+	-
3	+	-	-
4	+	+	+

Table 3.4: Showing the multiplication of responses (strain rate sensitivity, m) with the 2^2 factorial design from Table 3.3.

Run	A × m	B × m	AB × m
1	$-m_1$	$-m_1$	$+m_1$
2	$-m_2$	$+m_2$	$-m_2$
3	$+m_3$	$-m_3$	$-m_3$
4	$+m_4$	$+m_4$	$+m_4$
(sum of the responses)	ΔA	ΔB	ΔAB

and

$$MSB = N\left(\Delta/2\right)^2 \tag{3.15}$$

where r is the run number, n_r is the number of responses (say, elongation values) in run r, s_r is the standard deviation (see equation 3.3) and N is the total number of responses. Now, the F-distribution component is obtained by the following expression:

$$F_o = \frac{MSB}{MSE} \tag{3.16}$$

where the terms are defined earlier. This value is then compared with some critical F_α distributions such as $F_{0.05}$ or $F_{0.01}$. α values are the confidence levels and corresponding confidence interval can be calculated from $(1-\alpha)\times 100\%$. So, for $\alpha = 0.01$, the confidence interval will be 99%. $F_{0.05}$ or $F_{0.01}$ values are obtained from standard tables (Bate, 2006) in the format $F_\alpha\left(\upsilon_1, \upsilon_2\right)$, where υ is the degree of freedom and, υ_1 and υ_2 are expressed as:

$$\upsilon_1 = (\text{number of levels} - 1) \tag{3.17}$$

and

$$\upsilon_2 = \sum_r (n_r - 1)\,. \tag{3.18}$$

Now, if $F_o > F_\alpha$, then the effect of the corresponding variable is statistically significant.

3.5 Summary

Two variants of AZ31 and AZ61 alloys, containing around 0.30 and 1.20 wt% manganese, were received in the as-cast form. They were homogenised at the temperatures ranging from 420 to 480 °C for 24 hours and hot-rolled at 300 °C and 400 °C by 12% reduction in each pass to produce a refined and recrystallized microstructure. These rolled sheets were examined by the optical microscopy for the grain size determination, by the SEM for the second phase particle composition and size determination and by EBSD to evaluate the texture. Thermodynamic modelling was carried out to predict the phases present in these alloys. Tensile specimens were prepared from the rolled sheets and perturbed-rate tests were conducted at temperatures of 300, 350, 400 and 450 °C for two mean strain rates, 5×10^{-4} and 5×10^{-3} s^{-1}.

Metallographic samples were taken from the gauge and grip regions of the tensile samples to observe the grain growth that occurred. The elongation to failure values and strain rate sensitivity values were also determined. Several statistical calculations were performed on the mechanical results obtained. A series of constant strain rate tests (at 5×10^{-4} s^{-1}) were also carried out at 350 °C up to different intermediate strains for cavitation analysis. 20 BSE images were taken for each sample in the deformed areas and cavity area fractions and size distributions were determined. X-ray micro-tomography was also carried out for these intermediate strained specimens. 3D images were rendered and further analysis was performed on the raw data from tomography by using the Matlab and Fortran routines to establish cavity-particle relationships.

Chapter 4

Hot Deformation Behaviour of the Alloys

This chapter focuses on the flow characteristics of the alloys. Initially, the development of the microstructure from the cast materials is presented. Then, the aspects of the uniaxial tensile test and flow characteristics, at different alloy compositions, for different test parameters are revealed followed by statistical analyses to check the effects of the test parameters and compositions of the materials on elongation to failure (e_f) and strain rate sensitivity (m). After understanding the flow behaviour, attempts have been made to determine the extent of grain growth that occurred during deformation. One of the key features identified in the materials is a varying distribution of second phase particles. An extensive study was carried out to determine the particle composition and size distribution, and finally, a comparison has been made with the results of the predicted thermodynamically stable phases. Combining these information, suggestions have been made as to the failure mode during deformation.

4.1 Development of Initial Microstructure

4.1.1 Rolling of the As-cast alloys

The alloys were received in as-cast form. The sand-cast alloys (40 mm thickness) were homogenised at 420 °C to remove any effects of segregation and were rolled at 300 °C by 22 passes of equal strain (see Section 3.2.2). The cast microstructures are shown in Fig. 4.1. To understand the evolution of the refined grains, microstructures were examined after different number of passes of hot rolling. Fig. 4.2 shows the development of fine grains after different rolling passes. The continuous formation of smaller grains and concurrent refinement of the larger grains are also highlighted. The micrographs confirm that dynamic recrystallization (DRX) took place during

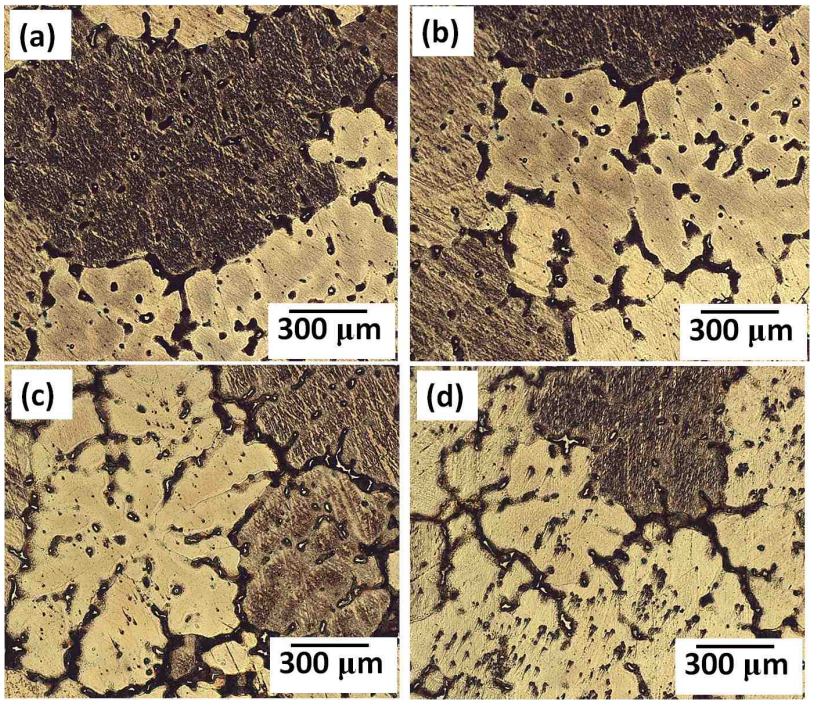

Figure 4.1: Optical images of the sand-cast microstructures of (a) AZ31LS, (b) AZ31HS, (c) AZ61LS and (d) AZ61HS. The precipitation of the second phase particles and the segregation of alloying elements are quite noticeable in the micrographs. The measured average grain sizes of the alloys are approximately 1000 μm.

hot rolling. The micrographs also show DRX to be dominated by nucleation of new grains at prior grain boundaries along with evidence of intragranular formation at twins (Fig. 4.3).

Fig. 4.3 shows some interesting features. A few grains have formed in the interior of a very coarse parent grain. 'A' shows an array of the grains at the boundary of the coarse matrix grain. 'B' shows several bands of grains embedded into the matrix grain. 'C' indicates the potential source of this interior grain nucleation as a deformation twin. Twins thus have assisted in recrystallization during the hot rolling by acting as a favourable site for new grain initiation. Formation mechanisms of the recrystallized grains by hot rolling in magnesium alloys has been reported previously for AZ31 and AZ61 alloys (del Valle et al., 2003; Stanford and Barnett, 2008) and the present observations are consistent with these works. Table 4.1 shows the measured refinement in the grain size during hot rolling.

The as-cast grain sizes of all alloys are approximately similar. It was observed that addition of more manganese did not contribute to any refinement of the cast structure (Table 4.1). Laser and co-workers (2006) varied the manganese content up to 0.80% in a conventional AZ31 alloy and had shown this did not achieve any effective grain refinement in the cast alloys after rolling. The grain refinement by hot rolling obtained in the current study is approximately by a factor of 125. The microstructure after complete hot rolling is homogenous as no initial grains are retained (Fig. 4.4).

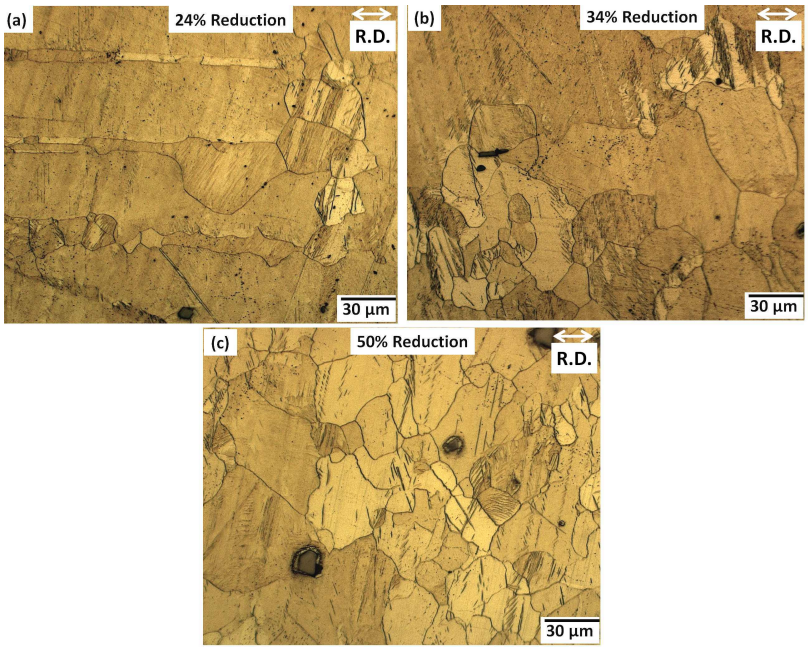

Figure 4.2: Optical micrographs of sand-cast AZ31HS during different passes of the rolling: (a) after 24% reduction, (b) 34% reduction and (c) 50% reduction. The continuous refinement of the grains through recrystallization is evident from the images. The rolling temperature was 300 °C. The rolling direction (R.D.) is also shown.

Table 4.1: The refining of the grains during the hot rolling of the sand-cast alloys at 300 °C

	Grain Size, μm						
		Reduction, %					
Alloy	**Cast**	**24**[a]	**34**	**50**	**75**	**87**	**95**
AZ31LS	1120.03± 53.72	17.81 ± 4.17	13.30 ± 2.44	13.83 ± 1.47	9.35 ± 0.82	8.23 ± 0.42	7.03 ± 0.23
AZ31HS	1216.46± 145.75	30.10 ± 17.52	19.59 ± 1.50	14.09 ± 4.05	7.16 ± 0.52	7.23 ± 0.23	7.10 ± 0.35
AZ61LS	935.58± 59.77	27.34 ± 8.65	12.59 ± 2.55	12.02 ± 2.98	8.73 ± 0.37	8.83 ± 0.54	9.31 ± 0.38
AZ61HS	994.18± 102.61	29.72 ± 7.06	12.26 ± 3.35	8.81 ± 1.86	8.13 ± 0.29	8.04 ± 0.40	8.09 ± 0.44

[a] Grain size calculations at 24% reduction include the recrystallized grains and parent grains also. Therefore, the size calculations at 24% contain a large scatter since only a small number of the original very large grains 1000 μm were sampled.

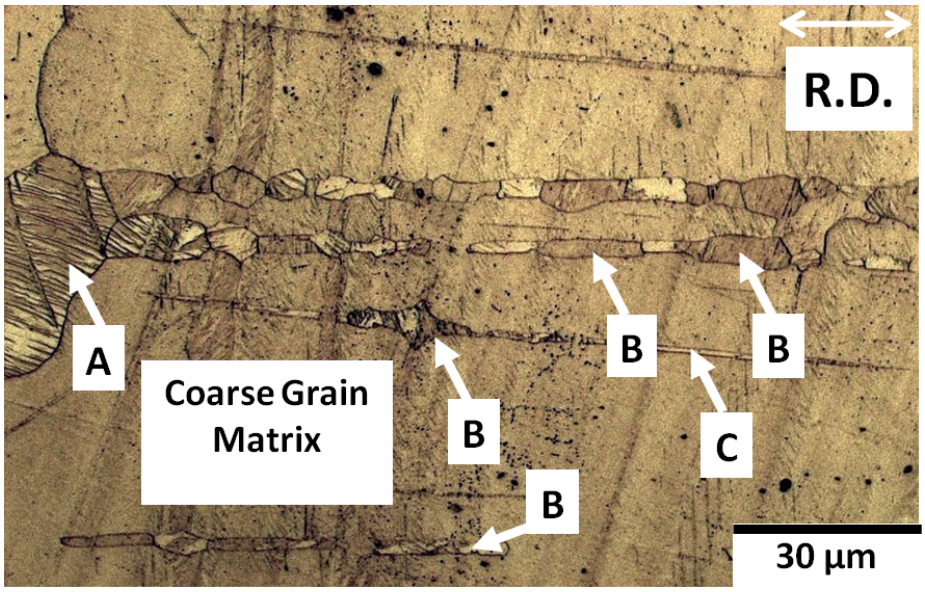

Figure 4.3: An optical micrograph of sand-cast AZ31HS alloy after 24% reduction by rolling. 'A' shows one of the refined grains at the boundary of a very large parent grain. 'B' represents new smaller refined grain formed inside the parent grain preferably at the twins 'C'. The rolling temperature was 300 °C.

Therefore, the recrystallization can be considered to be complete. Table 4.1 shows, after 50% reduction, the microstructure becomes fully recrystallized and grains are less than 20 μm in size (average size). Further reduction leads to refining of the small number of retained coarse grains to produce a more homogeneous microstructure.

The chill-cast alloys (25 mm thickness) with approximately the same compositions as the sand-cast alloys were rolled at 400 °C with a total compressive strain of 0.92. The rolled microstructures are shown in Fig. 4.5. Table 4.2 shows the average grain sizes of the chill-cast alloys obtained after the hot rolling. The average grain sizes are 7 to 9 μm and are approximately similar to those of the sand-cast alloys. However, the homogeneity of the recrystallized microstructure appears to be better than those rolled at 300 °C. The effect of the rolling temperature on the final grain size is apparently negligible. It is also noticeable that the initial thickness is not important for producing fine grains by hot rolling. The final grain size is almost entirely a function of the total compressive strain.

Table 4.2: Grain sizes of the chill-cast alloys

Alloy	**AZ31LC**	**AZ31HC**	**AZ61LC**	**AZ61HC**
Grain Size, μm	8.04 ± 0.44	8.34 ± 0.80	8.92 ± 0.65	8.16 ± 0.92

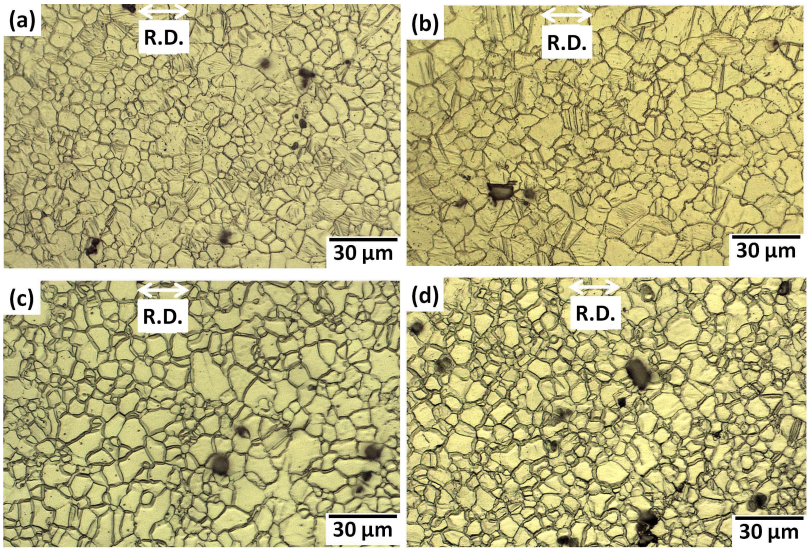

Figure 4.4: Optical images of the final hot-rolled microstructure of sand-cast (a) AZ31LS, (b) AZ31HS, (c) AZ61LS and (d) AZ61HS showing the refined grains of various sizes. The rolling temperature was 300 °C. Also, a small number of particles are observed at the grain boundaries.

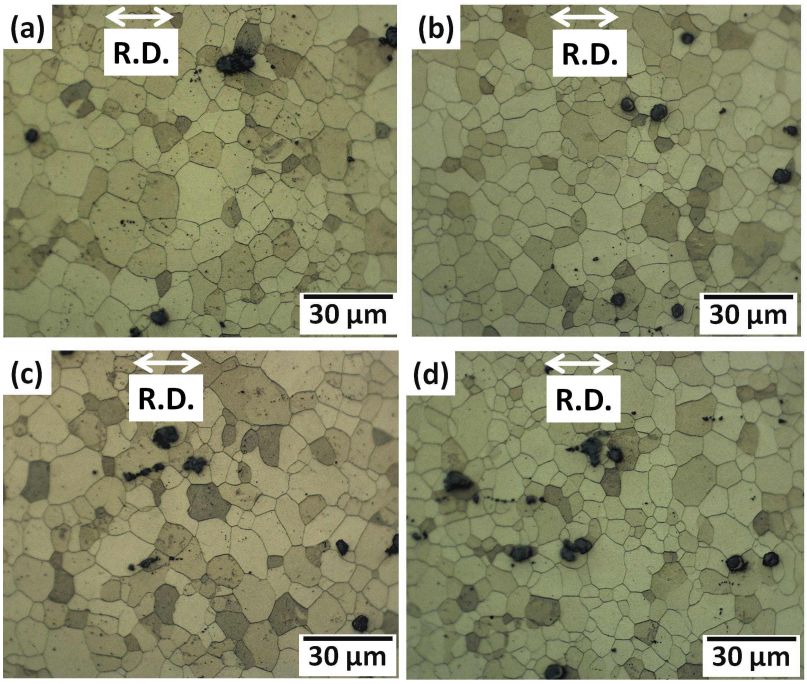

Figure 4.5: Optical micrographs of the final hot rolled chill-cast alloys: (a) AZ31LC, (b) AZ31HC, (c) AZ61LC and (d) AZ61HC. The rolling temperature was 400 °C. The average grain size is approximately 8 to 9 μm for all alloys.

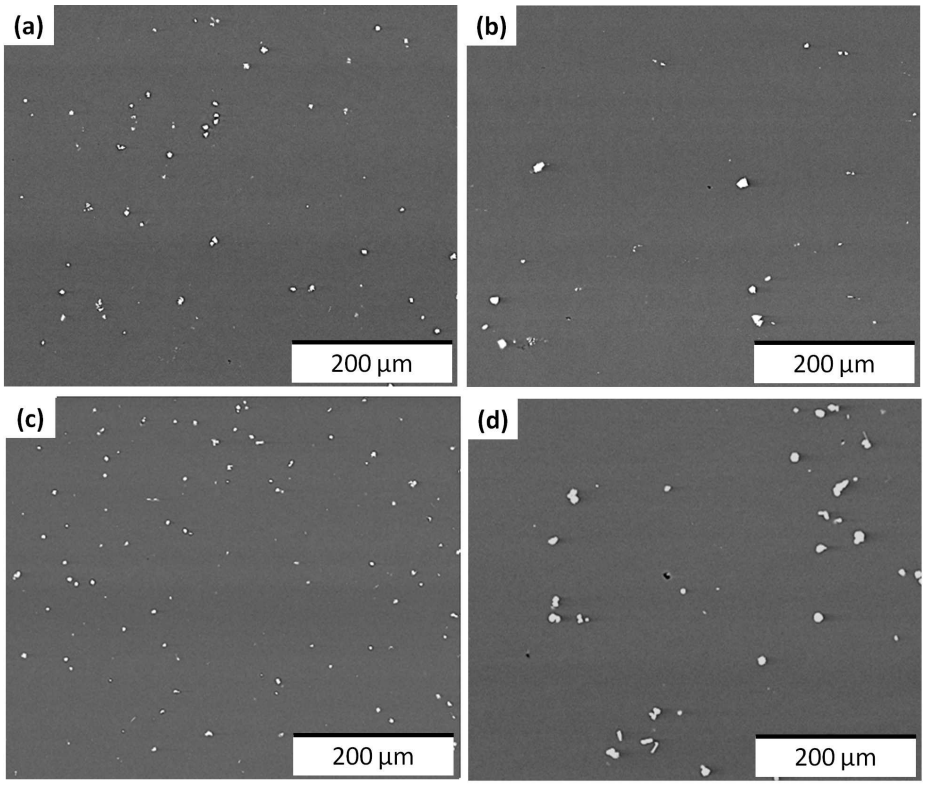

Figure 4.6: SEM micrographs of the sand-cast alloys showing the distributions of the coarser particles observed in the microstructures of sand-cast (a) AZ31LS, (b) AZ31HS, (c) AZ61LS and (d) AZ61HS.

4.1.2 Particle Analysis

4.1.2.1 Sand-cast Alloys

The sand-cast alloys contained a significant fraction of coarse second phase particles located at the grain boundaries. The distributions of the particles in the microstructure of different alloys are shown in Fig. 4.6.

The size of the coarse particles in the low manganese alloys appeared comparatively smaller than those of the higher manganese alloys. Specifically, in AZ61HS, the particle size was largest. The existence of finer particles was also studied and all of the alloys were found to contain fine particles (Fig. 4.7). They were not characterised in detail, but the mean size was approximately $0.10\,\mu$m. In Fig. 4.7b, the breaking up of a large particle during hot rolling is also shown. This type of particle fracture would result in a greater number of medium size particles in the rolled microstructure.

The size distributions of the coarse particles in the alloys were measured and the probability distribution functions (see Section 3.4.6) were evaluated. The term diameter, here, is the Feret Diameter of a region/feature, i.e., the furthest most distance between the two ends of any region. The plots are shown in Fig. 4.8, estimated from the experimental results obtained by analysing 10 SEM images for each alloy.

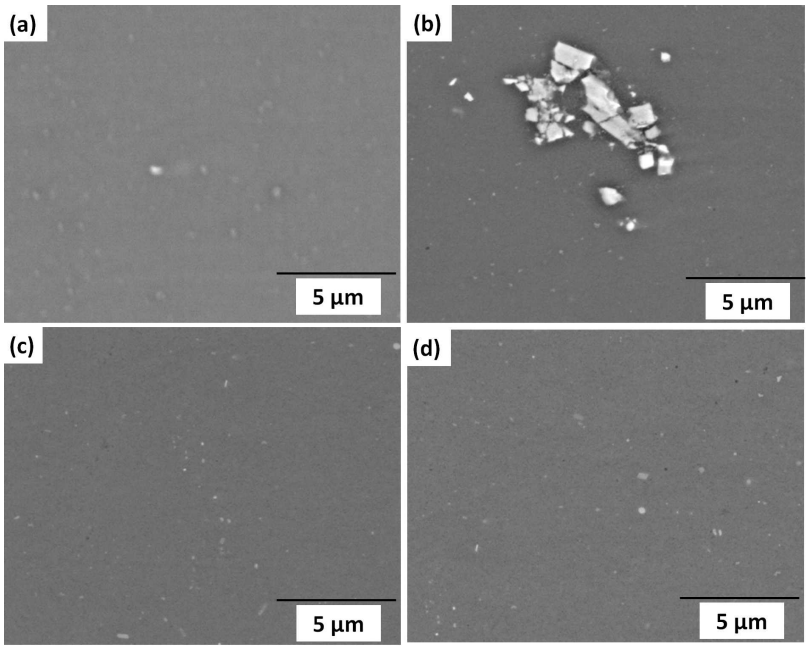

Figure 4.7: SEM micrographs of the fine particles observed in the sand-cast alloys: (a) AZ31LS, (b) AZ31HS, (c) AZ61LS and (d) AZ61HS. The particles have an average size of approximately 0.10 μm. Also, the breaking up of a larger particle during hot-rolling is shown in (b).

Most particles in AZ31LS are within a narrow range with 15 μm maximum size (Fig. 4.8a). The peak of the plot for AZ31LS is approximately between 3 and 5 μm. AZ61LS, which is a variant of AZ31LS with high aluminium, also shows a peak approximately at 5 μm (Fig. 4.8b). However, AZ61LS has a few particles which are larger in size than the biggest measured in AZ31LS. AZ31HS, the high manganese counterpart of AZ31LS, contains most particles of size 5 μm, and a high number of larger particles ($> 10\,\mu$m) are also observed. AZ61HS, containing the largest total alloying additions, shows an approximate peak at 5 μm, with a higher proportion of particles larger than 5 μm in size than other alloys. From the distribution plots, it appears that the variation of manganese content contributed most to the coarse particle size differences in the alloys. Moreover, in the high manganese variants, the extra aluminium in AZ61HS has produced a considerable increase in the number of particles >10 μm.

The compositions of the particles were determined using EDX in SEM. At least 30 points, for each alloy, were analysed. It was observed during the EDX examination that most of the measured particle compositions also picked up some matrix magnesium. Therefore, to reduce the effect from matrix, the element atomic fractions are plotted against magnesium atomic fractions and extrapolated to zero atomic fraction of magnesium (Fig. 4.9). This would give the actual compositions of the particles compensating for the matrix effect (Cliff et al., 1984; Lorimer et al., 1984), assuming near zero magnesium in the particles (which is expected from phase diagram

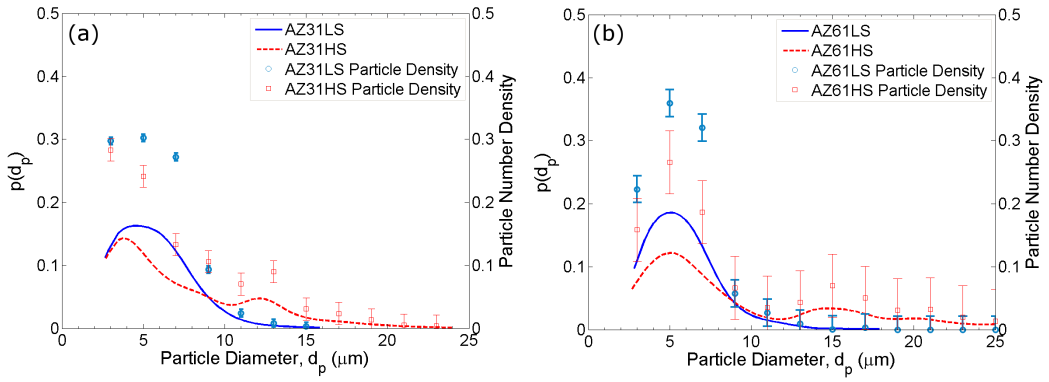

Figure 4.8: Plots of the probability distribution functions of the particle diameter of the sand-cast (a) AZ31LS and AZ31HS and (b) AZ61LS and AZ61HS. Normalised fraction of number of particles are also included.

calculations). For the low aluminium alloys, the composition is close to Al_8Mn_5 (60 to 65% Al and 38 to 45% Mn – atomic fraction basis), but, for the high aluminium alloys, the particle stoichiometry was close to $Al_{11}Mn_4$ (71 to 73% Al and 28 to 30% Mn).

To validate the observed compositions, thermodynamic modelling of the phases for all alloys was performed for a temperature range of 700 to 200 °C using JMatPro under the equilibrium condition and the major phases predicted are shown in Fig. 4.10. Though Scheil-Gulliver solidification provides a better simulation of solidification condition (Ohno et al., 2006), 24 hours of homogenisation should be sufficient to bring the system towards equilibrium and hence, phase predictions were made under the equilibrium condition. Al_8Mn_5 and $Al_{11}Mn_4$ were identified as the major second phases with some contribution from Al_4Mn at low temperature.

From the size distribution plots, large particles appear to be common in all alloys, though the frequency of them varies with the composition of the alloys. Smaller particles, if agglomerated together, may coalesce to form a large particle.

Moreover, according to the equilibrium phase diagram, the maximum solubility of manganese in magnesium is approximately from 0.10 to 0.15 wt% at the room temperature. The addition of manganese would result in more precipitation of the aluminium-manganese containing particles and as a consequence, the amount of aluminium would decrease in solution. In a ternary Mg-Al-Mn phase diagram, the addition of 2 to 10% aluminium results in a decrease of manganese solubility. So, in AZ61 alloys, more precipitation is expected. However, the decrease in solidus temperature with increasing manganese content complicates the situation, as manganese containing particles will form in the liquid as well as potentially precipitate in the solid state. This is reflected in the volume fractions of the phases obtained experimentally and predicted by JMatPro (Fig. 4.11). AZ31LS has the lowest fractions of second phase particles, whereas, in AZ61HS, the fraction is the largest. The experimentally

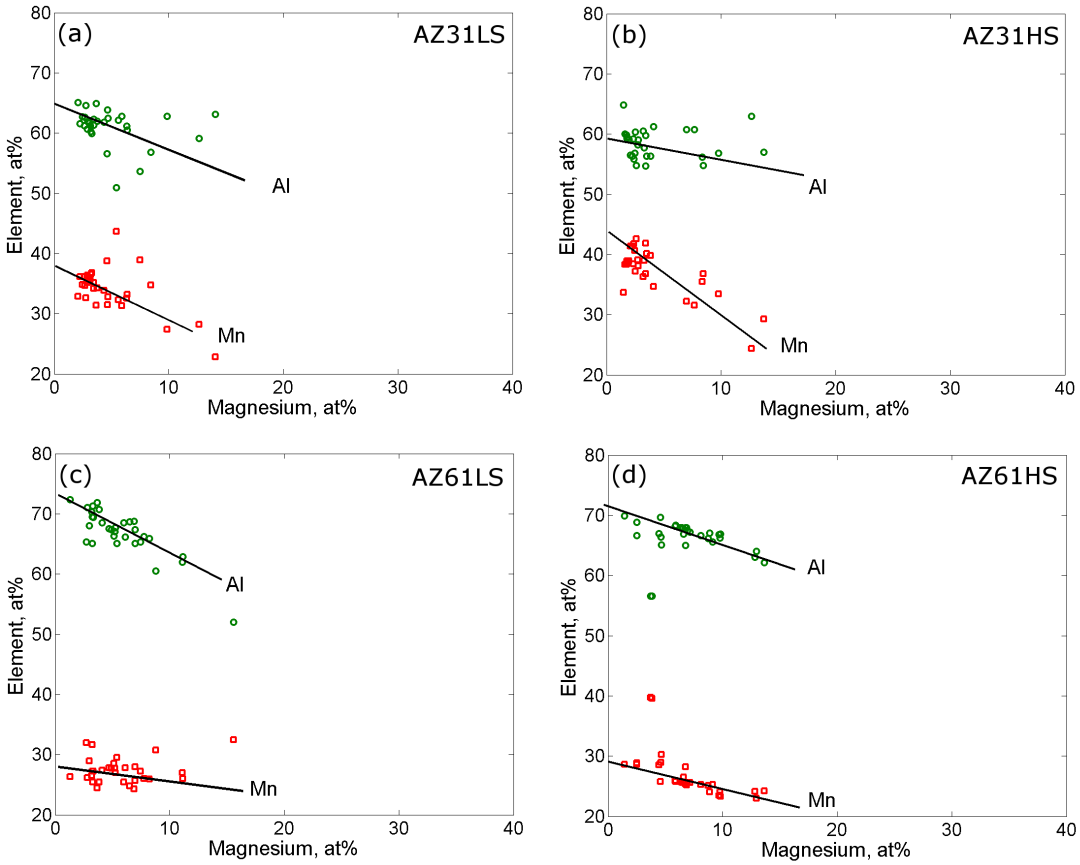

Figure 4.9: Plots of the variation of aluminium and manganese atomic fraction measured by EDX vs. magnesium for sand-cast (a) AZ31LS, (b) AZ31HS, (c) AZ61LS and (d) AZ61HS. Fitting lines are drawn for aluminium and manganese elements and extrapolated to zero atomic fraction magnesium, considering zero contribution from the matrix would give the compositions of the second phase particles containing aluminium and manganese (Cliff et al., 1984; Lorimer et al., 1984).

obtained particle fractions do not closely match with the predicted phase fractions. This may occur due to the magnification used for the particle study, since the smallest particles were not detected and thus will not contribute to the measured volume fraction.

4.1.2.2 Chill-cast alloys

Using the method described in Section 4.1.2.1, the particle composition of each alloy was determined (Figs. 4.12 and 4.13) for the chill-cast alloys. For the low aluminium alloys, the composition was close to Al_8Mn_5 (62 to 63 % Al and 38% Mn - atomic fraction basis), but, for the high aluminium alloys, the particle chemistry was close to $Al_{11}Mn_4$ (71% Al and 28 to 29% Mn - atomic fraction basis). The predicted compositions of the stable phases were Al_8Mn_5 for the low aluminium alloys and $Al_{11}Mn_4$ for the high aluminium alloys at the homogenisation temperature.

A comparison between the experimentally obtained volume fraction of particles

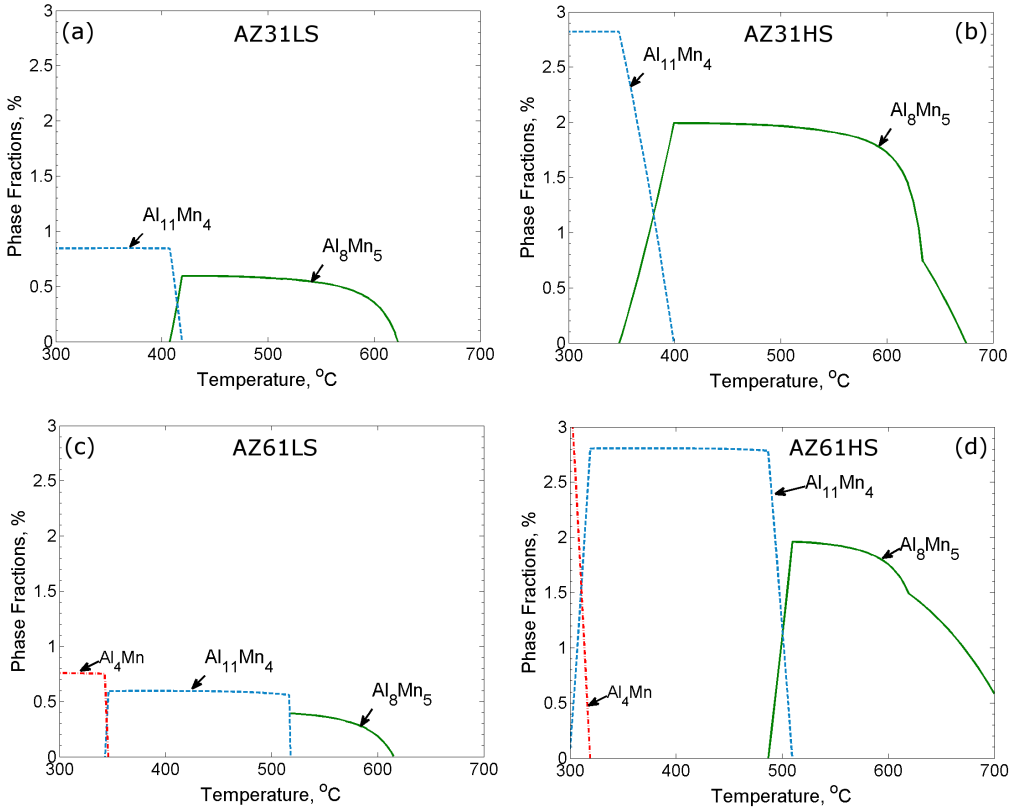

Figure 4.10: The plots of sand-cast (a) AZ31LS, (b) AZ31HS, (c) AZ61LS and (d) AZ61HS showing the evolution of the manganese containing phases with temperature, predicted under equilibrium condition using JMatPro thermodynamic software.

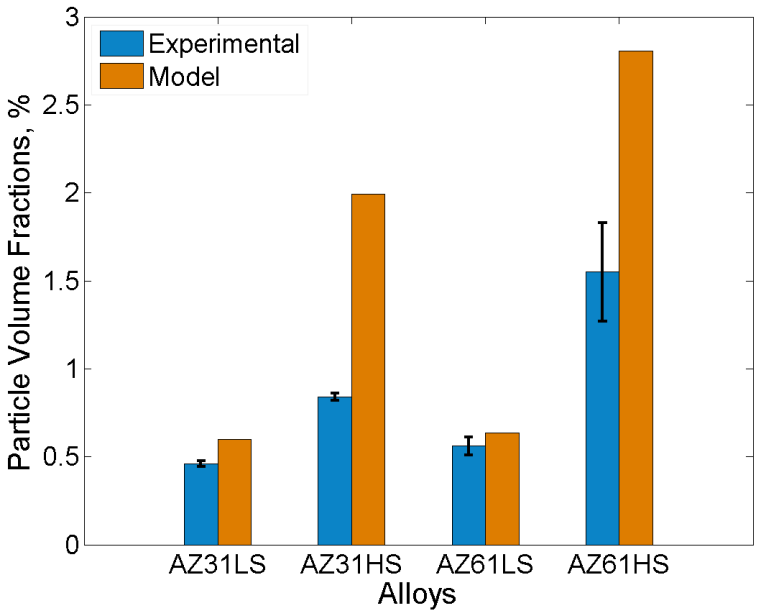

Figure 4.11: A comparison of the volume fractions of the particles measured experimentally with the predicted volume fractions of the second phases of the sand-cast alloys.

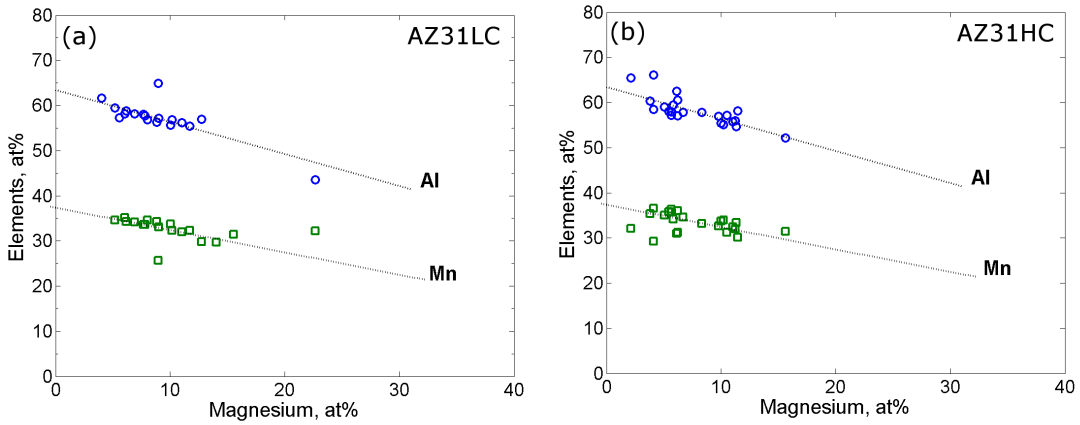

Figure 4.12: The plots of particle compositions showing the variation of aluminium and manganese atomic fraction against that of matrix, magnesium, of chill-cast (a) AZ31LC and (b) AZ31HC. Fitting lines are drawn for aluminium and manganese data points and extrapolated to zero atomic fraction Mg, since zero contribution from the matrix would give the correct compositions of the particles containing aluminium and manganese.

with the predicted phase fraction is shown in Fig. 4.14. Similar to the sand-cast alloys, the experimentally obtained volume fractions of particles are comparatively lower than the model predicted phase fraction, especially for the high manganese alloys.

Size distributions of the particles are shown in Fig. 4.15. For AZ31LC, most of the particles are within a range of diameter of 3 to 5 μm and AZ31HC contains particles in a similar size range with more particles in the larger size range of the plot. The higher aluminium variants contain particles almost within a range of 3 to 6 μm. For the high manganese alloys, the existence of large particles is evident. The modes of the data sets of particle sizes are 5, 3, 4 and 4 μm for AZ31LC, AZ31HC, AZ61LC and AZ61HC respectively. The fraction of particles, larger than 10 μm, are 3.35, 6.62, 4.73 and 8.84% of the total number of particles for AZ31LC, AZ31HC, AZ61LC and AZ61HC respectively. The average particle sizes are given in Table 4.3 together with the data from the chill-cast alloys. The average particle sizes are similar in all alloys. However, the major difference in the sizes lies in the larger size range.

The phase formed and fractions were very similar in the sand-cast and chill-cast alloys (within 10%). After rolling, the particle size distributions were also very similar.

4.1.3 Texture Development

The pole figures of the rolled alloys were constructed from EBSD data. For hexagonal metals, the texture is commonly represented by the orientation of the {0001} plane. The texture obtained for basal {0001}, prismatic $\{10\bar{1}0\}$ and pyramidal $\{11\bar{2}0\}$ planes are shown in terms of pole figures in Figs. 4.16 and 4.17.

A strong basal texture is observed in all alloys. Most of the poles are aligned

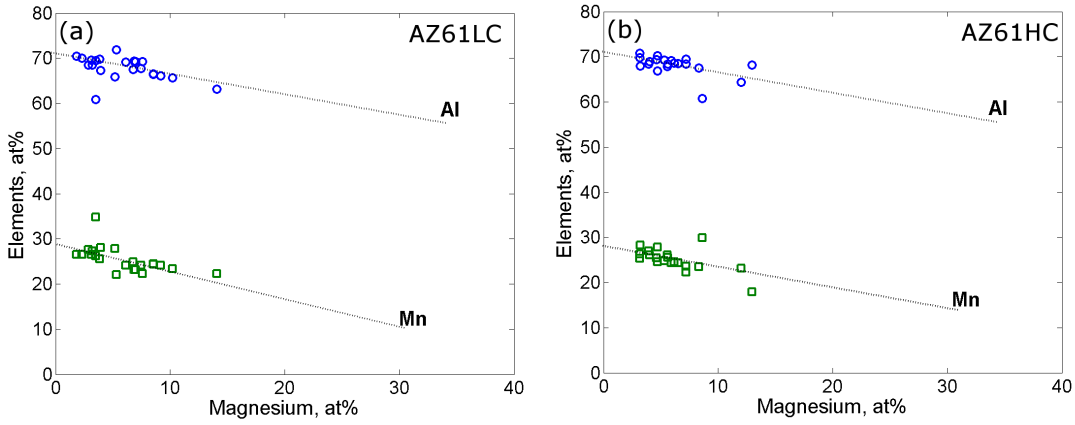

Figure 4.13: The plots of particle compositions showing the variation of aluminium and manganese atomic fraction against that of matrix, magnesium, of chill-cast (a) AZ61LC and (b) AZ61HC. Fitting lines are drawn for aluminium and manganese data points and extrapolated to zero atomic fraction magnesium, since zero contribution from the matrix would give the correct compositions of the particles containing aluminium and manganese.

Table 4.3: Average particle diameter, d_p, of the alloys, calculated from the total data populations.

Alloy	**Particle Diameter,** d_p $(\mu m)^a$	
	Sand-cast	Chill-cast
AZ31L	5.50 ± 2.90	5.32 ± 2.27
AZ31H	6.14 ± 3.29	5.40 ± 2.73
AZ61L	5.67 ± 2.10	5.34 ± 2.56
AZ61H	5.98 ± 3.12	5.84 ± 2.83

[a] Errors are the standard deviations of the corresponding data sets.

parallel to the sheet thickness (ND). It implies that the c-axis, $\langle 0001 \rangle$ direction of the hcp magnesium crystals lies perpendicular to the rolling direction (RD). Though very similar texture were obtained in all alloys, the multiples of uniform distribution (MUD) intensity of the texture was altered by the addition of aluminium. AZ31LS and AZ31HS show stronger textures which are slightly weakened by the addition of more aluminium. No splitting of the texture in the RD, as sometimes observed in magnesium alloy sheet (Al-Samman, 2009), was detected.

It is noteworthy that because of the strong rolling texture the deformation by tensile tests (discussed in the next section) was carried out in the "hard" orientation that require c-axis compression since the c-axis was perpendicular to the rolling direction and during the hot tensile tests, uniaxial stress was applied parallel to the rolling direction. This orientation is unfavourable for basal slip or $\{10\bar{1}2\}$ tension twinning and requires activation of one of the more difficult deformation modes, including prismatic and/or pyramidal slip. As a consequence, flow stress and strain

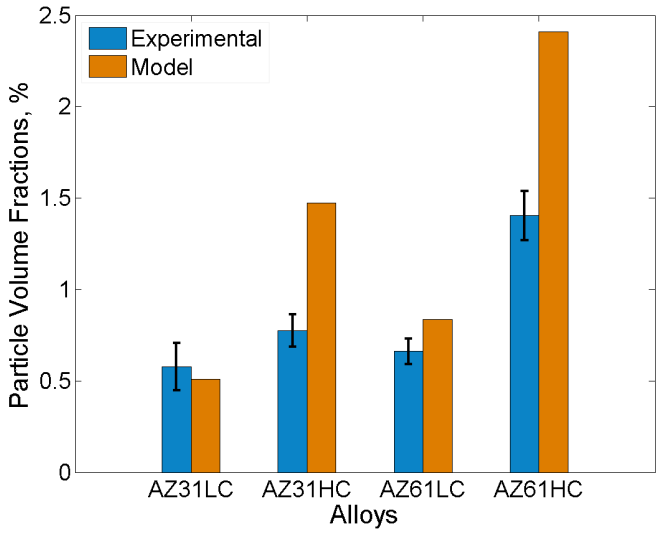

Figure 4.14: A bar chart showing the comparison between experimental and model predicted particle volume fractions for the chill-cast alloys. Corresponding errors are plotted from standard errors (SE).

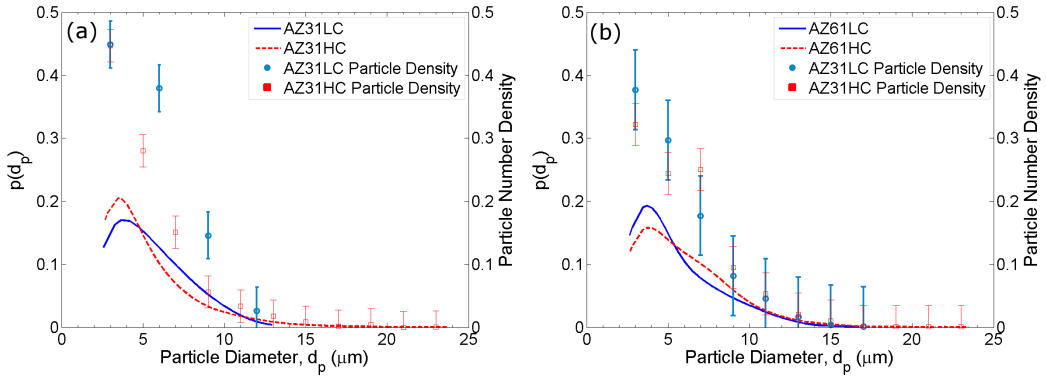

Figure 4.15: Plots of probability distribution functions of the particle diameter (d_p) of chill-cast (a) AZ31LC and AZ31HC and (b) AZ61LC and AZ61HC. Normalised fraction of number of particles are also included.

hardening rate would be expected to increase compared to c-axis extension or c-axis constraint mode (Barnett, 2001; Wang and Huang, 2003).

4.2 Flow Behaviour during Hot Deformation of the Alloys Investigated

The sand-cast alloys were hot deformed uniaxially under different test conditions with varying temperature (300 to 450 °C) and strain rate (5×10^{-4} and 5×10^{-3} s^{-1}). Having similar grain size and basal texture for all variants, the main difference between the alloys was the fraction and distribution of particles. The effect of the size distributions of the particles has yet not been reported in literature for magnesium

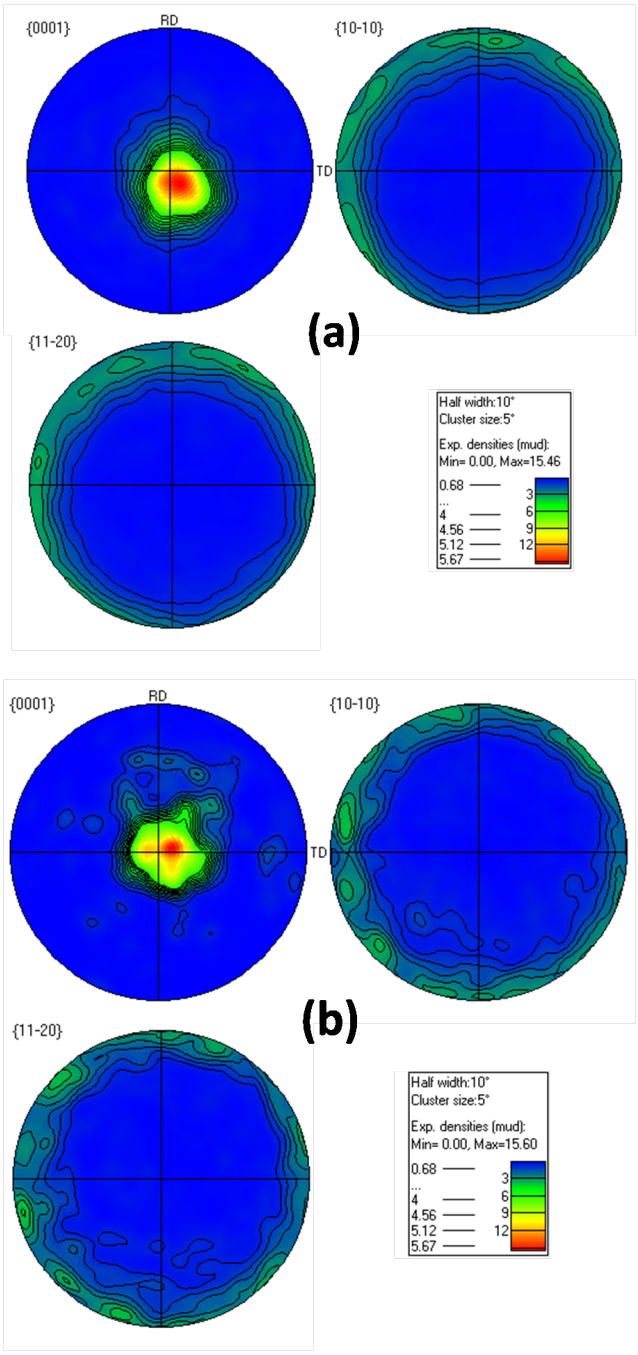

Figure 4.16: The pole figures of {0001},{10$\bar{1}$0} and {11$\bar{2}$0} planes for AZ31LS and AZ31HS in the final hot rolled condition. The alloys were rolled at 300 °C to a strain of 0.95. The maximum intensity for both alloys is very similar. A common basal texture is identified in both alloys.

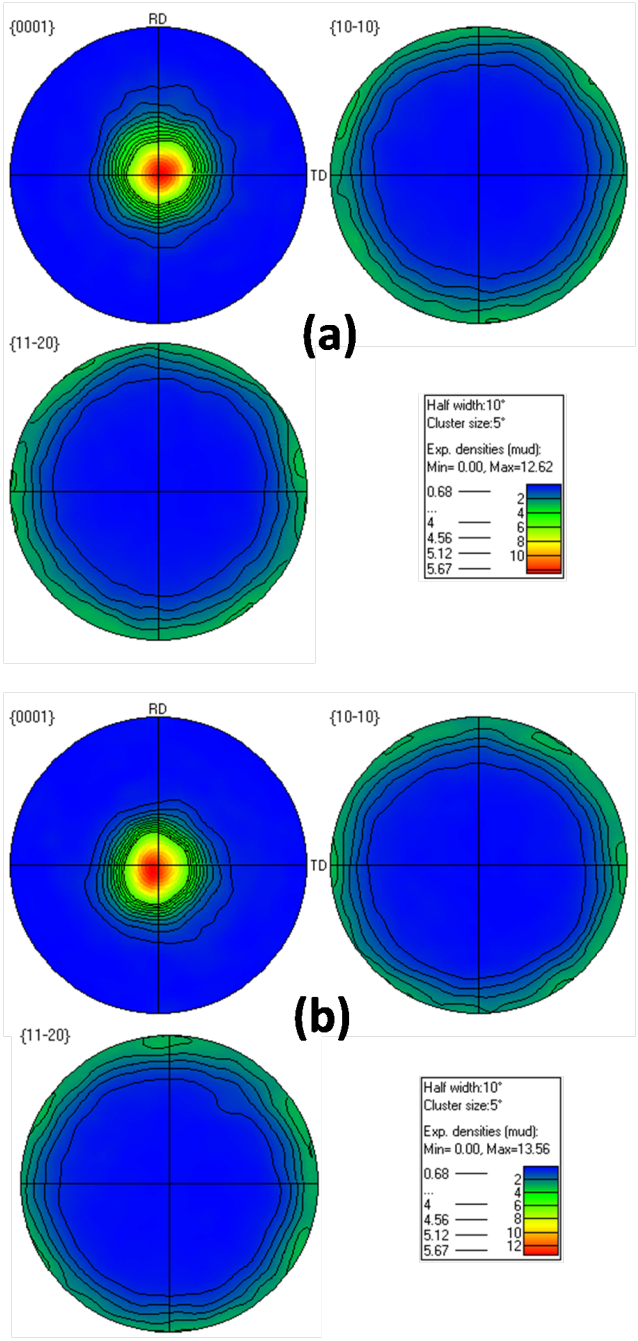

Figure 4.17: The pole figures of {0001}, $\{10\bar{1}0\}$ and $\{10\bar{1}0\}$ planes for AZ61LS and AZ61HS in the final hot rolled condition. The alloys were rolled at 300 °C to a strain of 0.95. The maximum intensity for both alloys varies slightly, but, the maximum intensities are lower than those of AZ31LS and AZ31HS indicating the weakening of texture, to some extent, by aluminium addition. A common basal texture is identified in both alloys.

alloys. However, in the alloys investigated, it is expected that the widely variation in the sizes of the particles will have significant effects on hot deformation behaviour.

4.2.1 Flow Characteristics of the Alloys

In Figs. 4.18 to 4.21, the true stress vs true strain curves of the alloys, deformed at a base strain rate of 5×10^{-4} s^{-1} with $\pm 10\%$ strain rate perturbation, are shown for different test temperatures. The steps in the curves correspond to the imposed strain rate jumps. Some characteristics of the flow curves are discussed below. The consequence of the flow behaviour parameters, such as elongation to failure (e_f) and strain rate sensitivity (m), are explained in a different section, together with the justification for the differences in performance along with the grain growth data.

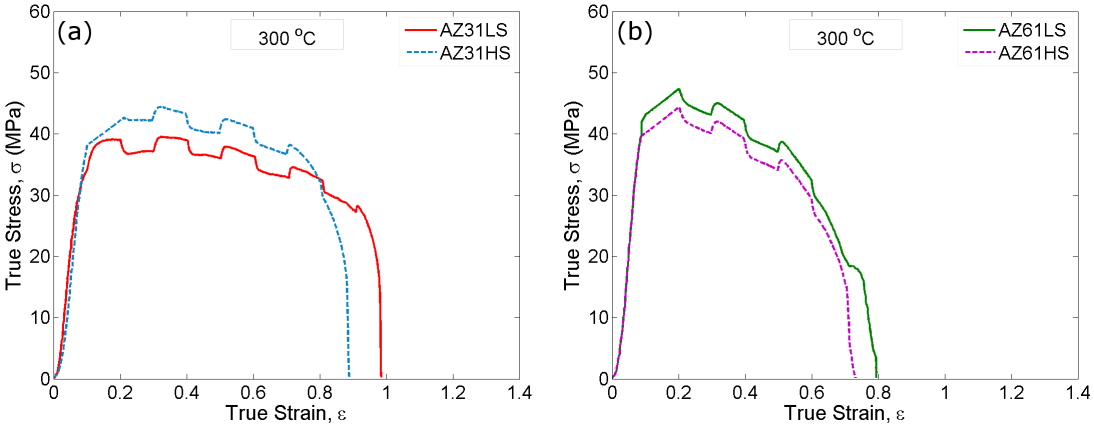

Figure 4.18: The true stress-strain curves of the sand-cast (a) AZ31LS and AZ31HS and (b) AZ61LS and AZ61HS deformed at 300 °C at a base strain rate of 5×10^{-4} s^{-1} with $\pm 10\%$ rate perturbation. The high rate of strain hardening followed by a rapid softening is obvious from the plots. The peak stress is at least 40 MPa. The failure true strain is less than 1.

Several common characteristics are observed in all alloys. With an increase of strain, the flow stress increases up to a peak stress. After reaching the peak stress, the flow curve becomes nearly flat, up to a certain strain, at the higher temperatures (>300 °C), followed by softening at different rates and ranges of strain. The rate of strain hardening was studied and found to be different for the different alloys in the temperature range investigated. However, the major difference was observed in the flow softening part. The competition between sustaining strain hardening and softening is affected by the composition of the alloys.

As temperature increases, the peak flow stress decreases by approximately 10 MPa. Also, with the increase of temperature, an increase in failure strain for all alloys is evident from the flow curves up to 400 °C. At 450 °C, a slightly lower failure strain was obtained. Moreover, a more prolonged strain hardening level was obtained with the increase of temperature.

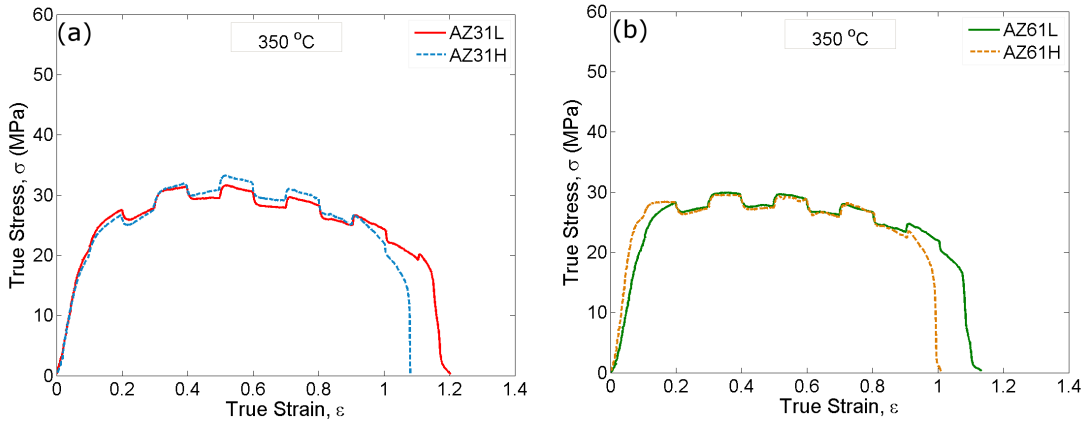

Figure 4.19: The true stress-strain curves of the sand-cast (a) AZ31LS and AZ31HS and (b) AZ61LS and AZ61HS deformed at 350 °C at a base strain rate of 5×10^{-4} s^{-1} with ±10% rate perturbation. A gradual strain hardening followed by a slower softening is obvious from the plots.

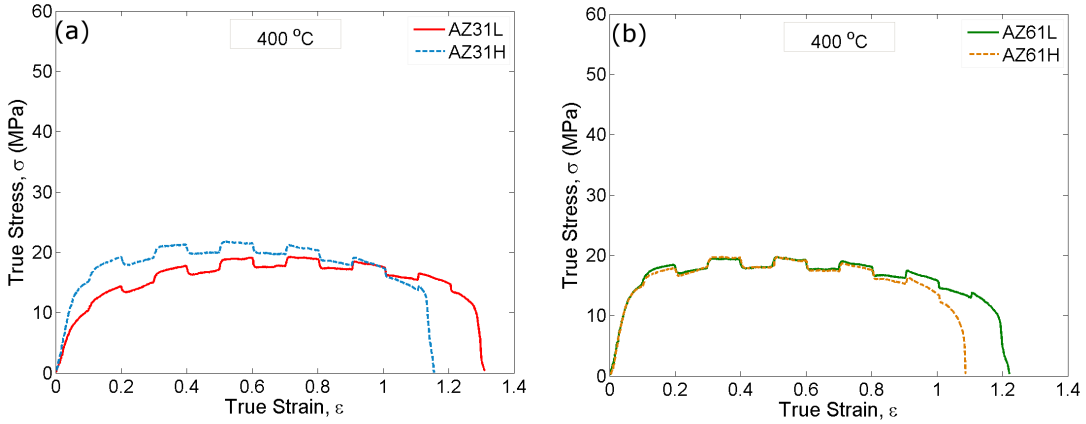

Figure 4.20: The true stress-strain curves of the sand-cast (a) AZ31LS and AZ31HS and (b) AZ61LS and AZ61HS deformed at 400 °C at a base strain rate of 5×10^{-4} s^{-1} with ±10% rate perturbation. The maximum flow stress has been decreased significantly compared to the low temperature flow curves.

Addition of more manganese does not affect the peak flow stress at any particular temperature (except 300 °C). However, more manganese shows a significant difference in the flow softening region. Alloys with higher manganese content failed comparatively earlier than the low manganese alloys. This is attributed to cavitation, promoted by the addition of manganese as discussed later.

The effect of adding more aluminium is mostly limited up to the strain hardening region. Due to the solid solution strengthening, the strain hardening region is shortened by adding more aluminium. This means that the peak stress was reached comparatively earlier than the low aluminium alloys.

Figs. 4.22 to 4.25 show the true stress-strain curves for the alloys at different temperatures deformed at a base strain rate of 5×10^{-3} s^{-1}, with ±10% strain rate perturbation. The maximum flow stress is increased by approximately 8 to 20 MPa

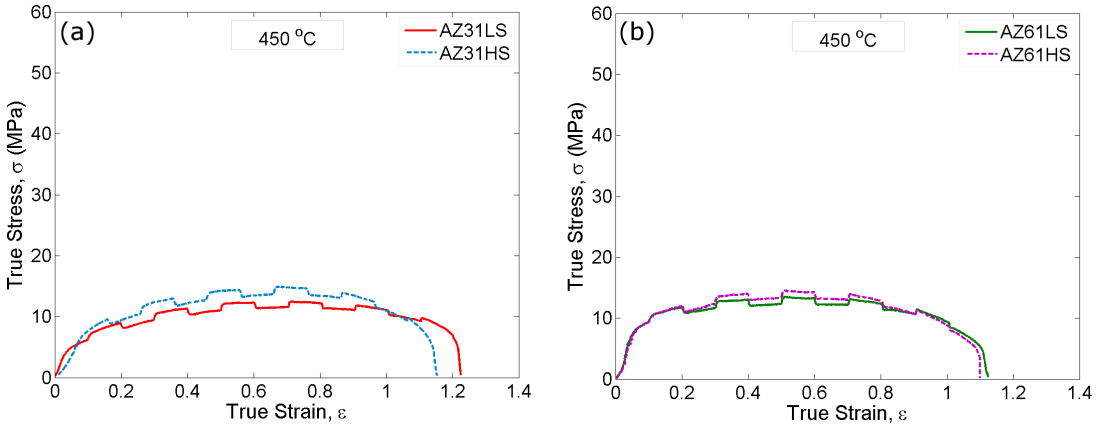

Figure 4.21: The true stress-strain curves of the sand-cast (a) AZ31LS and AZ31HS and (b) AZ61LS and AZ61HS deformed at 450 °C at a base strain rate of 5×10^{-4} s^{-1} with ±10% rate perturbation. At this, the highest deformation temperature, the average flow stress is lowest amongst the all of the test temperatures.

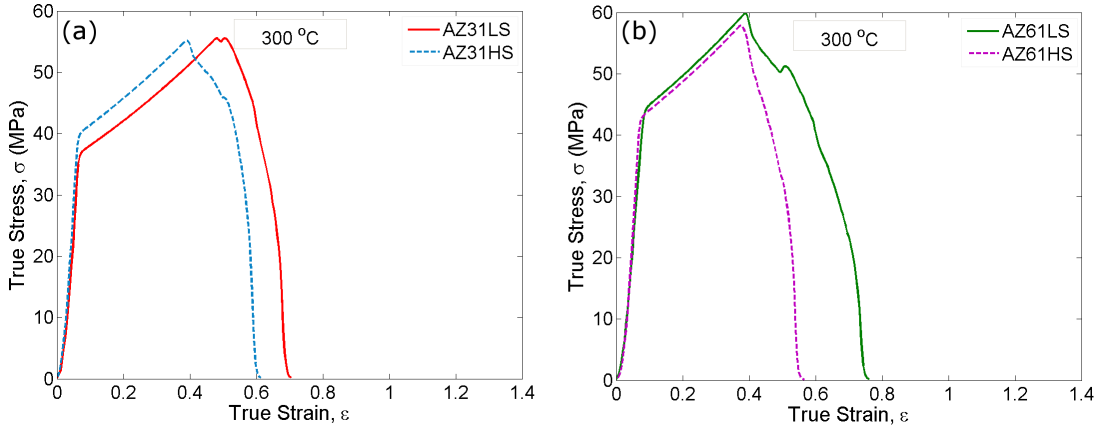

Figure 4.22: The true stress-strain curves of the sand-cast (a) AZ31LS and AZ31HS and (b) AZ61LS and AZ61HS deformed at 300 °C at a base strain rate of 5×10^{-3} s^{-1} with ±10% rate perturbation. The high rate of strain hardening followed by a rapid softening is obvious from the plots.

for all alloys, compared to the low strain rate condition, in the temperature range investigated. The alloys also failed at comparatively lower strains. Moreover, the strain hardening region is apparently shorter than the low strain rate condition. This implies that strain hardening occurs rapidly at this condition. The effect of temperature and addition of more manganese are similar to those discussed for the slow strain rate condition. The increase in flow stress with the addition of more solute aluminium is clearly identified at the high strain rate condition. A rapid strain hardening, as expected, is also evident by the addition of more aluminium.

In summary, temperature plays the key role in controlling flow behaviour. Flow stress is reduced with increasing temperature and a prolonged strain hardening region is observed at the low strain rate condition, attributed to the grain growth as discussed later. Addition of aluminium appears to slightly affect the strain hardening

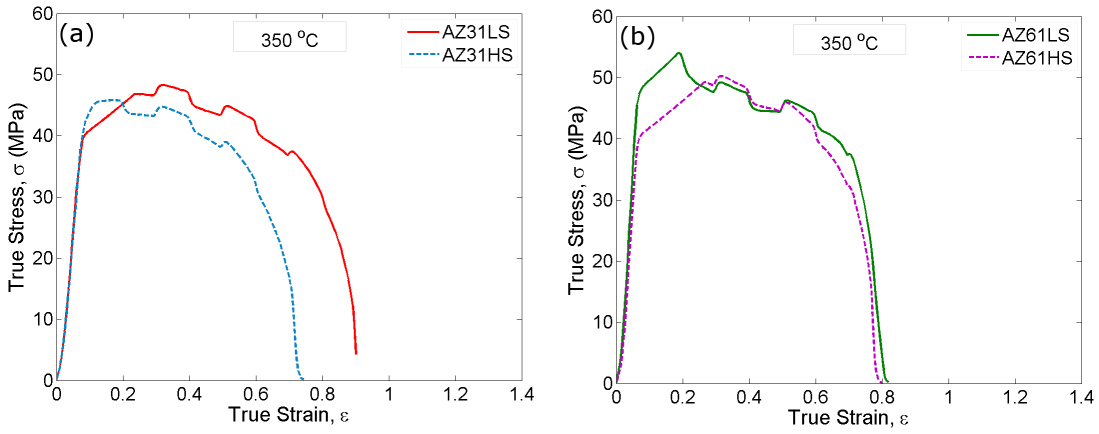

Figure 4.23: The true stress-strain curves of the sand-cast (a) AZ31LS and AZ31HS and (b) AZ61LS and AZ61HS deformed at 350 °C at a base strain rate of 5×10^{-3} s^{-1} with ±10% rate perturbation. Maximum flow stress level was similar in all alloys.

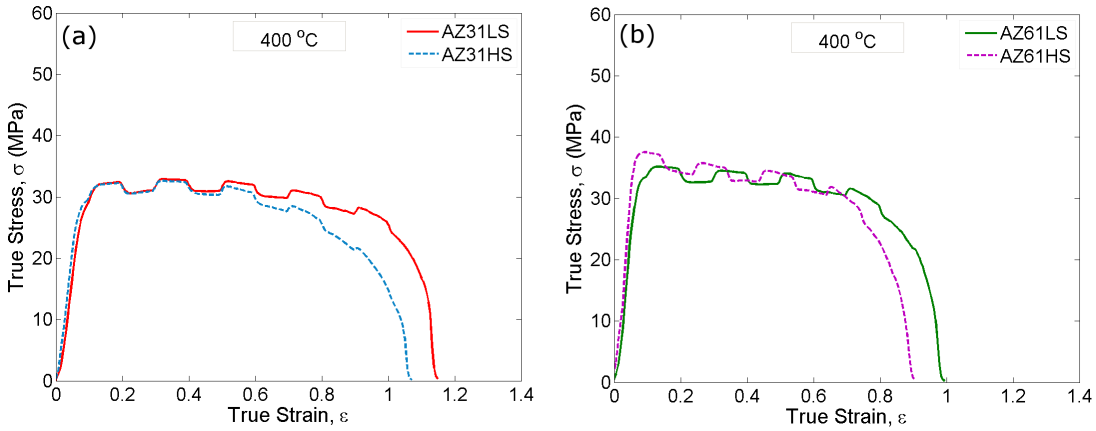

Figure 4.24: The true stress-strain curves of the sand-cast (a) AZ31LS and AZ31HS and (b) AZ61LS and AZ61HS deformed at 400 °C at a base strain rate of 5×10^{-3} s^{-1} with ±10% rate perturbation.

behaviour. On the other hand, the effect of manganese lies in the flow softening region, attributed to cavitation as discussed later.

4.2.2 Mechanism of Deformation

The flow behaviour of the alloys is strongly affected by the variation of temperature and strain rate. The effects of aluminium and manganese are small compared to the consequence of the test conditions. The flow characteristics of the alloys can be expressed as:

$$\sigma = f\left(\varepsilon, \dot{\varepsilon}, T, S\right) \tag{4.1}$$

where ε is the true strain, $\dot{\varepsilon}$ is the strain rate, T is the absolute temperature and S is a structure parameter related to the dislocation, grain size, alloy composition, etc. For a fixed temperature and strain rate condition, S and ε remain as the influential

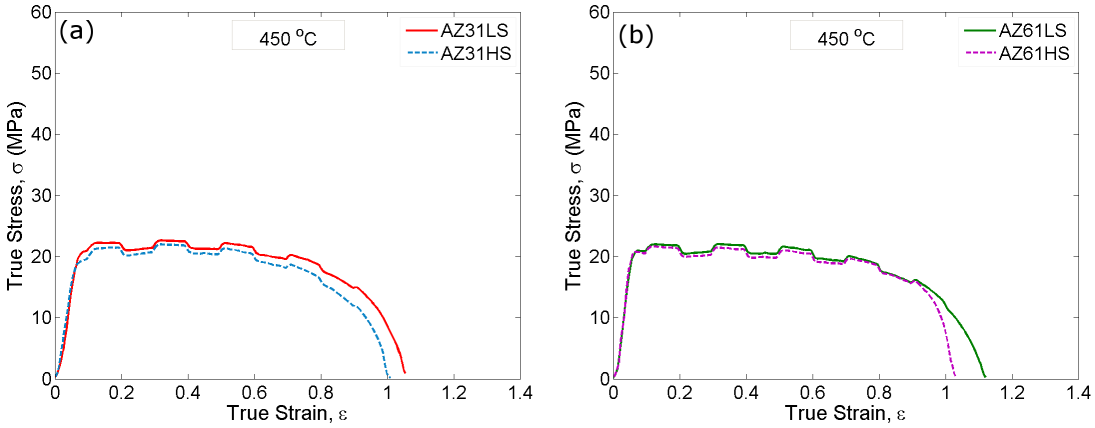

Figure 4.25: The true stress-strain curves of the sand-cast (a) AZ31LS and AZ31HS and (b) AZ61LS and AZ61HS deformed at 450 °C at a base strain rate of 5×10^{-3} s^{-1} with ±10% rate perturbation.

variables. As discussed in the preceding section, at a set of test parameters, the amount of strain hardening, the peak flow stress and the extent of strain softening vary and this can be attributed to the different compositions of the alloys and how these influence S. For example, at 350 °C, deformed under slow strain rate condition, the addition of aluminium has increased the rate of strain hardening (Fig. 4.26). The strain hardening rate, $\Theta = d\sigma/d\varepsilon$ (Dieter, 2001), was obtained from the corresponding flow curves. As Fig. 4.26 shows the effect of manganese on the strain hardening rate appears to be small or zero which is surprising since there are significant difference in particle distribution in the alloys. However, as already noted the hardening rates do increase with the addition of aluminium.

The activation energy for deformation provides information about the underlying rate controlling mechanism. The activation energy (Q) of deformation can be calculated from the flow stress dependency at elevated temperature using the simplified Equation 2.19 as (Frost and Ashby, 1982)

$$\dot{\varepsilon} = A_1 \sigma^n \exp\left(-\frac{Q}{RT}\right) \tag{4.2}$$

After rearranging,

$$\sigma = A_2 \dot{\varepsilon}^m \exp\left(\frac{mQ}{RT}\right) \tag{4.3}$$

Taking ln in both sides,

$$\ln \sigma = \frac{mQ}{RT} + \ln A_2 + m\dot{\varepsilon} \tag{4.4}$$

where A_1 and $A_2 (= 1/A_1^m)$ are constants, stress exponent $n = 1/m$. The peak flow stresses of the alloys at different temperatures were used to plot $\ln \sigma$ against

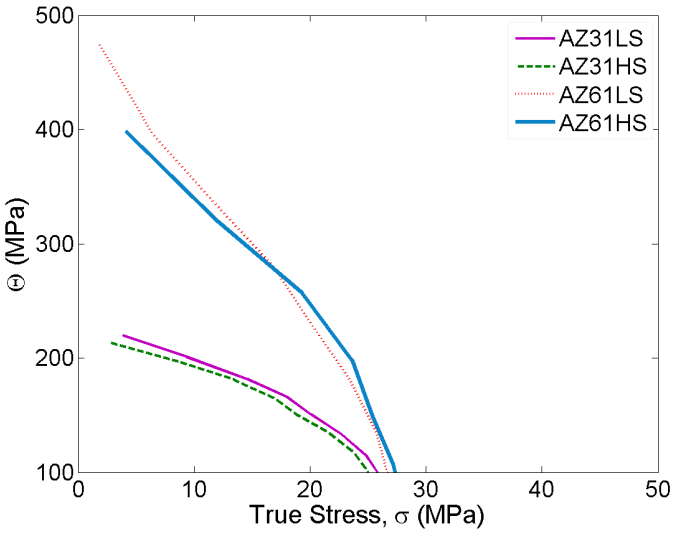

Figure 4.26: A plot of the strain hardening rate, Θ, against the flow stress of the sand-cast alloys deformed at 350 °C at a strain rate of 5×10^{-4} s^{-1}. A solute strengthening effect of aluminium addition is evident from the plot. To determine Θ, polynomial fits were used.

Table 4.4: Calculation of the average activation energies for the sand-cast alloys

Alloy	**Average Activation Energy** Q (kJ mol^{-1})	
	5×10^{-4} s^{-1}	[a] 5×10^{-3} s^{-1}
AZ31LS	75.19 ± 14.66	95.82 ± 6.29
AZ31HS	78.22 ± 13.95	93.80 ± 6.74
AZ61LS	83.99 ± 10.96	87.87 ± 3.50
AZ61HS	89.72 ± 14.77	94.57 ± 11.73

[a] Detailed calculation for this strain rate data is not shown.

$1/RT$ to obtain the slope mQ. Only slow strain rate data has been considered to plot this equation. From Fig. 4.27, the slope obtained is 26 kJ mol^{-1}. Using this value, the apparent activation energies can be determined from the average strain rate sensitivity (m) values of the alloys at different temperatures. Table 4.4 shows the calculated average activation energies of the alloys (averaged from data for all temperatures) for both strain rate conditions. The activation energy of lattice diffusion of pure magnesium is 135 kJ mol^{-1} and that of grain boundary diffusion is 92 kJ mol^{-1} (see Appendix A). This indicates the deformation mode of these alloys is likely to be dominated by grain boundary diffusion at all test temperature and strain rate conditions.

Since grain boundary diffusion is found to be the dominating diffusional process,

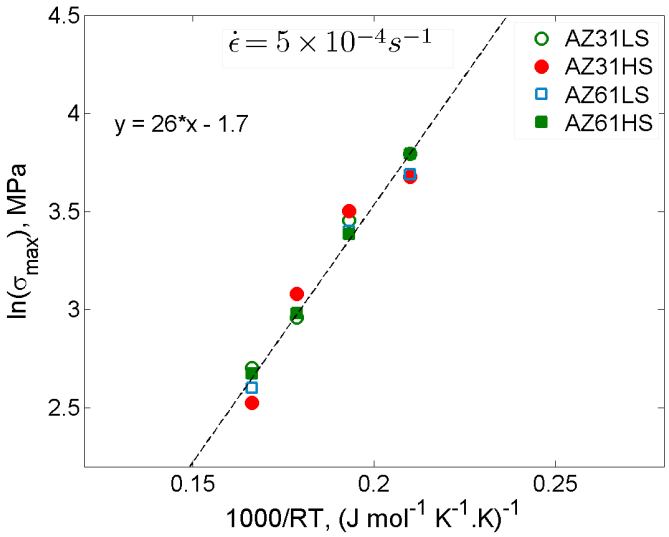

Figure 4.27: A plot of the logarithmic maximum flow stress, σ_{max}, as a function of the reciprocal of the absolute temperature (T) of the sand-cast alloys deformed at the strain rate of 5×10^{-4} s^{-1}. The slope of the curve, mQ, is 26 kJmol^{-1}. $1/T$ was normalised by $1000/R$ before plotting.

the dependency of deformation rate (p) on grain size is expected to be equal to 3 (see Table 2.6). Using the constitutive law of superplasticity (Equation 2.19), for both strain rate conditions, data can be plotted to check the whether a single mechanism is operating for the current test conditions. Fig. 4.28 shows that for both strain rate conditions, the data can be fitted to a line with a single slope. For the slow strain rate condition, the scattering of the data is likely to be a result of the grain growth during testing.

The stress exponent, n ($= 1/m$) varies between approximately 2.5 and 4. This parameter is often used to infer the mechanism of deformation (del Valle et al., 2005; McNelley et al., 2008; Watanabe et al., 2001) although this can be misleading. A n value of ~ 3 has previously been identified as indicating deformation dominated by a solute drag creep (SDC) process, with $n \sim 2$ corresponding to GBS. However, for SDC to dominate, the expected activation energy should be close to that for solute aluminium diffusion into magnesium which is equal to 143 kJ mol^{-1} (Frost and Ashby, 1982). In contrast, in the current study, Q was close to that for grain boundary diffusion which is expected for GBS. As discussed later (see Section 4.3), no substantial grain elongation occurred. Therefore, diffusion creep or dislocation creep are ruled out as dominating deformation modes.

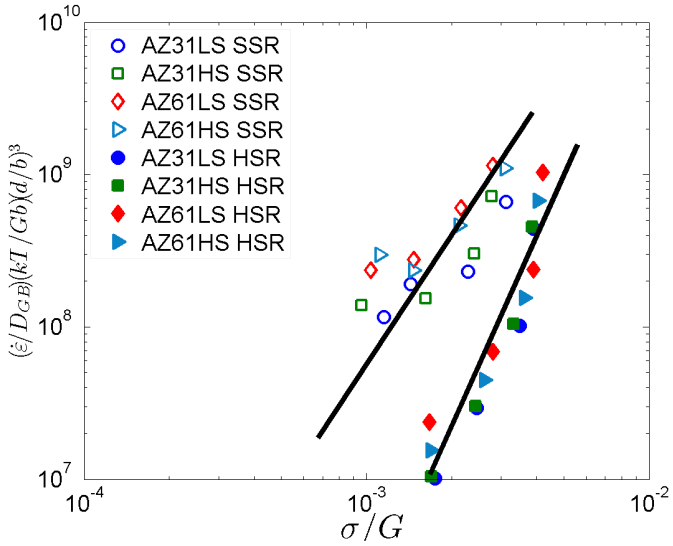

Figure 4.28: The relationship between normalised strain rate and normalised flow stress for the sand-cast alloys at the strain rate of 5×10^{-4} (SSR) and 5×10^{-3} (HSR) s^{-1} at all temperatures. D_{GB} was identified to be dominating in all alloys and hence p was 3.

4.2.3 Analyses of Strain Rate Sensitivity and Elongation to Failure

From the flow curves shown in the preceding section, the strain rate sensitivity (m) and elongation to failure (e_f) values of the alloys were determined. To find the relationship between composition and m and e_f values, analysis of variance (ANOVA) was performed on the m and e_f data. The changes of the m-values during straining are discussed further in Section 4.3 along with the grain growth results.

Fig. 4.29 shows the e_f plots of all alloys at different temperatures. Adding more manganese to AZ31LS or AZ61LS appears to have a detrimental effect on e_f. An addition of more aluminium to AZ31LS seems to show some reduction in e_f, but not to such an extent like the addition of manganese. A comparison between AZ31HS and AZ61HS shows a large drop in e_f with added aluminium, compared to the addition of aluminium to AZ31LS (to produce AZ61LS).

The consequence of the addition of aluminium and manganese on m is shown in Fig. 4.30. At 300 °C, the m-values are within the range of 0.25 to 0.30. With an increase in temperature, the m-values are increased. At 350 to 450 °C, m values are within the range of 0.30 to 0.42. The effect of aluminium or manganese is not clear from the plots. At 350 °C, addition of aluminium is not significant, in terms of m, considering the associated error bars. The addition of manganese appears to reduce the m slightly. At 400 °C, both the addition of aluminium or manganese has reduced m slightly. At 450 °C, the addition of manganese does not affect m, but the addition of aluminium slightly reduces m. Interactions that involve the combined effect of several variables may also be critical but are not easily identified from these plots.

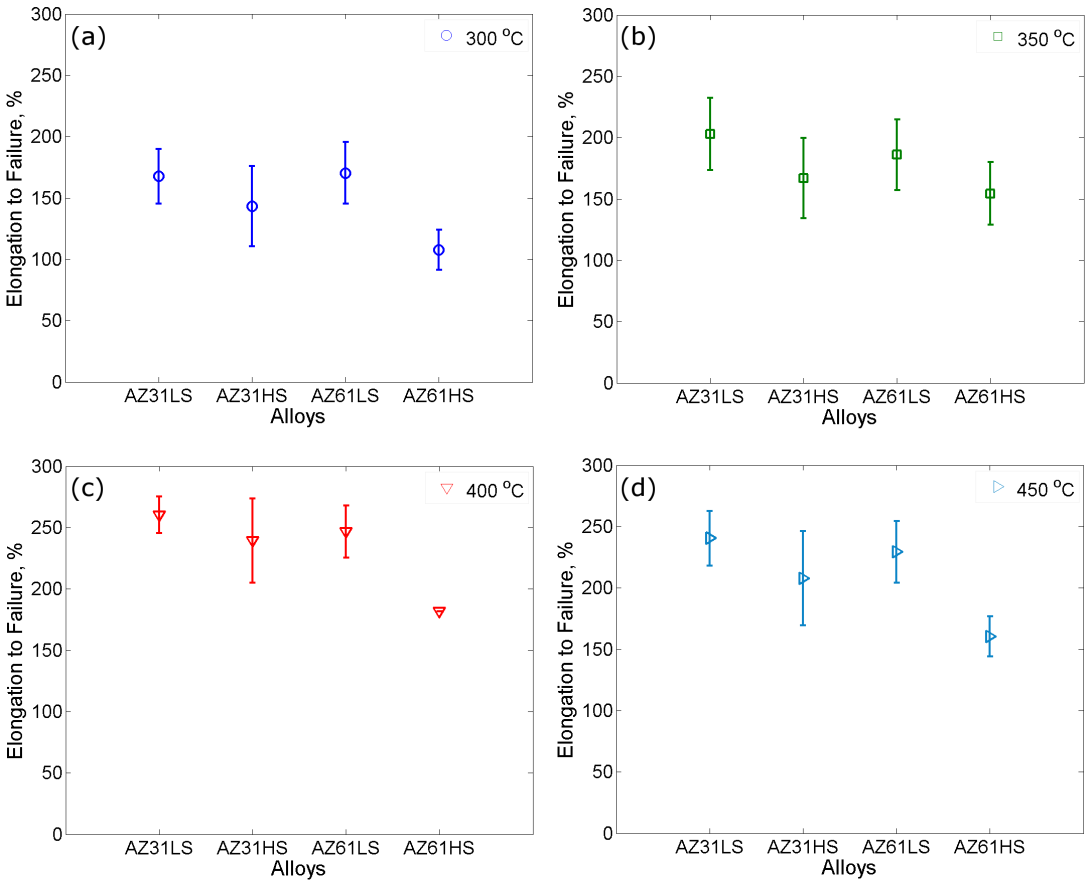

Figure 4.29: The elongation to failure (e_f) values of the sand-cast alloys at (a) 300, (b) 350, (c) 400 and (d) 450 °C deformed at a strain rate of 5×10^{-4} s^{-1}.

To get rid of this ambiguity, ANOVA was performed.

To perform ANOVA, the half-effects ($\Delta/2$) of the responses (e_f and m) were first calculated and corresponding Pareto charts are shown in Fig. 4.31. The half-effects of three variables were considered, indicated as A–aluminium content (3 and 6 wt%), B–manganese content (0.30 and 1.20 wt%) and C–temperature (350 and 400 °C). In Fig. 4.31a, temperature (variable C) is identified to have the most significant positive effect (increasing temperature increases e_f) on the elongation values. Then, addition of manganese has the second most vital effect, but, is negative. This is because addition of manganese reduces e_f. Aluminium was the third significant factor and also has a negative effect. However, this result is different when considering the m (Fig. 4.31b). Aluminium (A) appears to be the most influential variable and it has a negative effect on m followed by temperature (C) with a positive effect. Then, manganese (B) has the third major response with a negative trend.

From the Pareto charts, it can be seen that the single response of increasing aluminium or manganese content has a negative influence on m or e_f. Moreover, the interaction effect (AB) of these variables is also negative (Fig. 4.31a).

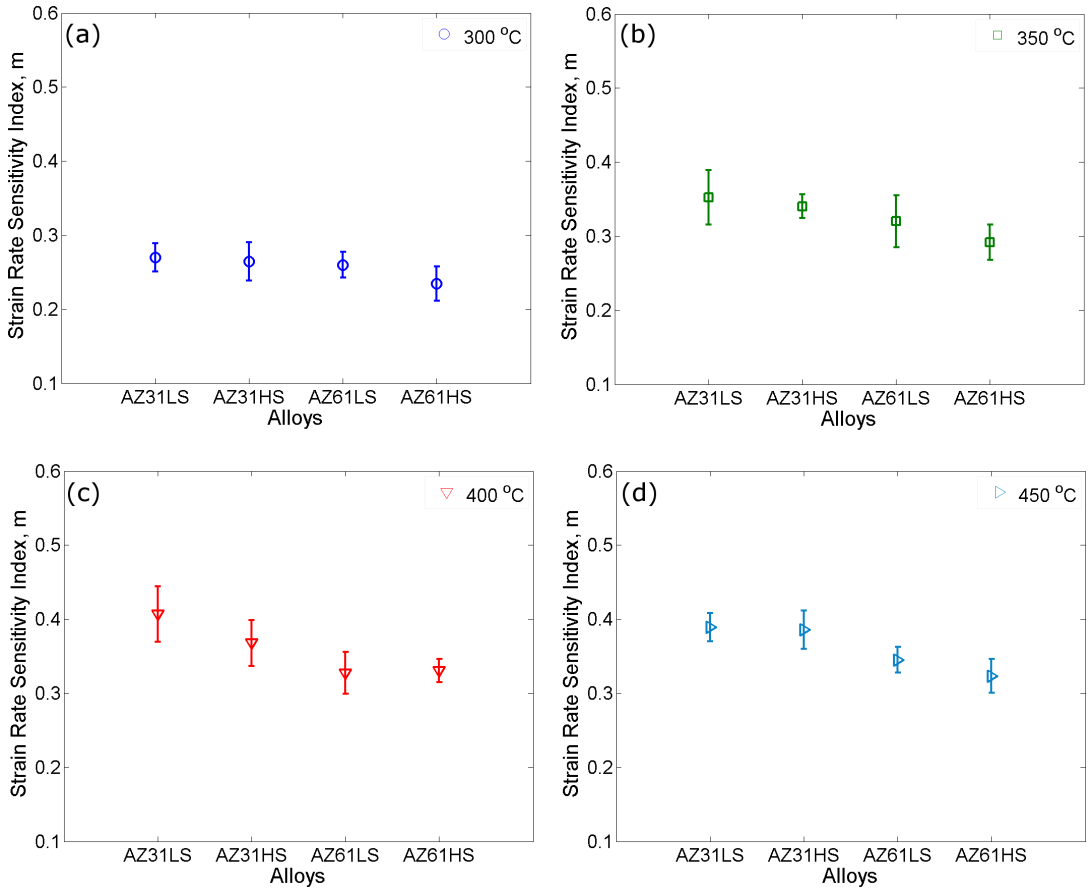

Figure 4.30: The strain rate sensitivity (m) values of the sand-cast alloys are shown for (a) 300, (b) 350, (c) 400 and (d) 450 °C deformed at a strain rate of 5×10^{-4} s^{-1}.

There are published data on AZ31 and AZ61 regarding their superplastic properties, but, still lacking are systematic investigations of these both alloys under a similar test condition. Zarandi and co-workers (2008) reported that addition of 3% aluminium to AZ31 improved e_f by nearly 20%. However, from their work, the effect of Al-Mn containing particles is not clear. The authors confirmed the observation of $Mg_{17}Al_{12}$ phase, and reported reduced precipitation of this phase with the increase of manganese level. On the other hand, this phase was completely absent in the current project. Also, the effect and the extent of cavitation were not clear in their study. Absence of any repeat work for the hot deformation in their work casts further uncertainty on the results.

After obtaining the half-effects of the variable responses, the F-distribution components were determined and are shown in Table 4.5. For a 99% confidence level, $F_{0.01}$ is 7.95 (Bate, 2006). Now, it can be seen that for both types of analyses (using e_f or m) the effects of single variables (A, B or C) are significant. The combined effect of aluminium and manganese (AB) and temperature and aluminium (CA) also influences e_f, whereas CA is the only combined effect significant in influcening m.

The effect of temperature (C) shows a positive effect on both e_f and m. The

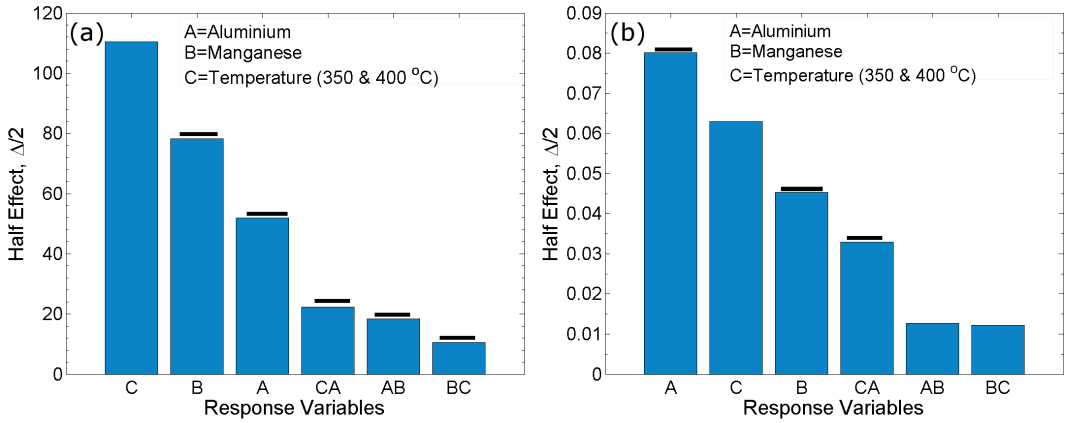

Figure 4.31: Pareto charts of the calculated half effects of the variables aluminium (A), manganese (B) and temperature (C) on the responses of (a) elongation to failure values (e_f) and (b) strain rate sensitivity (m) values of the sand-cast alloys. The horizontal lines on top of the bars represent a negative effect of that variable. The alloys were deformed at 350 and400 °C at a strain rate of 5×10^{-4} s^{-1}.

Table 4.5: Estimation of the F-distributions of the variables/responses

	A	**B**	**C**	**AB**	**BC**	**CA**
e_f	65	148	296	8	3	12
	S	**S**	**S**	**S**	**NS**	**S**
m	197	63	122	5	5	33
	S	**S**	**S**	**NS**	**NS**	**S**

[a] S=Significant; NS=Not Significant

contribution of manganese (B) is negative on e_f. This is due to the extensive cavitation at the temperature range used here and will be discussed in details in Chapter 5. The effect of aluminium (A) is not very significant in controlling e_f, but is an influential factor in determining m. Increasing aluminium content has a strong negative effect on m. As already discussed, addition of solutes increases strain hardening rate and this may reduce m due to the effect of solute drag (Schmidt and Miller, 1982). Recently, it was claimed that in magnesium alloys a reduction in m depended on the mobility of solute atoms (Stanford et al., 2010). Since activation energy for diffusion of solute aluminium into magnesium is 143 kJ mol^{-1} (Frost and Ashby, 1982), any diffusion of aluminium is unlikely to be rate controlling as the estimated Q was close to 92 kJ mol^{-1}. Moreover, solute structures, such as solute atmospheres and segregated solutes not attached to dislocations, have an adverse effect on m (Picu et al., 2006). Therefore, it is probable that with an increase of aluminium content, more segregation of solutes occurs away from the mobile

dislocations. This is believed to be the reason for reduction of m values at higher aluminium content. The combined effect from CA is significant since both single variables act in an opposite way on m-value but the observation that the combined effect is negative suggests that for the range of conditions used in this work, an increased temperature cannot overcome the effect of added aluminium solutes.

4.3 Grain Growth

4.3.1 Grain Growth Trends in the Alloys Investigated

During hot deformation, significant grain growth sometimes occurred in the alloys, largely depending on the test temperature. Fig. 4.32 shows the micrographs of the gauge regions of the alloys deformed at 350 °C at a strain rate of 5×10^{-4} s^{-1}. Substantial growth of grains is apparent in all alloys (note that the rolled grain size is 7 to 9 μm). Some cavities are also evident in all microstructures.

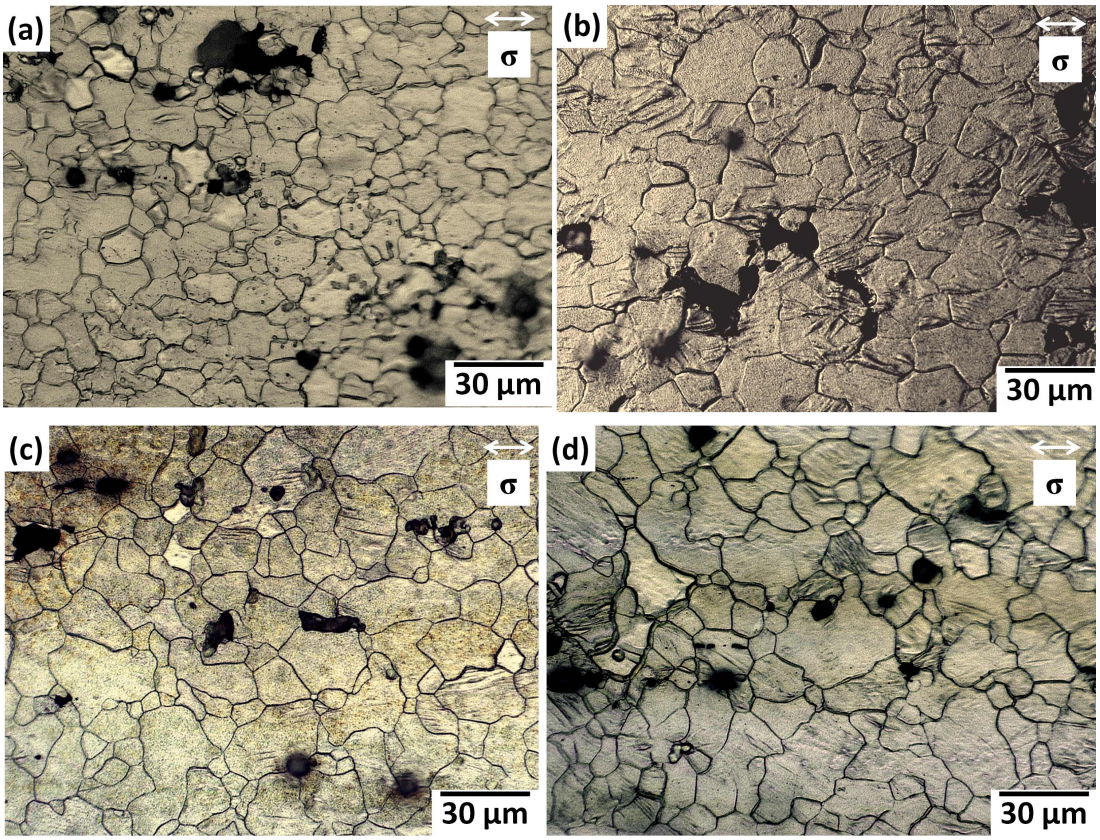

Figure 4.32: The growth of the grains in the gauge region of the failed specimens of (a) AZ31LS, (b) AZ31HS, (c) AZ61 and (d) AZ61HS after testing at 350 °C at a strain rate of 5×10^{-4} s^{-1}. The failure strains can be obtained from Fig. 4.29.

Figs. 4.33 and 4.34 show the average grain sizes of the alloys in the grip (d_{gr}) and gauge (d_g) regions at different temperatures. The grain growth in the grips is without any straining effect and therefore this reflects the static grain growth of the

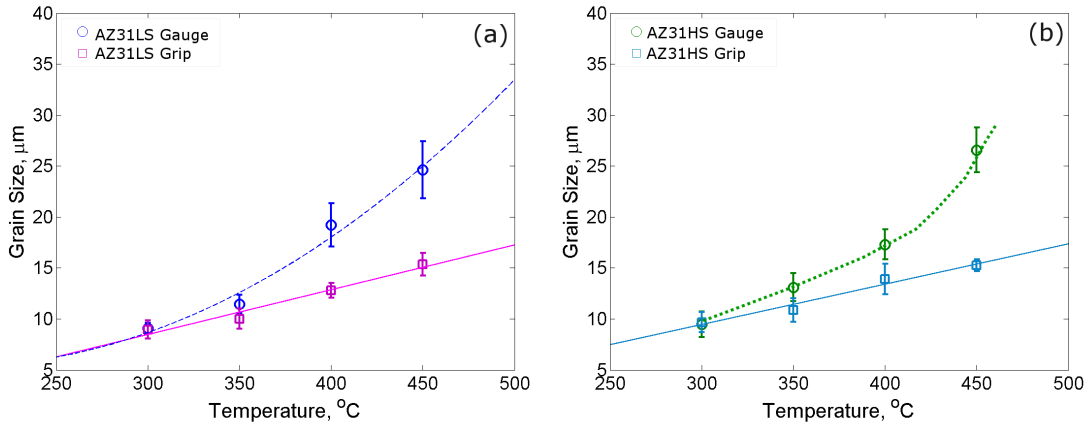

Figure 4.33: The average grain sizes of the grip and gauge sections of the deformed tensile specimens of the sand-cast (a) AZ31LS and (b) AZ31HS at different temperatures at a strain rate of 5×10^{-4} s^{-1}. The error bars were calculated using the standard error (SE) estimation method.

alloys at different temperatures. At the slow strain rate condition, the time inside the furnace chamber varied from 25 to 43 minutes, depending on the strain following the preheating of the specimens for 20 minutes. Depending on the annealing time, therefore, the size of the grains varied in the grip region. However, in the high aluminium alloys, more rapid grain growth is observed.

In the gauge region, faster growth of grains, compared to the grip region, is evident. The as-rolled average grain sizes of the alloys are 7 to 9 μm, whereas during straining, grains have increased in average size by approximately 2 to 3 times. From the plots, it can be seen that grain growth in the gauge length region also appears more pronounced for the high aluminium content alloys. Moreover, a substantial growth of grains due to straining is observed in all alloys at 450 °C. The dynamic grain growth (DGG) rate therefore appears to be controlled mainly by temperature. Otherwise there is no reason that DGG has less influence at 350 °C than 400 °C, since the difference between failure strains at 350 and 400 °C is subtle. Therefore, two trends are identified: grain growth is larger in the higher aluminium content alloys and grain growth rate increases with temperature.

One interesting feature in the microstructures, at different strains and of the failed specimens, is that there is no evidence of grain refining for any alloys. In addition, the stress strain curves do not show a very long steady state during deformation, typical of recrystallization. Dynamic recrystallization does not therefore appear to occur in any of the alloys under the conditions studied.

To check if any elongation of the grains occurs, aspect ratios were measured for the AZ61HS alloy deformed at 400 °C. Grain sizes were measured along the tensile direction and normal to the tensile direction separately in both grip (d_{gr}) and gauge (d_g) regions. The aspect ratio was 1.08±0.11 at the grip (non-deformed part) and

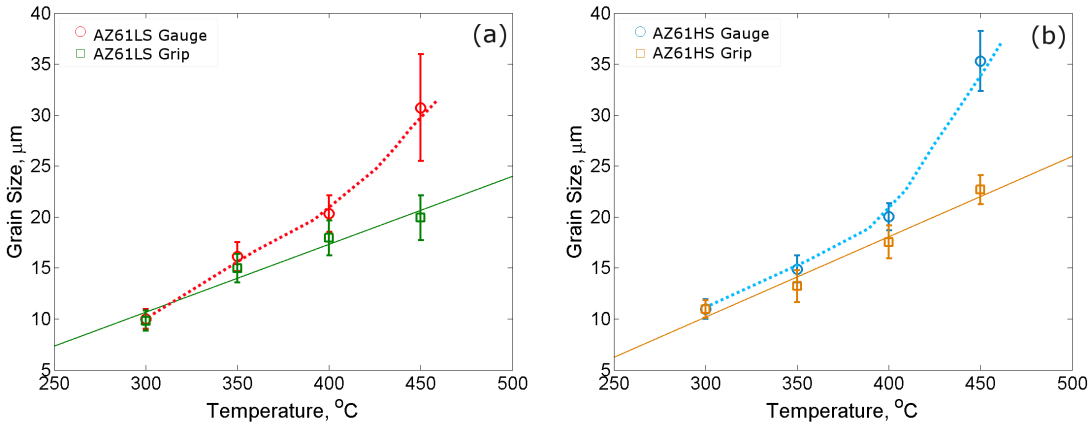

Figure 4.34: The average grain sizes of the grip and gauge sections of the deformed tensile specimens of sand-cast (a) AZ61LS and (b) AZ61HS at different temperatures at a strain rate of 5×10^{-4} s^{-1}. The error bars were calculated using the standard error (SE) estimation method.

1.15±0.03 at the gauge (deformed part) regions. Considering the associated errors, there is no notable elongation of the grains. This is also true for all alloys (Fig. 4.32).

Fig. 4.35 shows the variation of grain sizes of the alloys after failure at all temperatures investigated as a function of e_f. The largest e_f-values are associated with the largest grain sizes, this is to be expected since the e_f directly relates to the time available for grain growth and also the largest elongations tend to occur at higher temperature, where grain growth is fastest. It was shown earlier that strain hardening regions in the flow curves are extended at higher temperature. The extent of grain growth is consistent with the observed hardening of the flow curves. A more extended strain hardening region retards the onset of plastic instability and improves e_f. But, particularly at 450 °C, where the grain growth is largest, e_f is slightly lower than that of 400 °C. The decrease of m due to the grain growth reduces the plastic stability of flow and adversely affect e_f. However, even where grain growth is similar, as highlighted for AZ31LS and AZ31HS at 350 °C, e_f can be very different suggesting grain growth is not the dominant factor controlling failure.

To understand the effect of aluminium and manganese addition, grain sizes in the as-rolled and deformed condition (both in the grip and gauge regions) are shown in Fig. 4.36 for two different temperatures. It is evident that grain growth at 350 °C is similar in both the grip and gauge regions. The effect of DGG is more pronounced at 450 °C. Also, the manganese addition does not have any influence on growth kinetics (c.f. AZ31LS and AZ31HS or AZ61LS and AZ61HS). On the other hand, the addition of more aluminium increases the growth of grains in the gauge region. This is the opposite effect to that usually expected for solute addition, when adding solute reduces grain growth rate by increasing drag opposing boundary migration (Humphreys and Hatherly, 2004). However, in the present work, it is likely

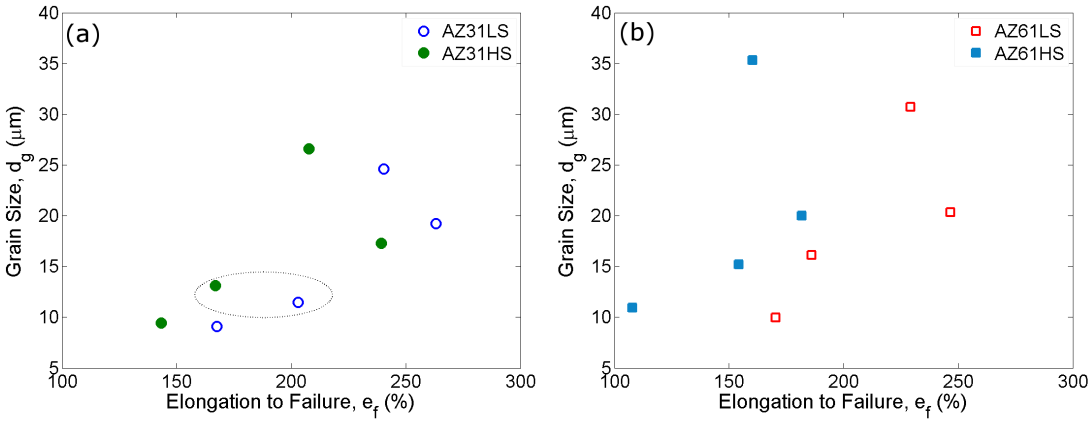

Figure 4.35: The average grain sizes in the gauge regions (d_g) of sand-cast (a) AZ31LS and AZ31HS and (b) AZ61LS and AZ61HS, deformed between 300 and 450 °C at a strain rate of 5×10^{-4} s^{-1}, plotted as a function of the elongation to failure (e_f) of the alloys. A dashed circle is drawn to show the growth data of AZ31LS and AZ31HS at 350 °C.

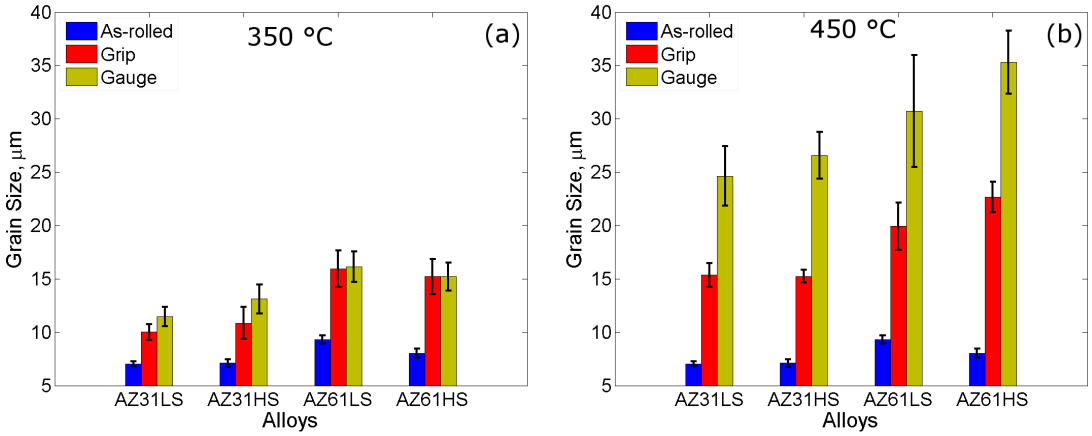

Figure 4.36: Grain sizes at (a) 350 and (b) 450 °C in the gauge and grip regions of the sand-cast alloys after superplastic testing deformed at a strain rate of 5×10^{-4} s^{-1}. As-rolled grain sizes are also included.

that all the alloys contained sufficient aluminium to saturate the solute drag effect. The addition of extra aluminium (i.e., in AZ61LS and AZ61HS) does not provide any extra relaxation, but accelerates grain growth in the gauge region probably as a result of the increased flow stress with extra aluminium.

4.3.2 Variation of Strain Rate Sensitivity during Hot Deformation

Strain rate sensitivity (m) depends on strain rate, temperature, concurrent grain growth and strain hardening and softening of flow stress (Pilling and Ridley, 1989). At a fixed temperature and strain rate condition, grain size becomes the dominating variable.

Increasing temperature typically increases m. This is evident from Fig. 4.30

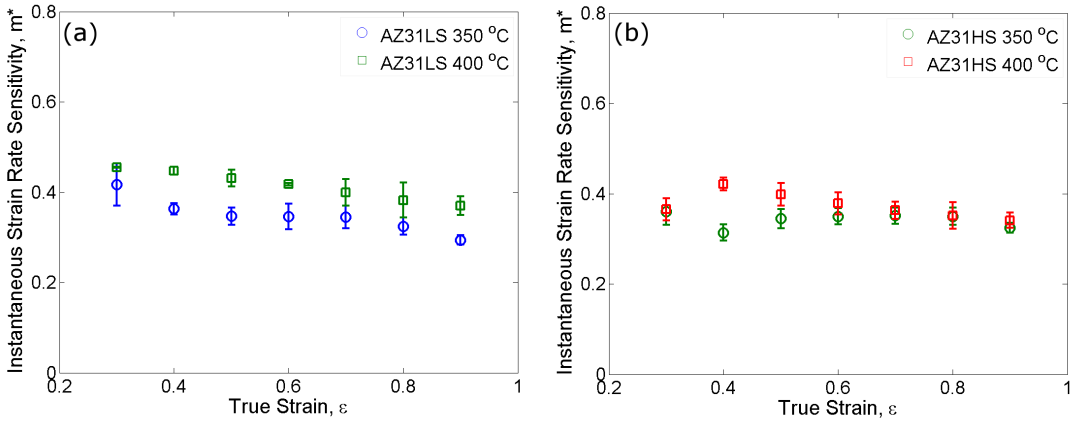

Figure 4.37: The instantaneous strain rate sensitivity (m^*) values are plotted as a function of strain for sand-cast (a) AZ31LS and (b) AZ31HS for two different temperatures (350 and 400 °C). The deformation strain rate was 5×10^{-4} s^{-1}.

showing m increasing with temperature. However, at 450 °C, a decrease in m is observed. From the examination of grain growth in the previous section, it is obvious that extensive growth of grains at 450 °C is responsible for the drop in m. From literature, it is confirmed that a decrease in initial grain size increases m (del Valle and Ruano, 2006; Figueiredo and Langdon, 2009a) due to enhanced sliding of grains. However, since the initial microstructures are similar in the current study, the effect of grain coarsening appears to adversely affect m. In an Al-5.76Mg aluminium alloy, m was increased with increasing temperature at a particular strain rate but above a certain temperature, m started to decrease due to a pronounced coarsening of grains (Nieh et al., 1998). For the alloys in the current study, the observed behaviour is similar, with the critical temperature above which m starts to decrease being between 400 and 450 °C.

To understand the grain size effect during testing, specimens were deformed to different pre-set strains and grain sizes were measured and compared with the instantaneous strain rate sensitivity, m^*. In Figs. 4.37 and 4.38, m^*-values at different strains are shown for two temperatures (350 and 400 °C). The m^*-values at different strains were averaged from the repeat test results and the corresponding error bars are also shown. At 400 °C, m^* is slightly higher than that at 350 °C for the strain range shown. A trend is common at both temperatures for all alloys—m^* decreases during deformation. The variation of grain sizes at these strains is shown in Fig. 4.39. The observed grain growth can explain the observed reduction in m^* with strain.

4.4 Examination of Fractured Specimens

At a particular temperature and strain rate condition, the behaviour of all the alloys was approximately the same in the strain hardening region, except for the effect

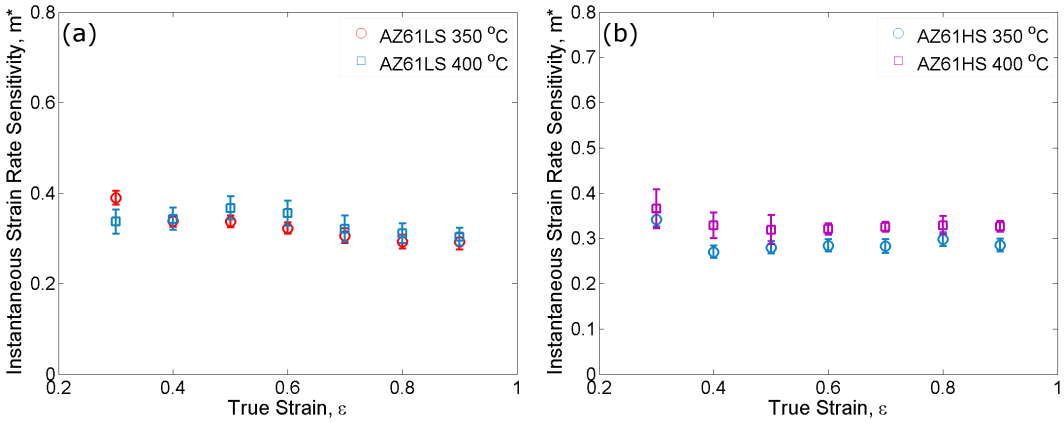

Figure 4.38: The instantaneous strain rate sensitivity (m*) values are plotted as a function of strain for the sand-cast (a) AZ61LS and (b) AZ61HS for two different temperatures (350 and 400 °C). The strain rate was 5×10^{-4} s^{-1}.

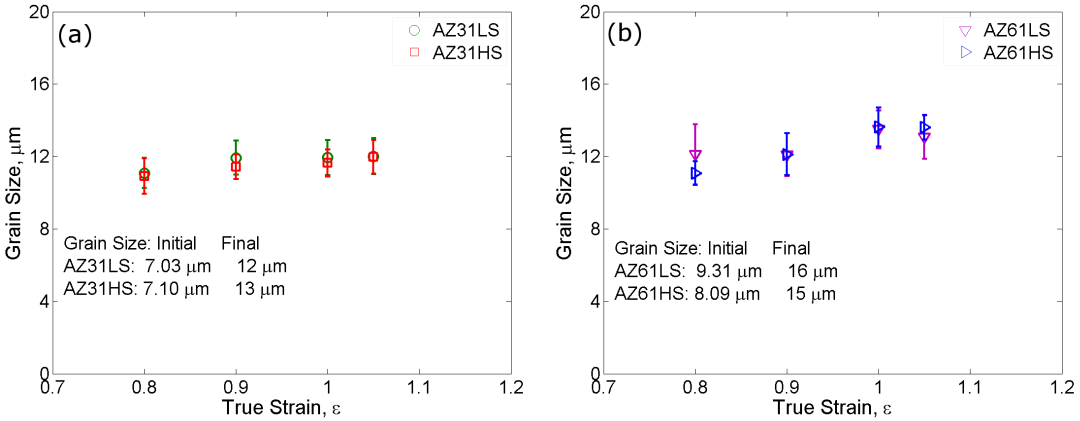

Figure 4.39: Plots of the variations of the grain size of the sand-cast (a) AZ31LS and AZ31HS and (b) AZ61LS and AZ61HS during deformation at 350 °C at a strain rate of 5×10^{-4} s^{-1}. The error bars were calculated using the standard error estimation method (Section 3.4.2).

of aluminium. At a particular temperature and strain rate, the flow curves also showed similar flow stresses. The addition of higher levels of aluminium provided a slight strength increase due to an extra solute strengthening contribution. These solute atoms, however, do not provide efficient pinning of the grain boundaries. As a consequence, all of the alloys show pronounced grain growth. The major difference between alloys lies in the flow softening behaviour and failure strain. Flow softening is often due to recrystallisation during deformation. However, in the current study, there is no evidence of recrystallization during deformation; rather flow softening may be explained by simultaneous grain growth and, as will be shown later, cavitation. In this section, an initial examination of failed specimens is reported. This suggests cavitation is critical in controlling failure and a detailed study of cavity formation and growth is presented in chapter 5.

The micrographs of AZ31LS and AZ31HS in the gauge region, near to the tip, are shown in Figs. 4.40 to 4.43. Two distinguishable features are observed from these micrographs. The failure modes of the alloys vary with temperature. At 300 °C, a very low level of cavitation is observed in all alloys and at any other temperature, a significant number of cavities is observed. At 300 °C, a low m provided the least plastic stability of flow and a neck formation was inevitable. On the other hand, as the temperature increased, increased m gives better resistance to neck propagation and the failure occurred by cavity growth and coalescence. However, it is not possible to quantify whether the cavities were grown from a single site or they were coalesced to form a larger cavity. This will be considered in the next chapter. In this section, the discussion is limited to the effect of temperature.

In Figs. 4.40 to 4.43, there is no indication of stringer-like cavities. Except at 300 °C, the cavities are large and appear coalesced in clusters. Also, the shapes of the cavities appear similar and are elongated along the tensile axis. Coalescence of cavities appears to also occur along the stress axis. Both large and small cavities are found and they seem to be located randomly at the grain boundaries. As discussed in the next chapter, a higher stress is required for formation of a cavity. Therefore, in the specimens deformed at lower temperature, more cavities are expected. However, from the micrographs, it is clear that at 300 °C, the size of the cavities is small. One obvious reason is diffusion. At 300 °C, reduced diffusional activity may not allow the growth of the cavities to a detectable size.

With the increase of temperature, it is expected that mobility of the vacancies increases resulting in a higher vacancy flux into the already developed cavities. Thus, at higher temperature, cavities become comparatively large. In Chapter 5, it will be shown that initial cavity growth is controlled by diffusion, which is obviously temperature dependent. Therefore, at elevated temperature, the higher growth of cavities is not surprising. For an AZ31 alloy with 0.30% manganese, Lee and Huang (2004)

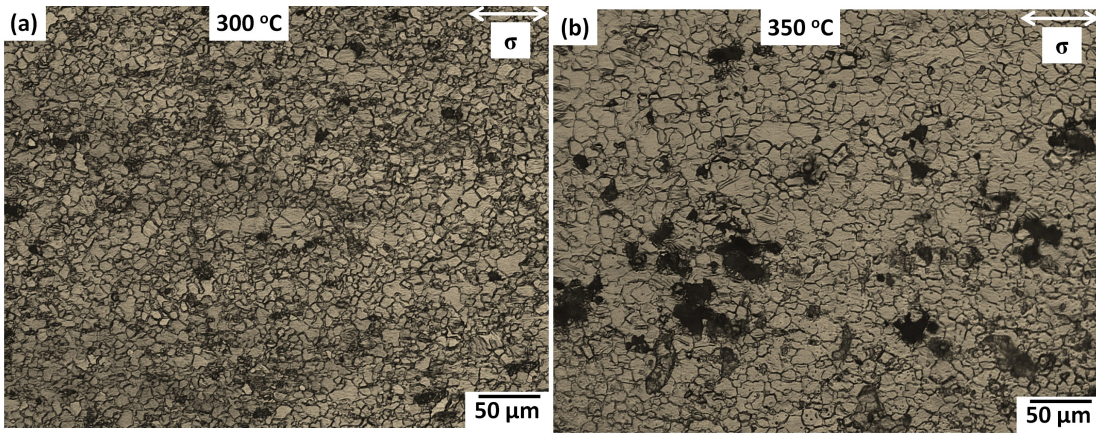

Figure 4.40: The optical micrographs from the gauge section of the sand-cast AZ31LS deformed at (a) 300 and (b) 350 °C at a strain rate of 5×10^{-4} s^{-1} showing the cavities.

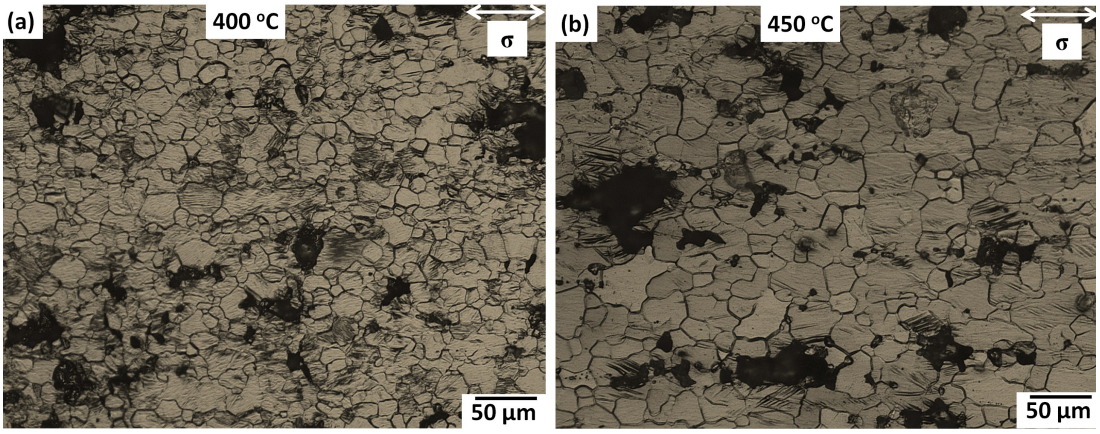

Figure 4.41: The optical micrographs from the gauge section of the sand-cast AZ31LS deformed at (a) 400 and (b) 450 °C at a strain rate of 5×10^{-4} s^{-1} showing the cavities.

observed growth of the cavities was accelerated at higher temperature. The growth of cavities, if initially diffusion dependent, would also depend on total grain boundary area available to provide rapid diffusion pathways along grain boundary.

For a 1420 aluminium alloy, Ye and co-workers (2009) observed cavity growth initially occurred at the coarser and elongated grains (grown during deformation). There was no information about the second phase particles in the microstructure and they considered grain boundary triple points as the nucleation sites of cavities. However, for the current alloys, no preferential cavity formation was observed at the grain boundaries of large grains (Fig. 4.44). The cavities are found at the boundaries of grains of different sizes and larger cavities are extended over few grain boundaries. A detailed study of cavitation that explains these observations is reported in the next chapter.

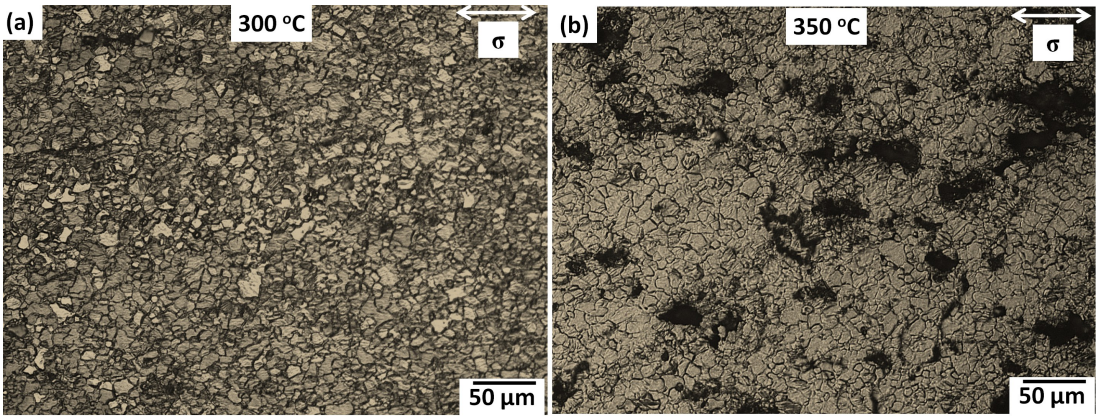

Figure 4.42: The optical micrographs from the gauge section of AZ31HS deformed at (a) 300 and (b) 350 °C at a strain rate of 5×10^4 s^{-1} showing the cavities.

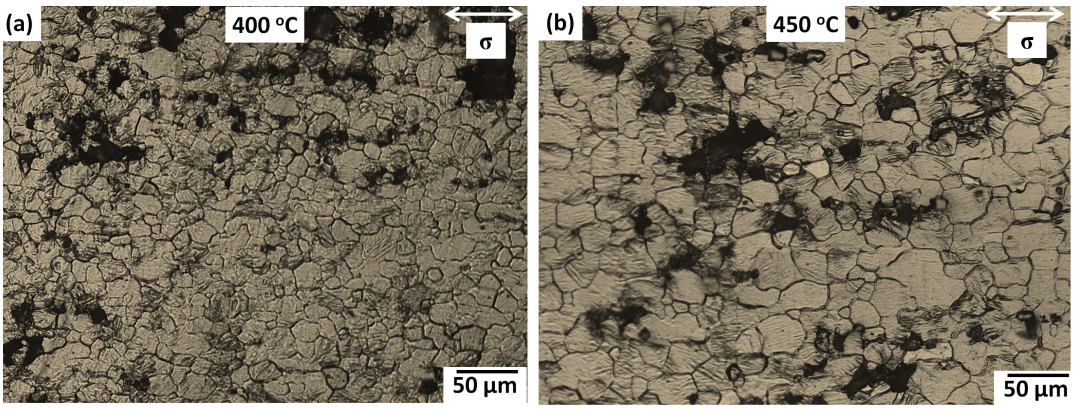

Figure 4.43: The optical micrographs from the gauge section of AZ31HS deformed at (a) 400 and (b) 450 °C at a strain rate of 5×10^{-4} s^{-1} showing the cavities.

4.5 Summary

- Hot rolling of the as-cast alloys refined the microstructure and a homogeneous grain structure (<10 μm) was obtained for all alloys. A typical basal texture was developed during rolling.

- All alloys contained Al-Mn particles of varying amounts depending on composition. The volume fraction of these particles was higher for the high manganese alloys. Also, increased manganese content led to a greater range of particle sizes.

- Flow stress of the alloys decreased with increasing temperature. Addition of solute aluminium showed a prolonged strain hardening to higher strain levels but this was a small effect. A marked difference was found in the strain softening regions attributed to cavitation.

- The activation energy for deformation was close to that for grain boundary

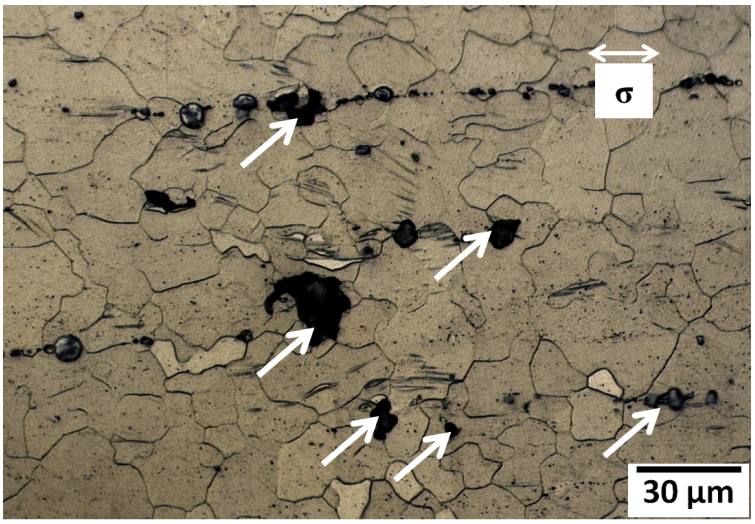

Figure 4.44: An optical micrograph of AZ31HS showing the positions of the cavities deformed up to $\varepsilon = 0.80$ at 350 °C at a strain rate of 5×10^{-4} s^{-1}.

diffusion in all alloys and a single mechanism of deformation was identified. The observation that stress exponent (n) values were between 2.5 and 4, the activation energy was close to that for grain boundary diffusion and no grain elongation was observed during deformation are consistent grain boundary sliding, as the dominating mechanism of deformation.

- Strain rate sensitivity, m, was reduced slightly during testing due to the growth of grains. Aluminium was identified as influencing m by the analysis of variance which is likely to be an effect of solute segregation.

- Grain growth was observed the extent of which was dependant on temperature. The manganese content apparently did not have any effect on grain growth. However, additional aluminium was found to accelerate growth kinetics in the gauge region probably due to slightly increase in flow stress with more aluminium.

- Elongation to failure (e_f) of the alloys was increased with temperature up to 400 °C. But, a further increase of temperature reduced e_f due to reduced stability of flow by extensive grain growth which restricted efficiency of sliding. Addition of aluminium did not have any significant effect on e_f. But, manganese addition adversely affected e_f by promoting cavitation. This is investigated in more detail in the next chapter.

Chapter 5

Cavity Controlled Failure Mechanism

In the preceding chapter, it was concluded that the failure of the alloys occurred predominantly, except at 300 °C, by the formation of cavities. Cavitation leads to flow softening of the alloys during deformation. At different temperatures, different fractions of cavities were observed. Variation in particle content was identified as the major difference among the alloys in terms of cavity formation. At 350 °C, cavitation was observed as the dominant failure mode and dynamic grain growth (DGG) occurred to a similar extent in all alloys. Consequently, the former remained as an explanation for differences in behaviour. Therefore, a detailed study on cavitation was performed at this temperature at a constant strain rate of 5×10^{-4} s^{-1} on the chill-cast alloys having similar compositions to the sand-cast alloys. The alloys were deformed to pre-set strains of 0.80 to 1.05 and a study of cavitation was carried out using optical, scanning electron microscopy (SEM) and X-ray micro-tomography (μCT). This chapter focuses on the cavity formation sites, growth mechanisms of cavities and factors promoting cavitation.

5.1 Cavity Formation Sites

Cavity formation sites were investigated qualitatively and quantitatively. In this section, a qualitative description of the observed cavity formation is presented.

SEM images of AZ61HC, deformed to different pre-set strains—ranging from 0.80 to 1.05—at 350 °C under a constant strain rate of $5 \times 10^{-4}\,s^{-1}$ are shown in Fig. 5.1. These micrographs show the development of the cavities in the gauge regions, in the unetched SEM images, close to the failed surface. Several characteristics are common at all strains. There are some single cavities which appear close to the particles (marked A). However, a similar number of isolated cavities is observed which

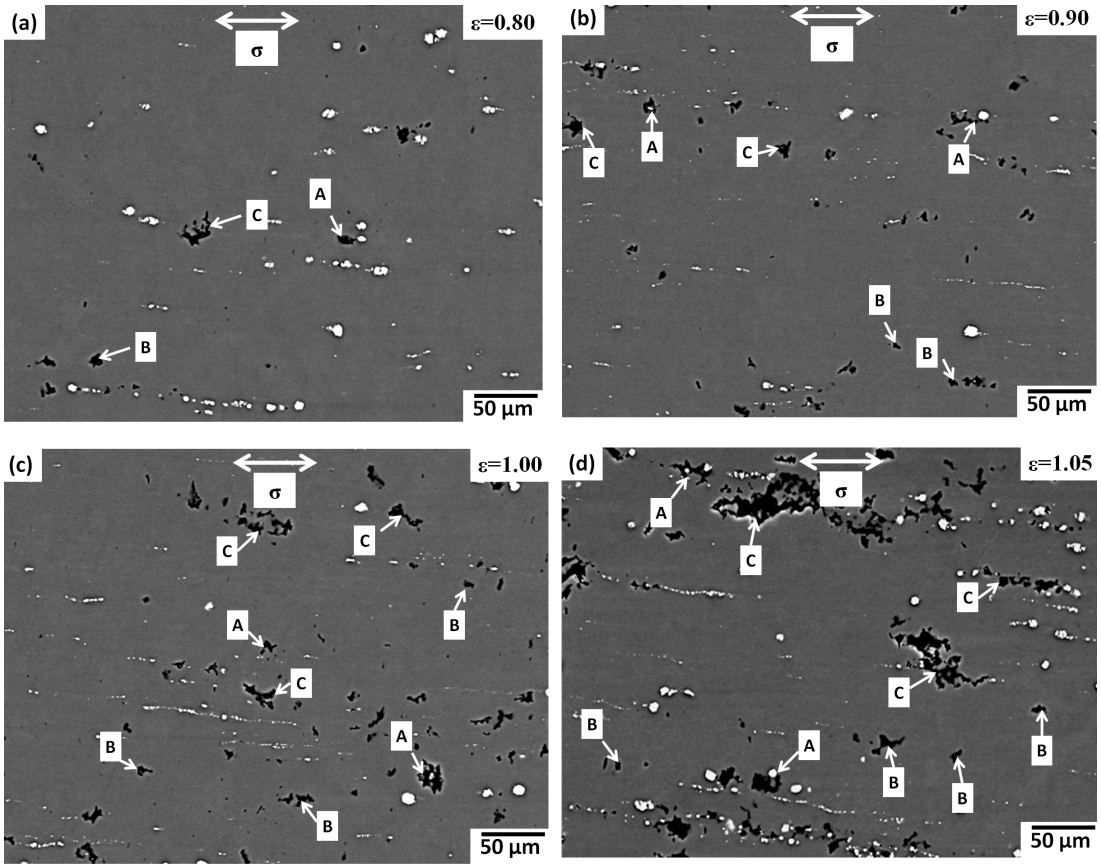

Figure 5.1: SEM images of the gauge surfaces of AZ61HC pre-strained to (a) 0.80, (b) 0.90, (c) 1.00 and (d) 1.05 at 350 °C at a constant strain rate of $5 \times 10^{-4}\, s^{-1}$. Cavities are marked A if they are close to any particles or B if they are located far from the particles. Large coalesced cavities are marked C. Tensile axis (σ) is shown by the arrow.

are not apparently formed close to any particles (marked B). With the increase of strain, more coalesced cavities are developed in the microstructure (marked C). It is obvious from these micrographs that the number of cavities is increased during deformation. The existence of small cavities, even at the strain of 1.05, is attributed to the continuous nucleation of cavities during deformation. SEM observation leads to the suggestion that particles act as a source of formation of cavities, but other irregularities may as well be susceptible sources of cavitation since a large fraction of cavities are not associated with any particles.

Fig. 5.2 shows SEM images of AZ61LC strained to 0.80 and 0.90. Several cavities are formed near a region of large, broken and agglomerated particles (marked 1). Also, a small number of particles are located close to a large cavity (marked 2). This cavity may form by the early coalescence of the closely spaced cavities, which then may grow as a single cavity. Fig. 5.2b also shows a globular shaped cavity appearing close to several particles (marked 3). Also, a cavity can be seen to grow between two particles.

Fig. 5.3 shows SEM images of two specimens of AZ61LC deformed to the strains of

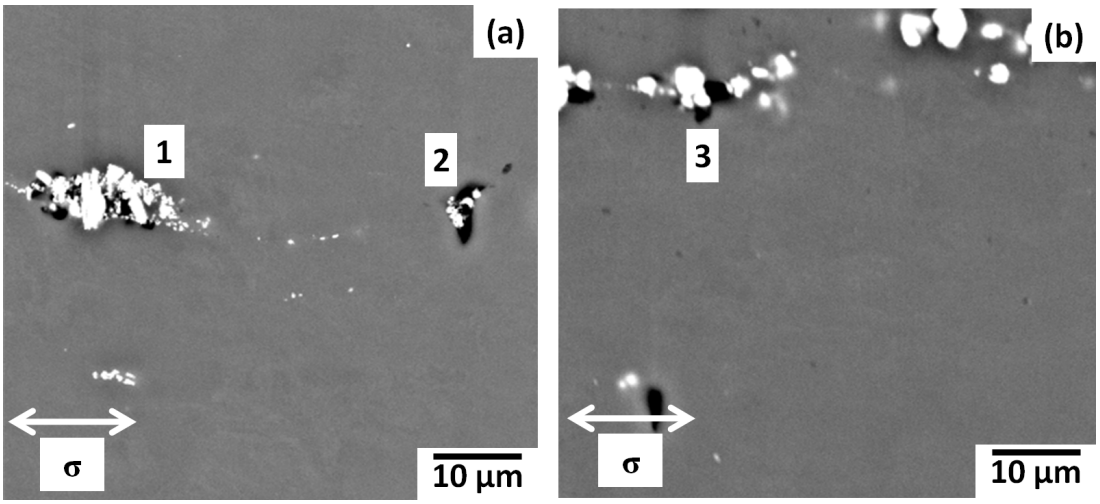

Figure 5.2: SEM images of the gauge surfaces of AZ61LC pre-strained to (a) 0.80 and (b) 0.90 at 350 °C at a constant strain rate of $5 \times 10^{-4}\, s^{-1}$. A few small cavities are formed in an agglomerated particle region (marked 1). A few small particles are located close to a large single cavity (marked 2). A globular shaped cavity has formed near to a large particle (marked 3). Tensile axis (σ) is shown by the arrow.

1.00 and 1.05. In Fig. 5.3a, approximately half of the cavities were developed close to the particles. However, there are still some cavities which do not have any particles in the close proximity. In Fig. 5.3b, a very large coalesced cavity is apparently formed from a small number of closely spaced particles. Also, similar to the earlier micrographs, half of the cavities do not have any particles attached to them. This implies that a particle may not be the only source acting in assisting in the nucleation of a cavity. The occurrence of the clustering of particles contributes to early joining of small cavities, to form a large cavity. Therefore, the presence of particles can be considered as a source of formation of cavities during deformation, but there is still a doubt about the proportion of cavities truly nucleated from particles.

It is also clear that the size of the particles, close to the cavities, vary. This suggests that either different sizes of particles are able to assist in formation of a cavity or some other mechanisms may be operating during nucleation and growth of a cavity.

Images from AZ31LC and AZ31HC are not shown since qualitatively they show the same behaviour as the AZ61 alloys discussed here.

5.2 Quantification of Cavities

From the specimens deformed at 350 °C to different pre-set strains—ranging from 0.80 to 1.05—at a constant strain rate of $5 \times 10^{-4}\,\mathrm{s}^{-1}$, 20 SEM BSE images for each condition for each alloy were acquired at ×250 magnification at the same brightness and contrast level and analysed using ImageJ to quantify cavities (see Section 3.4.3).

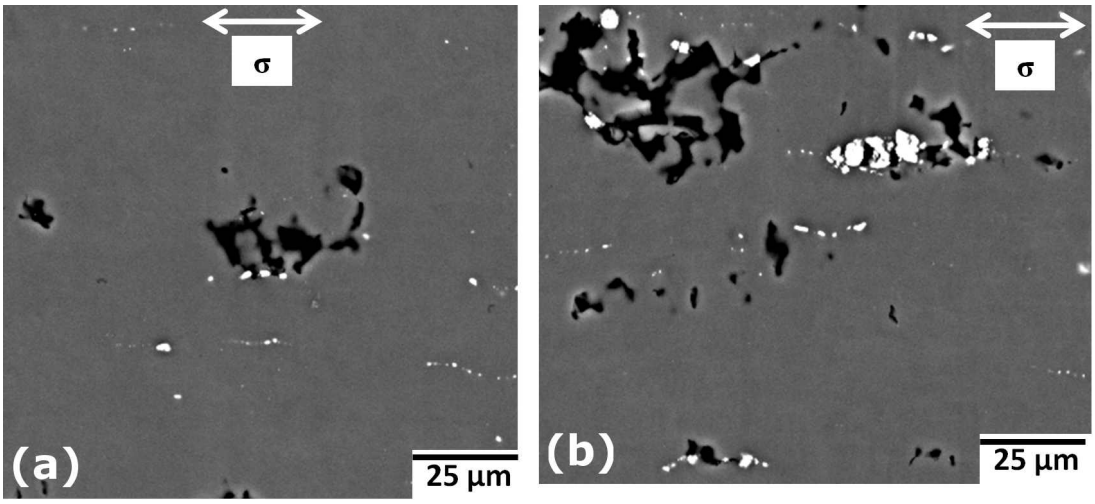

Figure 5.3: The development of the cavities at strain of a) 1.00 and b) 1.05 for AZ61LC at temperature 350 °C deformed at a strain rate of $5 \times 10^{-4}\, s^{-1}$. Tensile axis ($\sigma$) is shown by the arrow.

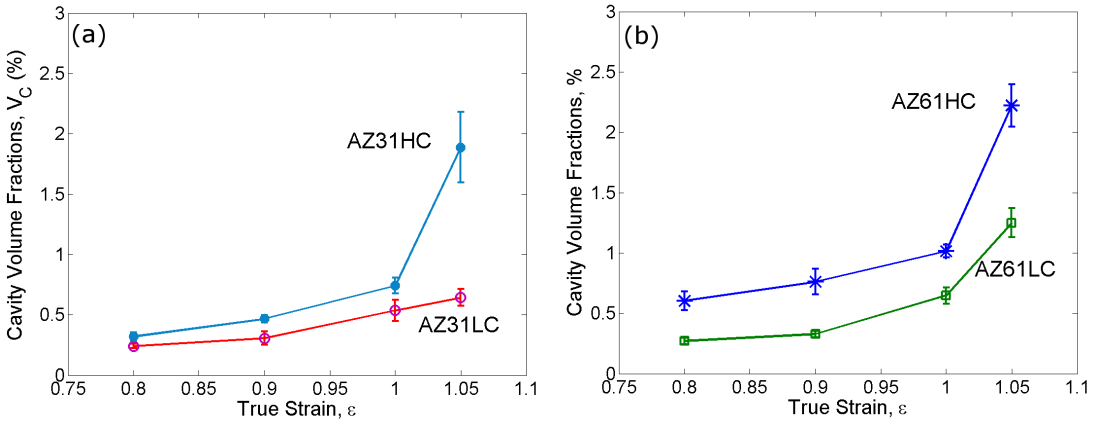

Figure 5.4: Plots showing cavity volume fraction (V_c) at different strains for (a) AZ31LC and AZ31HC and (b) AZ61LC and AZ61HC. Error bars are produced from standard error (SE).

Due to resolution limitations inherent in the magnification used, any cavity size less than 1.50 μm was ignored. A total of 70 mm^2 surface area was investigated for each specimen to obtain sufficient number of cavities to be statistically valid.

Fig. 5.4 shows the cavity volume fractions (V_c) at different strains. It is clear from the plots that in AZ61HC, containing the largest fraction of particles, cavities are developed at a higher rate followed by AZ31HC (containing the second largest fraction of particles). In the strain range from 0.80 to 1.00, the volume fractions of cavities are less than 0.75%, which increased rapidly at $\varepsilon = 1.05$. The largest V_c observed is approximately 2.1% at $\varepsilon = 1.05$ for AZ61HC. The low manganese alloys (AZ31LC and AZ61LC) show a fairly similar tendency for cavity development, except at $\varepsilon = 1.05$ where AZ61LC contains a higher cavity fraction.

From the V_c plot, the failure mode of the alloys cannot be clearly revealed, since

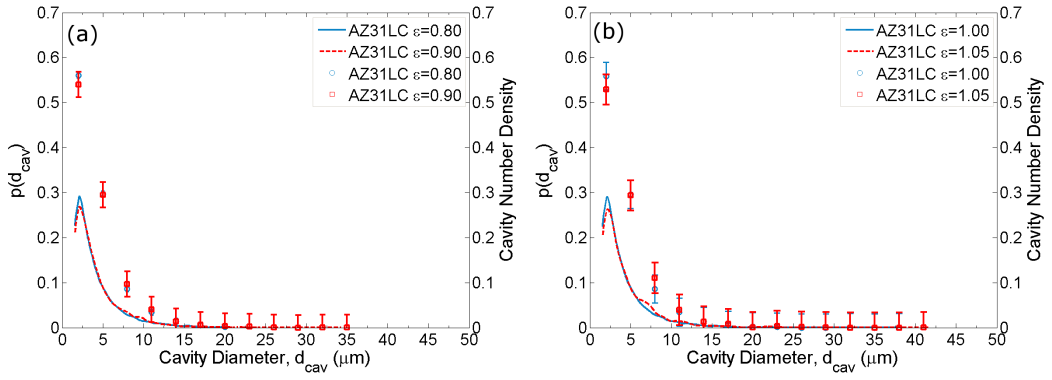

Figure 5.5: Plots of probability distribution functions of cavity diameter (d_{cav}) of AZ31LC at different strains of (a) 0.80 and 0.90 and (b) 1.00 and 1.05 deformed at 350 °C at a strain rate of 5×10^{-4} s^{-1}. Normalised fraction of number of cavities are also included.

the cavity volume fractions appear to be low, even at $\varepsilon = 1.05$. But, it is also apparent that after $\varepsilon = 1.00$, the rate of cavity growth is increased substantially and very rapid coalescence of cavities has taken place. The coalescence of the cavities eventually leads to the failure of the material even after a small further increment in strain. Also, the distribution of cavities is not uniform throughout the gauge section. More cavities were observed near to the fracture surface.

The cavity size distributions are shown in Figs. 5.5 to 5.8. At $\varepsilon = 0.80$, AZ31LC has most of its cavities in the range 3 to 7 μm (Fig. 5.5) and further deformation shifts the peak slightly to a larger size. An important feature of the plotted distributions is that at all strains (except 0.80) there are a small number of cavities which have grown extensively (>20 μm). The number of these larger cavities is increased with straining. With the exception of a few larger cavities, the cavitation trend in this alloy is similar at all strains. The major difference is observed in the 5 to 10 μm size range and at the 25 to 40 μm size range. Approximately 70 to 72% of the cavities are less than 5 μm at all strains and 5 to 7% of the total cavities belong to a size greater than 10 μm.

In AZ31HC (Fig. 5.6), most cavities are in the size range 3 to 8 μm up to a strain of 1.00, but many cavities have considerably increased in size at $\varepsilon = 1.05$. A small number of cavities have grown extensively up to 30 μm at all strain levels with more coalesced cavities at strains of 1.00 and 1.05. The peak is shifted by few microns to the larger size end with increasing strain. The major difference between this alloy and the low manganese variant (AZ31LC) lies in the number of the cavities. The higher manganese variant, having a comparatively higher number of particles, has formed more cavities. Also, the sizes of the cavities vary over a wider range than in AZ31LC.

In AZ61LC (Fig. 5.7), most cavities were found within the range 3 to 6 μm at $\varepsilon = 0.80$, and during deformation the size is increased. Cavities are approximately

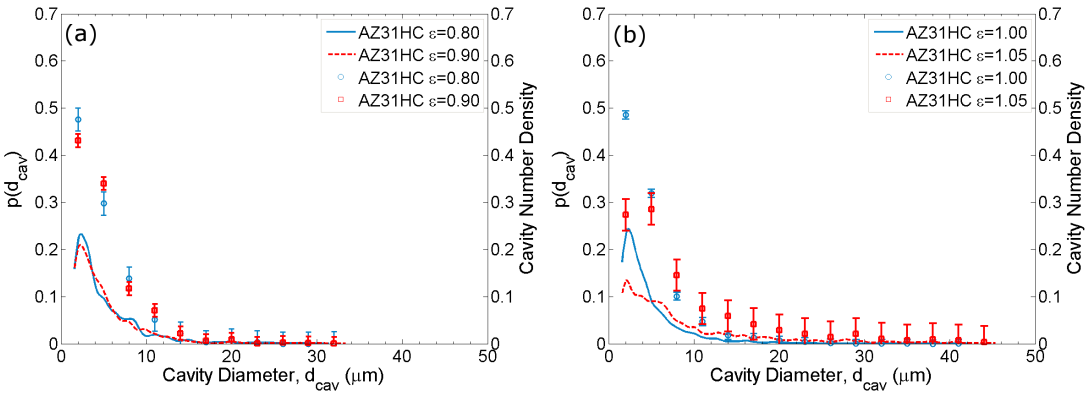

Figure 5.6: Plots of probability distribution functions of cavity diameter (d_{cav}) of AZ31HC at different strains of (a) 0.80 and 0.90 and (b) 1.00 and 1.05 deformed at 350 °C at a strain rate of 5×10^{-4} s^{-1}. Normalised fraction of number of cavities are also included.

10 to 12 μm in size at $\varepsilon = 1.05$. Up to the strain of 0.90, the maximum cavity size is limited to 20 μm. This may be associated with the distribution of the particles in this alloy. Since particles are suspected as a potent source of cavitation, if the particles are not closely spaced, the chance of coalescence and formation of larger cavities becomes limited.

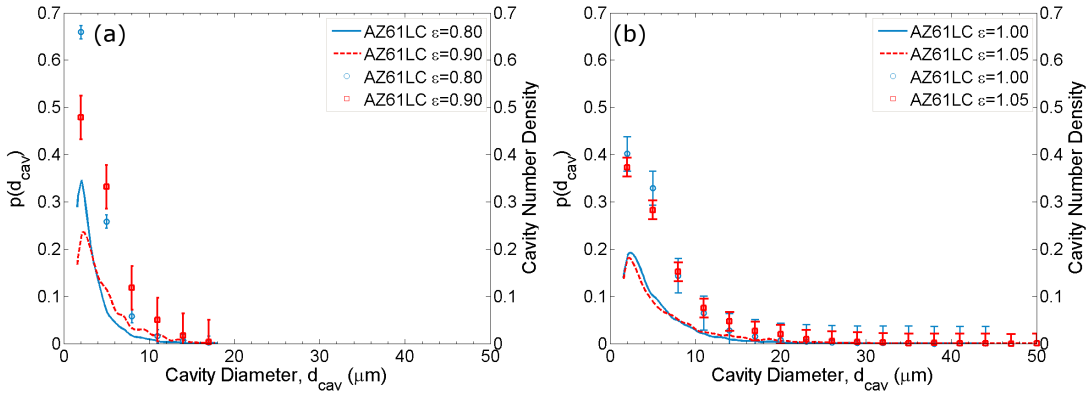

Figure 5.7: Plots of probability distribution functions of cavity diameter (d_{cav}) of AZ61LC at different strains of (a) 0.80 and 0.90 and (b) 1.00 and 1.05 deformed at 350 °C at a strain rate of 5×10^{-4} s^{-1}. Normalised fraction of number of cavities are also included.

In AZ61HC (Fig. 5.8), at $\varepsilon = 0.80$, the initial cavity size is approximately 3 to 8 μm, but with the increase of strain the cavities grow and more cavities of larger size are observed. At $\varepsilon = 1.05$, a large number of big cavities have developed and there are more cavities of 40 μm or larger in this alloy than any other. Approximately 70 to 75% of the total cavity population are less than 5 μm in size up to a strain of 1.00, whereas at the strain of 1.05, approximately 30% of the total cavities are greater than this size. The number of total cavities greater than 10 μm varies as well. 5 to 10% of the total cavities are greater than 10 μm up to a strain of 1.00, but at $\varepsilon = 1.05$ greater coalescence produced an increase of the fraction of cavities greater than 10 μm to

18%.

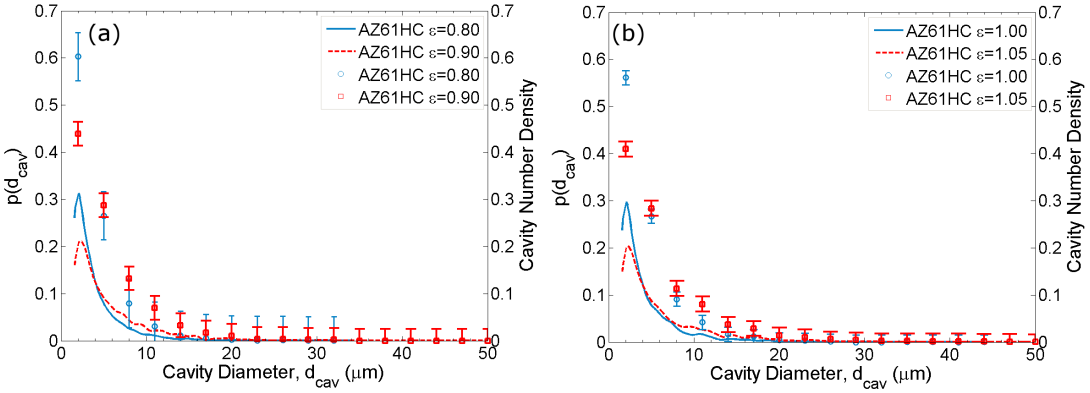

Figure 5.8: Plots of probability distribution functions of cavity diameter (d_{cav}) of AZ61HC at different strains of (a) 0.80 and 0.90 and (b) 1.00 and 1.05 deformed at 350 °C at a strain rate of 5×10^{-4} s^{-1}. Normalised fraction of number of cavities are also included.

Finally, the number of cavities developed during deformation is shown in Fig. 5.9 for AZ31LC and AZ61HC—containing the lowest and highest volume fractions of particles respectively. In both alloys, the number of cavities increases during straining but in AZ61HC the rate of increase appears to be higher than in AZ31LC.

After quantifying the cavities, inferences can be made about the effects of the alloy composition on cavitation behaviour. Formation of cavities appears to be related to the particle distribution, and the particles thus appear to have played the key role in controlling cavitation. The number of cavities is low in AZ31LC and AZ61LC—containing the smaller volume fraction of particles. Moreover, these alloys also contain a lower number of very large particles. If larger particles are responsible for earlier nucleation of cavities at low strains, such as $\varepsilon = 0.80$, the number of cavities should be small in these two alloys, at least in the earlier stages of deformation. This can be rationalised to the observation of lower number of cavities at low strains in these alloys, whereas for AZ31HC and AZ61HC, the number of cavities is comparatively higher at $\varepsilon = 0.80$, indicating a higher cavity nucleation rate. This may imply that larger particles contribute to nucleation of cavities at low strains. Moreover, large cavities are observed at all strains for all alloys, signifying the occurrence of the growth and coalescence of cavities simultaneously with nucleation.

In summary, the fraction of the total number of cavities which are smaller than 5 μm and greater than 10 μm is shown in Table 5.1. In AZ31LC, approximately 70% of the total cavities are smaller than 5 μm in size at the strain of 0.80. This proportion remains similar at $\varepsilon = 1.05$. Also, the proportion of large cavities (>10 μm) is similar at both strains. In AZ31HC, approximately 65% of the cavities are smaller than 5 μm at $\varepsilon = 0.80$ and this fraction is decreased by 14% at $\varepsilon = 1.05$. Also, the number of cavities larger than 10 μm is increased by two times between strains of 0.80 and 1.05. Approximately 70% of the cavities in AZ61LC are less than 5 μm in size at a strain of

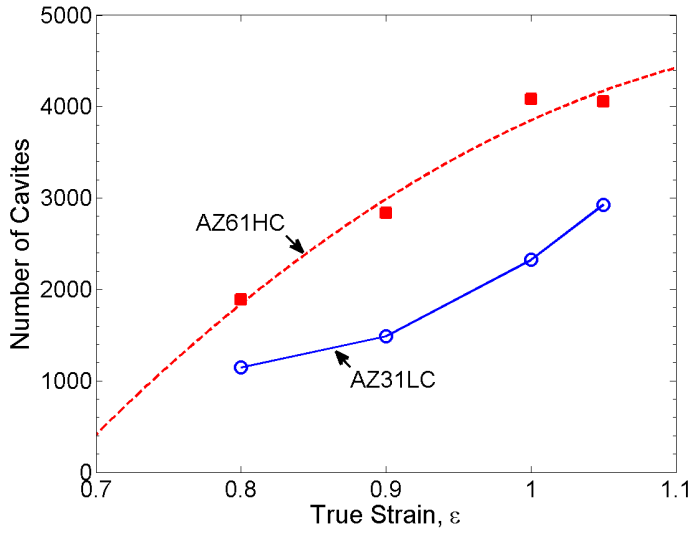

Figure 5.9: A plot showing the comparison of the total number of cavities at different strains for AZ31LC and AZ61HC deformed at 350 °C at a strain rate of 5×10^{-4} s^{-1}, the least and highest particle containing alloys respectively.

Table 5.1: A comparison chart for the fraction (percentage) of the number of cavities for different size ranges for all alloys

	$\varepsilon = 0.80$		$\varepsilon = 1.05$	
Strain	$<5\,\mu$m	$>10\,\mu$m	$<5\,\mu$m	$>10\,\mu$m
AZ31LC	72.99	5.39	71.12	5.98
AZ31HC	64.05	8.18	50.74	15.42
AZ61LC	67.13	5.59	53.56	12.72
AZ61HC	77.63	4.65	57.33	17.76

0.80, whereas approximately half of the total cavities belong to that size range at the higher strain (1.05). The number of cavities larger than 10 μm has doubled during deformation. AZ61HC contains highest proportion of the total cavity number (78%) at a size below 5 μm at $\varepsilon = 0.80$. Also, at $\varepsilon = 1.05$, approximately 60% of the cavities are less than 5 μm. Except AZ31LC, the similarity in the fractions of cavities with a size >10 μm size for all alloys suggests that a single cavity growth mechanism may be operating in all cases. In AZ31LC, it is apparent that the extent of growth is low which is attributed to the smaller volume fraction of particles in this alloy, since a presence of small volume fraction of particles means particles are less closely spaced and the chance of coalescence of cavities becomes low.

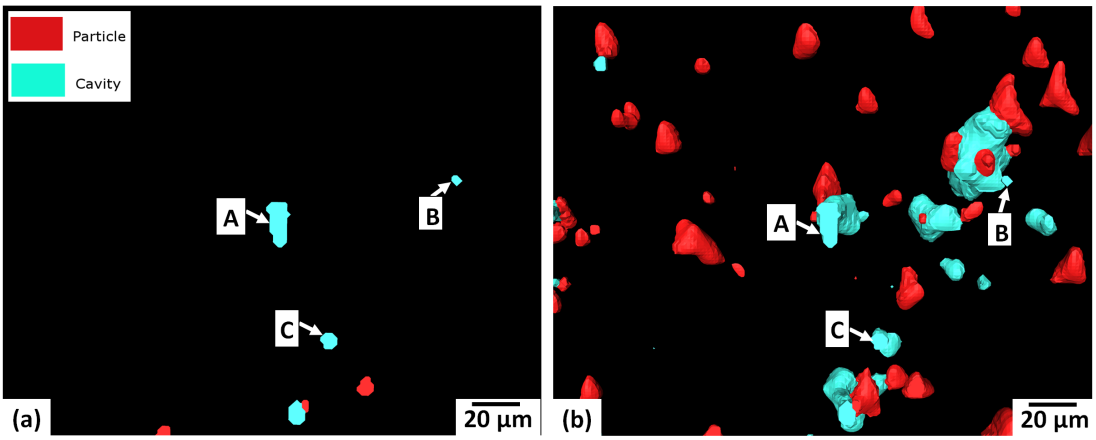

Figure 5.10: a) A 2D surface view of a random area of the 3D volume of AZ61HC deformed to a strain of 1.05 at 350 °C at a strain rate of 5×10^{-4} s^{-1}. A, B and C cavity regions are not connected with any particle. b) But, if the view is transformed into a 3D view by extending the depth of the surface, particles are found attached to the cavity regions of A and B. C is still observed to be not associated with any particle.

5.3 Determination of Particle-cavity Association by X-ray Tomography

In the SEM micrographs, approximately half of the cavities observed cannot clearly be associated with any particles. This type of traditional 2D observation can however lead to misleading identification of the cavity formation sites. A cavity may appear without any connection with a particle, but in reality it may have a close neighbourhood with a particle beneath the surface. To understand the cavitation behaviour and determine the true formation sites, X-ray micro-tomography (μCT) was carried out for the specimens deformed to different pre-set strains—ranging from 0.80 to 1.05.

The ambiguity of the particle/cavity association in a 2D section, shown in Figs. 5.1 to 5.3, can be illustrated with the aid of tomography by creating an imaginary 2D surface in the 3D volume of a specimen. Fig. 5.10 shows a single 2D orthoslice (the black background) drawn at the back of a random volume-rendered section of AZ61HC deformed to a strain of 1.05. Three cavities (marked A, B and C) do not appear to have any association with particles (Fig. 5.10a), resembling the observation made in the SEM. However, if the orthoslice is moved through the volume thickness direction, A and B cavity regions can clearly be seen to be associated with particles (Fig. 5.10b). However, cavity region C is still not attached to any particle. If the orthoslice is moved further in the thickness direction (not shown), then this region is also found to be associated with a particle region. Therefore, a 2D study alone, such as that performed in the SEM, may lead to an incorrect conclusion being drawn about the particle/cavity correlation.

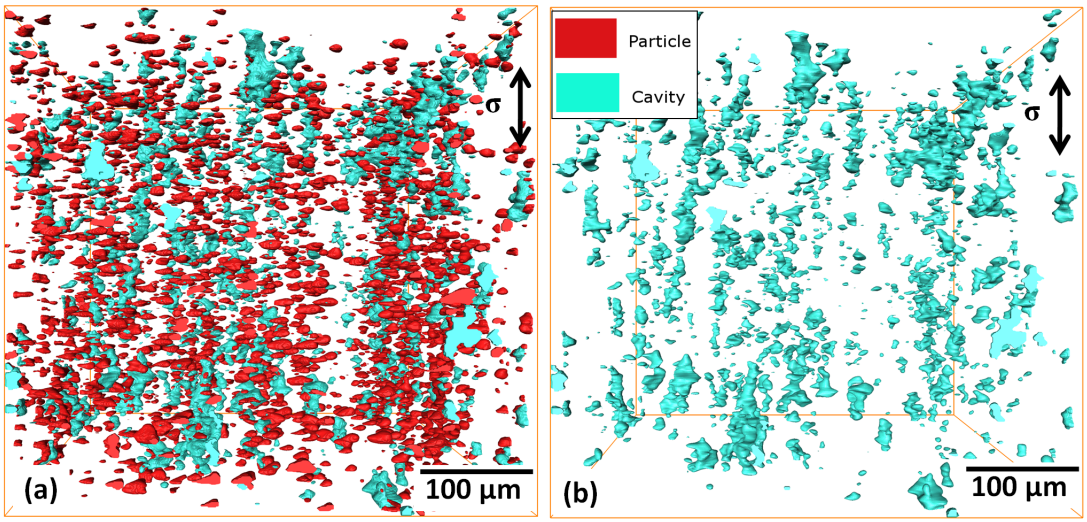

Figure 5.11: Reconstructed and rendered 3D sub-volumes of 350×430×400 μm^3 of AZ61HC deformed to a strain of 1.05 showing a) the particles and the cavities, and b) only cavities.

5.3.1 Qualitative Approach

A series of 3D images, at different enlargements, were extracted from the 3D volume of AZ31HC, strained to 1.05 at 350 °C. Fig. 5.11a shows the distribution of particles and cavities in a sub-volume of $350 \times 430 \times 400$ μm^3. The particles are found to be distributed throughout the whole volume, with evidence of some clustering and alignment of particle stringers in the rolling direction (parallel to the tensile axis (TA)). Regions of intense cavitation appear to be associated with regions containing the greatest number of particles. Like the particles, the cavities are also distributed in ill-defined stringers aligned along the TA (Fig. 5.11b). Many of the cavities have complex morphologies that may be a result of cavity coalescence. Most of the cavities are not equiaxed, and the long axis is generally approximately parallel to the TA.

Fig. 5.12a shows magnified images of some typical cavity/particle features. Two cavities (marked A and B) were observed to have emerged from the particle-matrix interface of a single particle and have grown fastest in the direction of the TA. Another cavity (marked C), formed from a particle in a plane behind that of the first can be seen to have grown towards and coalesced with cavity B. The coalescence of cavities B and C are clearly revealed in another perspective view (Fig. 5.12b). It can be seen in this figure that contact between the two cavities occurs over a small region and is in the early stages. The original morphology of the individual cavities, which is roughly cylindrical with a long axis aligned close to the TA, is preserved.

More advanced coalescence of a number of cavities can change the cavity morphology, making it more complex, and examples of this are shown in Fig. 5.13. Here, several cavities have coalesced together and formed a large cavity of irregular shape. The large cavity has a roughly oblate spheroidal morphology, but with

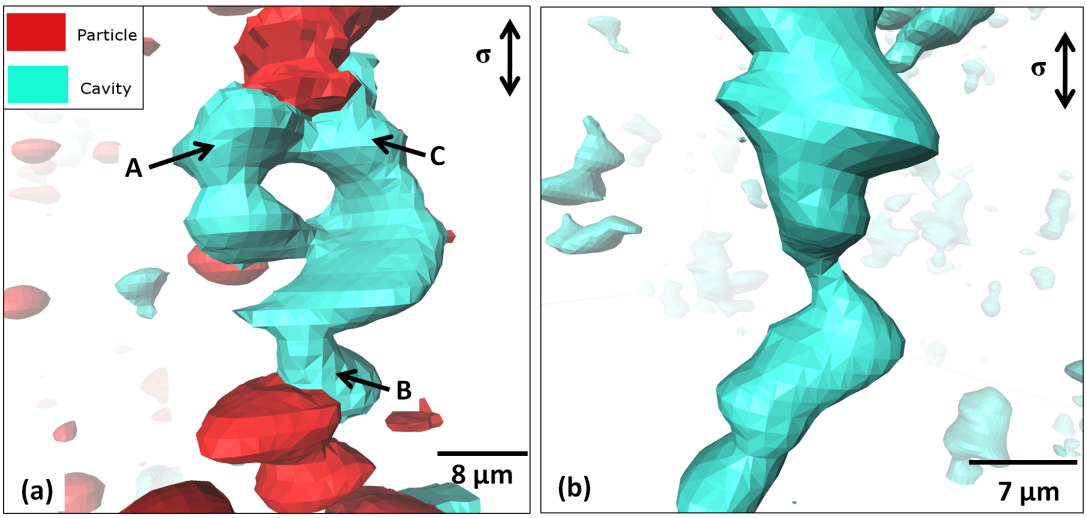

Figure 5.12: 3D rendered images of AZ61HC at $\varepsilon = 1.05$, deformed at 350 °C at a strain rate of 5×10^{-4} s^{-1}, showing a) the direction of two growing cavities and b) the initial process of coalescence of two cavities deformed at 350 °C at a strain rate of 5×10^{-4} s^{-1}. Both cavities are growing along the tensile direction (a).

several branches in different directions that presumably are remnants of the original constituent cavities (Fig. 5.13a). Other coalesced cavity regions show very different shapes, for example Fig. 5.13b shows a coalesced cavity with a very irregular surface and a ribbon like morphology.

Different sizes of particles act as the cavity formation sites. Most of the particles can be classified to be spheroidal in shape (Fig. 5.14a). Qualitatively, it has been observed that agglomerations of small particles are more potent in causing extensive cavitation than single large particles. Fig. 5.14b shows an isolated very large particle (approximately 15 μm diameter). It can be seen that a small cavity has just started to form at this particle. However, at the same strain level, agglomerations of smaller particles, such as shown in Fig. 5.15a, have led to much greater cavitation, with regions containing high cavity fractions and extensive coalesced cavities (Fig. 5.15b). The tomography data (Fig. 5.15a) suggests there is an interconnected network of particles. However, it should be borne in mind that particles that are within the spatial resolution distance (1.22 μm^3) from each other may erroneously be connected in the image rendering process. The SEM observations suggest that features such as that observed in Fig. 5.15a consist of agglomerations of isolated particles with separation less than the spatial resolution of the micro tomography. However, effectively these agglomerations do seem to behave as one very large interconnected "super-particle" and the constraint placed on deformation about such regions appears to be responsible for the high levels of local cavitation.

Given the high number density of particles capable of initiating cavitation, it is always found to be the case that the largest cavities are formed by cavity coalescence.

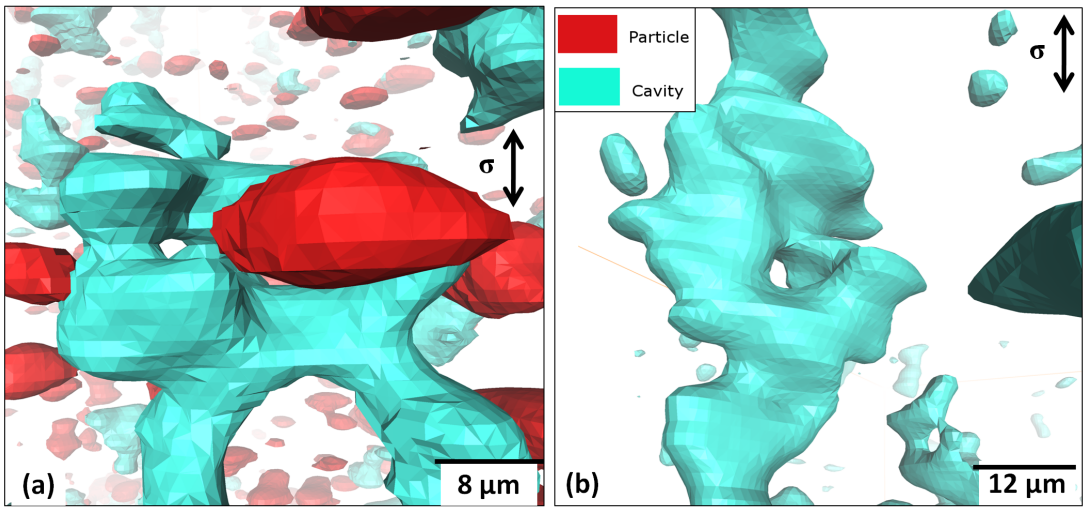

Figure 5.13: The complex shapes of the cavities of AZ61HC, deformed to a strain of 1.05 at 350 °C at a strain rate of 5×10^{-4} s^{-1}, are shown. a) The large cavity is formed by the coalescence of smaller cavities and the large cavity has some branches in different directions. b) The coalesced cavity has a ribbon like morphology.

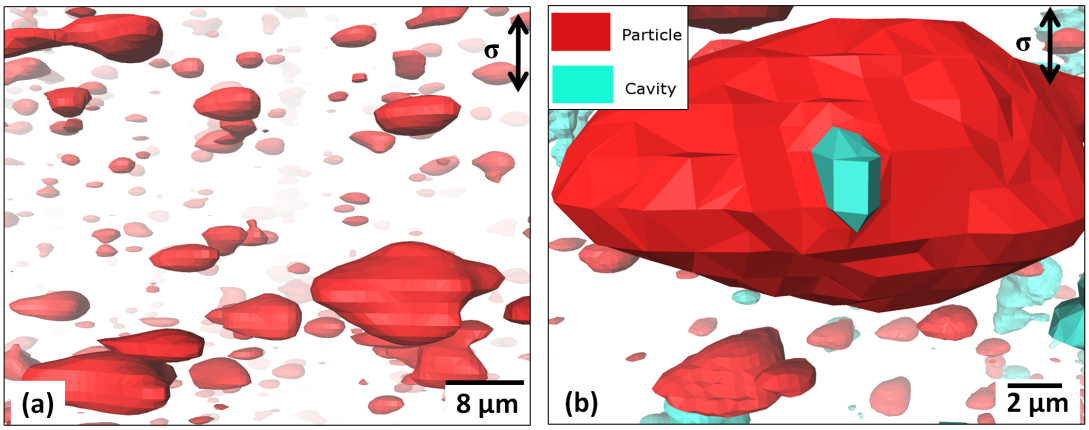

Figure 5.14: a) The shapes of the particles of AZ61HC at $\varepsilon = 1.05$, deformed at 350 °C at a strain rate of 5×10^{-4} s^{-1}, are approximately spherical. b) A large particle of approximately 15 μm in diameter has nucleated a small cavity.

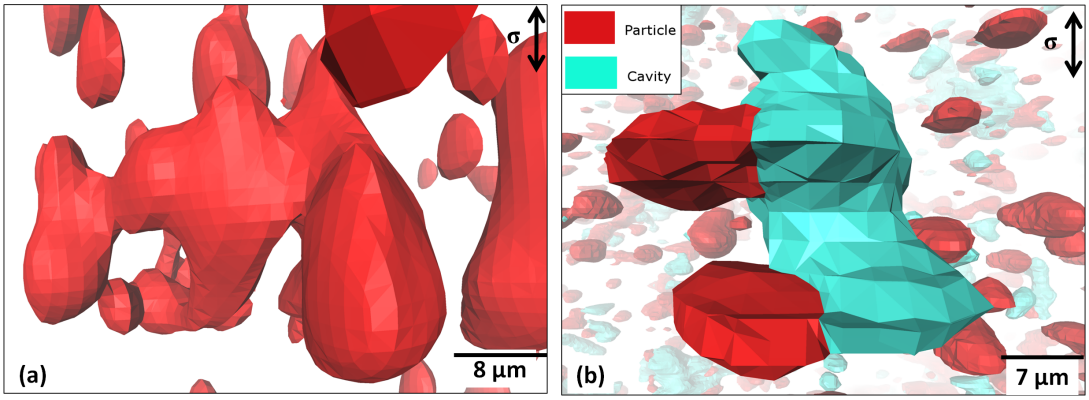

Figure 5.15: 3D rendered images of AZ61HC at $\varepsilon = 1.05$, deformed at 350 °C at a strain rate of 5×10^{-4} s^{-1}, showing a) the agglomeration effect on particles and b) the effect of agglomeration on cavitation. The closely-spaced particles appear connected due to the resolution limits of the tomography. These particles nucleated closely-spaced cavities which coalesced at low strains, forming a large cavity.

Cavity shape tends to evolve as the cavities grow. The smallest cavities are approximately spherical in shape, consistent with a diffusion controlled growth mechanism. Larger cavities tends to become elongated in the direction of the TA, indicative of plasticity controlled growth. The largest cavities have complex morphologies associated with coalescence as already discussed.

Particle/cavity contact area at the interface varies depending on the position of cavity formation with respect to the TA. If the cavity forms in a region of particle/matrix interface perpendicular to the tensile stress direction, then the cavity is formed from a small region in the interface and grows without an increase in contact with the corresponding particle (Fig. 5.16a). On the other hand, if the interface is broken almost along the tensile stress direction, then the newly formed cavity grows keeping a close contact with the particle, and with an increase in particle/cavity contact area (Fig. 5.16b).

5.3.2 Estimation of Particle and Cavity Size Distributions

To determine the diameter of the particle and cavity regions, the moment of inertia tensor of each region was computed and from the eigenvectors of these matrices (see Appendix B for details), the principal axes (a, b and c) were determined. The maximum principal axis was considered as the diameter (d_p) of a particular particle region.

From the tomography data set, a sub-volume of $500 \times 500 \times 700$ μm^3 was cropped, and the d_p of the particles were measured. This analysis considers only particles greater than 1.8 μm in size due to the resolution limits inherent in the data. Approximately 31 000 particles of various sizes were detected after refining single voxels present in the volume to reduce noise of data and the corresponding size distribution

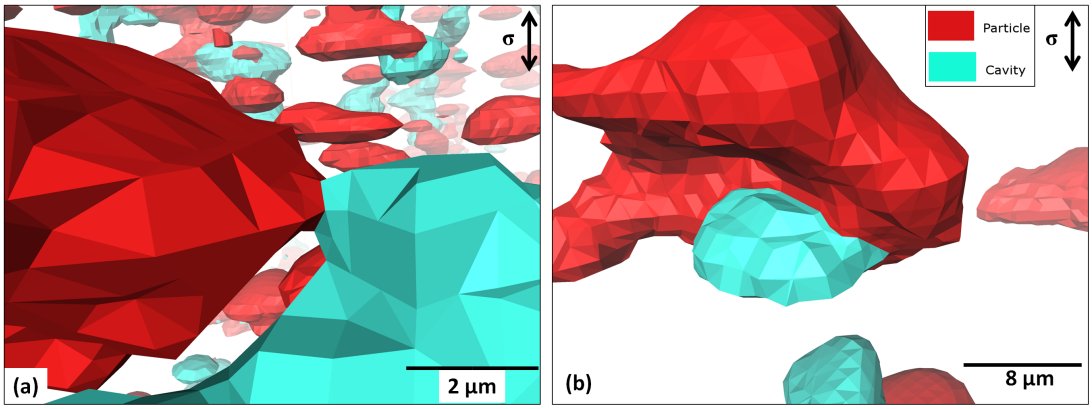

Figure 5.16: 3D rendered images of AZ61HC at $\varepsilon = 1.05$, deformed at 350 °C at a strain rate of 5×10^{-4} s^{-1}, showing particle/cavity interfaces. If cavities are formed perpendicular to the TA (a), a small contact area is maintained with the particle. On the other hand, if a cavity is formed parallel to the TA (b), the interface increases in area as the cavity grows.

is plotted in Fig. 5.17 as a probability distribution function of d_p. It is apparent from the plot that the peak corresponds to a mode d_p of approximately 3 μm, with 4% of the total particles present in the larger size range of 10 to 40 μm. These apparently very large particles are actually the agglomerated particles (Fig. 5.15). The average d_p was approximately 4 μm.

To compare the size distribution from 3D data set with the SEM data, the probability distribution function for AZ61HC, obtained from SEM data, is also included in Fig. 5.17. It is apparent that the range of occurrence of most population of size is approximately 2 to 4 μm, compared to 3 to 5 μm estimated for the SEM data. The SEM data shows that the average d_p is approximately 6 μm, compared to 4 μm calculated in tomography data. From the tomography data set, the presence of a large number of small particles is evident. Also, statistically the tomography estimation based on 31 000 particles is more valid. Therefore, the size distribution from 3D data set can be considered as the true d_p distribution for particles above the resolution limit.

From the raw data, sub-volumes of similar dimension, used in particle analysis, were cropped, and the volume fractions and size distributions of cavities were measured. The cavity volume fractions are shown in Table 5.2. At the largest strain, the cavity volume fraction approaches 1%. The cavity volume fractions appear to be too small to cause failure by cavitation, which is obviously attributed to the large gauge area scanned during μCT. All size distributions were estimated from the longest major axis of each cavity region, a similar approach applied to particle size estimation. About 19 000 cavities were detected in the specimen deformed to a strain of 1.05, while only 7500 were detected at the strain of 0.80.

The cavity size distributions at different strains are shown in Fig. 5.18. In all specimens, deformed to a pre-set strain ranging from 0.80 to 1.05, the mode of the

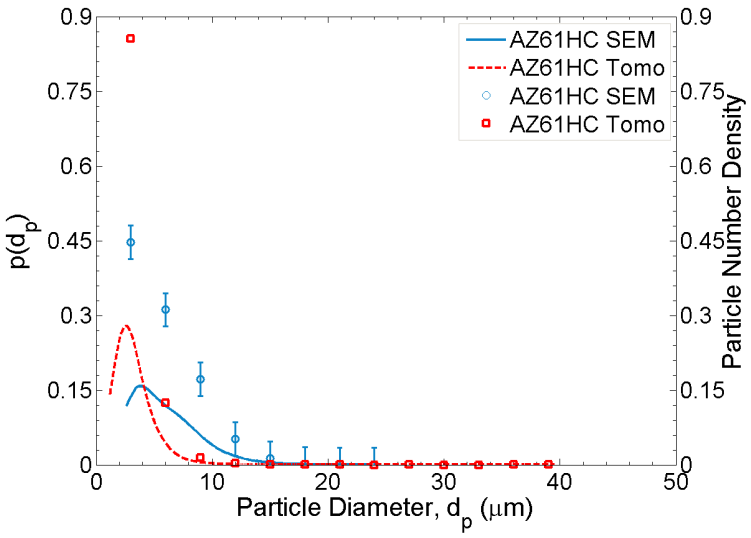

Figure 5.17: A semi-log plot of the probability distribution function of the particle diameter (d_p) of AZ61HC from the 3D data set, deformed at 350 °C at a strain rate of 5×10^{-4} s^{-1}. The peak corresponds to the maximum occurrence of sizes at approximately 2 to 4 μm. The size distribution from SEM data is also incorporated in this plot. Normalised fraction of number of particles are also included.

Table 5.2: Cavity volume fractions obtained from the tomography data at temperature 350 °C at a strain rate of 5×10^{-4} s^{-1}

Strain	0.80	0.90	1.00	1.05
Cavity Volume Fractions, %	0.18	0.47	0.49	0.92

size distribution is 3 μm. This is also revealed in the plots. In terms of proportion of cavities, almost 80% of the total cavities, in the specimen deformed to 0.80, are less than 5 μm in size, whereas 90% of the cavities belong to that size group in the specimen deformed to a strain of 1.05. This is not unexpected, since the total number of the cavities is increased by approximately two and half times during deformation (between strains of 0.80 and 1.05). The major difference observed lies in the size range of 20 to 30 μm, which is attributed to the extensive coalescence of cavities mostly due to the agglomeration of particles. At a strain of 0.80, approximately 2% of cavities are greater than 20 μm in size, while this number fraction shifts to 4% at $\varepsilon = 1.05$.

5.3.3 Methodology Developed for Particle/Cavity Association

Two methods were developed to analyse tomography data and determine the tendency for particle/cavity association: a) the spatial correlation function and b) the

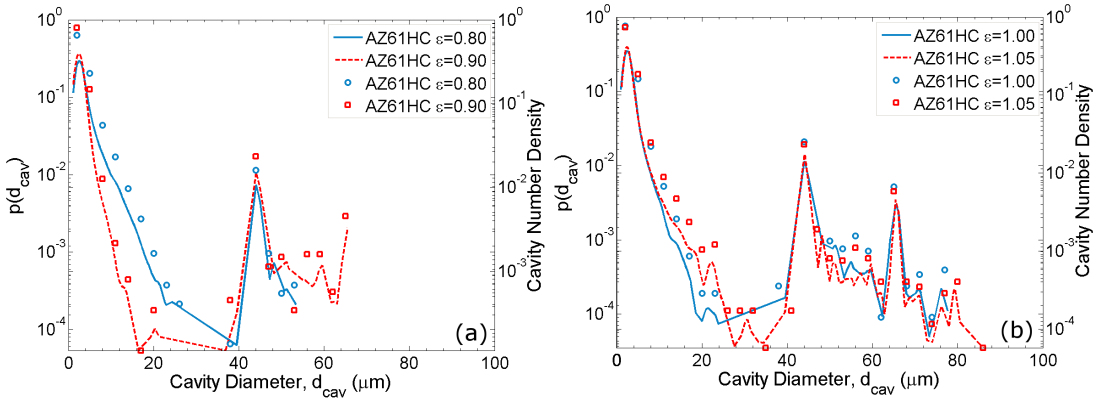

Figure 5.18: A semi-log plot of probability distribution functions of the diameters of the cavities of AZ61HC at strains of (a) 0.80 and 0.90 and (b) 1.00 and 1.05, deformed at 350 °C at a strain rate of 5×10^{-4} s^{-1}. Normalised fraction of number of cavities are also included.

particle/cavity normalised intersection distribution. Both methods were performed on the same data set since each gives distinct information. The spatial correlation function gives the distribution of spacing (or the probability of finding in a given spacing) between particle and cavity voxels and can thus be used to investigate any tendency for clustering of particles and cavities. The normalised intersection distribution is determined by measuring the intersection (overlap) between particles and cavities as the particles are artificially dilated. This provides a measure of the proximity of particle and cavity surfaces, which can be compared against that expected for a random distribution.

5.3.3.1 Spatial Correlation Function

A program was developed in Fortran (written by Prof Pete S. Bate, University of Manchester) to calculate the particles/cavity correlation function. Correlation is used in statistics to find out the linear association between two events and a correlation function can be used to get the correlation of two features as a function of distance; i.e., the relative probability of two features being separated by a given distance can be determined. Consider single regions of cavity and particle (x_c and x_p) which are separated by a vector $\mathbf{\Delta x}$ (Fig. 5.19a).

Now, the relative probability can be calculated for a given value of $\mathbf{\Delta x}$ that there is a particle and cavity with separation $\mathbf{\Delta x}$. Consider a function defined for particles, $p(x)$, which is equal to one if there is a particle at position x or zero if there is not. A similar function, $c(x)$, can be defined pertaining to cavities. The un-normalized particle-cavity correlation is given by

$$f(\Delta x) = \int_{\Psi} p(x).\, c(x + \Delta x)\, \mathrm{d}x \tag{5.1}$$

where Ψ is the spatial domain over which the integral is being evaluated. To get the normalised, relative probability of a particle cavity separation of $\mathbf{\Delta x}$, the function f needs to be divided by the product of fractions of particles and cavities. Using Fast Fourier Transform, the above mentioned convolution integral can be solved efficiently as

$$F = P.C^* \tag{5.2}$$

where F, P and C are the Fourier transforms of f, p and c, and * denotes the complex conjugate.

To interpret the result, f can be plotted as a function of radius

$$r = |\Delta x| = \left(\Delta x_1^2 + \Delta x_2^2 + \Delta x_3^2\right)^{1/2} \tag{5.3}$$

where Δx_1^2, Δx_2^2 and Δx_3^2 are the components of $\mathbf{\Delta x}$ in three orthogonal directions defined as the Euclidian distance between two points in 3D space.

5.3.3.2 Particle/cavity Normalised Intersection Distribution

To determine the fraction of particle and cavity regions in contact, a dilation and intersection checking routine was developed in Matlab. 3D arrays defining the co-ordinates of all particle and cavity voxels were first defined. After constructing the 3D arrays, particle regions were dilated by a predefined distance and a check for cavity regions intersecting the dilated particle regions was performed. The number of intersected regions was then divided by the total number of cavity regions to get normalized data for each pre-defined dilation. A schematic presentation of the steps followed is shown and explained in Fig. 5.19b.

5.3.4 Establishment of Particle-cavity Relationships

Using Matlab and Fortran routines (mentioned in Section 5.3.3), two relationships between particles and cavities were established for a sub-volume of 500×500×700 μm^3 and compared with random sets of particle and cavity regions contained in a sub-volume of same dimensions. If cavities were not associated with particles, the position of the cavities would be random. In view of this, random coordinates for the particle and cavity regions were generated in Matlab followed by tagging, region developing and analysing in a procedure similar to the one carried out for the experimental data. The sizes of the random regions were usually one to few microns depending on neighbourhood of voxel coordinates.

From the correlation plot (Fig. 5.20a), the radial distance between particle and cavity voxels is shown up to maximum distance of 50 μm. A peak was obtained at

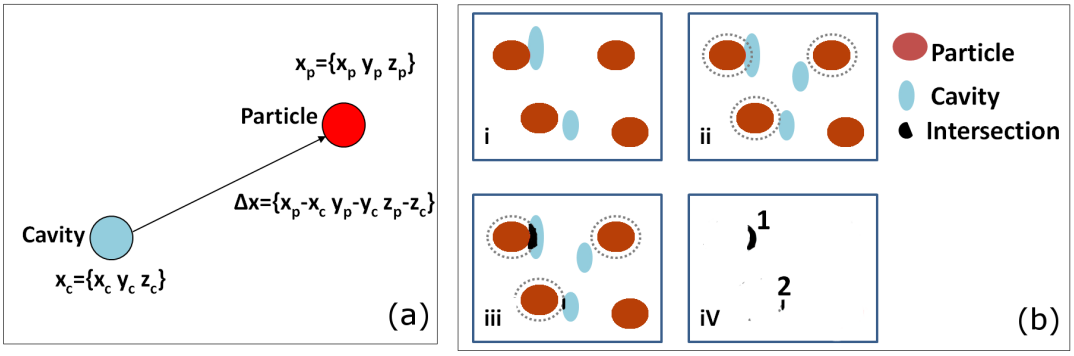

Figure 5.19: a) A schematic representation of the method applied in correlation estimation. Positions of a particle (x_p) and a cavity (x_c) in 3D space are marked and the distance, $\mathbf{\Delta x}$, between them is shown. b) A series of schematic drawings showing the steps in calculating the particle-cavity intersections by dilation: i) shows the particle and cavity regions; ii) shows the dilation of the particle regions by the dashed circles; iii) shows the intersections of the dilated particle and cavity regions and iv) shows only the intersected regions (marked 1 and 2).

a radial distance of approximately 5 to 8 μm which corresponds to the occurrence of the maximum number of pairs of voxels (of particles and cavities) separated from each other by that distance. The correlation plot does not provide the information on particle/cavity association in a straightforward way since it considers each voxel present in the sub-volume instead of regions of particles or cavities (here, the term region means a particle or cavity containing connected voxels of similar type).

To understand the origin of the peak, a particle of 3 μm and a cavity of 3 μm can be considered since the mode size of the particle and cavity regions was close to 3 μm. In this case, the distance between voxels of a particle and voxels of a connecting cavity would vary from the minimum distance between two voxels ($\sim$1 μm) to 6 μm, the distance from a voxel at the far side of the particle to that at the far side of the connected cavity. The mean separation will depend on the particle and cavity shape, but will lie between these extremes (and would be 3.18 μm for perfectly spherical particles and cavities). Given that this distance will increase for non-spherical particles and cavities, the measured peak is indicative of a preference for cavities and particles to be in close association. On the other hand, if the distribution of cavities is random, no such peak is observed; instead at 1 μm distance (minimum distance between two voxels), a minimum is formed meaning the lowest probability of occurrence at that distance. This minimum is obtained since the size of the random cavities and particles were 1 μm^3 and a particle and a cavity cannot share a single voxel. Therefore, it is plausible that the peak obtained at 5 to 8 μm distance is due to the majority of the cavities being associated with particles.

In contrast to the correlation method, the dilation-and-intersection method considers regions of particles and cavities containing more than one voxel in each type

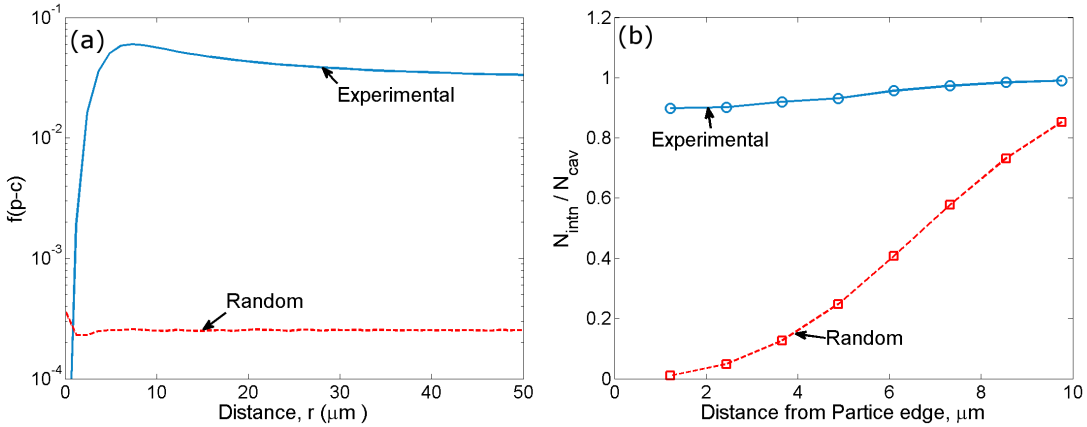

Figure 5.20: a) A semi-log correlation function ($f(p-c)$) plot showing the distribution between particle (p) and cavity (c) voxels of chill-cast AZ61HC at $\varepsilon = 1.05$, deformed at a strain rate of 5×10^{-4} s^{-1}, separated by a pre-defined radial distance, r. b) The number of overlaps of cavity and particle regions (N_{intn}) normalised by the total number of cavities (N_{cav}) in the sub-volume are shown. The dashed lines show probable distributions if the particles and cavities are randomly located in the sub-volume.

of region. According to this method, approximately 90% of the cavities (Fig. 5.20b) had their edges connected with particle edges by a single voxel distance. With an increase of distance from particle edges, the fraction of cavities attached to particles approaches unity. This implies that though some cavities (approximately 10%) were not physically attached to any particles, they were located a short distance from particles. Now, for a random distribution of cavities, a parabolic shape curve is obtained with only 1% of the total cavities at a distance of 1.22 μm from particle edges compared to the 90% intersections obtained at 1.22 μm distance in the experimental data.

Finally, only the particles with neighbouring cavities were identified in a cropped sub-volume and their frequencies were recorded for a bin width of 1 μm. The estimated number of particles truly attached to cavities (N_{p-c}) for each bin width was normalised by the number of particles (N_p) present in that size range in the cropped sub-volume. Fig. 5.21 shows two distributions of particles at the strains of 0.90 and 1.05 plotted using this methodology. At a strain of 0.90, a greater fraction of particles larger than 10 μm are associated with cavities compared to small particles (<10 μm). However, not all the large particles have connected cavities. At a strain of 1.05, however, more than 50% of the large particles are associated with cavities and the contribution to assist in cavity formation by the small particles (<10 μm) is increased by approximately four times compared to those at the strain of 0.90. These results confirm that nucleation of cavities is a continuous process and large particles generally form more cavities prior to small particles. Interestingly, this figure also shows that even at the highest strain not all the large particles form cavities.

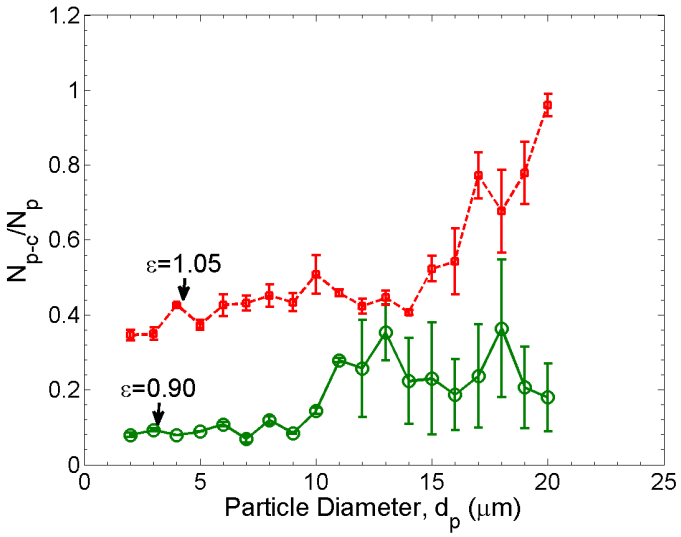

Figure 5.21: Plots of the number of particles of AZ61HC truly associated with cavities (N_{p-c}) normalised by the total number of particles (N_p) at each particle size group at the strain of 0.90 and 1.05 deformed at 350 °C at a strain rate of 5×10^{-4} s^{-1}. To obtain the sizes of particles which truly nucleate cavities, sub-volumes of 250×250×300 μm^3 dimensions were cropped off from the original volume.

5.4 Probability of Pre-existing Cavities

It is necessary to consider whether all cavities are truly nucleated during tensile deformation. In the as-rolled alloys, a small number of cavities were observed in the microstructure which are believed to be formed during large deformation from the hot-rolling as they were not observed in the homogenised microstructure. There exists an ambiguity about the sustainability of pre-existing cavities formed during the thermo-mechanical treatment. Chokshi and Mukherjee (1989a) proposed an expression for the healing time required for pre-existing cavities to sinter in the absence of any external stress, defined as

$$t = \frac{r_{cav}^4 kT}{1.6\Omega\delta D_{gb}\gamma} \tag{5.4}$$

where r_{cav} is the cavity radius, k is the Boltzmann's constant, Ω is the atomic volume, δD_{gb} is the product of grain boundary width (δ) and grain boundary diffusion coefficient (D_{gb}) and γ is the surface energy. At 350 °C, for a pre-existing cavity of diameter 1 μm, this model predicts it would require only 30 s to heal the cavity without any external stress (values of the parameters are given in Appendix A). The time required for complete healing of cavities of different radii is shown in Fig. 5.22 for different temperatures. In the current study, 20 minutes of holding time was applied to stabilise temperature in the hot-chamber prior to carrying out the tensile tests. This time should be sufficient to heal most of the pre-existing cavities

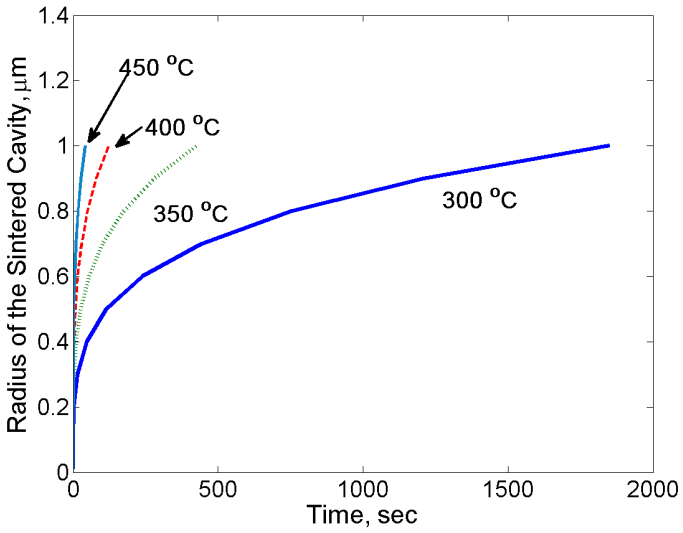

Figure 5.22: A plot showing sintering time required for different cavity radii (r_{cav}). This plot explains that a cavity of 1 μm diameter would require only 30 s to be sintered during stress-free annealing at 350 °C.

of sub-micron size. However, Bae and Ghosh (2002a) doubted about the complete elimination of pre-existing cavities by annealing and pointed out that unstable cavity shape, unfavourable surface tension conditions, etc., may hinder the complete healing. Partial elimination of the pre-existing cavities by diffusion should be able to minimize the size and frequency of pre-existing cavities. Also, during deformation, the number of cavities increases which shows a continuous nucleation trend of cavities. Therefore, it is highly likely that the cavities observed during deformation are not nucleated or grown solely from pre-existing cavities.

5.5 Nucleation of Cavities

Nucleation of a cavity occurs when a local stress developed during deformation at a microstructural irregularity fails to be accommodated rapidly (see Section 2.5.1). In the alloys investigated, cavitation has occurred mostly at the grain boundary particles. In Section 5.3.1, 3D tomographic images clearly reveal that cavities are closely associated with particles. The correlation method (Fig. 5.20a) shows a very high probability that cavities are located closely with particles. Moreover, the dilation-and-intersection method (Fig. 5.20b) measures edges-to-edge distance between particle and cavity regions and approximately 90% cavities are associated with particles. Therefore, qualitatively and quantitatively, the location of most cavities is confirmed to be close to particles. However, approximately 10% of the cavities are spaced about a distance of 2 to 8 μm from particle edges in AZ61HC. This may occur due to the probability of some cavity formation at grain boundary triple points.

Table 5.3: Estimation of critical particle diameter below which a particle does not assist in formation of a cavity at a strain rate of 5×10^{-4} s^{-1}

	Critical Particle Diameter, d_p^{crit} (μm)	
Model	30 MPa	35 MPa
Needleman-Rice	10.50	11.00
Chokshi-Mukherjee	1.00	1.10

Since SEM images of cavitation in other alloys are similar to AZ61HC, therefore, the particle/cavity association should be similar in other alloys.

From Fig. 5.21, it is evident that at a certain strain, not all particles are associated with cavities. Also, the number of the cavities increases during straining. Therefore, it is very probable that there exists a critical particle diameter (d_p^{crit}) below which a particle does not assist in cavity formation. The presence of a critical size also explains the differences in cavitation behaviour in the alloys. This supposition leads to the consideration of a critical diffusion length over which local stresses can be relaxed quickly. This maximum diffusion length required to relax a perturbation can be rationalised with a minimum size of a particle. If a particle has a size equal to this diffusion length, an incomplete relaxation occurs and a cavity is formed. Now, since the diffusion path can be either a grain boundary or the lattice itself, the value of the diffusion length varies. When grain boundary diffusion dominates, the critical diffusion length is Λ_{GB} (see Equation 2.23 on page 68). Now, if the relaxation occurs by lattice diffusion, the critical diffusion length (Λ_L) is modified following Equation 2.24.

At 350 °C, the critical particle diameter, following Needleman-Rice expression (Equation 2.23), is given in Table 5.3 using the values of the parameters from Appendix A. Table 5.3 also includes the critical particle diameter for 30 and 35 MPa; this gives the approximate critical diameter for all alloys.

These critical diameter values are three times higher than the value predicted for a fine-grained AZ91 alloy at 250 °C at a strain rate of 10^{-3} s^{-1} (Mussi et al., 2006). The key reason for the difference is the use of a lower temperature. Since cavity nucleation is a diffusion-controlled phenomenon (see Section 2.5.1), at higher temperatures relaxation of concentrated stress is more rapid than at lower temperature. Hence, at higher temperature, the critical diffusion path to nucleate a cavity is large. Even though the critical size is big, nucleation of cavities is likely to occur in the current study, since AZ61HC contained approximately 3% of the total particle population greater than d_p^{crit} (from the μCT data).

In contrast, estimation based on tomography data reveals that also particles

smaller than predicted d_p^{crit} nucleated cavities in this alloy (Fig. 5.21). This may happen due to the domination of other diffusion paths, since Λ_{GB} considers grain boundary diffusion only. Considering lattice diffusion as the dominating diffusion process, critical diffusion path (Λ_L) for stress relaxation were also calculated, following Chokshi-Mukherjee expression (Equation 2.24 on page 68). At 350 °C, the critical particle diameter then becomes approximately 1 μm (Table 5.3). Consequently, all particles detected in the alloys would act as sites for nucleation of cavities if lattice diffusion is the dominating diffusion process. However, Fig. 5.21 shows that small particles nucleated cavities almost only in the later stages of deformation. Moreover, grain boundary diffusion was identified as the dominating diffusion process (see Section 4.2.2). Combining these two facts, lattice diffusion cannot explain the observed trends in Fig. 5.21.

The formation of cavities at the small particles and large particles ($> d_p^{crit}$) at the same time can be explained by the concurrent grain growth experienced by the alloys. Since nucleation of a cavity depends on stress level (Equation 2.22 in 67), an increase in grain size influences nucleation of a cavity (Section 2.5.5). A higher stress allows a smaller cavity to remain stable after formation (i.e., it would not sinter out). Since grain growth leads to a local increase in stress, cavities of smaller radii can become stable after nucleation. Therefore, this is very likely that even if the critical diffusion length is larger than a particle, a stable cavity can nucleate due to the local increase in stress level. As a consequence, due to the concurrent grain growth, small particles act as cavity formation sites, consistent with the experimentally observed trend (Fig. 5.21).

It is very likely that agglomeration of particles influences cavitation. In some random regions in the volume, agglomeration of the particles is observed (Figs. 5.2a and 5.15a). Cavities nucleated from closely spaced particles would coalesce rapidly, forming a large cavity. If the spacing of the agglomerated particles is less than the critical particle diameter required for nucleation of a cavity, nucleation may occur from a particle (within the cluster) having a diameter less than the critical diameter since the relaxation of the concentrated stress would be hindered by the surrounding particles. Therefore, the degree of agglomeration is an important factor in an alloy containing coarse particles since particles smaller than the critical particle diameter required for nucleation of a cavity may form cavities depending on spacing of the agglomerated particles.

Since other alloys (AZ31LC, AZ31HC and AZ61LC) contain a variation of particle sizes, the cavitation behaviour is similar to AZ61HC discussed above. The major reason for different number of cavities is due to the difference in number of particles. The effect of particle agglomeration is shown to affect the cavitation level and the presence of agglomerated particles is a potent source of coalescence of cavities leading

Table 5.4: A list of groups assigned to different cavity sizes

Group	**Cavity Size, d_{cav} (μm)**
Small	$5 \leq d_{cav}$
Medium	$5 < d_{cav} \leq 10$
Large	$10 < d_{cav} \leq 15$
Very Large	$d_{cav} > 15$

to premature failure. The agglomeration is most apparent in the high manganese alloys; this is the major reason for the lower e_f of AZ31HC and AZ61HC.

5.6 Growth of Cavities

5.6.1 Investigation by SEM

Both SEM and μCT have been used to investigate the growth of cavities. To do this from the SEM images, the orientation of the longest dimension of each cavity with respect to the TA was first determined in ImageJ. 20 SEM BSE images were analysed at $\times$250 magnification. The orientation was calculated from the angle between the Feret Diameter of each region and the TA (horizontal direction in the SEM images). Then, the cavities are assigned to four groups based on their sizes (Table 5.4).

In producing the histograms of orientation, cavities of each orientation group (0–15, 16–30, 31–45, 46–60, 61–75 and 76–90°) are normalised with respect to the total number of cavities belong to the cavity size group (under consideration) to visualise the variation between different groups. The reason for performing this grouping is to check whether different mechanisms operate during growth of cavities depending on orientation. Only the results from AZ61HC are presented here, since the major difference in the alloys is in the particle content. Therefore, the results from the highest particle containing alloy is representative of the growth mechanisms observed in other alloys.

At $\varepsilon = 0.80$, the orientations of the small size cavities are mostly randomly distributed (Fig. 5.23a), but, the medium, large and very large cavities are oriented preferentially towards the TA (0° orientation represents the Feret Diameter parallel to the tensile direction) (Fig. 5.23b). At $\varepsilon = 0.90$, most small and medium size cavities are distributed less than 45° to the TA (Fig. 5.24a), and for the large and very large cavities, the orientation is even more inclined towards the TA (Fig. 5.24b). At $\varepsilon = 1.00$ (Fig. 5.25) and $\varepsilon = 1.05$ (Fig. 5.26), the small and the medium cavities are preferentially oriented towards the TA and larger cavities have their major axis oriented <30° to the TA.

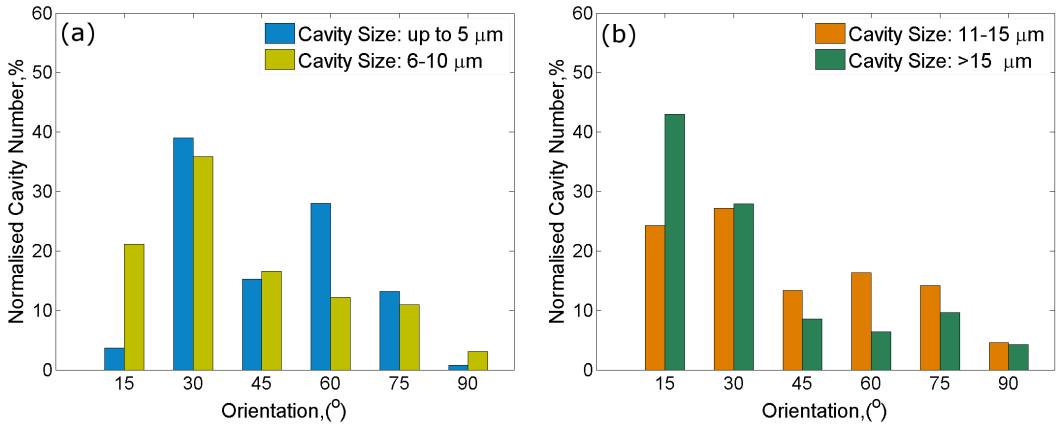

Figure 5.23: Histograms of orientation of the cavities separated based on their sizes for AZ61HC at $\varepsilon = 0.80$, deformed at 350 °C at a strain rate of 5×10^{-4} s^{-1}. (a) shows histograms of small and medium size cavities and (b) shows the corresponding histograms for large and very large size cavities.

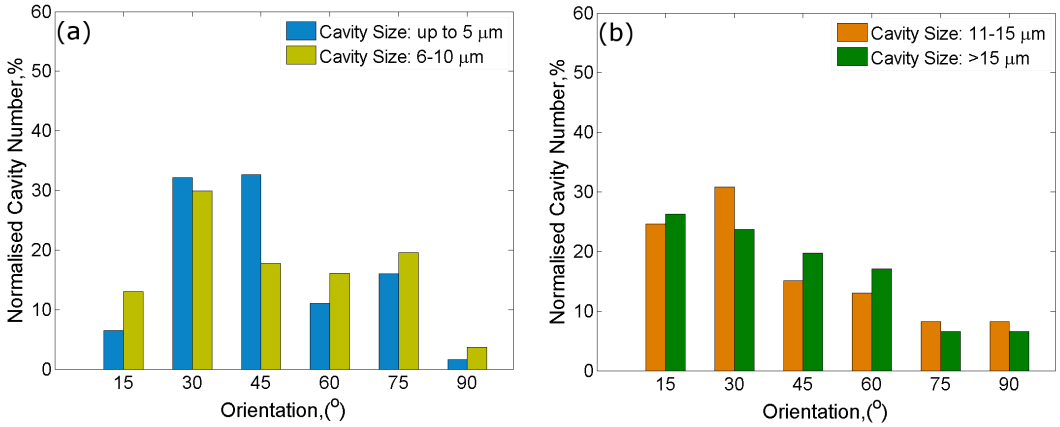

Figure 5.24: Histograms of orientation of the cavities separated based on their sizes for AZ61HC at $\varepsilon = 0.90$, deformed at 350 °C at a strain rate of 5×10^{-4} s^{-1}. (a) shows histograms of small and medium size cavities and (b) shows the corresponding histograms for large and very large size cavities.

Now, the histograms of circularity of the cavity regions are estimated and the cavities are grouped in a similar way to that used in the orientation plots (Table 5.4). The circularity was calculated using the formula—circularity $= 4\pi\,(A_{cav}/P_{cav}^2)$ (Endoh, 2006)—where A_{cav} is the surface area and P_{cav} is the perimeter of a cavity region. If the circularity is 1, then the shape is a perfect sphere and if the circularity deviates far from 1, then the shape is defined as elongated or elliptical. The number of cavities belong to different circularity ranges are normalised by the total number of cavities in the corresponding size group.

At $\varepsilon = 0.80$ (Fig. 5.27a), most small cavities in AZ61HC are approximately round in shape ($0.80 >$ circularity ≤ 1). The medium size cavities are intermediate in circularity. The larger cavities are predominantly less spherical in shape and for the very large cavities, the shape is far from spherical (Fig. 5.27b). At $\varepsilon = 0.90$, most

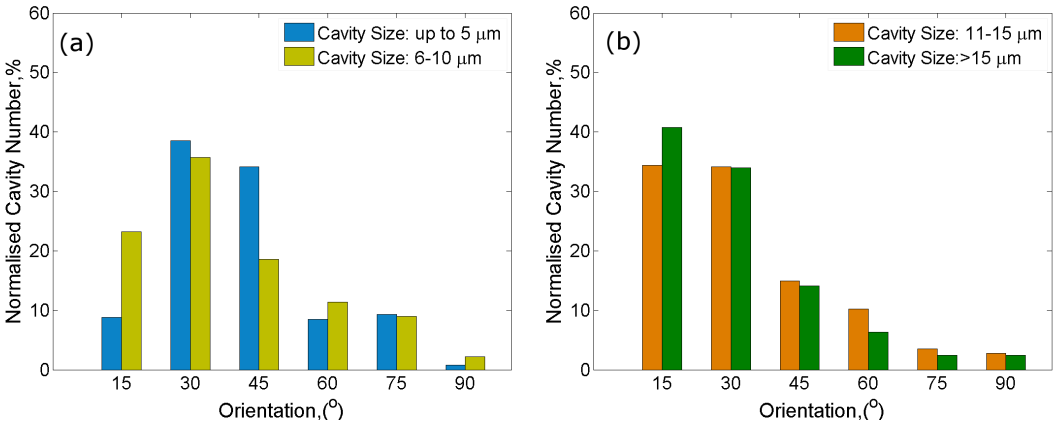

Figure 5.25: Histograms of orientation of the cavities separated based on their sizes for AZ61HC at $\varepsilon = 1.00$, deformed at 350 °C at a strain rate of 5×10^{-4} s^{-1}. (a) shows histograms of small and medium size cavities and (b) shows the corresponding histograms for large and very large size cavities.

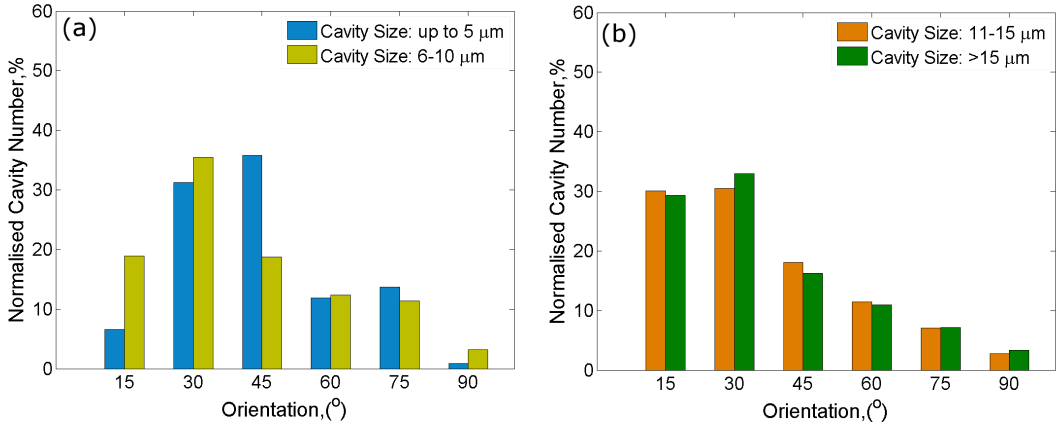

Figure 5.26: Histograms of orientation of the cavities separated based on their sizes for AZ61HC at $\varepsilon = 1.05$, deformed at 350 °C at a strain rate of 5×10^{-4} s^{-1}. (a) shows histograms of small and medium size cavities and (b) shows the corresponding histograms for large and very large size cavities.

small cavities are spherical in shape but with the increase of size, the shape becomes elongated (Fig. 5.28). Similar trends are observed for the cavities at $\varepsilon = 1.00$ and 1.05 (Figs. 5.29 and 5.30). Small cavities are close to spherical in shape, but with the increase of size, most cavities become elongated in shape. It may be concluded that shape of cavities changes during growth.

From the orientation and circularity histograms, it is obvious that there is a probability that two different mechanisms operate during the growth of cavities, since different shapes of cavities are observed at different cavity sizes. Cavity growth may occur by either stress-induced diffusion (Beere and Speight, 1978) or plasticity (Hancock, 1976). Diffusion growth leads to a spherical cavity shape to minimise the surface area. On the other hand, plasticity driven growth results in an elongated shape (see Section 2.5.2).

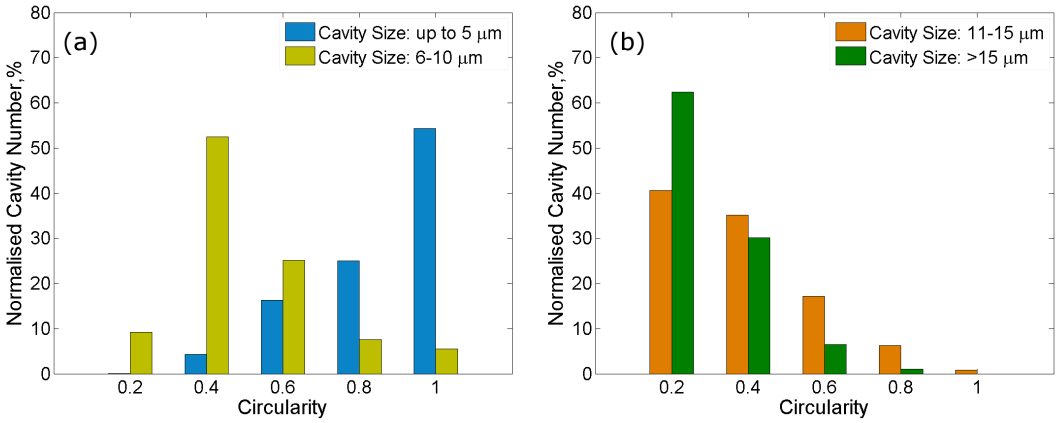

Figure 5.27: Histograms of circularity (shape factor) of the cavities separated based on their sizes for AZ61HC at $\varepsilon = 0.80$, deformed at 350 °C at a strain rate of 5×10^{-4} s^{-1}. (a) shows histograms of small and medium size cavities and (b) shows the corresponding histograms for large and very large size cavities.

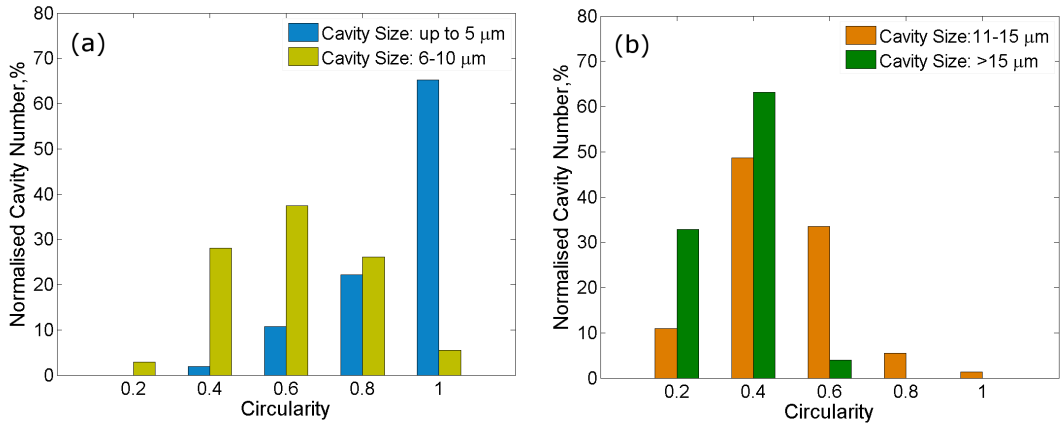

Figure 5.28: Histograms of circularity (shape factor) of the cavities separated based on their sizes for AZ61HC at $\varepsilon = 0.90$, deformed at 350 °C at a strain rate of 5×10^{-4} s^{-1}. (a) shows histograms of small and medium size cavities and (b) shows the corresponding histograms for large and very large size cavities.

The initial growth occurs by diffusion of vacancies from the surrounding boundary. Growth by diffusion depends on diffusion paths. Diffusional growth can be enhanced if a growing cavity intersects several grain boundaries. In such a case, diffusion along several boundaries leads to a rapid growth of a cavity.

After a certain critical size, plasticity controlled growth dominates during the relaxation of the stress concentration. This is evident since elongated cavities are observed in the circularity plots.

To determine the contribution of different growth models, it is necessary to find out the critical radius for transition between these mechanisms. Using the values of the parameters (presented in Appendix A), the growth rates are calculated using Equations 2.27 and 2.29 and plotted in Fig. 5.31.

From Fig. 5.31, the transition cavity diameter ($2r^t_{cav}$) between the diffusion and

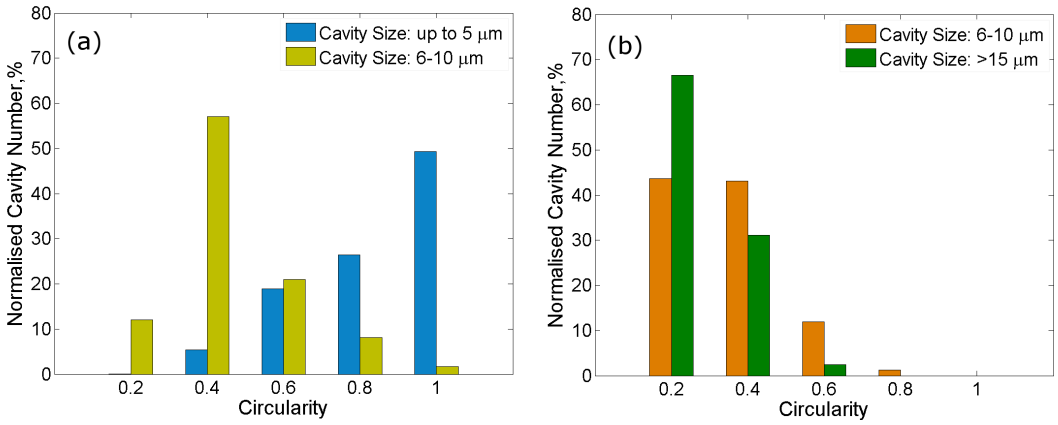

Figure 5.29: Histograms of circularity (shape factor) of the cavities separated based on their sizes for AZ61HC at $\varepsilon = 1.00$, deformed at 350 °C at a strain rate of 5×10^{-4} s^{-1}. (a) shows histograms of small and medium size cavities and (b) shows the corresponding histograms for large and very large size cavities.

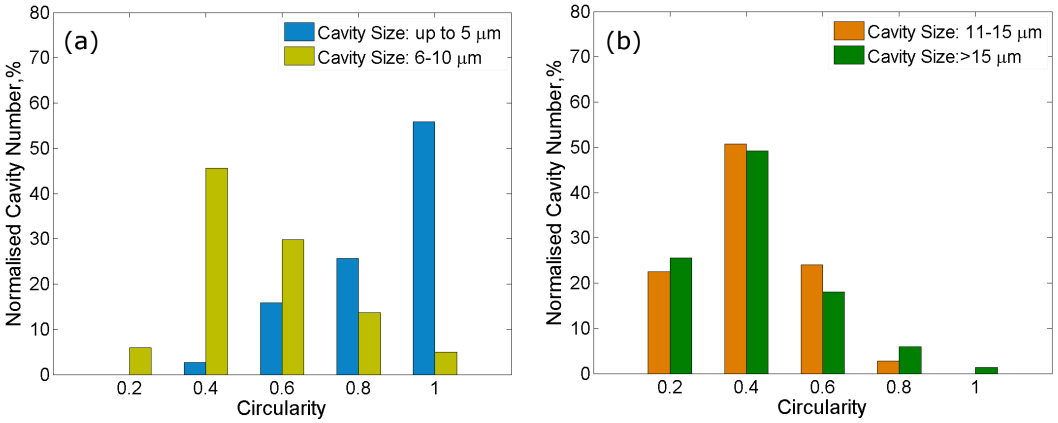

Figure 5.30: Histograms of circularity (shape factor) of the cavities separated based on their sizes for AZ61HC at $\varepsilon = 1.05$, deformed at 350 °C at a strain rate of 5×10^{-4} s^{-1}. (a) shows histograms of small and medium size cavities and (b) shows the corresponding histograms for large and very large size cavities.

plasticity controlled growth is calculated as approximately 6 μm. If this value is compared with the orientation and circularity plots, the shape (close to spherical) and the orientation (less inclined towards TA) of the small cavities (<5 μm) fit very well with the diffusion model. It implies that for the small cavities, the diffusion process is dominating but once the transition diameter is exceeded, plasticity induced growth is the controlling factor.

Some inconsistencies are observed such that some smaller cavities are approximately elliptical and also some larger cavities are almost spherical in shape. There are several possibilities that may lead to these behaviours. Since, sometimes, a few particles are agglomerated together, it is possible to have closely spaced smaller cavities which are found to coalesce together, forming a different shape rather than the spherical. This also explains the differences in orientation for some cavities.

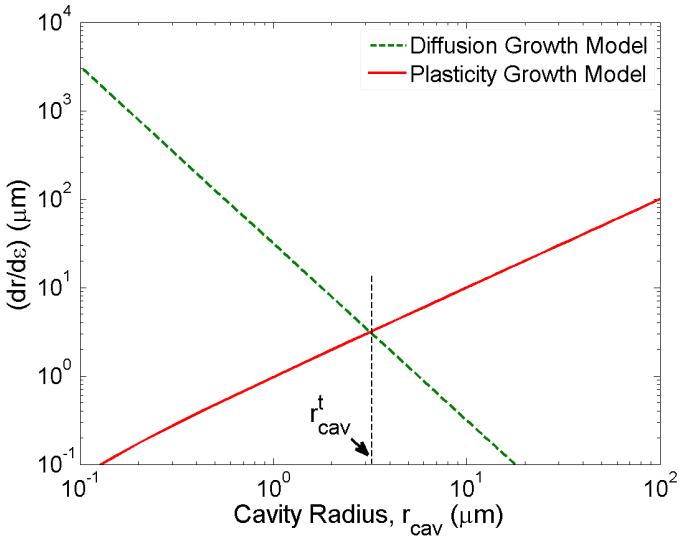

Figure 5.31: Cavity growth rates for AZ61HC at different cavity radii (r_{cav}) using different growth models at 350 °C at a strain rate of 5×10^{-4} s^{-1}. A transition radius (r^t_{cav}) of 3 μm from diffusion to plasticity mechanism is obtained.

Moreover, from the circularity plots, for the larger cavity group, a few large cavities are observed to be spherical in shape. This may occur if the cavities, growing by the diffusion process, are intersected by several grain boundaries and this results in a faster diffusion process that leads to a final cavity shape that is approximately spherical. It is also possible that the coalescence of cavities could lead to a near spherical shaped cavity by coincidence.

In summary, since most small cavities are circular and randomly distributed, they have grown by vacancy diffusion. Above a critical size, plasticity controlled growth dominates and leads to a rapid increase of cavity size. However, some large cavities may remain spherical due to coalescence and some small cavities deviate from spherical size due to constraint by particle agglomeration.

5.6.2 Investigation by X-ray Micro-Tomography

From the SEM study on growth of cavities (see Section 5.6.1), two different growth mechanisms are identified. However, it is important to check whether the sectioning effect (see Section 5.3) has any consequence on the conclusions made about the growth of cavities. Using the 3D data set already discussed (see Section 5.3.2), the orientation and shapes of the cavities were determined. To produce the required information about particle shape, a custom routine was written in Matlab. Briefly, at first, each region was considered as an ellipsoid (See Appendix B for details) followed by estimation of moment of inertia tensor of the ellipsoid to get the major and minor axes (a and b) and the polar axis (c), where $a > b > c$. Then, the angle between the major axis (a) and the tensile direction (z-axis of the 3D data set) was determined.

Using this method for all regions present in the data set, a histogram for a bin width of 15° was plotted.

The cavity regions are grouped in a similar way to the orientation plots for the SEM data (Table 5.4). Also, the aspect ratios a/b and b/c were calculated. These aspect ratios give the elongation and flatness of a region (Endoh, 2006), since a, b and c can be considered as the length, breadth and thickness of a region respectively. Then, these regions are distinguished based on aspect ratios (a/b and b/c). Three different types of region are labelled: spherical ($a/b = b/c = 1$); elliptical ($a/b \leq 3$) and rod-like ($a/b > 3$). The classification is made based on previous work on creep induced cavities (Isaac et al., 2008). The orientation histograms of these regions were also produced.

The orientation of the cavities in AZ61HC, at different strains of 0.80, 0.90, 1.00 and 1.05, are plotted as histograms in Figs. 5.32 to 5.35. The data are grouped for different sizes of cavity based on Table 5.4. The size, here, denotes the major axis (a) of an ellipsoid. The orientation of the small (5 μm) cavities, are totally random at all strains, though the proportion of cavities aligned close to the TA increased with the increment of strain. For the medium size cavities, the orientation is also mostly random; however, at $\varepsilon = 1.05$, most of the medium sized cavities are oriented within 30° of the TA. For the size range of 11 to 15 μm, the cavities are mostly aligned perpendicular to the tensile direction up to $\varepsilon = 1.00$. After this strain, most of the cavities of that size range are randomly oriented in the volume. The very large cavities (>15 μm in size), are mostly aligned either parallel or perpendicular to the TA.

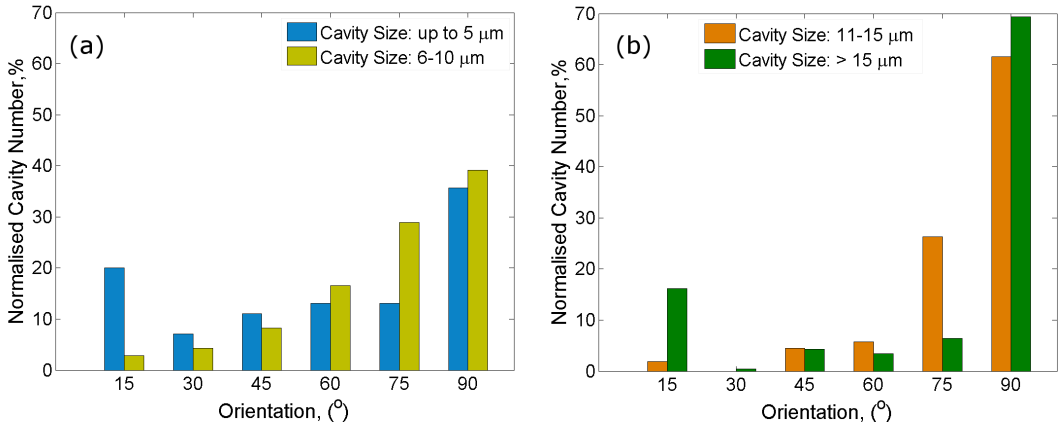

Figure 5.32: Histograms of orientation of cavities separated based on their sizes for AZ61HC, deformed at 350 °C at a strain rate of 5×10^{-4} s^{-1}, at $\varepsilon = 0.80$ from the μCT data. (a) shows histograms of small and medium size cavities and (b) shows the corresponding histograms for large and very large size cavities.

The deviation of the orientation from the TA obtained from the histograms, in the first instance, appears to be contradictory to the SEM results for the large cavity

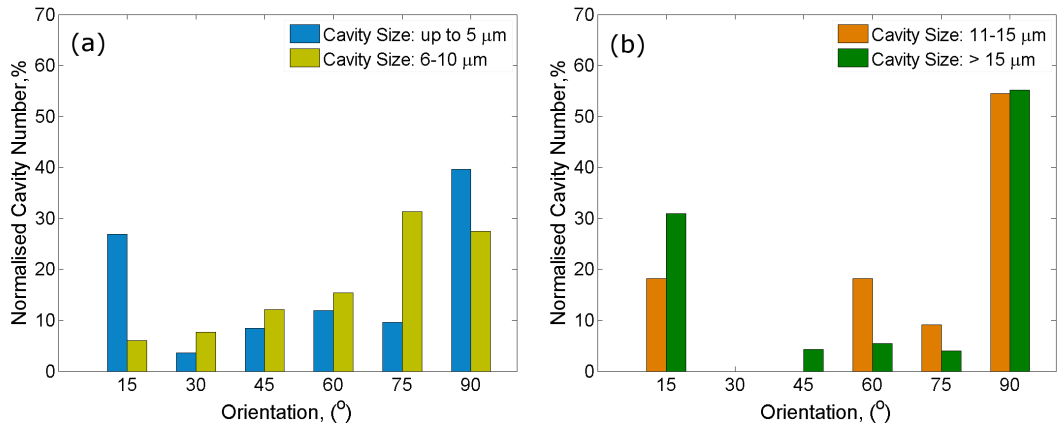

Figure 5.33: Histograms of orientation of cavities separated based on their sizes for AZ61HC, deformed at 350 °C at a strain rate of 5×10^{-4} s^{-1}, at $\varepsilon = 0.90$ from the μCT data. (a) shows histograms of small and medium size cavities and (b) shows the corresponding histograms for large and very large size cavities.

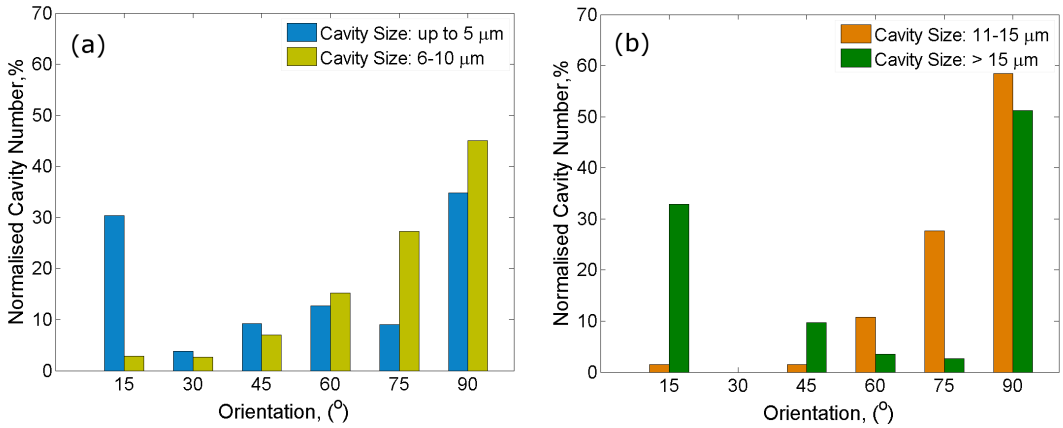

Figure 5.34: Histograms of orientation of cavities separated based on their sizes for AZ61HC, deformed at 350 °C at a strain rate of 5×10^{-4} s^{-1}, at $\varepsilon = 1.00$ from the μCT data. (a) shows histograms of small and medium size cavities and (b) shows the corresponding histograms for large and very large size cavities.

size (see Section 5.6.1). From the 3D data, very large cavities are observed oriented either parallel or perpendicular to the TA. This is not revealed in the SEM due to the sectioning effect. In particular, cavities that are elongated perpendicular to the TA would not be revealed as such in the sections used for the SEM study (cut parallel to the TA). Also, coalescence of cavities is direction-independent and the shape is usually complex. Thus, 3D investigation reveals no strong preference for alignment parallel to the TA.

Before classifying the shapes of the cavities, the aspect ratios a/b (termed as elongation) and b/c (termed as flatness) are plotted on a semi-log scale for different strains of AZ61HC (Fig. 5.36). Two lines are drawn on each plot to clarify the variation. It is obvious that more elongated regions are obtained with an increase of strain. These elongated cavities are also less flat. For most cavities, the elongation

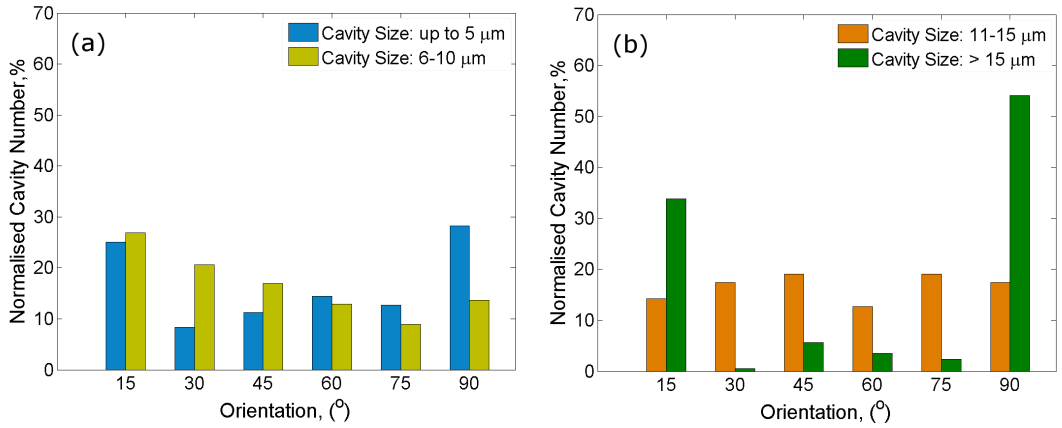

Figure 5.35: Histograms of orientation of cavities separated based on their sizes for AZ61HC, deformed at 350 °C at a strain rate of 5×10^{-4} s^{-1}, at $\varepsilon = 1.05$ from the μCT data. (a) shows histograms of small and medium size cavities and (b) shows the corresponding histograms for large and very large size cavities.

value is less than 3 with a flatness value of approximately 2. Now, as mentioned earlier, cavities are arbitrarily categorized, based on the histogram plot, as spheroid ($a/b = b/c = 1$), ellipsoid ($a/b \leq 3$) and rod-like ($a/b > 3$). Since no cavity is a perfect sphere, a range ($1.2 > a/b > 1$) is allowed for spherical type cavities. It is assumed that elliptical shape would be sustained till the major axis (a) becomes three times higher than the minor axis (b). If a is greater than three times of b, then the region is considered as a rod-like elongated cavity. In Fig. 5.13b, an elongated cavity of complex shape is shown which is included in the rod-like classification.

Fig. 5.37 shows the orientation of elliptical and rod-like cavities at different strains. Since spheroids cannot have any preferred orientation, they are not included in the analysis. When the cavities are grown to become elliptical or rod-like in shape, the orientation is apparently random. No preferred orientation with the TA is observed. This is due to the extensive coalescence together with branching of the cavities.

The numbers of different types of cavities per unit volume are estimated (Fig. 5.38). The number of spheroids increases until the strain reaches 1.00, and afterwards the number has started to decrease. On the other hand, the number of the rod-like cavities shows a trend of continuous increase. The elliptical cavities occupy the largest fraction of the total cavity population and the number has increased during deformation. As already discussed in the SEM section, spherical cavities are predominantly grown by diffusion and at the largest strain, the number of spherical cavities is decreased. Plasticity-controlled growth of cavities leads predominantly to the elliptical cavities. The rod-like cavities, being very elongated, are partly due to the branching effect of the coalesced cavities.

Though the orientation of the cavities in the μCT does not show any systematic trend taking account the coalescence effect, unlike the observation from the SEM

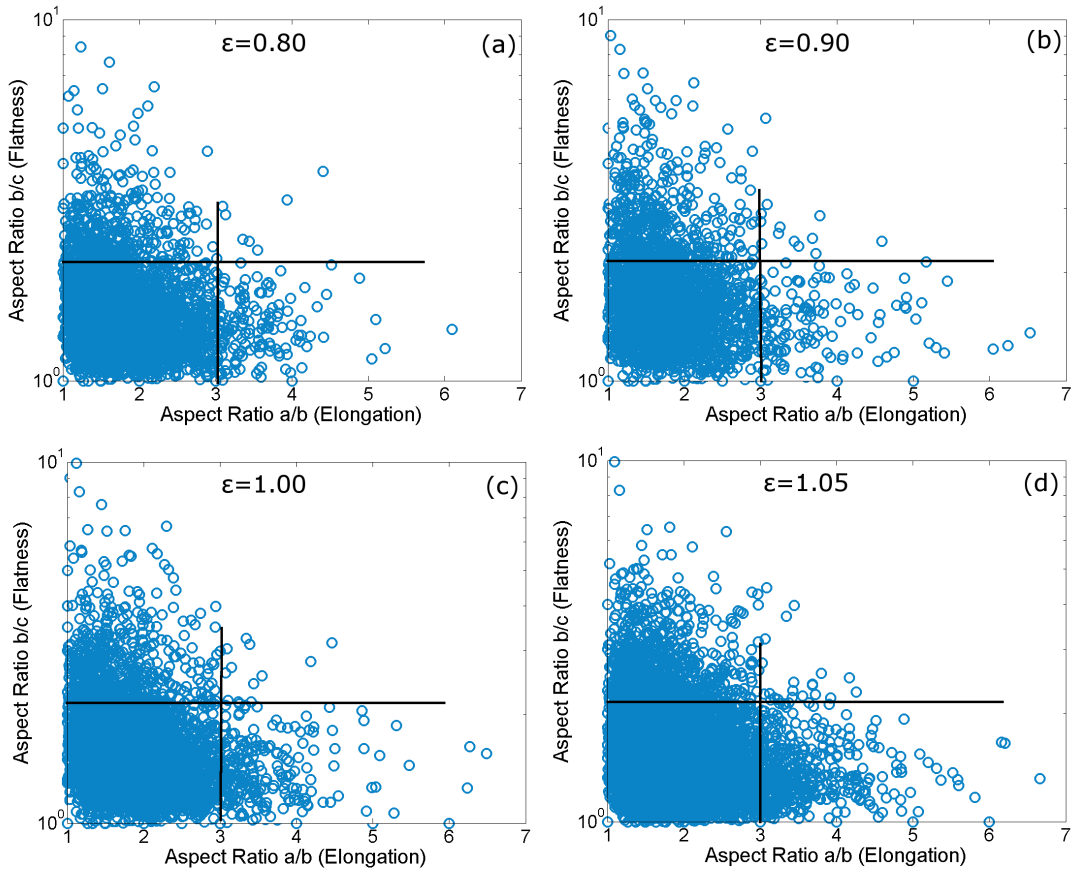

Figure 5.36: Plots of aspects ratios, a/b (elongation) vs b/c (flatness), of AZ61HC, deformed at 350 °C at a strain rate of 5×10^{-4} s^{-1}, at the strain of (a) 0.80, (b) 0.90, (c) 1.00 and (d) 1.05. Lines are drawn to guide the eye.

data, a similar growth mechanism is confirmed.

Finally, the growth models are compared with the experimental data from SEM and μCT (Fig. 5.39). The largest cavities, assuming they represent the earliest cavities to nucleate, at different strains were picked up and their growth rates ($dr/d\varepsilon$) were calculated. The growth rates obtained from the SEM data were taken from all alloys studied in the current project and for the μCT data, growth rates were taken from AZ61HC. The growth rates deviate greatly from the model predicted rates. For the SEM data, a fitting curve was drawn and it shows a difference in predicted and experimental rates by a factor of 5. Since the models do not consider any effect of coalescence, such anomalies are not surprising.

5.6.3 Coalescences of Cavities

In Sections 5.1 and 5.3.1, large cavities are observed both in SEM and μCT. These large cavities were formed by coalescence of closely spaced cavities. In the preceding section, it was shown that large cavities are mostly governed by plasticity controlled growth.

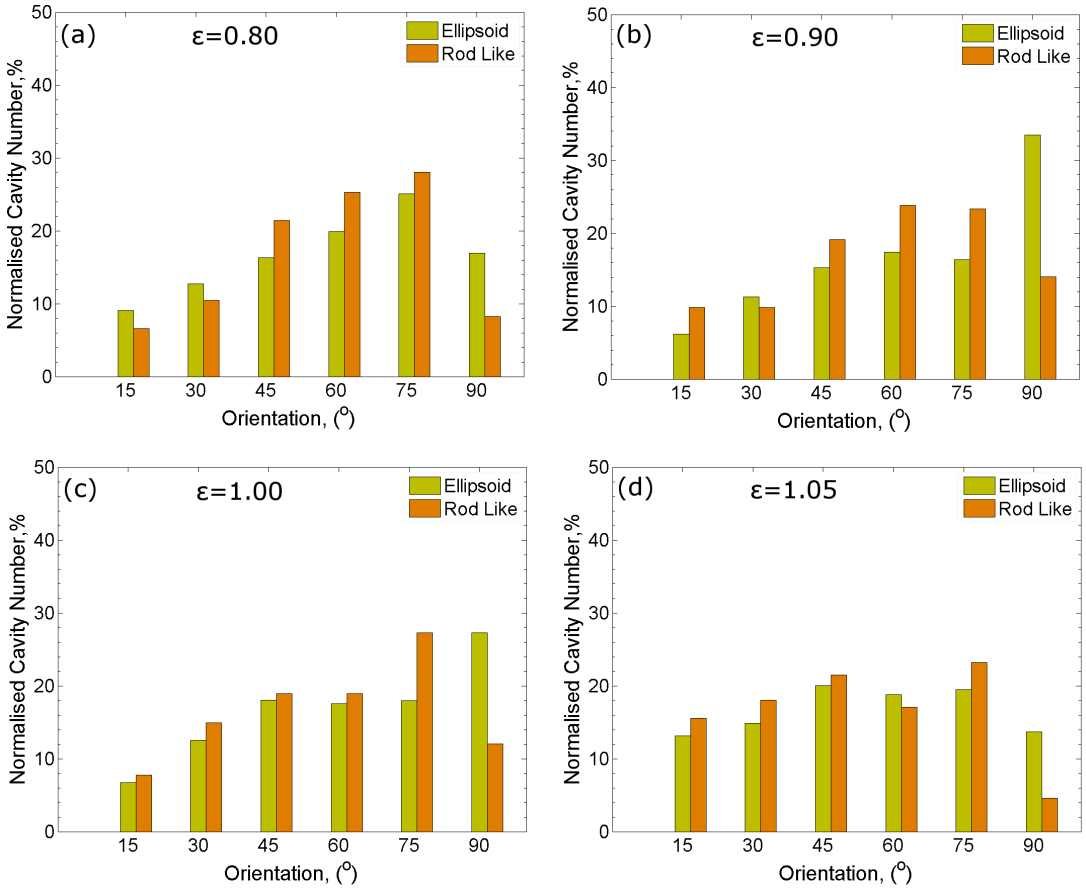

Figure 5.37: Histograms of orientation of cavities classified based on their aspect ratios for AZ61HC, deformed at 350 °C at a strain rate of 5×10^{-4} s^{-1}, at the strain of (a) 0.80, (b) 0.90, (c) 1.00 and (d) 1.05.

Volume fraction of cavities at different strains can be used to calculate the theoretical cavity growth rate parameter (η) using Equation 2.31. The growth rate parameter at different temperatures was estimated and is shown in Table 5.5. It can be seen that for a particular alloy η is similar at all temperatures. Now, from the volume fraction data of different alloys for different pre-set strains, η can also be estimated and compared with the theoretical data. The plots of experimental η calculations are shown in Figs. 5.40 and 5.41 at 350 °C.

Except AZ31LC, the theoretical η is close to the experimental data. The major difference comes from the level of cavitation in the alloys which directly depends on number of particles. As a consequence, the cavity growth rate parameter is higher in the high manganese alloys. During the coalescence process, the local area adjacent to the cavities suffers load shedding resulting in a local high stress which increases the local cavity growth rate (Càceres and Wilkinson, 1984a; Wilkinson and Càceres, 1986). This is reflected in the high manganese alloys having a higher η.

The fluctuation between theoretical and experimental growth rate parameters is attributed to the different coalescence level in the alloys due to differences in particle

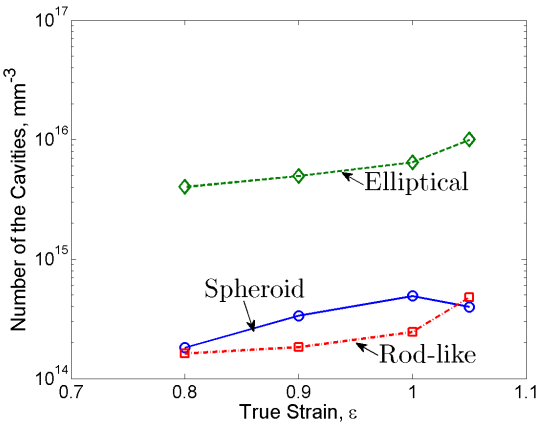

Figure 5.38: A plot of number of the cavities, classified into spheroids, elliptical and rod-like shapes based on their aspect ratios, at different strains for AZ61HC, deformed at 350 °C at a strain rate of 5×10^{-4} s^{-1}.

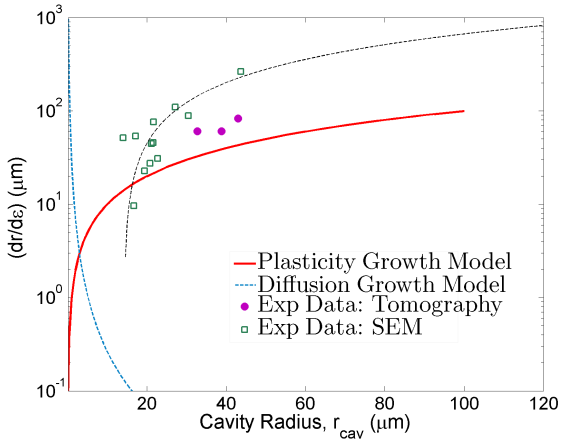

Figure 5.39: A plot of average cavity growth rate ($dr/d\varepsilon$) showing a comparison between theoretical models based on diffusion and plasticity and experimental data from SEM and μCT for the chill-cast alloys deformed at 350 °C at a strain rate of 5×10^{-4} s^{-1}.

fraction and spacing. From the μCT, it was confirmed that most cavities originated at the particle/matrix interfaces. It was also argued that if particles are agglomerated, the chance of cavitation and coalescence is very high. Therefore, the higher growth rate in the high manganese alloys is not unexpected. However, it should be borne in mind that particles act to nucleate cavities. If particles are closely spaced, the chances of early coalescence increases. Since a large particle fraction means a reduced inter-particle spacing and particles are the source of cavitation, a larger fraction of particles eventually leads to more extensive coalescence of cavities. The $\eta_{\text{experimental}}$ values for the low manganese alloys are small which is due to the lower particle fraction (and lower particle spacing) of these alloys. Moreover, η-values become smaller for a higher strain rate sensitivity value (Pilling and Ridley, 1988a). Since AZ31LC had the largest m, a lower η for AZ31LC is not surprising.

Table 5.5: Estimation of cavity growth rate parameter (η) at a strain rate of 5×10^{-4} s^{-1}

Temperature, °C	AZ31LC	AZ31HC	AZ61LC	AZ61HC
300	3.74	3.83	3.90	4.35
350	4.37	4.55	4.88	5.42
400	3.69	4.16	4.75	4.70
450	3.89	3.93	4.48	4.82

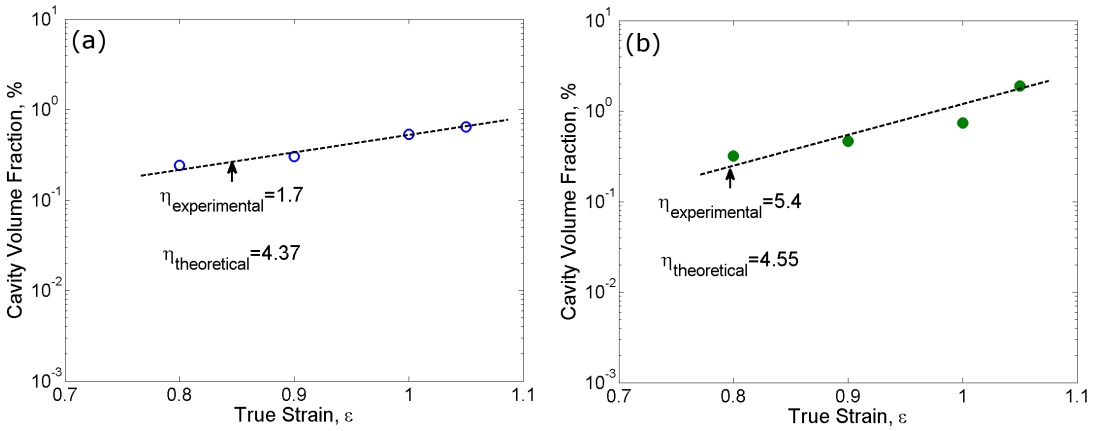

Figure 5.40: A comparison between theoretical and experimental cavity growth rate parameter (η) obtained by plotting cavity volume fraction against true strains for (a) AZ31LC and (b) AZ31HC deformed at 350 °C at a strain rate of 5×10^{-4} s^{-1}.

5.7 Continuous Nucleation of Cavities

There exists a debate in literature about the occurrence of continuous nucleation of cavities during deformation. For an AZ31 alloy, Lee and Huang (2004) showed that a plateau in the number of cavities was observed after a certain strain. Moreover, Pilling and Ridley (1989) argued that resolution limitation of microscopy might not detect the very small cavities which might grow during deformation and ultimately would become visible at a higher strain.

However, in the alloys investigated in the current study, the number of cavities has increased profoundly during straining. This is confirmed by μCT. In AZ61HC, tomography data has detected an increase in the number of cavities by a factor of 3 during straining from 0.80 to 1.05. In Fig. 5.21, the actual number of particles associated with cavities was plotted for two strain levels of AZ61HC at 350 °C. This reveals that at the higher strain, more particles are associated with cavities. Also, cavities of different shapes and sizes are evident in the microstructure and spherical cavities are observed even at the largest strain. Moreover, if the cavities were nucleated at approximately the same time and grown from a small size (not visible under imaging in SEM and μCT) as argued by Pilling and Ridley, the size of

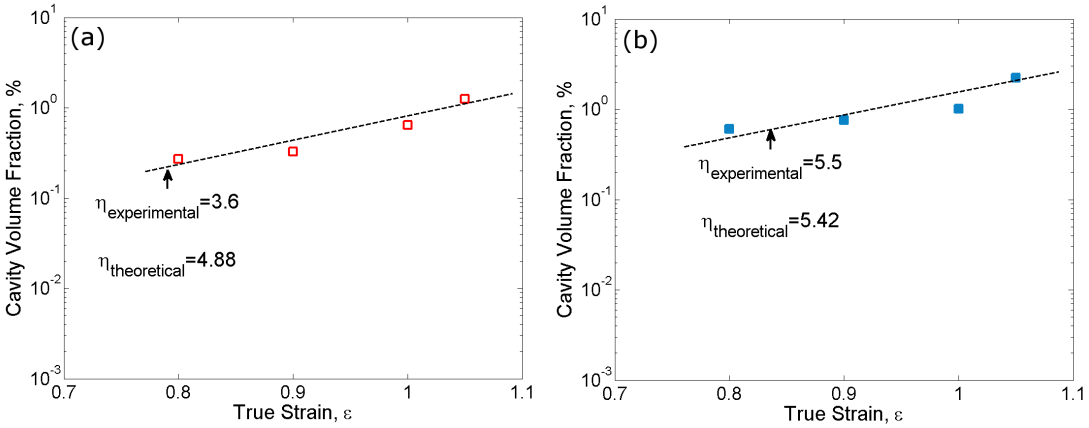

Figure 5.41: A comparison between theoretical and experimental cavity growth rate parameter (η) obtained by plotting cavity volume fraction against true strains for (a) AZ61LC and (b) AZ61HC deformed at 350 °C at a strain rate of 5×10^{-4} s^{-1}.

the cavities should be approximately similar as they grow during deformation (except the coalesced cavities). However, this is not the case in the current study. Therefore, in the present work, the nucleation of cavities is a continuous process.

5.8 Parameters affecting Cavitation

Particles are identified as the key source of cavitation in the alloys investigated. Moreover, large particles are more likely to promote nucleation of cavities. Recently, Taleff and co-workers (2001) suggested that large particles (>5 μm) might not accelerate cavitation. However, in the current study, large particles are shown to be more likely to form cavities earlier. The volume fraction of particles is also very important. If the particles are closely spaced, cavities are also closely spaced since particles are the source of cavities. As a result, coalescence of cavities occurs early during deformation, leading to larger cavities. It was shown earlier that plasticity controlled growth depends on the size of cavities. A large coalesced cavity will also grow faster.

A pronounced grain growth was observed for all alloys. The growth of grains increases local stresses and as a consequence the stress required to form a stable cavity may be reached, forming more cavities. Though AZ31LC and AZ61LC had the least volume fraction of particles, the cavity volume fraction in AZ61LC was higher due to the comparatively higher grain growth experienced by the latter alloy (since the latter alloy had more aluminium).

Temperature has a different effect. At higher temperature, the accommodation of deformation by diffusion is more rapid. Therefore, the diffusion path (critical particle diameter) required for incomplete accommodation increases (Table 5.6). An increase of temperature also decreases flow stress (see Section 2.2), increasing the size

Table 5.6: Calculation of critical particle diameter (d_p^{crit}) for AZ31HC at different temperatures and strain rates

	Critical Particle Diameter, d_p^{crit} (μm)	
Temperature, °C	5×10^{-4} s^{-1}	5×10^{-3} s^{-1}
300	7.29	3.76
350	11.14	5.73
400	14.50	7.74
450	17.16	9.60

of a stable cavity (Equation 2.22 in Section 2.5.1). As a result, with an increase of temperature, the nucleation rate is reduced. However, at a higher temperature, once formed cavities grow by diffusion at a faster rate. Therefore, overall the chance of failure by cavitation is increased.

A higher strain rate increases stress concentration near an irregularity, and therefore more cavities are expected to nucleate. However, a comparatively low m leads to a reduced resistance towards neck growth and failure may occur by necking before cavity induced failure. At the high strain rate condition, the critical particle size is smaller (Table 5.6) but the time available to grow the cavities is also reduced. Therefore, depending on the test condition, cavitation behaviour of an alloy varies.

5.9 Summary

- Extensive cavitation was observed in all alloys prior to failure (except at 300 °C).
- From the SEM images, approximately half of the cavities were found closely associated with particles. Particles of different sizes were observed to nucleate cavities.
- The volume fraction of cavities was increased significantly during deformation and high manganese alloys had the largest volume fraction of cavities. Quantification based on SEM images shows that a significant number of large cavities (>20 μm) were present in all alloys.
- Tomography images revealed that extensive cavity coalescence occurred during deformation. This leads to complex shaped large cavities that had several branches in different directions which were the remnants of the original cavities.
- To determine the association of particles and cavities from the tomography data, two methodologies were developed. The correlation plot showed that most of

the particle and cavity voxels were within a distance which confirmed their close association. The dilation and intersection method measured the distance between particle and cavity regions and 90% cavities were found attached to particles. Results were compared with generated random data set to check validity of the methodoligies.

- The particles, truly connected with cavities, were tagged from the tomography data. At $\varepsilon = 0.90$, mostly large particles were found to nucleate cavities. In contrast, at $\varepsilon = 1.05$, particles of all sizes nucleated cavities. Moreover, not all large particles nucleated cavities. Depending on the concurrent grain growth, different sizes of particles act as cavity nucleation site.

- Cavities up to a diameter of $6\,\mu$m were grown by stress controlled diffusion and growth of the larger cavities was governed by plasticity. However, the commonly used models do not account for coalescence of cavities and hence do not correctly predict cavity growth rate.

- Agglomeration of particles had a significant effect on cavitation. If particles are closely spaced, it is possible that smaller particles, generally not nucleating cavities, can act as a cavity formation site. Moreover, coalescence of these closely spaced cavities occurs early, leading to large cavities. This is one of the reasons for higher cavitation in the high manganese alloys.

- Analysis of tomography data showed that most cavities were elliptical in shape and several other were rod-like (thin and very elongated) due to the effect of coalescence. A small number of spherical cavities were observed even at the largest strain which clearly indicated that nucleation of cavities was a continuous phenomenon. Also, the continuous increase of cavity number during deformation supported this observation.

- Since particles are the key parameter for cavitation, alloys having a lower fraction of particles showed fewer cavities. Therefore the low manganese alloys had the least volume fraction of cavities. However, extensive grain growth in the high aluminium and low manganese alloy (AZ61LC) increased local stress which allowed nucleation of cavities with smaller radii. This is one of the reasons for the increased cavitation in AZ61LC compared to AZ31LC.

- At 300 °C, the least formation of cavities was observed which was due to the lower diffusional growth of cavities. The failure of the alloys occurred predominantly by cavitation at 350 and 400 °C. At 450 °C, rapid diffusional activity prevented extensive nucleation of cavities, but the cavities that did form grew faster by diffusion.

Chapter 6

Conclusions

The hot deformation behaviour and failure mode of four AZ series magnesium alloys with different levels of aluminium and manganese have been studied over a range of temperatures and strain rates typical of those used for superplastic forming. Cavitation at large aluminium-manganese intermetallic particles has been shown to be the main failure mechanism with differences between the alloys attributed mainly to the different distribution of these particles. Only at the lowest test temperature used (300 °C) cavitation was not dominant and in this case failure occurred by diffuse necking. Below the key findings of this project are highlighted.

- Hot rolling of the alloys with an equal strain of 0.12 in each rolling pass successfully produced a dynamically recrystallized microstructure having an average grain size 7 to 9 μm and strong basal texture.

- The alloys contained a significant fraction of coarse particles. These were aluminium-manganese intermetallics with varying stoichiometric formulae depending on alloy composition. The volume fraction of the particles was found to be higher for the high manganese alloys. The size distribution of the particles varied significantly, primarily depending on manganese content, and particles agglomerates greater than 20 μm were evident in the higher manganese alloys.

- The flow behaviour of the alloys was similar up to the maximum stress level. The only difference was found to be a weak effect of aluminium solute which provided some additional solute solution strengthening and a slight increase in flow stress in the high aluminium alloys. Flow softening occurred in all alloys, but a more rapid softening was found for the high manganese alloys. At any particular test condition, manganese content apparently controlled the strain to failure.

- The activation energy of deformation was close to that for grain boundary diffusion for all test conditions and coupled with lack of grain elongation this

suggests the deformation of the alloys was likely to be dominated by sliding of grains.

- Strain rate sensitivity (m) values increased with increasing temperature but at 450 °C, the values were reduced slightly due to extensive grain growth. Using analysis of variance method, addition of aluminium found to reduce m-values.

- Apart from temperature, the strain to failure (e_f) was most strongly influenced by the manganese content of the alloys. Manganese forms particles which appeared to act as cavity formation sites.

- Grain growth occurred at all temperatures. But, at 450 °C, substantial growth was observed leading to an increase in grain size up to a factor of 4. Apart from temperature, the growth of grains was influenced by the addition of aluminium, with a higher level of aluminium leading to an increased grain growth rate. Grain growth during testing decreased m-values gradually.

- The volume fraction of cavities increased during testing and the high manganese alloys showed a higher cavity volume fraction.

- SEM observation showed that at least half of the cavities were associated with particles. To confirm the association of particles and cavities, X-ray micro tomography was carried out and two different methodologies were developed to quantitatively study the particle/cavity association. Both methods confirmed that cavities were closely associated with particles and 90% cavities were connected to particles.

- Tomography revealed that at lower strains, cavities formed almost exclusively at the largest particles only. At larger strains, progressively smaller particles became cavity formation sites. This is expected since grain growth increased the local stresses which allowed cavities formed at smaller particles to become stable.

- Measurement of cavity shape and theoretical calculations suggest that the growth of cavities of size less than 6 μm was controlled by stress-induced diffusional processes and the growth of larger cavities was governed by plasticity. Tomography data revealed the importance of coalescence of cavities in controlling cavity shape and orientation.

- The coalescence of cavities depended on particle volume fraction since particles were the source of cavitation. The larger the number of particles, the greater was the chance of coalescence. This was the reason for lower e_f of the high manganese alloys.

- Agglomeration of particles had a significant effect. This allowed smaller particles to nucleate cavities even if individually they were below the critical size for cavity formation. Moreover, such closely-spaced cavities coalesced early, leading to very large cavities.

References

Abramoff, M. D., P. J. Magelhaes, and S. J. Ram (2004). "Image Processing with ImageJ". In: *Biophotonics International* 11.7, pp. 36–42. (Cit. on p. 89).

Aghion, E., B. Bronfin, and D. Eliezer (2001). "The role of the magnesium industry in protecting the environment". In: *Journal of Materials Processing Technology* 117.3, pp. 381–385. (Cit. on p. 18).

Agnew, S. R. (2004). "Wrought magnesium: A 21st century outlook". In: *JOM* 56.5, pp. 20–21. (Cit. on p. 26).

Agnew, S. R., M. H. Yoo, and C. N. Tomé (2001). "Application of texture simulation to understanding mechanical behavior of Mg and solid solution alloys containing Li or Y". In: *Acta Materialia* 49.20, pp. 4277–4289. (Cit. on pp. 31, 34).

Aigeltinger, E. H. and R. C. Gifkins (1977). "Cavitation during diffusion creep of a magnesium alloy". In: *Journal of Materials Science* 12.5, pp. 915–918. (Cit. on p. 78).

Akhtar, A. and E. Teghtsoonian (1969). "Solid solution strengthening of magnesium single crystals–ii the effect of solute on the ease of prismatic slip". In: *Acta Metallurgica* 17.11, pp. 1351–1356. (Cit. on p. 28).

Al-Samman, T. (2009). "Comparative study of the deformation behavior of hexagonal magnesium-lithium alloys and a conventional magnesium AZ31 alloy". In: *Acta Materialia* 57.7, pp. 2229–2242. (Cit. on pp. 31, 106).

Al-Samman, T. and G. Gottstein (2008). "Influence of strain path change on the rolling behavior of twin roll cast magnesium alloy". In: *Scripta Materialia* 59.7, pp. 760–763. (Cit. on p. 83).

Alden, T. H. (1967). "The origin of superplasticity in the sn-5%bi alloy". In: *Acta Metallurgica* 15.3, pp. 469–480. (Cit. on p. 40).

Ando, D., J. Koike, and Y. Sutou (2010). "Relationship between deformation twinning and surface step formation in AZ31 magnesium alloys". In: *Acta Materialia* 58.13, pp. 4316–4324. (Cit. on p. 32).

Argon, A. S. and S. Takeuchi (1981). "Internal stresses in power-law creep". In: *Acta Metallurgica* 29.11, pp. 1877–1884. (Cit. on p. 56).

Ash, B. A. and C. H. Hamilton (1988). "Strain and strain-rate hardening characteristics of a superplastic AlLiCuZr alloy". In: *Scripta Metallurgica* 22.2, pp. 277–282. (Cit. on p. 63).

Ashby, M. F. (1972). "A first report on deformation-mechanism maps". In: *Acta Metallurgica* 20.7, pp. 887–897. (Cit. on p. 42).

Ashby, M. F. and R. A. Verrall (1973). "Diffusion-accommodated flow and superplasticity". In: *Acta Metallurgica* 21.2, pp. 149–163. (Cit. on p. 52).

Bae, D. H. and A. K. Ghosh (2002a). "Cavity formation and early growth in a superplastic Al-Mg alloy". In: *Acta Materialia* 50.3, pp. 511–523. (Cit. on pp. 77, 151).

— (2002b). "Cavity growth during superplastic flow in an Al-Mg alloy: I. Experimental study". In: *Acta Materialia* 50.5, pp. 993–1009. (Cit. on pp. 77, 78).

Ball, A. and M. M. Hutchison (1969). "Superplasticity in the Aluminium Zinc Eutectoid". In: *Metal Science* 3.1, pp. 1–7. (Cit. on pp. 41, 48).

Balluffi, R. W. and L. L. Seigle (1957). "Growth of voids in metals during diffusion and creep". In: *Acta Metallurgica* 5.8, pp. 449–454. (Cit. on pp. 65, 66, 69, 70).

Barnett, M. R. (2001). "Influence of deformation conditions and texture on the high temperature flow stress of magnesium AZ31". In: *Journal of Light Metals* 1.3, pp. 167–177. (Cit. on p. 107).

— (2003). "A taylor model based description of the proof stress of magnesium AZ31 during hot working". In: *Metallurgical and Materials Transactions A* 34.9, pp. 1799–1806. (Cit. on p. 31).

Barnett, M. R., Z. Keshavarz, A. G. Beer, and D. Atwell (2004). "Influence of grain size on the compressive deformation of wrought Mg-3Al-1Zn". In: *Acta Materialia* 52.17, pp. 5093–5103. (Cit. on p. 33).

Barnett, M. R., Z. Keshavarz, and M. Nave (2005). "Microstructural features of rolled Mg-3Al-1Zn". In: *Metallurgical and Materials Transactions A* 36.7, pp. 1697–1704. (Cit. on p. 37).

Bate, P. S. (2001). "The effect of deformation on grain growth in Zener pinned systems". In: *Acta Materialia* 49.8, pp. 1453–1461. (Cit. on p. 63).

— (2006). *MSc class notes*. (Cit. on pp. 93, 119).

Bate, P. S., F. J. Humphreys, N. Ridley, and B. Zhang (2005). "Microstructure and texture evolution in the tension of superplastic Al-6Cu-0.4Zr". In: *Acta Materialia* 53.10, pp. 3059–3069. (Cit. on p. 51).

Bauer, R. W. and H. G. F. Wilsdorf (1973). "Void initiation in ductile fracture". In: *Scripta Metallurgica* 7.11, pp. 1213–1220. (Cit. on p. 65).

Beere, W. and M. V. Speight (1978). "Creep cavitation by vacancy diffusion in plastically deforming solid". In: *Metal Science* 12, pp. 172–176. (Cit. on pp. 69, 70, 156).

Bell, R. L. and T. G. Langdon (1967). "An investigation of grain-boundary sliding during creep". In: *Journal of Materials Science* 2.4, pp. 313–323. (Cit. on p. 46).

Bohlen, J., D. Letzig, and K.U. Kainer (2007). "New perspectives for wrought magnesium alloys". In: *Materials Science Forum* 546-549.PART 1, pp. 1–10. (Cit. on p. 19).

Brandes, E. A. and G. B. Brook (1998). *Smithells Light Metals Handbook*. Oxford: Elsevier Butterworth-Heinemann, p. 176. (Cit. on p. 82).

Brinkman, J. A. (1955). "Mechanism of pore formation associated with the Kirkendall effect". In: *Acta Metallurgica* 3.2, pp. 140–145. (Cit. on p. 65).

Burton, B. (1974). "On the growth of grain boundary cavities in poiycrystalline materials". In: *Philosophical Magazine* 30.4, pp. 953–956. (Cit. on p. 71).

Càceres, C. H. and A. Blake (2002). "The Strength of Concentrated Mg-Zn Solid Solutions". In: *physica status solidi (a)* 194.1, pp. 147–158. (Cit. on p. 28).

Càceres, C. H. and D.S Wilkinson (1984a). "Large strain behaviour of a superplastic copper alloy–I. Deformation". In: *Acta Metallurgica* 32.3, pp. 415–422. (Cit. on pp. 57, 164).

Càceres, C. H. and D.S. Wilkinson (1984b). "Large strain behaviour of a superplastic copper alloy–II. Cavitation and fracture". In: *Acta Metallurgica* 32.3, pp. 423–434. (Cit. on pp. 74, 75).

Cannon, W. R. (1972). "The contribution of grain boundary sliding to axial strain during diffusion creep". In: *Philosophical Magazine* 25.6, pp. 1489–1497. (Cit. on pp. 47, 48).

Celotto, S. (2000). "TEM study of continuous precipitation in Mg-9 wt%Al-1 wt%Zn alloy". In: *Acta Materialia* 48.8, pp. 1775–1787. (Cit. on p. 27).

Chang, J., E. Taleff, and P. Krajewski (2009). "Effect of Microstructure on Cavitation during Hot Deformation of a Fine-Grained Aluminum-Magnesium Alloy as Revealed through Three-Dimensional Characterization". In: *Metallurgical and Materials Transactions A* 40.13, pp. 3128–3137. (Cit. on pp. 77, 78).

Chen, C. W. and E. S. Machlin (1956). "On the mechanism of intelcrystalline cracking". In: *Acta Metallurgica* 4.6, pp. 655–656. (Cit. on p. 66).

Chino, Yasumasa, Katsuya Kimura, and Mamoru Mabuchi (2009). "Deformation characteristics at room temperature under biaxial tensile stress in textured AZ31 Mg alloy sheets". In: *Acta Materialia* 57.5, pp. 1476–1485. (Cit. on p. 37).

Chokshi, A. H. and T. G. Langdon (1987). "Model for diffusional cavity growth in superplasticity". In: *Acta Metallurgica* 35.5, pp. 1089–1101. (Cit. on p. 71).

— (1990). "The nucleation and growth of cavities in a superplastic quasi-single phase copper alloy". In: *Acta Metallurgica et Materialia* 38.5, pp. 867–877. (Cit. on p. 76).

Chokshi, A. H. and A. K. Mukherjee (1989a). "An analysis of cavity nucleation in superplasticity". In: *Acta Metallurgica* 37.11, pp. 3007–3017. (Cit. on pp. 68, 150).

— (1989b). "The cavitation and fracture characteristics of a superplastic Al–Cu–Li–Zr alloy". In: *Materials Science and Engineering: A* 110, pp. 49–60. (Cit. on pp. 76, 77).

Chokshi, A. H., K. M. A., and T. G. Langdon (1993a). "Superplasticity in advanced materials". In: *Materials Science and Engineering: R: Reports* 10.6, pp. 237–274. (Cit. on p. 38).

Chokshi, A. H., A. K. Mukherjee, and T. G. Langdon (1993b). "Superplasticity in advanced materials". In: *quoted in Bengough, G.D.: Materials Science and Engineering: R: Reports* 10.6, pp. 237–274. (Cit. on p. 42).

Chokshi, Atul H. (1986). "Development of cavity growth maps for superplastic materials". In: *Journal of Materials Science* 21.6, pp. 2073–2082. (Cit. on p. 71).

Christian, J. W. and S. Mahajan (1995). "Deformation twinning". In: *Progress in Materials Science* 39.1-2, pp. 1–157. (Cit. on p. 32).

Chuvil'deev, V. N., T. G. Nieh, M. Yu. Gryaznov, A. N. Sysoev, and V. I. Kopylov (2004a). "Low-temperature superplasticity and internal friction in microcrystalline Mg alloys processed by ECAP". In: *Scripta Materialia* 50.6, pp. 861–865. (Cit. on p. 39).

Chuvil'deev, V. N., T. G. Nieh, M. Yu. Gryaznov, V. I. Kopylov, and A. N. Sysoev (2004b). "Superplasticity and internal friction in microcrystalline AZ91 and ZK60 magnesium alloys processed by equal-channel angular pressing". In: *Journal of Alloys and Compounds* 378.1-2, pp. 253–257. (Cit. on p. 39).

Clark, J. B. (1968). "Age hardening in a Mg-9 wt% Al alloy". In: *Acta Metallurgica* 16.2, pp. 141–152. (Cit. on p. 27).

Clark, M. A. and T. H. Alden (1973). "Deformation enhanced grain growth in a superplastic Sn-1% Bi alloy". In: *Acta Metallurgica* 21.9, pp. 1195–1206. (Cit. on p. 63).

Cliff, G., D.J. Powell, R. Pilkington, P.E. Champness, and G.W. Lorimer (1984). "X-ray microanalysis of second phase particles in thin foils". In: *Inst. Phys. Conf. Ser. Electron Microscopy and Analysis, Paper presented at EMAG, Guildford, 30 August–2 September 1983*. Ed. by P. Doig. Vol. No. 68: Chapter 3. London: The Institute of Physics, pp. 63–66. (Cit. on pp. 101, 103).

Coble, R. L. (1963). "A Model for Boundary Diffusion Controlled Creep in Polycrystalline Materials". In: *Journal of Applied Physics* 34.6, pp. 1679–1682. (Cit. on p. 45).

Cottrell, A. H. (1961). "Intercrystalline Creep Fractures". In: *Structural Processes in Creep*. Vol. Special Report Number 70. London: The Iron and Steel Institute, pp. 1–18. (Cit. on p. 67).

Cottrell, A. H. and M. A. Jaswon (1949). "Distribution of Solute Atoms Round a Slow Dislocation". In: *Proceedings of the Royal Society of London. Series A. Mathematical and Physical Sciences* 199.1056, pp. 104–114. (Cit. on p. 54).

Davies, C. and M. Barnett (2004). "Expanding the extrusion limits of wrought magnesium alloys". In: *JOM* 56.5, pp. 22–24. (Cit. on p. 26).

Davies, P. W. and J. P. Dennison (1958). "Void nucleation sites in creep of metals". In: *Nature* 182.4628, pp. 131–132. (Cit. on p. 66).

Davies, P. W. and K. R. Williams (1969). "Strain-Induced Cavity Development during Creep". In: *Metal Science* 3, pp. 48–50. (Cit. on p. 75).

Del Valle, J., M. Pérez-Prado, and O. Ruano (2005). "Deformation mechanisms responsible for the high ductility in a Mg AZ31 alloy analyzed by electron backscattered diffraction". In: *Metallurgical and Materials Transactions A* 36.6, pp. 1427–1438. (Cit. on pp. 60, 116).

Del Valle, J. A. and O. A. Ruano (2006). "Influence of the grain size on the strain rate sensitivity in an Mg-Al-Zn alloy at moderate temperatures". In: *Scripta Materialia* 55.9, pp. 775–778. (Cit. on p. 125).

Del Valle, J. A., M. T. Pérez-Prado, and O. A. Ruano (2003). "Texture evolution during large-strain hot rolling of the Mg AZ61 alloy". In: *Materials Science and Engineering A* 355.1-2, pp. 68–78. (Cit. on pp. 35, 37, 96).

Del Valle, J. A., F. Carreño, and O. A. Ruano (2006). "Influence of texture and grain size on work hardening and ductility in magnesium-based alloys processed by ECAP and rolling". In: *Acta Materialia* 54.16, pp. 4247–4259. (Cit. on p. 33).

Derby, B. and M. F. Ashby (1987). "A Microstructural model for primary creep". In: *Acta Metallurgica* 35.6, pp. 1349–1353. (Cit. on p. 56).

Dieter, G. E. (2001). *Mechanical Metallurgy*. SI Metric. Singapore: McGraw-Hill Book Company, Chapter 4, 6, 8 and 20. (Cit. on pp. 29, 32, 33, 56, 114).

Ding, S. X., C. P. Chang, and P. W. Kao (2009). "Effects of Processing Parameters on the Grain Refinement of Magnesium Alloy by Equal-Channel Angular Extrusion". In: *Metallurgical and Materials Transactions A* 40.2, pp. 415–425. (Cit. on p. 37).

Doege, E., K. Droder, and St. Janssen (2003). "Deformation of Magnesium". In: *Magnesium - Alloys and Technologies*. Ed. by K. U. Kainer. Weinheim: Wiley - VCH Verlag GmbH & Co, pp. 72–89. (Cit. on p. 25).

Dupuy, L. and J. J. Blandin (2002). "Damage sensitivity in a commercial Al alloy processed by equal channel angular extrusion". In: *Acta Materialia* 50.12, pp. 3253–3266. (Cit. on p. 77).

Ecob, N. and B. Ralph (1983). "The effect of grain size on deformation twinning in a textured zinc alloy". In: *Journal of Materials Science* 18.8, pp. 2419–2429. (Cit. on p. 32).

Eddahbi, M., J. A. del Valle, M. T. Pérez-Prado, and O. A. Ruano (2005). "Comparison of the microstructure and thermal stability of an AZ31 alloy processed by ECAP and large strain hot rolling". In: *Materials Science and Engineering: A* 410-411, pp. 308–311. (Cit. on p. 82).

Edington, J. W., K. N. Melton, and C. P. Cutler (1976). "Superplasticity". In: *Progress in Materials Science* 21.1-2, pp. 61–170. (Cit. on pp. 40, 41, 44–46, 49, 54, 57).

Edward, G.H. and M.F. Ashby (1979). "Intergranular fracture during power-law creep". In: *Acta Metallurgica* 27.9, pp. 1505–1518. (Cit. on p. 71).

Endoh, S. (2006). *Powder Technology Handbook*. Edition 3rd. Boca Raton, Florida: CRC Press, Taylor & Francis Group, Chapter 1.3. (Cit. on pp. 155, 160).

Erickson, S. C. (1990). "Pure Metals, Magnesium". In: *Metals Handbook, Properties and Selection: Nonferrous Alloys and Special-Purpose Materials*. Vol. 2. USA: ASM International. (Cit. on p. 22).

Fan, Z., Y. Wang, M. Xia, and S. Arumuganathar (2009). "Enhanced heterogeneous nucleation in AZ91D alloy by intensive melt shearing". In: *Acta Materialia* 57.16, pp. 4891–4901. (Cit. on p. 28).

Feldkamp, L. A., L. C. Davis, and J. W. Kress (1984). "Practical cone-beam algorithm". In: *Journal of the Optical Society of America A* 1.6, pp. 612–619. (Cit. on p. 88).

Figueiredo, R. B. and T. G. Langdon (2008). "Record Superplastic Ductility in a Magnesium Alloy Processed by Equal-Channel Angular Pressing". In: *Advanced Engineering Materials* 10.1-2, pp. 37–40. (Cit. on pp. 38, 39, 62).

— (2009b). "Strategies for achieving high strain rate superplasticity in magnesium alloys processed by equal-channel angular pressing". In: *Scripta Materialia* 61.1, pp. 84–87. (Cit. on p. 41).

— (2009a). "Principles of grain refinement and superplastic flow in magnesium alloys processed by ECAP". In: *Materials Science and Engineering: A* 501.1-2, pp. 105–114. (Cit. on p. 125).

Fisher, J. C. (1955). "A dislocation model for the origin of fracture cracks in metal crystals". In: *Acta Metallurgica* 3.1, pp. 109–110. (Cit. on p. 66).

Friedel, J. (1964). *Dislocations*. Vol. 3. Solid State Physics. Oxford: Pergamon Press Ltd., pp. 6, 279, 290. (Cit. on pp. 44, 48).

Frost, H. J. and M. F. Ashby (1982). *Deformation-Mechanism Maps: The Plasticity and Creep of Metals and Ceramics*. Oxford: Pergamon Press, Chapter 2 and 6. (Cit. on pp. 45, 56, 114, 116, 120).

Furui, M., H. Kitamura, H. Anada, and T. G. Langdon (2007). "Influence of preliminary extrusion conditions on the superplastic properties of a magnesium alloy processed by ECAP". In: *Acta Materialia* 55.3, pp. 1083–1091. (Cit. on p. 39).

Galano, M., F. Audebert, A. G. Escorial, I. C. Stone, and B. Cantor (2009). "Nanoquasicrystalline Al-Fe-Cr-based alloys. Part II. Mechanical properties". In: *Acta Materialia* 57.17, pp. 5120–5130. (Cit. on p. 77).

Galiyev, A., R. Kaibyshev, and G. Gottstein (2001). "Correlation of plastic deformation and dynamic recrystallization in magnesium alloy ZK60". In: *Acta Materialia* 49.7, pp. 1199–1207. (Cit. on p. 36).

Gehrmann, R., M. M. Frommert, and G. Gottstein (2005). "Texture effects on plastic deformation of magnesium". In: *Materials Science and Engineering A* 395.1-2, pp. 338–349. (Cit. on p. 34).

Ghosh, A. K. (1977). "Tensile instability and necking in materials with strain hardening and strain-rate hardening". In: *Acta Metallurgica* 25.12, pp. 1413–1424. (Cit. on p. 58).

Gibeling, J.G. and W.D. Nix (1980). "A numerical study of long range internal stresses associated with subgrain boundaries". In: *Acta Metallurgica* 28.12, pp. 1743–1752. (Cit. on p. 56).

Gifkins, R. C. (1956). "A mechanism for the formation of intergranular cracks when boundary sliding occurs". In: *Acta Metallurgica* 4.1, pp. 98–99. (Cit. on pp. 66, 67, 75).

— (1976). "Grain-boundary sliding and its accommodation during creep and superplasticity". In: *Metallurgical and Materials Transactions A* 7.7, pp. 1225–1232. (Cit. on p. 50).

— (1978). "Grain rearrangements during superplastic deformation". In: *Journal of Materials Science* 13.9, pp. 1926–1936. (Cit. on pp. 51–53).

— (1991). "Ductility and strain-rate control mechanisms in superplasticity". In: *Scripta Metallurgica et Materialia* 25.6, pp. 1397–1400. (Cit. on p. 51).

— (1994). "Grain-boundary participation in high-temperature deformation: an historical review". In: *Materials Characterization* 32.2, pp. 59–77. (Cit. on pp. 50, 51).

Gifkins, R. C., T. G. Langdon, and D. McLean (1975). "Grain-Boundary Sliding and Axial Strain during Diffusional Creep". In: *Metal Science* 9, pp. 141–144. (Cit. on p. 47).

Glicksman, M. E. and R. N. Hills (2001). "Non-equilibrium segregation during alloy solidification". In: *Philosophical Magazine A: Physics of Condensed Matter, Structure, Defects and Mechanical Properties* 81.1, pp. 153–159. (Cit. on p. 88).

Goods, S.H and W.D Nix (1978). "The coalescence of large grain boundary cavities in silver during tension creep". In: *Acta Metallurgica* 26.5, pp. 753–758. (Cit. on p. 74).

Greenwood, G.W. and J. E. Harris (1965). "Note on vacancy condensation on particles". In: *Acta Metallurgica* 13.8, pp. 936–936. (Cit. on p. 67).

Greenwood, J. Neill, D. R. Miller, and J. W. Suiter (1954). "Intergranular cavitation in stressed metals". In: *Acta Metallurgica* 2.2, pp. 250–258. (Cit. on p. 65).

Groves, G. W. and A. Kelly (1963). "Independent slip systems in crystals". In: *Philosophical Magazine* 8.89, pp. 877–887. (Cit. on p. 30).

Gudmundsson, H., D. Brooks, and J.A. Wert (1991). "Mechanisms of continuous recrystallization in an Al–Zr–Si alloy". In: *Acta Metallurgica et Materialia* 39.1, pp. 19–35. (Cit. on p. 62).

Hamilton, C. H., C. C. Bampton, and N. E. Paton (1982). "Superplasticity in High Strength Aluminum Alloys". In: *Superplastic Forming of Structural Alloys*. Ed. by N. E. Paton and C. H. Hamilton. San Diego: The Metallurgical Society of AIME, pp. 173–189. (Cit. on p. 40).

Hancock, J. W. (1976). "Creep cavitation without a vacancy flux". In: *Metal Science* 10, pp. 319–325. (Cit. on pp. 72, 156).

Harper, J and J.E Dorn (1957). "Viscous creep of aluminum near its melting temperature". In: *Acta Metallurgica* 5.11, pp. 654–665. (Cit. on p. 46).

Harris, G. W., V. J. Haddrell, and G. A. Rickards (1962). "Metallographic examination of intergranular creep cavities in two magnesium alloys". In: *Journal of Nuclear Materials* 6.1, pp. 144–147. (Cit. on p. 78).

Harris, J. E. (1965). "An analysis of creep ductility of magnox Al80 and its implications". In: *Journal of Nuclear Materials* 15.3, pp. 201–207. (Cit. on p. 67).

Hart, E. W. (1957). "On the role of dislocations in bulk diffusion". In: *Acta Metallurgica* 5.10, pp. 597–597. (Cit. on p. 56).

— (1967). "A theory for flow of polycrystals". In: *Acta Metallurgica* 15.9, pp. 1545–1549. (Cit. on p. 57).

Herring, C. (1950). "Diffusional Viscosity of a Polycrystalline Solid". In: *Journal of Applied Physics* 21.5, pp. 437–445. (Cit. on p. 44).

Hosokawa, H., H. Iwasaki, T. Mori, M. Mabuchi, T. Tagata, and K. Higashi (1999). "Effects of Si on deformation behavior and cavitation of coarse-grained Al-4.5Mg alloys exhibiting large elongation". In: *Acta Materialia* 47.6, pp. 1859–1867. (Cit. on p. 78).

Housh, S., B. Mikucki, and A. Stevenson (1990). *ASM Handbook, Properties and Selection: Nonferrous Alloys and Special-Purpose Materials*. Vol. Volume 2. USA: ASM International, Chapter Selection and Application of Magnesium and Magnesium Alloys. (Cit. on pp. 24, 25).

Hull, D. and D. E. Rimmer (1959). "Growth of grain-boundary voids under stress". In: *Philosophical Magazine* 4.42, pp. 673–687. (Cit. on pp. 68, 69).

Humphreys, F. J. and M. Hatherly (2004). *Recrystallization and Related Phenomena*. 2nd Edition. Oxford: Elsevier Ltd, Chapter 5 and 13. (Cit. on pp. 34–36, 123).

Humphries, C. W. and N. Ridley (1978). "Cavitation during the superplastic deformation of an α/β brass". In: *Journal of Materials Science* 13.11, pp. 2477–2482. (Cit. on p. 77).

Imayev, R. M., G. A. Salishchev, O. N. Senkov, V. M. Imayev, M. R. Shagiev, N. K. Gabdullin, A. V. Kuznetsov, and F. H. Froes (2001). "Low-temperature superplasticity of titanium aluminides". In: *Materials Science and Engineering A* 300.1-2, pp. 263–277. (Cit. on p. 39).

Ion, S. E., F. J. Humphreys, and S. H. White (1982). "Dynamic recrystallisation and the development of microstructure during the high temperature deformation of magnesium". In: *Acta Metallurgica* 30.10, pp. 1909–1919. (Cit. on pp. 34, 35).

Isaac, A., F. Sket, W. Reimers, B. Camin, G. Sauthoff, and A. R. Pyzalla (2008). "In situ 3D quantification of the evolution of creep cavity size, shape, and spatial orientation using synchrotron X-ray tomography". In: *Materials Science and Engineering: A* 478.1-2, pp. 108–118. (Cit. on p. 160).

Janeček, M., M. Popov, M. G. Krieger, R. J. Hellmig, and Y. Estrin (2007). "Mechanical properties and microstructure of a Mg alloy AZ31 prepared by equal-channel angular pressing". In: *Materials Science and Engineering A* 462.1-2, pp. 116–120. (Cit. on p. 82).

Jiang, Xinggang, Jianzhong Cui, and Longxiang Ma (1993). "The influence of the rolling direction on the mechanical behavior and cavity formation during

superplastic deformation of 7075 A1 alloy". In: *Acta Metallurgica et Materialia* 41.9, pp. 2721–2727. (Cit. on p. 77).

Jin, Q., S. Shim, and S. Lim (2006). "Correlation of microstructural evolution and formation of basal texture in a coarse grained Mg-Al alloy during hot rolling". In: *Scripta Materialia* 55.9, pp. 843–846. (Cit. on p. 35).

Kai, M., Z. Horita, and T. G. Langdon (2008). "Developing grain refinement and superplasticity in a magnesium alloy processed by high-pressure torsion". In: *Materials Science and Engineering: A* 488.1-2, pp. 117–124. (Cit. on p. 37).

Kaibyshev, R. and O. Osipova (2005). "Superplastic behaviour of an Al-Li-Cu-Mg alloy". In: *Materials Science and Technology* 21.10, pp. 1209–1216. (Cit. on p. 39).

Kainer, K. U. and F. von Buch (2003). "The Current State of Technology and Potential for further Development of Magnesium Applications". In: *Magnesium Alloys and Technology*. Ed. by K. U. Kainer. Weinheim: Wiley - VCH Verlag GmbH & Co, pp. 1–22. (Cit. on p. 23).

Kashyap, B. and K. Tangri (1987). "On the contribution of concurrent grain growth to strain". In: *Metallurgical and Materials Transactions A* 18.4, pp. 417–424. (Cit. on p. 64).

Kassner, M. E. and M. Pérez-Prado (2004). *Fundamentals of Creep in Metals and Alloys*. Oxford: Elsivier, Chapter 2, 3, 4 and 5. (Cit. on pp. 49, 56).

Kawasaki, M. and T. G. Langdon (2007). "Principles of superplasticity in ultrafine-grained materials". In: *Journal of Materials Science* 42.5, pp. 1782–1796. (Cit. on p. 37).

Kawasaki, M., C. Xu, and T. G. Langdon (2005). "An investigation of cavity growth in a superplastic aluminum alloy processed by ECAP". In: *Acta Materialia* 53.20, pp. 5353–5364. (Cit. on pp. 76, 78).

Kim, W. J., S. W. Chung, C. S. Chung, and D. Kum (2001). "Superplasticity in thin magnesium alloy sheets and deformation mechanism maps for magnesium alloys at elevated temperatures". In: *Acta Materialia* 49.16, pp. 3337–3345. (Cit. on pp. 38, 43, 59, 61).

Kim, Y. M., C. D. Yim, and B. S. You (2007). "Grain refining mechanism in Mg-Al base alloys with carbon addition". In: *Scripta Materialia* 57.8, pp. 691–694. (Cit. on p. 28).

King, J. F. (2007). "Magnesium: commodity or exotic". In: *Materials Science and Technology* 23.1, pp. 1–14. (Cit. on pp. 18, 19).

Koike, J. and R. Ohyama (2005). "Geometrical criterion for the activation of prismatic slip in AZ61 Mg alloy sheets deformed at room temperature". In: *Acta Materialia* 53.7, pp. 1963–1972. (Cit. on p. 37).

Kulas, M., W. Green, E. Taleff, P. Krajewski, and T. McNelley (2006). "Failure mechanisms in superplastic AA5083 materials". In: *Metallurgical and Materials Transactions A* 37.3, pp. 645–655. (Cit. on pp. 75, 78).

Langdon, T. G. (1970). "Grain boundary sliding as a deformation mechanism during creep". In: *Philosophical Magazine* 22.178, pp. 689–700. (Cit. on p. 47).

— (1991). "The physics of superplastic deformation". In: *Materials Science and Engineering: A* 137, pp. 1–11. (Cit. on p. 42).

— (1994). "A unified approach to grain boundary sliding in creep and superplasticity". In: *Acta Metallurgica et Materialia* 42.7, pp. 2437–2443. (Cit. on p. 48).

— (2000). "Identifiying creep mechanisms at low stresses". In: *Materials Science and Engineering A* 283.1-2, pp. 266–273. (Cit. on p. 47).

Langdon, T. G. (2009). "Seventy-five years of superplasticity: historic developments and new opportunities". In: *Journal of Materials Science* 44.22, pp. 5998–6010. (Cit. on p. 38).

Langdon, T. G. and F. A. Mohamed (1976). "Deformation mechanism maps for ceramics". In: *Journal of Materials Science* 11.2, pp. 317–327. (Cit. on p. 45).

Laser, T., M. R. Núrnberg, A. Janz, Ch. Hartig, D. Letzig, R. Schmid-Fetzer, and R. Bormann (2006). "The influence of manganese on the microstructure and mechanical properties of AZ31 gravity die cast alloys". In: *Acta Materialia* 54.11, pp. 3033–3041. (Cit. on pp. 29, 96).

Lee, C. J. and J. C. Huang (2004). "Cavitation characteristics in AZ31 Mg alloys during LTSP or HSRSP". In: *Acta Materialia* 52.10, pp. 3111–3122. (Cit. on pp. 61, 78, 79, 127, 166).

Lee, D (1969). "The nature of superplastic deformation in the Mg-Al eutectic". In: *Acta Metallurgica* 17.8, pp. 1057–1069. (Cit. on p. 40).

Lee, S., M. Furukawa, Z. Horita, and T. G. Langdon (2003). "Developing a superplastic forming capability in a commercial aluminum alloy without scandium or zirconium additions". In: *Materials Science and Engineering A* 342.1-2, pp. 294–301. (Cit. on p. 39).

Lee, S. M. and T. G. Langdon (2001). "High strain rate superplasticity in a Zn - 22equal-channel angular pressing". In: *Materials Science Forum* 357-359, pp. 321–326. (Cit. on p. 39).

Li, F., D. H. Bae, and A. K. Ghosh (1997). "Grain elongation and anisotropic grain growth during superplastic deformation in an Al–Mg–Mn–Cu alloy". In: *Acta Materialia* 45.9, pp. 3887–3895. (Cit. on p. 63).

Li, H.B., J. Zhao, J.T. Luo, and M. Hang (2007). "Superplastic Behaviors of Casting AZ31 Magnesium Alloy". In: *Materials Science Forum* 551-552, pp. 237–239. (Cit. on p. 61).

Lin, H. K., J. C. Huang, and T. G. Langdon (2005). "Relationship between texture and low temperature superplasticity in an extruded AZ31 Mg alloy processed by ECAP". In: *Materials Science and Engineering A* 402.1-2, pp. 250–257. (Cit. on p. 39).

Livesey, D. W. and N. Ridley (1982). "Effect of grain size on cavitation in superplastic Zn-Al eutectoid". In: *Journal of Materials Science* 17.8, pp. 2257–2266. (Cit. on p. 77).

Livesey, D. W., N. Ridley, and A. K. Mukherjee (1984). "Activation energies for superplastic tensile and compressive flow in microduplex α/β copper alloys". In: *Journal of Materials Science* 19.11, pp. 3602–3611. (Cit. on p. 41).

Lorimer, G. W., G. Cliff, P. E. Champness, C. Dickinson, F. Hasan, and P. Kenway (1984). "In-situ X-ray microanalysis of second phase particles in thin foils". In: *Analytical Electron Microscopy*. Ed. by D.B. Williams and D.C. Joy. San Francisco: San Francisco Press, pp. 153–156. (Cit. on pp. 101, 103).

Lou, X.Y., M. Li, R. K. Boger, S. R. Agnew, and R. H. Wagoner (2007). "Hardening evolution of AZ31B Mg sheet". In: *International Journal of Plasticity* 23.1, pp. 44–86. (Cit. on pp. 33, 34).

Luo, A. and M. O. Pekguleryuz (1994). "Cast magnesium alloys for elevated temperature applications". In: *Journal of Materials Science* 29.20, pp. 5259–5271. (Cit. on pp. 27, 28).

Ma, Z. Y. and R. S. Mishra (2003). "Cavitation in superplastic 7075Al alloys prepared via friction stir processing". In: *Acta Materialia* 51.12, pp. 3551–3569. (Cit. on pp. 76, 77).

Maire, E., J. Y. Buffiére, L. Salvo, J. J. Blandin, W. Ludwig, and J. M. Létang (2001). "On the Application of X-ray Microtomography in the Field of Materials Science". In: *Adv. Eng. Mater.* 3.8, pp. 539–546. (Cit. on p. 88).

Matsubara, K., Y. Miyahara, Z. Horita, and T. G. Langdon (2003). "Developing superplasticity in a magnesium alloy through a combination of extrusion and ECAP". In: *Acta Materialia* 51.11, pp. 3073–3084. (Cit. on p. 39).

Matsuki, K., H. Morita, M. Yamada, and Y. Murakami (1977). "Relative motion of grains during superplastic flow in an Al-9Zn-1 wt.Mg alloy". In: *Metal Science* 11, pp. 156–163. (Cit. on p. 48).

McLean, D. (1966). "The physics of high temperature creep in metals". In: *Reports on Progress in Physics* 29.1, pp. 1–33. (Cit. on p. 67).

McNelley, T. R., D.J. Michel, and A. Salama (1989). "The Mg-concentration dependence of the strength of A1–Mg alloys during glide-controlled deformation". In: *Scripta Metallurgica* 23.10, pp. 1657–1662. (Cit. on p. 55).

McNelley, T. R., K. Oh-Ishi, A. P. Zhilyaev, S. Swaminathan, P. E. Krajewski, and E. M. Taleff (2008). "Characteristics of the Transition from Grain-Boundary Sliding to Solute Drag Creep in Superplastic AA5083". In: *Metallurgical and Materials Transactions A* 39.1, pp. 50–64. (Cit. on p. 116).

Miller, D. A. and T. G. Langdon (1980). "Independent and sequential cavity growth mechanisms". In: *Scripta Metallurgica* 14.1, pp. 143–148. (Cit. on p. 73).

Miller, D. A., F. A. Mohamed, and T. G. Langdon (1979). "An analysis of cavitation failure incorporating cavity nucleation with strain". In: *Materials Science and Engineering* 40.2, pp. 159–166. (Cit. on p. 68).

Miyahara, Y., Z. Horita, and T. G. Langdon (2006). "Exceptional superplasticity in an AZ61 magnesium alloy processed by extrusion and ECAP". In: *Materials Science and Engineering: A* 420.1-2, pp. 240–244. (Cit. on p. 39).

Mohamed, F. A. and T. G. Langdon (1974). "The transition from dislocation climb to viscous glide in creep of solid solution alloys". In: *Acta Metallurgica* 22.6, pp. 779–788. (Cit. on p. 55).

— (1976). "Deformation mechanism maps for superplastic materials". In: *Scripta Metallurgica* 10.8, pp. 759–762. (Cit. on p. 42).

— (1981). "Flow localization and neck formation in a superplastic metal". In: *Acta Metallurgica* 29.5, pp. 911–920. (Cit. on p. 58).

Mohri, T., M. Mabuchi, M. Nakamura, T. Asahina, H. Iwasaki, T. Aizawa, and K. Higashi (2000). "Microstructural evolution and superplasticity of rolled Mg-9Al-1Zn". In: *Materials Science and Engineering A* 290.1-2, pp. 139–144. (Cit. on p. 62).

Mordike, B. L. and P. Lukac (2006). "Magnesium Technology: Metallurgy, Design Data, Applications". In: *Magnesium Technology: Metallurgy, Design Data, Applications*. Ed. by Horst E. Friedrich and Barry L. Mordike. Berlin Heidelberg: Springer-Verlag. Chap. Physical Metallurgy, Chapter 3. (Cit. on pp. 28, 29).

Mordike, B. L., K. Harbodt, Lukáč, and H. Westengen (2006). *Magnesium Technology: Metallurgy, Design Data and Applications*. Ed. by H. E. Friedrich and B. L. Mordike. Springer-Verlag. Chap. Chapter 1, Chapter 1, 3 and 5. (Cit. on pp. 18, 24, 25).

Mott, N. F. (1953). "Bakerian Lecture. Dislocations, Plastic Flow and Creep". In: *Proceedings of the Royal Society of London. Series A. Mathematical and Physical Sciences* 220.1140, pp. 1–14. (Cit. on pp. 46, 55).

Mukherjee, A. K. (1971). "The rate controlling mechanism in superplasticity". In: *Materials Science and Engineering* 8.2, pp. 83–89. (Cit. on p. 49).

Murai, T., S. I. Matsuoka, S. Miyamoto, and Y. Oki (2003). "Effects of extrusion conditions on microstructure and mechanical properties of AZ31B magnesium alloy extrusions". In: *Journal of Materials Processing Technology* 141.2, pp. 207–212. (Cit. on p. 81).

Mussi, A., J. J. Blandin, L. Salvo, and E. F. Rauch (2006). "Resistance to strain-induced damage of an ultrafine-grained magnesium alloy deformed in superplastic conditions". In: *Acta Materialia* 54.14, pp. 3801–3809. (Cit. on pp. 78, 152).

Myshlyaev, M. M., H. J. McQueen, A. Mwembela, and E. Konopleva (2002). "Twinning, dynamic recovery and recrystallization in hot worked Mg-Al-Zn alloy". In: *Materials Science and Engineering A* 337.1-2, pp. 121–133. (Cit. on p. 35).

Nabarro, F. (2002). "Creep at very low rates". In: *Metallurgical and Materials Transactions A* 33.2, pp. 213–218. (Cit. on p. 46).

Nave, M. K. and M. R. Barnett (2004). "Microstructures and textures of pure magnesium deformed in plane-strain compression". In: *Scripta Materialia* 51.9, pp. 881–885. (Cit. on p. 32).

Needleman, A. and J. R. Rice (1980). "Plastic creep flow effects in the diffusive cavitation of grain boundaries". In: *Acta Metallurgica* 28.10, pp. 1315–1332. (Cit. on p. 68).

Neishi, K., Z. Horita, and T. G. Langdon (2001). "Achieving superplasticity in a Cu-40plastic deformation". In: *Scripta Materialia* 45.8, pp. 965–970. (Cit. on p. 39).

Nicolaou, P. D. and S. L. Semiatin (1999). "Modeling of cavity coalescence during tensile deformation". In: *Acta Materialia* 47.13, pp. 3679–3686. (Cit. on p. 74).

— (2000). "An analysis of the effect of continuous nucleation and coalescence on cavitation during hot tension testing". In: *Acta Materialia* 48.13, pp. 3441–3450. (Cit. on p. 74).

Nieh, T. G., J. Wadsworth, and O. D. Sherby (1997). *Superplasticity in Metals and Ceramics*. Cambridge: Cambridge University Press, pp. 32–57. (Cit. on p. 59).

Nieh, T. G., L. M. Hsiung, J. Wadsworth, and R. Kaibyshev (1998). "High strain rate superplasticity in a continuously recrystallized Al-6%Mg-0.3%Sc alloy". In: *Acta Materialia* 46.8, pp. 2789–2800. (Cit. on p. 125).

Obara, T., H. Yoshinga, and S. Morozumi (1973). "$\{1122\}\langle 1123\rangle$ Slip system in magnesium". In: *Acta Metallurgica* 21.7, pp. 845–853. (Cit. on p. 31).

Ohno, M., D. Mirkovic, and R. Schmid-Fetzer (2006). "Phase equilibria and solidification of Mg-rich Mg-Al-Zn alloys". In: *Materials Science and Engineering: A* 421.1-2, pp. 328–337. (Cit. on p. 102).

Panicker, R., A. H. Chokshi, R. K. Mishra, R. Verma, and P. E. Krajewski (2009). "Microstructural evolution and grain boundary sliding in a superplastic magnesium AZ31 alloy". In: *Acta Materialia* 57.13, pp. 3683–3693. (Cit. on pp. 60, 61).

Park, K., D. Hwang, Y. Lee, Y. Kim, and D. H. Shin (2003). "High strain rate superplasticity of submicrometer grained 5083 Al alloy containing scandium

fabricated by severe plastic deformation". In: *Materials Science and Engineering A* 341.1-2, pp. 273–281. (Cit. on p. 39).

Pekguleryuz, M. O. and A. A. Kaya (2003). "Creep Resistant Magnesium Alloys for Powertrain Applications". In: *Advanced Engineering Materials* 5.12, pp. 866–878. (Cit. on p. 25).

Pérez-Prado, M. T., J. A. del Valle, and O. A. Ruano (2004). "Effect of sheet thickness on the microstructural evolution of an Mg AZ61 alloy during large strain hot rolling". In: *Scripta Materialia* 50.5, pp. 667–671. (Cit. on pp. 61, 82).

Pettersen, G., H. Westengen, R. Høier, and O. Lohne (1996). "Microstructure of a pressure die cast magnesium–4wt.% aluminium alloy modified with rare earth additions". In: *Materials Science and Engineering A* 207.1, pp. 115–120. (Cit. on p. 25).

Picu, R. C., G. Vincze, J. J. Gracio, and F. Barlat (2006). "Effect of solute distribution on the strain rate sensitivity of solid solutions". In: *Scripta Materialia* 54.1, pp. 71–75. (Cit. on p. 120).

Pilling, J. (1985). "Effect of coalescence on cavity growth during superplastic deformation". In: *Materials Science and Technology* 1, pp. 461–465. (Cit. on p. 74).

Pilling, J. and N. Ridley (1988a). "Cavitation in Aluminium Alloys during Superplastic Flow". In: *Superplasticity in Aerospace*. Ed. by H. C. Heikkenen and T. R. McNelley. Proceedings of a symposium sponsored by the Shaping and Forming Committee. The Metallurgical Society, Inc., pp. 183–198. (Cit. on pp. 77, 79, 165).

— (1988b). "Cavitation in Superplastic Alloys and the Effect of Hydrostatic Pressure". In: *Res mechanica* 23.1, pp. 31–63. (Cit. on pp. 72, 73).

Pilling, J and N. Ridley (1989). *Superplasticity in Crystalline Solids*. London: The Institute of Metals, Chapter 1, 3–6. (Cit. on pp. 38, 39, 42, 49, 50, 52, 53, 56, 64, 124, 166).

Pilling, J., D. W. Livesey, J. B. Hawkyard, and N. Ridley (1984). "Solid state bonding in superplastic Ti-6Al-4V". In: *Metal Science* 18.3, pp. 117–122. (Cit. on p. 71).

Polmear, I. J. (1994). "Magnesium alloys and applications". In: *Materials Science and Technology* 10, pp. 1–16. (Cit. on p. 27).

— (2006). *Light Alloys: From Traditional Alloys to Nanocrystals*. Oxford: Butterworth-Heinemann, Elsevier, Chapter 5. (Cit. on pp. 24, 25, 27, 81).

Raj, R. and M. F. Ashby (1975). "Intergranular fracture at elevated temperature". In: *Acta Metallurgica* 23.6, pp. 653–666. (Cit. on p. 67).

Raj, R. and F.F. Lange (1985). "On the retention of equiaxed grain structure after superplastic and other forms of high temperature deformation". In: *Acta Metallurgica* 33.4, pp. 699–703. (Cit. on p. 60).

Reed-Hill, R. E. and W. D. Robertson (1957). "Additional modes of deformation twinning in magnesium". In: *Acta Metallurgica* 5.12, pp. 717–727. (Cit. on p. 32).

Reed-Hill, Robert E. (1973). *Physical Metallurgy Principles*. New York: D. Van Nostrand Company, Chapter 8. (Cit. on p. 54).

Ridley, N., D. W. Livesey, and A. K. Mukherjee (1984). "Effect of strain, strain rate and temperature on cavity size distribution in a superplastic copper-base alloy". In: *Journal of Materials Science* 19.4, pp. 1321–1332. (Cit. on p. 73).

Ridley, N., P. S. Bate, and B. Zhang (2005). "Material modelling data for superplastic forming optimisation". In: *Materials Science and Engineering: A* 410-411, pp. 100–104. (Cit. on pp. 63, 86).

Ridley, N., P. S. Bate, and B. Zhang (2007). "Effect of strain rate path on cavitation in superplastic aluminium alloy". In: *Materials Science and Engineering A* 463.1-2, pp. 224–230. (Cit. on pp. 68, 77).

Riedel, H. (1987). *Fracture at High Temperatures*. Materials Research and Engineering. Heidelberg: Springer-Verlag, Chapter 1–6. (Cit. on pp. 68, 69).

Sagat, S. and D.M.R. Taplin (1976). "Fracture of a superplastic ternary brass". In: *Acta Metallurgica* 24.4, pp. 307–315. (Cit. on p. 72).

Saunders, N., Z. Guo, X. Li, A.P. Miodownik, and J.-Ph. Schillé (2003). "Using JMatPro to Model Materials Properties and Behaviour". In: *JOM* 55.12, pp. 60–65. (Cit. on p. 88).

Schmidt, C.G. and A. K. Miller (1982). "The effect of solutes on the strength and strain hardening behavior of alloys". In: *Acta Metallurgica* 30.3, pp. 615–625. (Cit. on p. 120).

Seitz, F. (1953). "On the porosity observed in the Kirkendall effect". In: *Acta Metallurgica* 1.3, pp. 355–369. (Cit. on p. 65).

Senkov, O. N. and V. A. Likhachev (1986). "The Effect of Grain Growth on the Plastic Instabilities and Uniaxial Tensile Ductilities in Superplastic Alloys". In: *physica status solidi (a)* 98.2, pp. 441–452. (Cit. on p. 63).

Senkov, O. N. and M. M. Myshlyaev (1986). "Grain growth in a superplastic Zn-22% Al alloy". In: *Acta Metallurgica* 34.1, pp. 97–106. (Cit. on p. 64).

Sherby, O. D. and P. M. Burke (1968). "Mechanical behavior of crystalline solids at elevated temperature". In: *Progress in Materials Science* 13, pp. 323–390. (Cit. on p. 55).

Sherby, O. D. and E. M. Taleff (2002). "Influence of grain size, solute atoms and second-phase particles on creep behavior of polycrystalline solids". In: *Materials Science and Engineering A* 322.1-2, pp. 89–99. (Cit. on p. 55).

Sherby, O. D. and J. Wadsworth (1982). "Development and Characterization of Fine-Grain Superplastic Materials". In: *AMS Materials Science Seminar*. Ed. by George Krauss. Deformation, Processing, and Structure. St. Louis, Missouri: Deformation, Processing, and Structure, American Society for Metals 1984, pp. 355–389. (Cit. on pp. 40, 52, 59, 60).

— (1989). "Superplasticity–Recent advances and future directions". In: *Progress in Materials Science* 33.3, pp. 169–221. (Cit. on pp. 38, 40).

Sherby, O. D. and J. Weertman (1979). "Diffusion-controlled dislocation creep: a defense". In: *Acta Metallurgica* 27.3, pp. 387–400. (Cit. on p. 55).

Shibutani, T., T. Kitamura, and R. Ohtani (1998). "Creep cavity growth under interaction between lattice diffusion and grain-boundary diffusion". In: *Metallurgical and Materials Transactions A* 29.10, pp. 2533–2542. (Cit. on p. 71).

Sigler, J. A. and D. Kuhlmann-Wilsdorf (1967). "Calculations on the Mechanical Energy of Vacancy Condensation Loops, Stacking Fault Tetrahedra, and Voids". In: *physica status solidi (b)* 21.2, pp. 545–556. (Cit. on p. 65).

Silverman, B. W. (1992). *Density Estimation for Statistics and Data Analysis*. Monographs on Statistics and Applied Probability. London: Chapman & Hall/CRC, p. 42. (Cit. on p. 92).

Sitdikov, O., R. Kaibyshev, and T. Sakai (2003). "Dynamic recrystallization based on twinning in coarse-grained Mg". In: *Materials Science Forum* 419-422.I, pp. 521–526. (Cit. on p. 35).

Slutsky, L. J. and C. W. Garland (Aug. 1957). "Elastic Constants of Magnesium from 4.2 °K to 300 °K". In: *Physical Review* 107.4, pp. 972–976. (Cit. on p. 59).

Somekawa, H. and T. Mukai (2007). "Effect of dominant diffusion process on cavitation behavior in superplastic Mg-Al-Zn alloy". In: *Scripta Materialia* 57.11, pp. 1008–1011. (Cit. on p. 78).

Spingarn, J.R. and W.D. Nix (1978). "Diffusional creep and diffusionally accommodated grain rearrangement". In: *Acta Metallurgica* 26.9, pp. 1389–1398. (Cit. on p. 53).

Stalmann, A., W. Sebastian, H. Friedrich, S. Schumann, and K. Dröder (2001). "Properties and Processing of Magnesium Wrought Products for Automotive Applications". In: *Advanced Engineering Materials* 3.12, pp. 969–974. (Cit. on p. 27).

Stanford, N. and M. R. Barnett (2008). "Fine grained AZ31 produced by conventional thermo-mechanical processing". In: *Journal of Alloys and Compounds* 466.1-2, pp. 182–188. (Cit. on pp. 33, 37, 96).

Stanford, N., I. Sabirov, G. Sha, A. La Fontaine, S. Ringer, and M. R. Barnett (2010). "Effect of Al and Gd Solutes on the Strain Rate Sensitivity of Magnesium Alloys". In: *Metallurgical and Materials Transactions A* 41.3, pp. 734–743. (Cit. on p. 120).

Stock, S. R. (2008). "Recent advances in X-ray microtomography applied to materials". In: *International Materials Reviews* 53, pp. 129–181. (Cit. on p. 87).

Stowell, M. J. (1980). "Cavity growth in superplastic alloys". In: *Metal Science* 14, pp. 267–272. (Cit. on pp. 72, 74).

— (1983). "Failure of superplastic alloys". In: *Metal Science* 17, pp. 1–11. (Cit. on p. 68).

Stowell, M. J., D. W. Livesey, and N. Ridley (1984). "Cavity coalescence in superplastic deformation". In: *Acta Metallurgica* 32.1, pp. 35–42. (Cit. on p. 74).

Takigawa, Y., J. V. Aguirre, E. M. Taleff, and K. Higashi (2008). "Cavitation during grain-boundary-sliding deformation in an AZ61 magnesium alloy". In: *Materials Science and Engineering: A* 497.1-2, pp. 139–146. (Cit. on pp. 61, 78).

Taleff, E., G. Henshall, T. Nieh, D. Lesuer, and J. Wadsworth (1998). "Warm-temperature tensile ductility in Al-Mg alloys". In: *Metallurgical and Materials Transactions A* 29.3, pp. 1081–1091. (Cit. on p. 55).

Taleff, E., P. Nevland, and P. Krajewski (2001). "Tensile ductility of several commercial aluminum alloys at elevated temperatures". In: *Metallurgical and Materials Transactions A* 32.5, pp. 1119–1130. (Cit. on pp. 78, 167).

Tan, J. C. and M. J. Tan (2003a). "Dynamic continuous recrystallization characteristics in two stage deformation of Mg-3Al-1Zn alloy sheet". In: *Materials Science and Engineering A* 339.1-2, pp. 124–132. (Cit. on p. 62).

— (2003b). "Superplasticity and grain boundary sliding characteristics in two stage deformation of Mg-3Al-1Zn alloy sheet". In: *Materials Science and Engineering A* 339.1-2, pp. 81–89. (Cit. on p. 61).

Tegart, W. J. McG. (1961). "Activation energies for high temperature creep of polycrystalline magnesium". In: *Acta Metallurgica* 9.6, pp. 614–617. (Cit. on p. 55).

Vagarali, S. S. and T. G. Langdon (1981). "Deformation mechanisms in h.c.p. metals at elevated temperatures–I. Creep behavior of magnesium". In: *Acta Metallurgica* 29.12, pp. 1969–1982. (Cit. on p. 59).

Vagarali, S. S. and T. G. Langdon (1982). "Deformation mechanisms in h.c.p. metals at elevated temperatures–II. Creep behavior of a Mg-0.8% Al solid solution alloy". In: *Acta Metallurgica* 30.6, pp. 1157–1170. (Cit. on p. 55).

Valiev, R. Z. and T. G. Langdon (2006). "Principles of equal-channel angular pressing as a processing tool for grain refinement". In: *Progress in Materials Science* 51.7, pp. 881–981. (Cit. on p. 37).

Von Batchelder, F. W. and R. F. Raeuchle (1957). "Lattice Constants and Brillouin Zone Overlap in Dilute Magnesium Alloys". In: *Physical Review* 105.1, pp. 59–61. (Cit. on p. 22).

VSG (2010). *Avizo 5.1 3D Visualization Software User Manual*. http://www.vsg3d.com. Burlington, MA. (Cit. on p. 90).

Wang, L., M. Song, and R. Liu (2006). "Superplasticity and superplastic instability of AZ31B magnesium alloy sheet". In: *Transactions of Nonferrous Metals Society of China (English Edition)* 16.2, pp. 327–332. (Cit. on p. 61).

Wang, Y. and J. Huang (2004). "Transition of dominant diffusion process during superplastic deformation in AZ61 magnesium alloys". In: *Metallurgical and Materials Transactions A* 35.2, pp. 555–562. (Cit. on p. 61).

Wang, Y. N. and J. C. Huang (2003). "Texture analysis in hexagonal materials". In: *Materials Chemistry and Physics* 81.1, pp. 11–26. (Cit. on p. 107).

Wang, Y.N. and J.C. Huang (2007). "The role of twinning and untwinning in yielding behavior in hot-extruded Mg-Al-Zn alloy". In: *Acta Materialia* 55.3, pp. 897–905. (Cit. on p. 32).

Watanabe, H. and M. Fukusumi (2008). "Mechanical properties and texture of a superplastically deformed AZ31 magnesium alloy". In: *Materials Science and Engineering: A* 477.1-2, pp. 153–161. (Cit. on p. 61).

Watanabe, H., T. Mukai, and K. Higashi (1999b). "Superplasticity in a ZK60 magnesium alloy at low temperatures". In: *Scripta Materialia* 40.4, pp. 477–484. (Cit. on p. 62).

Watanabe, H., T. Mukai, M. Kohzu, S. Tanabe, and K. Higashi (1999a). "Effect of temperature and grain size on the dominant diffusion process for superplastic flow in an AZ61 magnesium alloy". In: *Acta Materialia* 47.14, pp. 3753–3758. (Cit. on pp. 43, 53, 60, 61).

Watanabe, H., H. Tsutsui, T. Mukai, M. Kohzu, S. Tanabe, and K. Higashi (2001). "Deformation mechanism in a coarse-grained Mg-Al-Zn alloy at elevated temperatures". In: *International Journal of Plasticity* 17.3, pp. 387–397. (Cit. on pp. 61, 116).

Watts, B. M., M. J. Stowell, and D. M. Cottingham (1971). "The variation in flow stress and microstructure during superplastic deformation of the Al-Cu eutectic". In: *Journal of Materials Science* 6.3, pp. 228–237. (Cit. on p. 63).

Weertman, J. (1955). "Theory of Steady-State Creep Based on Dislocation Climb". In: *Journal of Applied Physics* 26.10, pp. 1213–1217. (Cit. on pp. 46, 55).

— (1957). "Steady-State Creep of Crystals". In: *Journal of Applied Physics* 28.10, pp. 1185–1189. (Cit. on p. 54).

Weidmann, E. (1993). *Metallography and Microstructure*. Vol. 9. ASM International, Electrolyte Polishing. (Cit. on p. 85).

Wilkinson, D. S. and C. H. Càceres (1984). "On the mechanism of strain-enhanced grain growth during superplastic deformation". In: *Acta Metallurgica* 32.9, pp. 1335–1345. (Cit. on p. 63).

Wilkinson, D. S. and C. H. Càceres (1986). "Mechanism of plastic void growth during superplastic flow". In: *Materials Science and Technology* 2, pp. 1086–1092. (Cit. on p. 164).

Xu, C., M. Furukawa, Z. Horita, and T. G. Langdon (2005). "Influence of ECAP on precipitate distributions in a spray-cast aluminum alloy". In: *Acta Materialia* 53.3, pp. 749–758. (Cit. on p. 39).

Yang, Q. and A. K. Ghosh (2006). "Production of ultrafine-grain microstructure in Mg alloy by alternate biaxial reverse corrugation". In: *Acta Materialia* 54.19, pp. 5147–5158. (Cit. on p. 82).

— (2008). "Formability of Ultrafine-Grain Mg Alloy AZ31B at Warm Temperatures". In: *Metallurgical and Materials Transactions A* 39.11, pp. 2781–2796. (Cit. on p. 62).

Yavari, P., D. A. Miller, and T. G. Langdon (1982). "An investigation of harper-dorn creep–I. Mechanical and microstructural characteristics". In: *Acta Metallurgica* 30.4, pp. 871–879. (Cit. on p. 46).

Ye, L., X. Zhang, D. Zheng, S. Liu, and J. Tang (2009). "Superplastic behavior of an Al–Mg–Li alloy". In: *Journal of Alloys and Compounds* 487.1-2, pp. 109–115. (Cit. on p. 128).

Yi, S., J. Bohlen, F. Heinemann, and D. Letzig (2010). "Mechanical anisotropy and deep drawing behaviour of AZ31 and ZE10 magnesium alloy sheets". In: *Acta Materialia* 58.2, pp. 592–605. (Cit. on pp. 31, 37).

Yin, D. L., K. F. Zhang, G. F. Wang, and W. B. Han (2005). "Superplasticity and cavitation in AZ31 Mg alloy at elevated temperatures". In: *Materials Letters* 59.14–15, pp. 1714–1718. (Cit. on p. 61).

Zarandi, F., G. Seale, R. Verma, E. Essadiqi, and S. Yue (2008). "Effect of Al and Mn additions on rolling and deformation behavior of AZ series magnesium alloys". In: *Materials Science and Engineering A* 496.1-2, pp. 159–168. (Cit. on pp. 61, 119).

Zhang, M. X., P. M. Kelly, M. Qian, and J. A. Taylor (2005). "Crystallography of grain refinement in Mg-Al based alloys". In: *Acta Materialia* 53.11, pp. 3261–3270. (Cit. on p. 28).

Zhilyaev, A. P. and T. G. Langdon (2008). "Using high-pressure torsion for metal processing: Fundamentals and applications". In: *Progress in Materials Science* 53.6, pp. 893–979. (Cit. on p. 37).

Appendix A

Parameters used in the Current Study

Table A.1: Material constants and parameters used in the current project

Parameter	**Symbol**	**Value**
Atomic Volume[a]	Ω (m^3)	2.33×10^{-28}
Boltzmann's Constant	k (J K^{-1})	1.38×10^{-23}
Surface Energy	γ (J m^{-2})	0.56
Berger's Vector[a]	**b** (m)	3.21×10^{-10}
Grain Boundary Width	δ (m)	$2\times(3.21 \times 10^{-10})$
Pre-exponential for Grain Boundary Diffusion[a]	δD_{GB} (m^3 s^{-1})	5×10^{-12}
Pre-exponential for Lattice Diffusion[a]	$D_{o,L}$ (m^2 s^{-1})	10^{-4}
Activation Energy for Grain Boundary Diffusion[a]	Q_{GB} (kJ mol^{-1})	92
Activation Energy for Lattice Diffusion[a]	Q_L (kJ mol^{-1})	135
Molar Gas Constant	R (J mol^{-1} K^{-1})	8.314

[a] Source: FROST, H. J. & ASHBY, M. F. (1982) Deformation-Mechanism Maps, Oxford, Pergamon Press.Chapter 6

Appendix B

Methodology for Defining Axes of Regions from 3D Data Set

After identifying 3D coordinates of each voxel for each region of the X-ray micro tomography data set and tagging the similar type of connected voxels as a single region of particle or cavity, the list of coordinates was used to determine size, aspect ratio and orientation. From the 3D images, it was obvious that most of the regions are not spherical. Therefore, instead of considering the regions as spheroid to get the corresponding radii, it is useful to determine the major (a), minor (b) and polar axes (c) considering the regions as ellipsoids.

According to Newton's first law, a moment of inertia (I) of an object of mass M is defined as

$$I = MR^2 \tag{B.1}$$

where R is the distance between the axis and the centroid of the object. I is also known as the second moment of mass. Now, for a volume or system of reference XYZ containing a continuum of N objects, I can be defined as

$$I = \sum_{i=1}^{N} M_i R_i^2. \tag{B.2}$$

Mass inertia components of I for the system mentioned above can be defined as the symmetric inertia tensor or inertia matrix $\acute{I}$ as

$$\acute{I} = \begin{pmatrix} I_{xx} & I_{xy} & I_{xz} \\ I_{yx} & I_{yy} & I_{yz} \\ I_{zx} & I_{zy} & I_{zz} \end{pmatrix} \tag{B.3}$$

where I_{xx}, I_{yy} and I_{zz} are the mass moments of inertia of the volume about the x, y and z axes and I_{xy}, I_{xz}, I_{yx}, I_{yz}, I_{zx} and I_{zy} are mass products of inertia about the

corresponding pair of axes. These moments of inertia and products of inertia can be obtained from the 3D coordinate list as

$$I_{xx} = \int (y - y_o)^2 + (z - z_o)^2 \, \mathrm{d}M \tag{B.4}$$

$$I_{yy} = \int (x - x_o)^2 + (z - z_o)^2 \, \mathrm{d}M \tag{B.5}$$

$$I_{zz} = \int (x - x_o)^2 + (y - y_o)^2 \, \mathrm{d}M \tag{B.6}$$

$$I_{xy} = I_{yx} = -\int (x - x_o)^2 + (y - y_o)^2 \, \mathrm{d}M \tag{B.7}$$

$$I_{xz} = I_{zx} = -\int (x - x_o)^2 + (z - z_o)^2 \, \mathrm{d}M \tag{B.8}$$

$$I_{zy} = I_{yz} = -\int (y - y_o)^2 + (z - z_o)^2 \, \mathrm{d}M \tag{B.9}$$

where $(x_o \, y_o \, z_o)$ is the coordinates of the centroid for a particular object and $(x \, y \, z)$ is the coordinates of position of that object. The symmetric $\acute{I}$ has positive eigenvalues and three orthogonal eigenvectors. Using Matlab, these eigenvalues and eigenvectors of $\acute{I}$ can be promptly solved. Then, the angle between axis of rotation for each object in the volume or system and the corresponding eigenvectors can be determined.

Using this methodology for each region of particles and cavities, the orientation with respect to tensile (z-axis of the 3D data set) can be defined.

Now, using the eigenvalues of the inertia tensor matrix of the regions, a rectangle of similar dimension containing the ellipsoid can be drawn to obtain the corresponding dimensions of each region. From this rectangle, a, b and c which belong to the major, minor and polar axes of an ellipsoid, can be determined.

To determine the eigenvalues and eigenvectors, an existing Matlab script (Dr. T. J. Marrow, University of Manchester) was modified.

MOON, F. C. (1998) Applied Dynamics: with Applications to Multibody and Mechatronic Systems, New York, John Wiley & Sons, Inc., 185